Electronic structure/function relationships in metal nanowires: components for molecular electronics

Vihar Petkov Georgiev

Linacre College

Thesis submitted for the Degree of Doctor of Philosophy

Hilary Term 2011

Department of Chemistry, University of Oxford

Abstract

Electronic structure/function relationship in metal nanowires: components for molecular electronics

Vihar Petkov Georgiev
Linacre College

Thesis submitted for the Degree of Doctor of Philosophy
Hilary Term 2011
Department of Chemistry, University of Oxford

The dramatic expansion of the electronics industry over the past 40 years has been based on the progressive reduction in size of the silicon-based semiconductor components of integrated circuits. The miniaturisation of semi-conductor circuits cannot, however, continue indefinitely, and we are rapidly approaching the stage where quantum effects will prevent further dramatic improvements in computer performance using existing technology. As a result, the field of molecular electronics, which seeks to identify and develop much smaller molecular analogues of the transistors that make up integrated circuits, has expanded rapidly over the past few years.

Recent studies suggested that extended metal atom chains (EMAC) may have many potential applications in molecular electronics, but it is clear that this potential can only be realised if we establish a link between the fundamental electronic properties of these systems and the transport of electrons. For this reason the ultimate goal of this thesis is to relate the electronic structure of extended metal chains to their electron transport properties. We address the problem using non-equilibrium Green's function, in conjugation with density functional theory.

In the results sections of this thesis we present calculations on tricobalt, trichromium and trinickel chains. Our data suggested that in the trimetal chains, the dominant electron transport channel is the σ manifold, while the π systems establish the contact with the electrodes. The implication of this is that even when the highly polarized π channels are strongly rehybridised by the applied electric field, current flow is not affected. In the trichromium systems we find that the distortion of the chain away from the symmetric equilibrium structure does not perturb the current flow but rather enhances it. Our rather counter intuitive conclusion is therefore that 'broken wires' (highly unsymmetric) are more efficient conductors than their symmetric counterparts. We have performed calculation on longer penta- and heptacobalt structures chains to establish the extent to which longer structures attenuate the conductance. Our calculations show significant oscillations of the conductance due to development of a one-dimensional band structure about the Fermi level. The evolution of the electron transport properties in cobalt chains with different length is a complex one, but it is clear that narrowing the band gap in longer chains makes it increasingly likely that the Fermi level will be in resonance with one or more of the orbitals of the extended metal atom chain.

Preface

This thesis is an account of work carried out by the author in the Chemistry Department, University of Oxford, under the supervision of Prof. John E McGrady. No part of this thesis has previously been submitted for a degree in this University or elsewhere. The work of other authors has been freely drawn and is duly acknowledged in the text. A list of references is given at the end of the thesis.

Work presented in this thesis has been or will be published in the following scientific journals and presented in conference proceedings:

Papers:

1. 'The influence of unsymmetric distortions on electron transport through metal atom chains: when is a molecular wire 'broken'?'

   Vihar P. Georgiev and John E. McGrady, *J. Am. Chem. Soc.,* **2011,** in press.

2. 'Efficient spin Filtering through cobalt-base extended metal atom chains'

   Vihar P. Georgiev and John E. McGrady, *Inorg. Chem.*, **2010**, 49(12), 5591-5597.

Posters and presentations:

1. Presentation at Graduate Symposium, Inorganic Chemistry Laboratory, University of Oxford, UK, **2010**.

2. Presentation at QuantumWise Workshop, Copenhagen, Denmark, **2009.**

3. Flash and Poster Presentation at 42nd IUPAC Conference, Glasgow, UK, **2009.**

4. Flash and Poster Presentation at 3rd ScotChem Computational Chemistry Symposium, Edinburgh, UK, **2009**.

5. Presentation at Device Modeling Group Meeting, Glasgow, UK, **2008**.

6. Poster Presentation at 2nd ScotChem Computational Chemistry Symposium, Glasgow, UK, **2008**.

Acknowledgments

I would like to express my deep gratitude to my supervisor, Prof. John McGrady, for his guidance and support. He has been an excellent supervisor and he was always helpful and encouraging when I faced problems in the course of my research.

As a member of the McGrady group over the last couple of years I have been fortunate to work with Muhsen Al-Ibadi, Dr. Thomas Darvin, Tobias Krämer, P.J. Mohan, and Evdokia Salamanova, whom I would like to thank for their stimulating feedback. Additionally, I want to thank Prof. Michel Etienne and Dr. Ekaterina Zueva. Our conversations helped me to expand my knowledge in my main field of research and beyond. I hope that we will be able to continue our work in the future.

I want to make a special acknowledgement to Anna Andrzejewska for her help, support and understanding. Without her encouragement this thesis would not be possible.

Last but not least, I want to thank my parents, Anelia and Petko Petkovi, for their support and believing in my skills and potential. [Накрая бих искал да благодаря на мойте родители, Анелия и Петко, за това че винаги са били до мен и са ме подкрепяли във всичко. Без тях, моето образувание нямаше да бъде възможно. Благодаря Ви от все сърце.]

Table of Contents

Chapter 1

Introduction

1.1 An overview of molecular electronics

One of the most often searched words in the Google search engine in 2010 was 'Ipad'. It is no surprise then that this tablet and similar electronic devices are a common feature in our lives and that they create a trend in the electronics industry at the beginning of the twenty first century. Nowadays these new products need not only to be powerful and fast but also mobile and multifunctional. In order to create a perfect device from the point of view of technology and marketing, the first step is to understand the computational architecture that allows these devices to work.

The 'heart' of each electronic device is an integrated circuit built from transistors, wires and diodes on a single chip. Each chip contains millions, nowadays even billions, of transistors. A larger number of transistors makes the chip faster and able to handle more tasks simultaneously. Hence, in order to increase the productivity and efficiency of any electronic-based systems it is enough to increase the number of the transistors. This, however, can prove problematic. On the one hand, more transistors require more space and therefore devices bigger in size but, on the other hand, the costumers demand smaller, cheaper, more powerful and mobile devices. The only possible way to achieve this target is to decrease the size of the integrated circuit components. This

trend for miniaturisation without compromising the power and the performance is at the moment the main driving force in the industry of electronic devices.

In 1965 Gordon Moore[1] predicted that with each new generation of memory chips and microprocessor units being released on the market, the device size will be reduced by 33%, the chip size will decrease by 50% and the number of components on a chip will quadruple every three years. So far this prediction has proved accurate and on this basis transistors should reach atomic dimensions by 2012. At these dimensions, however, the silicon-based technology will meet several physical and economic limitations.[2-4] From an economic point of view Moore's Second Law, stating that facility costs also follow an exponential growth, is valid. This is due to the fact that R&D, manufacture and tests become more and more expensive with each new generation. Additionally, it has been observed that the semiconductor industry cannot continue at the same rate of growth indefinitely because it would exceed the gross world product at some point.[5] On the other hand, fundamental barriers for solid state transistors, such as thermal or heat dissipation, leakage current and thermal noise, exist.[6] Hence, if we want to develop better and more efficient electronic devices in the future, we should endeavour to overcome these problems.

To understand these physical limitations the scientists need a detailed knowledge about how the main building block of the microprocessor, that is a transistor, works. The second half of the twentieth century has seen significant progress in engineering and manufacturing of transistors based on solid state materials. The most popular transistor architecture in modern devices is a metal-oxide semiconductor field-effective transistor (MOSFET). A semiconductor is a substance, usually a solid chemical element or compound, which can conduct electricity under some conditions

but not others, making it a good medium for the control of electrical current. Some typical elements used as semiconductors are antimony, arsenic, boron, carbon, germanium, selenium, silicon, and tellurium. Common semiconductor compounds include gallium arsenide, indium antimonide and the oxides of most metals. The most popular semiconductor is silicon because it is an abundant and cheap resource, and most transistors and related components of integrated circuits are made from it.

The defining property of semiconductors is an ability to conduct electricity, dependent on temperature (intrinsic semiconductor) or on the levels of impurities, or dopants, added to them (extrinsic semiconductors). In the process of doping, a tiny concentration of atoms from another material is added to the pure semiconductor crystal lattice, increasing the conductance drastically. There are two ways of doping, p and n, where p stands for positive and n for negative (Figure 1-1).

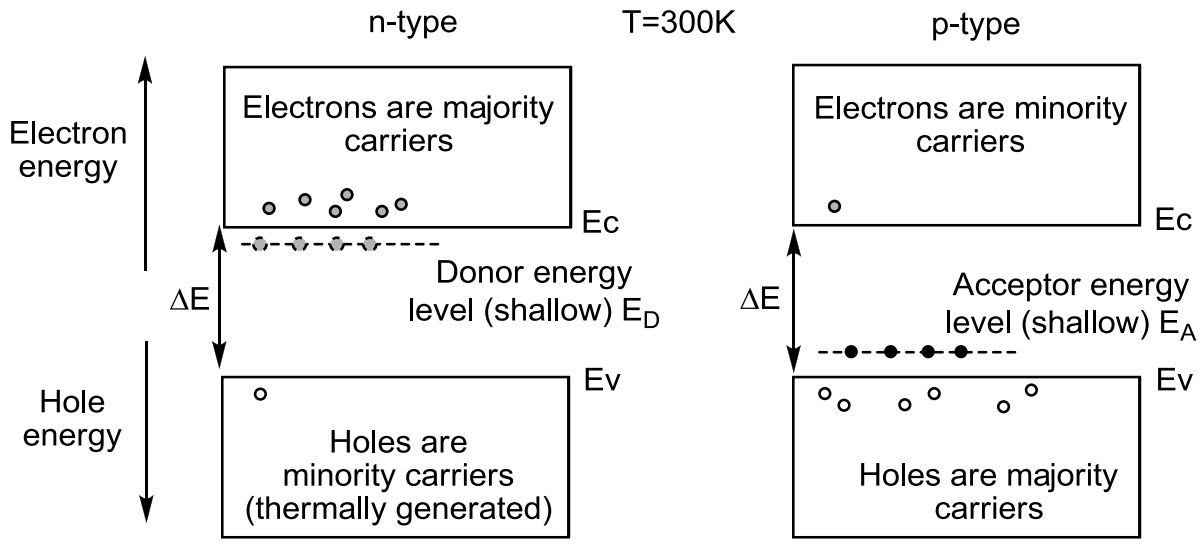

Figure 1-1: Electrical carriers in n-type (left) and p-type (right) extrinsic material at 300 K; E_c – energy of Conduction band, E_V – energy of Valence band and ΔE – the band gap.

In the process of n-doping, atoms with one extra valence electron are added to the pure semiconducting material. This creates a situation where loosely bound electrons lie close to the Fermi level, allowing current flow in the material to increase significantly. Hence, the n-type semiconductor carries current mainly in the form of negatively-charged electrons, in a manner similar to the conduction of current in a wire. On the other hand, p-doping occurs when atoms with fewer valence electrons are added to the semiconductor and current is predominantly carried by positively charged holes. In a semiconductor material, the flow of holes occurs in a direction opposite to the flow of electrons.

As noted above, the most popular transistors in modern electronic devices are MOSFET (metal-oxide semiconductor field effect transistors). From a practical point of view the MOSFET type of transistor was a major breakthrough in the technology because it allowed the construction of integrated circuit components on a single block of semiconducting material. Each such transistor has source, drain, gate electrodes, insulator layer and channel (Figure 1-2).

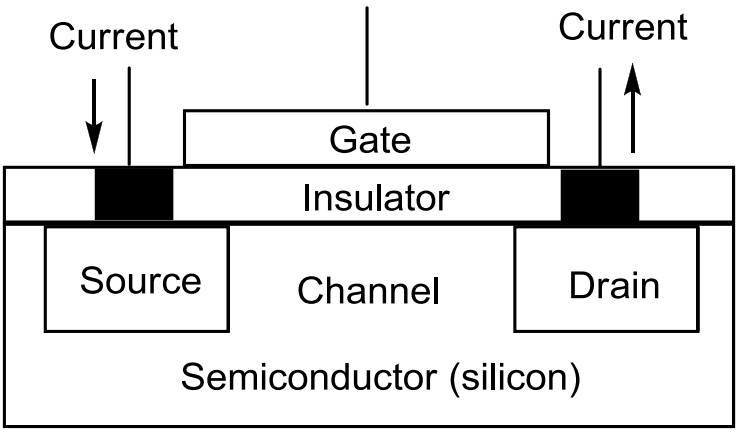

Figure 1-2: Simplified diagram of a field effect transistor.

The transistor can be compared simply to a valve which controls a water flow in a pipe or to a tap in a sink. By applying different voltages at the gate (closing off the tap or the valve) it is possible to control the current flow (water flow) in the transistor (Figure 1-2). The source and the drain are directly connected by a channel, while the polysilicon gate electrode is separated from the channel by an insulator layer, such as SiO_2. When the voltage on the gate is positive, electrons can flow from the source to the drain. In this way the channel conducts electricity and transistor is in an 'on' state. To 'turn off' the transistor, the voltage on the gate electrode is removed. Hence, by regulating the voltage of the gate we can easily switch 'on' and 'off' the transistor. This conceptually simple and reliable technology was the basis of the rapid growth of computer-controlled devices in the second half of the twentieth century.

From an engineering point of view the critical part in the transistor is the SiO_2 insulator layer – gate oxide. In order to achieve maximum efficiency, the gate oxide should be thick enough to isolate the gate electrode from the current-carrying electrodes. If this is not the case, the current will penetrate through to the gate oxide causing a chip fail. This in turn leads to the following question of how small the transistor can be and what is the minimal thickness of the gate oxide? More generally, what are physical limitations of the existing technology and MOSFET-based devices? In theory, gate oxide layers of less than 0.7 nm in thickness or of less than four layers of silicon atoms are unable to prevent the current leakage from the source to the gate electrode.[7,8] In practice, the gate oxide needs to be slightly thicker than the theoretical limit. For example, it can consist of five layers of silicon atoms, because the interface is rough on the atomic level. This limitation is fundamental and new technology is therefore needed in order to meet further demand for miniaturisation.

One attractive alternative to silicon-based architectures is to replace the solid state transistors and other components of the chip with molecules. In principle, they could be used as building blocks for switches, wires and storage elements in integrated circuits. This 'bottom-up' synthetic approach, known as field of molecular electronics, is the basis of the relatively new field of 'molecular electronics.' In short, molecular electronics deals with single molecular systems in which individual molecules are fundamental units of future computational components. Molecular electronics has four main advantages over the crystal-based technology. First, and most obvious, molecules are orders of magnitude smaller than the smallest accessible silicon-based component, and so they offer obvious advantages of scale. Second, the self-assembly properties of molecules at the nanometre scale allow the construction of complex circuits in a fast and cost-efficient way. Third, the physical properties of molecules can be tailored by chemical synthesis. This offers the possibility of engineering specific electronic functionalities. Finally, molecules can often exist in different isomeric forms with distinct optical and electronic properties.[9] Switching between isomers can potentially provide a basis for controlling current flow in the same way as the gate voltage in conventional devices. However, molecular electronics has some important disadvantages too. The main one is the instability of most molecules at high temperature. In some cases their synthesis may also require dangerous and toxic starting components which make the chemical synthesis a challenging and cost-ineffective task. On balance, however, molecule electronics has more advantages than disadvantages and it seems inevitable that it will form the basis of new computer architectures in the near future.

The attractive features set out in the previous paragraph have led to a rapid development in the molecular electronics field over the past two decades. This has been possible largely due to the invention and advances of scanning probe techniques which allowed manipulation and operation at an atomic level. During the 1990s a number of research groups attempted to measure the current that goes through a self-assembled monolayer using a scanning tunnelling microscope (STM)[10-13] or mechanically-controlled break junction technique.[14] Later researchers used atomic force microscopy[15-18] or an evaporated top metal contact[19-21] to measure the conductance in self-assembled monolayers. Unlike electron microscopy, these new methods do not require a partial vacuum and can be performed in air at standard temperature and pressure or even while submerged in a liquid reaction vessel. This allowed for the first time the measurement of current flow through organic molecules, such as DNA and proteins. However, organising the molecules in a monolayer has a number of disadvantages: it is not clear how many molecules lie between the electrodes and therefore whether the measured conductance corresponds to only one molecule. Additionally, the geometry of molecule and its junction to the an electrode interface, both of which have a strong influence over electron transport, are unknown, making reproducible measurements very difficult. The characteristics of a molecule device are not simply a function of the molecule itself, but also of the electrode. The key experiment that provided significant progress in this respect is the scanning tunnelling microscope (STM) break junction technique combined with multiple measurements of the conductance (to gather good statistical data).[22-31] This statistical approach makes it possible to compare the electron transport properties of different molecules and to identify trends that would be

otherwise hidden because of the random variations of molecular or molecule-junction geometry.[32,33] In addition, inelastic electronic tunnelling spectroscopy has revealed significant details of a molecule-electrode junction.[34-46] Unfortunately, even with this improvement of experiment technique the precise atomic-scale geometry remains debatable. Clearly the very limited knowledge of microscopic geometry of the molecule/electrode interface is a serious bottle-neck to our understanding of the properties of these systems.

Despite these problems, it has been possible over the past decade to measure the electron transport properties of chemical or biological systems. The big challenge is now to find molecules which behave analogously to different components of the integrated circuit (prototype wires, rectifiers, switches and transistors). Much of the progress can be divided into two distinct categories of molecule: conjugated organic systems and metal-organic complexes. We will discuss these two groups separately in the following paragraphs.

1.2 Conjugated organic systems

Organic conductors have a long history, dating at least as far as a 1911 paper on 'organic amalgams', in which McCoy and Moore stated that 'It is possible to prepare composite metallic substances from non-metallic constituent elements'.[47] In 1974 two pioneers in this field, Aviram and Ratner, introduced the idea that molecules could exhibit diode-like current-voltage characteristics.[48] They argued that a single molecule with an acceptor(A)-spacer-donor(D) structure could behave as a p-n junction diode

when placed between two electrodes. The molecule proposed by Aviram and Ratner consists of electron accepting group – tetracyanoquinodimethane (TCNQ) coupled to an electron donating group – tetrathiofulvalene (TTF) via a molecular bridge that isolates the two groups – methylene groups (-CH_2-), but through which electrons can tunnel (Figure 1-3).

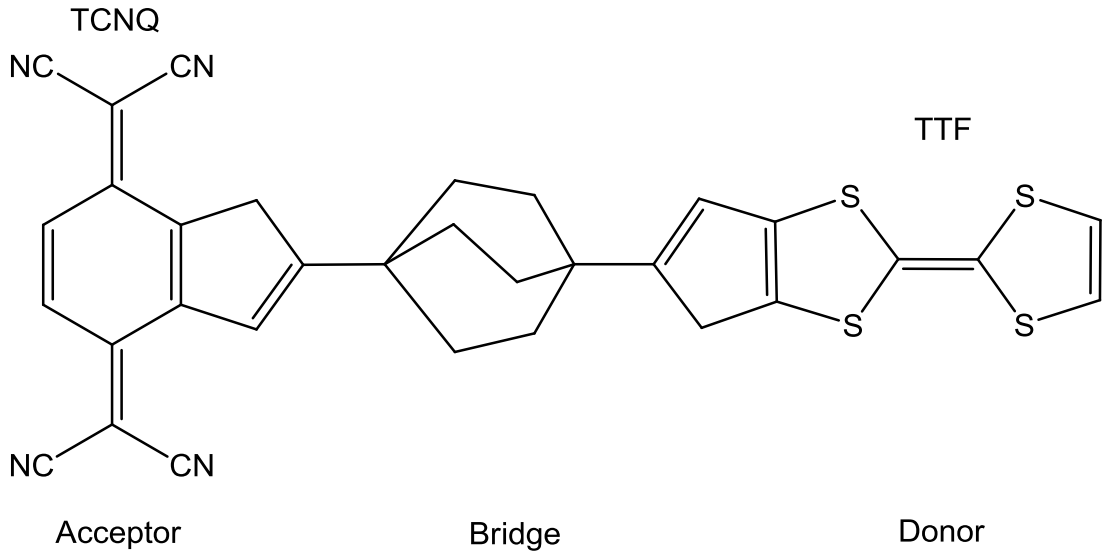

Figure 1-3: Chemical structure of the proposed molecule rectifier of Aviram and Ratner. The electron acceptor is TFF – tetrathiafulvalene and the donor is TCQN – tetracianoquinodimethane. The bridge consists of three parallel chains of methylene (-CH_2-) groups.

An electron donor is a molecular group with the highest occupied electronic state that lies at a high energy (closer to the vacuum). An electron acceptor is a molecular group that is easily charged, having low lying (further below the vacuum) unoccupied state. Thus, the 'downhill' direction of energy transfer is always from a donor to an acceptor for electrons or an alternative view is to think of holes flowing uphill from the acceptor to the donor. Hence, if metal electrode injects a charge into the donor, it will flow naturally to the acceptor, where it can pass into the second electrode of lower potential. Charge is not transfer in the opposite direction because of the probability of

transfer from an acceptor to a donor is tiny at room temperature. Hence, the systems should act as a molecule diode, passing current in one direction, but not the other.

In order to prove this idea Aviram et al. used a hemiquinone monolayer and the current-voltage characteristic was recorded.[49,50] The results revealed a rectifying behaviour in the current that flowed very efficiently in negative bias but not at positive one. It was pointed out that the catechol moiety in the hemiquinone acts as a donor, while the quinone part acts as an acceptor (Figure 1-4).

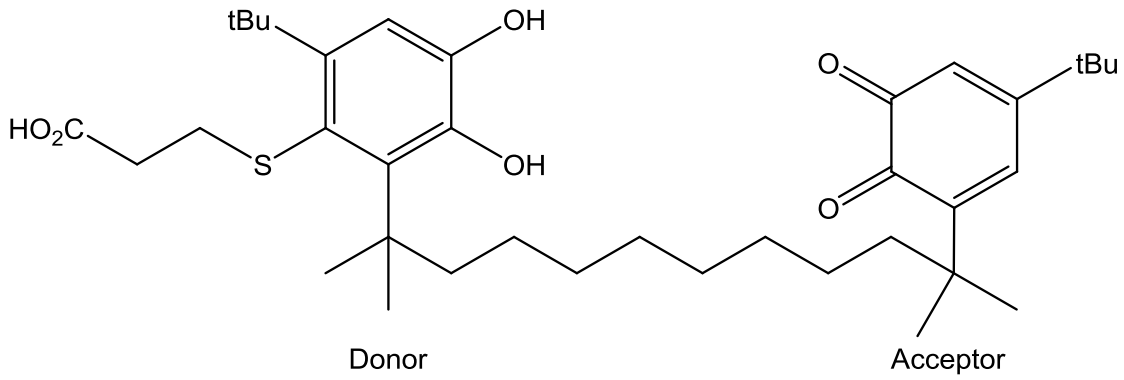

Figure 1-4: Hemiquinone built from a catechol moiety (Donor) and a quinone part (Acceptor).

This hypothesis was proven again twenty years later when Metzer[51] studied Langmuir-Blodgett (LB) films of γ–(n–hexadecyl) quinolinium tricyanoquinodimethanide (D – π spacer – A structure). They established strong rectification behaviour, although the investigated structure is a donor-acceptor system, it is slightly different from the system proposed by Aviram and Ratner. The major difference is that the donor and acceptor are connected with π-bridge instead of with alkane groups (Figure 1-5).

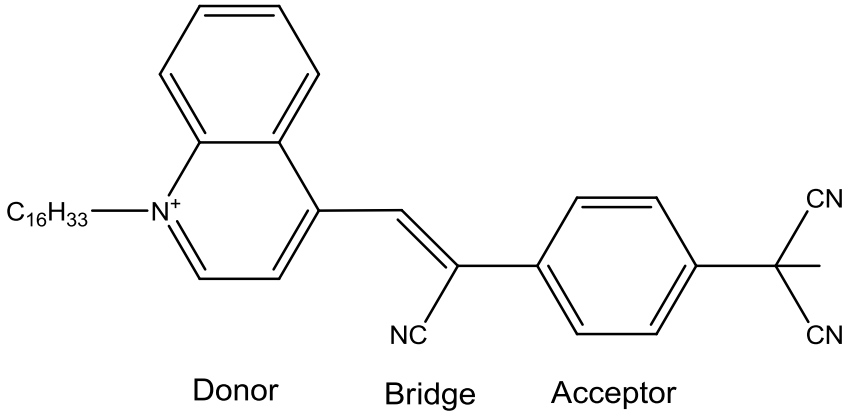

Figure 1-5: γ–(n–hexadecyl) quinolinium tricyanoquinodimethanide.

The above idea and experiments have stimulated the notion of synthesizing computers by chemistry. Numerous experiments and calculations have been performed in order to find the appropriate molecules. One example of more complex structures was later studied by Reichert et al., who showed diode-like properties in 'symmetric' and 'unsymmetric' organic molecules (Figure1-6).[52]

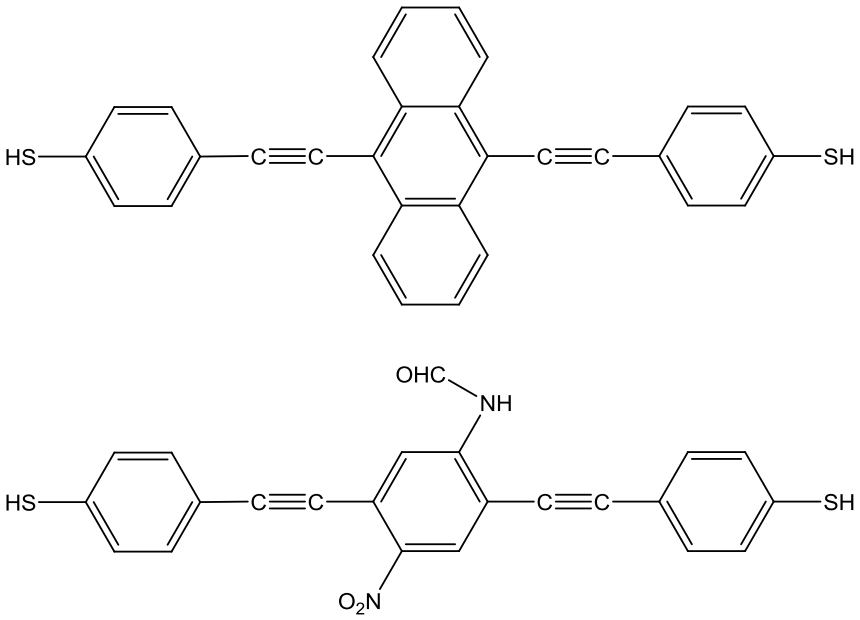

Figure1-6: A spatially 'symmetric' [9,10-Bis_(20-*para* mercaptophenyl)-ethinyl-anthracene] (top) and an 'unsymmetric' molecule [1,4-Bis_(20-*para*-mercaptophenyl)-ethinyl-2-acetyl-amino-5-nitro-benzene] (bottom).

A recent example of a molecular switch is the dithienylethene derivate shown in Figure 1-7. The central unit is photo-active and can exist in both closed and open form. Ring opening is initiated by visible light, while ultraviolet radiation closes it, the closed form being the better conductor.[53]

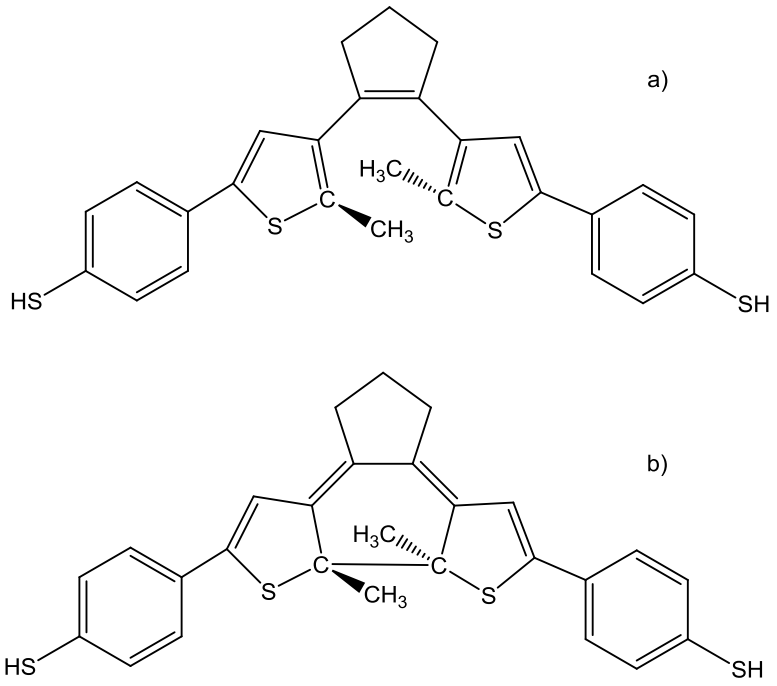

Figure 1-7: Structures of the molecules considered in the photo-switching molecule electronics devices. The open forms are shown on the top (a) and an additional *σ* bond that is present in the closed form is shown on the bottom (b).

Polymers also show promising properties for the electronics industry as they can be assembled into highly ordered and organised structures, where electron mobility is significantly higher than in the disordered polymer films.[54] In addition to the structure and mobility dependence, the polymers have other interesting and potentially useful properties. For example, Polyparaphenylene (PPP) and PolyparaphenyleneVinylene (PPV), shown in Figure 1-8, have high luminescence quantum yields in the solid state, a feature of major interest for light-emitting applications.[55,56] Polyfluorene (PF) and its

alternating copolymers may also be the basis of a new generation of light emitting polymers.[57] Polythiophene (PT) has high electron mobility due to its packing in well-organised chains.[58,59]

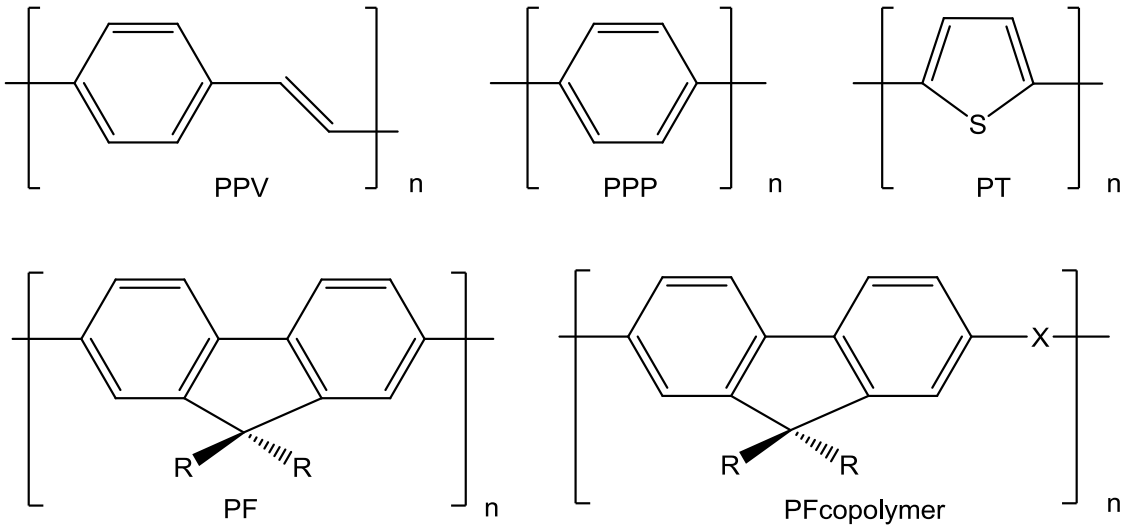

Figure 1-8: Different types of polymers as possible candidates for the molecular electronics industry. Polyparaphenylenevinylene (PPV), Polyparaphenylene (PPP), Polythiophene (PT), Polyfluorene (PF), Polyfluorene copolymer (PFcopolymer).

In the last ten to fifteen years fullerenes and the carbon nanotubes have become the focus of research in many theoretical and experimental groups. The first demonstration of how the conductance of a molecular junction could be controlled by a change in its electronic structure was reported by Joachim and Gimzewski, who studied a C_{60} molecule between a substrate and an STM tip.[60] The conductance increases by two orders of magnitude as a result of the distortion caused by displacement of the STM tip towards the molecule. Thus, the fullerene can behave as an electrochemical amplifier. Other fullerenes can undergo transformation from a metal to a semi-conductor in response to change in gate potential.[61]

Carbon nanotubes, first discovered in 1991, have also be a fertile ground for molecular electronics.[62] Single-walled carbon nanotubes (SWCNTs) have large elastic (kinetic energy is conserved) and phase scattering lengths[63-66] and, depending on their diameter and chirality, they can be either one-dimensional metals or semiconductors[67,68] (Figure 1-9).

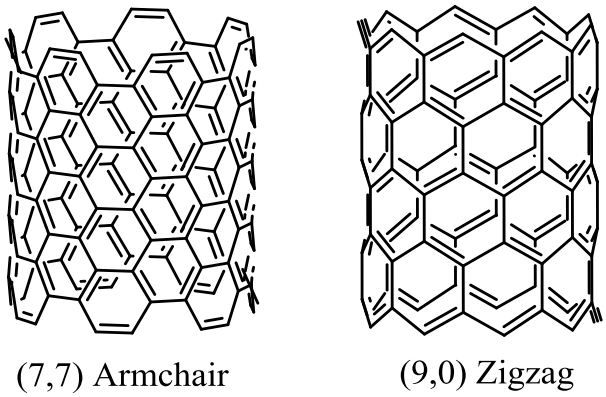

Figure 1-9: The two main types of carbon nanotubes – armchair and zigzag.

When connected to metallic electrodes, carbon nanotubes can exhibit either ballistic or diffusive electron transport. In the first category, electrons propagate freely inside of the conductor and the only resistance arises from the contacts. The conductance in such systems is independent of the length of the conductor. In diffusive transport, electrons can scatter, change their energy and perform a random walk to move from one contact to the other.[69] More information about different types of electron transport in nanostructures can be found in Chapter 2. CNTs are hollow and this raises the possibility of encapsulation of different molecules or metal nanoclusters. For example, a short nanotube filled with fullerene molecules was proposed as a potential memory element.[70] Heterojunctions between the tube and different metal

nanoclusters (Co, Fe, Ni and FeCo) also lead to good metallic conductivity.[71] A carbon nanotube has also recently been used to fabricate a field-effect transistor.[72]

Graphene (Figure 1-10), a one-atom-thick planar sheet of sp^2-hybridised carbon atoms in a honeycomb crystal lattice, has been the subject of intensive research. The long-range π-conjugation yields extraordinary thermal, mechanical and electrical properties.

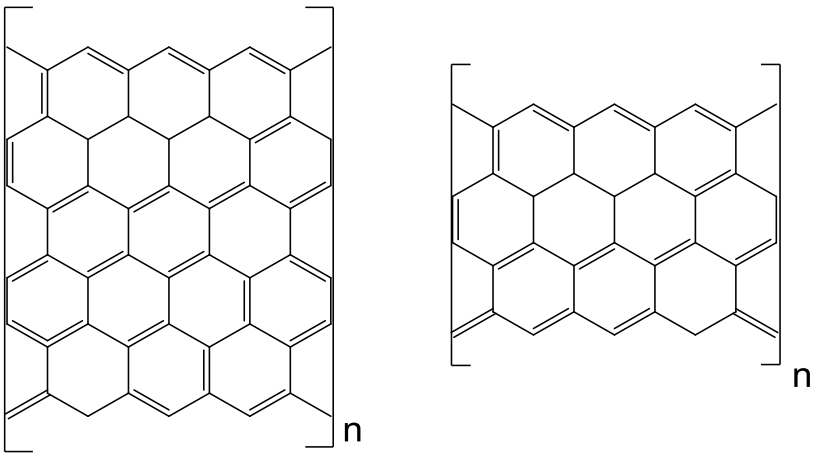

Figure 1-10: Two types of graphene sheets with different width and length.

In 2004 physicists from the University of Manchester and Institute for Microelectronics Technology, Chernogolovka, Russia isolated individual graphene planes[73] and measured extremely high carrier mobilities.[74-76] As a result of this experiment the Nobel Prize in Physics in 2010 was awarded to Novoselov and Gain 'for groundbreaking experiments regarding the two-dimensional material graphene'.

The fact that graphene is a 2D material with the thickness of one atom means that it provides a bridge between condensed matter physics and quantum mechanics and it opens new perspectives for carbon-based electronics. Effects typical for the quantum world are observed in graphene sheets at room temperature[77-81] and the first ever

detection of a single molecule adsorption event was reported.[82] These properties have generated intense interest in the possible implementation of graphene in the electronics industry. For example, graphene may find applications in future generations of high-speed radio frequency logistic devices, thermally and electrically conductive reinforced composites, sensors and transparent electrodes for displays and solar cells.[83-86]

Biological structures, such as DNA, have also been proposed as possible components in molecular electronics. The concept of using DNA as a conductor was first proposed in the middle of the 1990s, and the first direct electrical transport measurement on DNA molecule was published in 1998[87]. One year later measurements on '600 nm and 900 nm-long rope of DNA' were performed and structures shown to behave as ohmic conductors (i.e., the current-voltage (I-V) curve of the device is linear and symmetric).[88] DNA covalently bounded to the electrodes also proved to have metallic behaviour.[89,90] Marauccio et al. even demonstrated a field effect transistor based on a DNA base (deoxyquanosine derivates).[91] However, many other experiments show conflicting results, suggesting that DNA is semiconducting,[92-94] superconductor[95] or even an insulating one.[69] Hence, different measurement approaches, sample preparation, experimental set up or environmental conditions give very different results. The main problem in all experiments is the control over the contact between the DNA and electrodes.[96]

Proteins have also been considered in the construction of electronic devices.[97,98] Several research groups have recorded contrast tunnelling images of metalloproteins and enzymes under a variety of controllable conditions. A protein field-effective

transistor based on blue copper protein azuin has been fabricated and operates at room temperature and ambient pressure.[99]

1.3 Structures based on metal-organic complexes

The second main class of molecule junction considered here is that containing metal atoms or ions. Systems of this type constitute the bulk of the research in this thesis. Chains of metal atoms represent a visually appealing analogy to mesoscopic wires, and this has driven interest in integrating them into molecular electronics components.[100]

1.3.1 Small molecules

Metal atoms and linear chains of atoms represent the simplest possible models for the bulk metal present in macroscopic wires. Such systems should, at least in principle, have good electron transport properties due to the presence of partially filled levels at the Fermi level, and the predicted conductance should approach the limiting value of $2e^2/h \approx 77.4$ μS per conduction channel predicted for a perfect conductor (for more information see Chapter 2). Indeed, experiments performed on monovalent metal atoms, such as Na, Au, Cu and Ag, which have only one conduction channel, appear to confirm this prediction.[101,102]

The conductance of a single atom or metal wire can be measured either by mechanical method,[103,104] electrochemical etching or deposition.[105,106] Electron

microscopy can also measure the current that passes through a single atom or chain of atoms. STM experiments performed in 1998 by Ohnishi and co-workers[107] measured the conductance of a single chain of gold atoms suspended between gold electrodes. They stretch the fine gold wire to a break point. As the wire narrows down, quantum jumps are observed in the current. The plateaus between each jump correspond to stretching of the gold filament. It yields until another layer of atoms is peeled away, causing the number of the allowed states to fall. They verified that the conductance of a single chain of Au atoms is ~$2e^2/h$ and also that the conductance of a double chain is approximately twice this value. Hence, the steps occurring are almost exact multiples of conductance quantum G_0.

Whilst chains of bare metals are of intrinsic interest, they offer limited potential for bottom-up synthesis and self-assembly approach. More interesting from this perspective are well-defined molecular systems, typically involving a metal atom or ion surrounded by an array of ligands. This leads to the following question: what is the conductance in a single molecule?

One of the earliest experiments on small metal-based structures was published by Park[108] et al. in 2002. In this experiment the scientists examined two related molecules containing a Co ion bonded to polypyridyl ligands, attached to insulating chains of different ligands (Figure 1-11). Changing the length of the insulating chains alters the coupling of the ion to the electrodes, enabling the fabrication of devices that exhibit either single-electron or multi-electron phenomena.

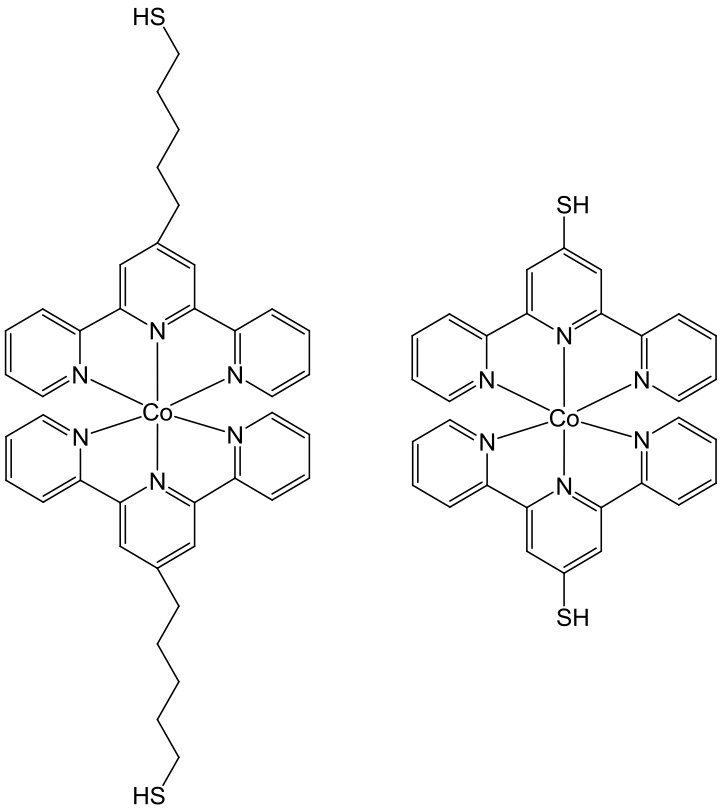

Figure 1-11: Two related molecules containing a Co ion bonded to polypyridyl ligands, attached to insulating tethers.

Some small inorganic molecules can behave as molecule transistors where the electronic states can be switched in a controlled way.[109-113] One recent notable example of a molecule transistor is a redox active transition metal (Os(II)/(III)) complex inserted between the working electrode and tip (Figure 1-12) in an electrochemical scanning tunnelling microscope (in situ STM).[114] This configuration resembles a single-molecule transistor, where the reference electrode corresponds to the gate electrode. Amplification on−off ratios up to 50 are found when the redox level is brought into the energy window between the Fermi levels of the electrodes by the overpotential ('gate voltage').

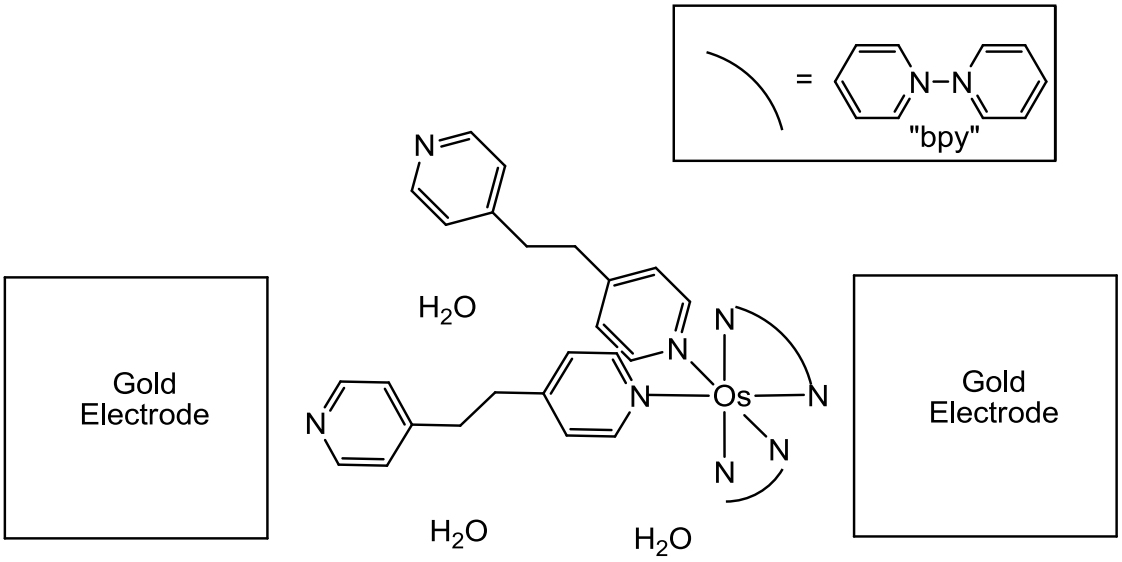

Figure 1-12: $[Os(bpy)_2(p2p)_2]^{2+/3+}$ between Au(111) electrodes; bpy – 2,2' bipyridine, p2p – 1,2-bis(-4-pyridyl)ethane.

Systems based on a sandwich structure, in which one metal atom is placed between two planar organic ligands, have also been the subject of much interest. The ferrocene derivative (Figure 1-13) exhibits a remarkably large conductance and a high structural flexibility with respect to rotation of the two cyclopentadienyl (Cp) rings.[115-118] Recent work by S. A. Getty and co-workers shows that the conductance of a ferrocene-based organometallic molecule wire exceeds 70% of the conductance quantum.[119] Conjugated organic oligomers of similar length show much lower molecular conductance.

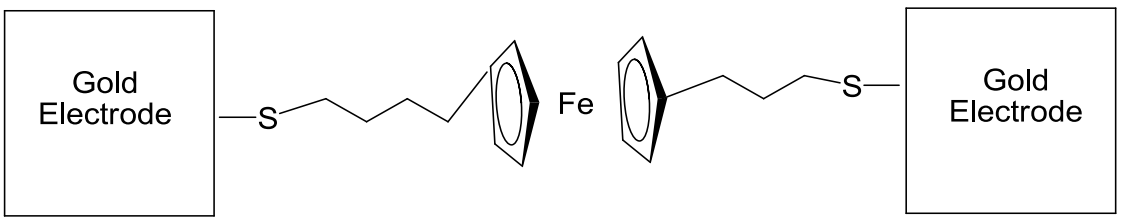

Figure 1-13: Ferrocene derivates placed between two electrodes.

Another example from the metallocene family is cobaltocene, which has been proposed to be a single-molecule spin valve.[120-122] Cobaltocene is closely related to ferrocene but with one additional electron, yielding a spin 1/2 moiety favourable for spintronics.[120] A molecule constructed from two cobaltocene units connected with a spacer is presented in Figure 1-14.

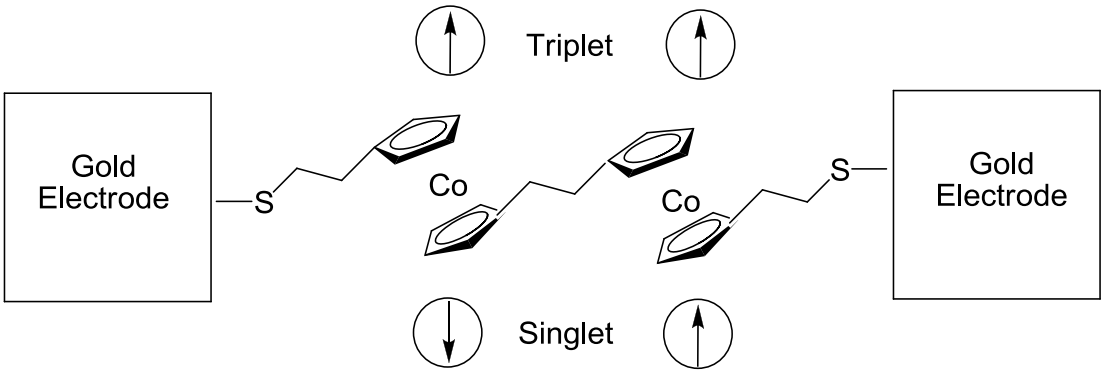

Figure 1-14: Two cobaltocene units in singlet and triplet states.

This structure can have two possible electronic states, a singlet and triplet, differing only in the coupling between the two metal centres. The antiparallel (singlet) configuration of the cobaltocene spins blocks electron transport near the Fermi energy, while the spin parallel (triplet) configuration supports much higher current. The energy difference between the antiparallel and parallel states depends on the insulating spacer separating the two cobaltocenes, allowing, at least in principle, switching through the application of a moderate magnetic field. We discuss this issue again in detail in Chapter 5 where we deal with electron transport through trinickel and NiPdNi wires.

1.3.2 Small oligomers

Organometallic multidecker sandwich clusters, where the magnetic moment increases with the cluster size, have recently been synthesised.[123-126] For example, transition metal borazine clusters made from 3d elements, such as V, Cr, Mn, Sc or Ti, are energetically stable (Figure 1-15 a).[127] The ground electronic states of the V and Mn borazine wires are highly-metallic and ferromagnetic, while the Cr and Sc structures are semiconductors and the Ti structure is an antiferromagnetic wire. V_nBz_{n+1} (Bz = C_6H_6) is an example of a sandwiched linear molecule or 'quantum line' that has been synthesized and characterised in detail. The experiment and theoretical studies suggested that this molecule should have one-dimensional structure which is settled by the metal-ligand interaction confined to single molecule axis. The unpaired electrons localized on metal atoms are coupled feromagnetically. These species could be used as potential one-dimensional molecule magnets.[128-131]

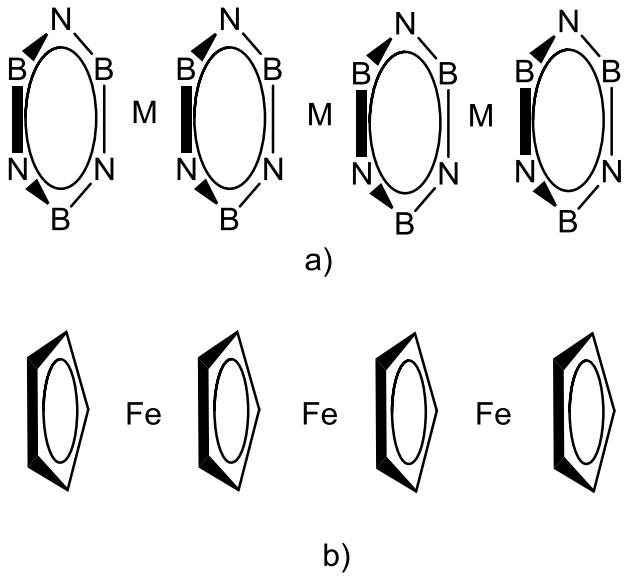

Figure 1-15: a) a transition metal borazine cluster, where M = V, Cr, Mn, Sc or Ti, b) sandwiched molecule wire – Fe_3Cp_4 (Cp=cyclopentadienyl).

An example of sandwich molecular wires (SMWs) is Fe_3Cp_4 (Figure 1-15 b). This molecule has been synthesized in the gas phase and characterised using mass spectroscopy.[132] The experiment revealed that these are the first linear molecules that combine HM (half metallic) behaviour, high SFE (spin filtering effect) and NDR (negative differential resistance). Moreover, they can be easily synthesized, suggesting that the SMWs are promising materials for application in the molecular electronics.[133]

The logical limit of clusters of metal ions of this type is represented by the class of Single Molecule Magnets (SMMs), which typically contain several metal centres linked by hard anionic bridging ligands. Recently two experiments measured transport through the archetypcal SMM, a $[Mn_{12}O_{12}(O_2C\text{-}C_6H_4\text{-}SAc)_{16}(H_2O)_4]$, in short Mn_{12} cluster, in a single-molecule transistor geometry.[134,135] Thiol groups connect the molecule to gold electrodes (Figure 1-16).

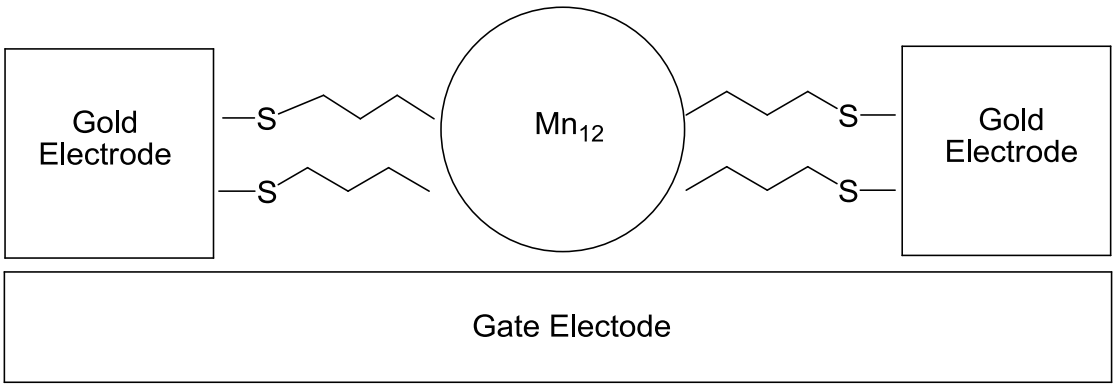

Figure 1-16: Schematic drawing of the Mn_{12} molecule (circle) trapped between electrodes. A gate changes the electrostatic potential on the molecule. The molecule diameter is about 3 nm. [134]

A negative differential resistance is observed originating from the rehybridization of the Mn_{12} molecular levels in an external electric field. Interestingly, the transport properties are sensitive to the internal spin configuration of the molecule. This may therefore enable one to infer the internal spin state of the molecule from a detailed knowledge of the I-V characteristics.[136] The transport properties of exchange coupled systems such as this will be the focus of Chapter 5.

1.3.3 Extended chains of metal atoms

The final class of structures, with which this thesis is primarily concerned, contains arrays of metal ions that are directly linked by covalent metal-metal interactions. They are thus distinct from the aggregates described in the previous section where interactions occur via ligands in a super exchange-type mechanism. These arrays can self-assemble by coordination bonding in one, two or three dimension,[137,138] but one-dimensional chains are especially interesting from the perspective of nanotechnology because they provide a direct analogy to molecule wires.[139-141] For example, the compound with molecular formula $[Pt_2(RCS_2)_4]$ (RSC_2^-=Dithiocarboxylato, R=Me or Et,) forms linear chains where the Pt_2 units are linked by direct bonds to form an infinite polymeric chain (Figure 1-17). These compounds show almost metallic electrical conductivity along the Pt-Pt axis in the solid phase.[142-146] A similar structure, $[Pt_2(n\text{-pentylCS}_2)_4]$, shows a transition from semiconductor to metallic behaviour with increasing temperature,[139] suggesting that metal-polymer-based nanowires could be suitable for device applications, such as molecule wires or transistors.

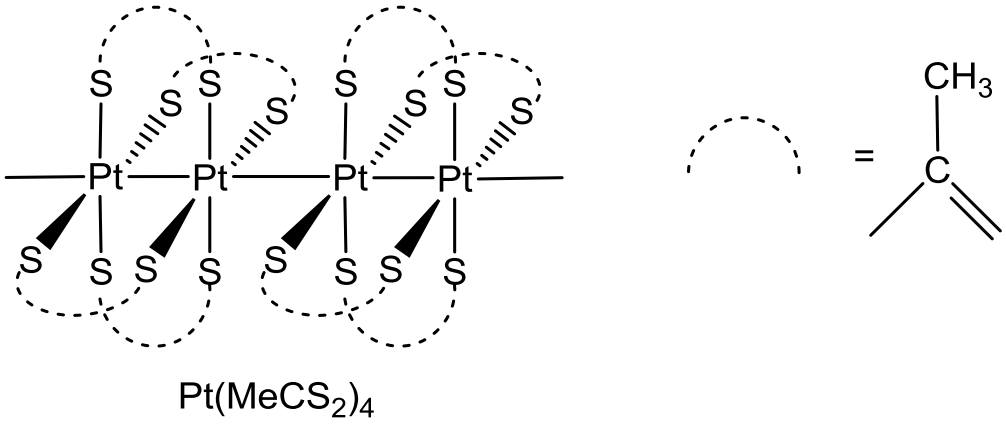

Figure 1-17: Repeat units of the 1D chain: $[Pt_2(CH_3CS_2)_4]$.

The tetracyanoplatinate compounds known as Krogmann salts[147-149] are perhaps the classic examples of one-dimensional chains. The $[Pt(CN)_4]^{2-}$ units form infinite chains linked by Pt-Pt bonds (Figure 1-18), and partial oxidation (by Br_2, for example) causes strong fluctuations in the Pt-Pt distances between 3.5 and 2.95 Å. The conductivity along the Pt-Pt axis in the oxidised $K_2Pt(CN)_4[Br]_{0.3}$ form increases by a factor of ~10^{10} compared to unoxidised forms.[150]

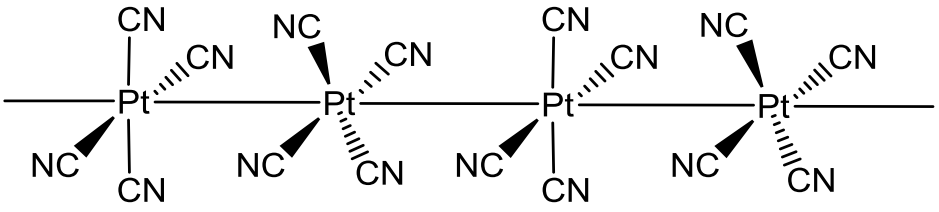

Figure 1-18: Stacking of $[Pt(CN)_4]^{2-}$ units in Krogmann salts.

A closely related system is $[Rh(L)_4(BF_4)_{1.5}]$[151] L=CH_3CN (Figure 1-19), which is isoelectronic with $K_2Pt(CN)_4[Br]_{0.3}$. This structure has alternating Rh-Rh separations 2.84 and 2.93 Å, and the strong Peierls' distortion quenches the conductance so that the system is a semiconductor at low temperatures.

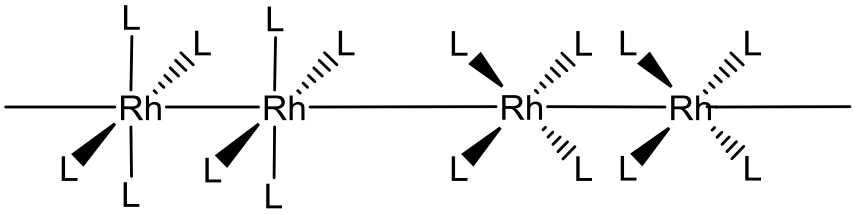

Figure 1-19: Chain structure of $Rh(L)_4(BF_4)_{1.5}$ - (L = CH_3CN).

In the examples described above the ligands are either mono- or bidentate, and the formation of infinite chains relies on unsupported metal-metal bonds between the monomer or dimer units. An alternative strategy is to synthesise extended polydentate ligands where the length of the metal chains is determined by the denticity. Two major types of ligands have been used for this purpose: conjugated polyenes and oligo-α-pyridylamine ligands (Figure 1-20).

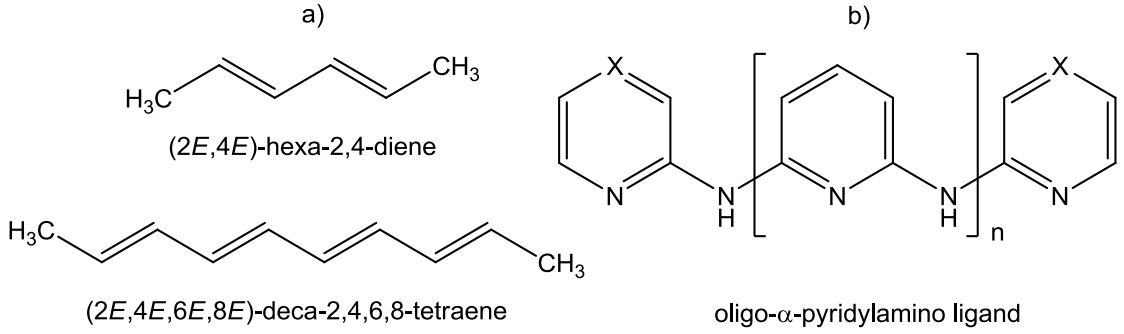

Figure 1-20: a) Conjugated polyenes and b) oligo-α-pyridylamino ligand; n varies from 0 to 6, X = C,N.

The structure of $[Pd_4(Ph(CH)_8Ph)_2(py)_2]^{2+}$, a typical example of a chain sandwiched between two polyene ligands, is presented in Figure 1-21.[152] The two alkene units at each metal centre complete an approximately square planar coordination geometry about each of the metal centres. In the crystal structure, the Pd−Pd−Pd−Pd skeleton is highly linear (Pd-Pd-Pd-Pd = 178.25(4)°), and each Pd−Pd length (outer, 2.7322(8) Å;

inner, 2.654(1) Å) is normal and consistent with the four-centred, six-electron bond of the Pd_4 core.

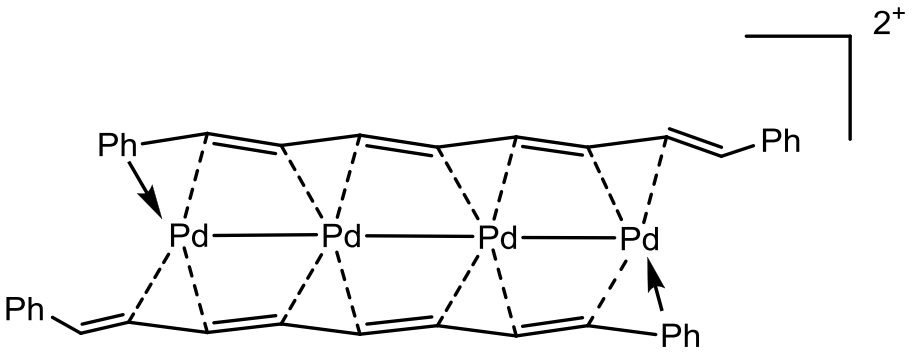

Figure 1-21: Structure of $[Pd_4(Ph(CH)_8Ph)_2(py)_2]^{2+}$.

Complexes of the family of oligo-α-polypyridylamino ligands[153] (Figure 1-20 b) have been the subject of intense development in the last twenty years, mainly in the groups of Peng and Cotton but latterly also of Murillo and Berry. The first report of a complex of a ligand of this type appeared in 1968 when the complex $Ni_3(dpa)_4Cl_2$ (dpa = dipyridylamido)[154] was incorrectly formulated as containing two nickel atoms surrounded by a square-planar array of dipyridylamido moieties bonded to a central tetrahedral nickel atom (Figure 1-22 a).

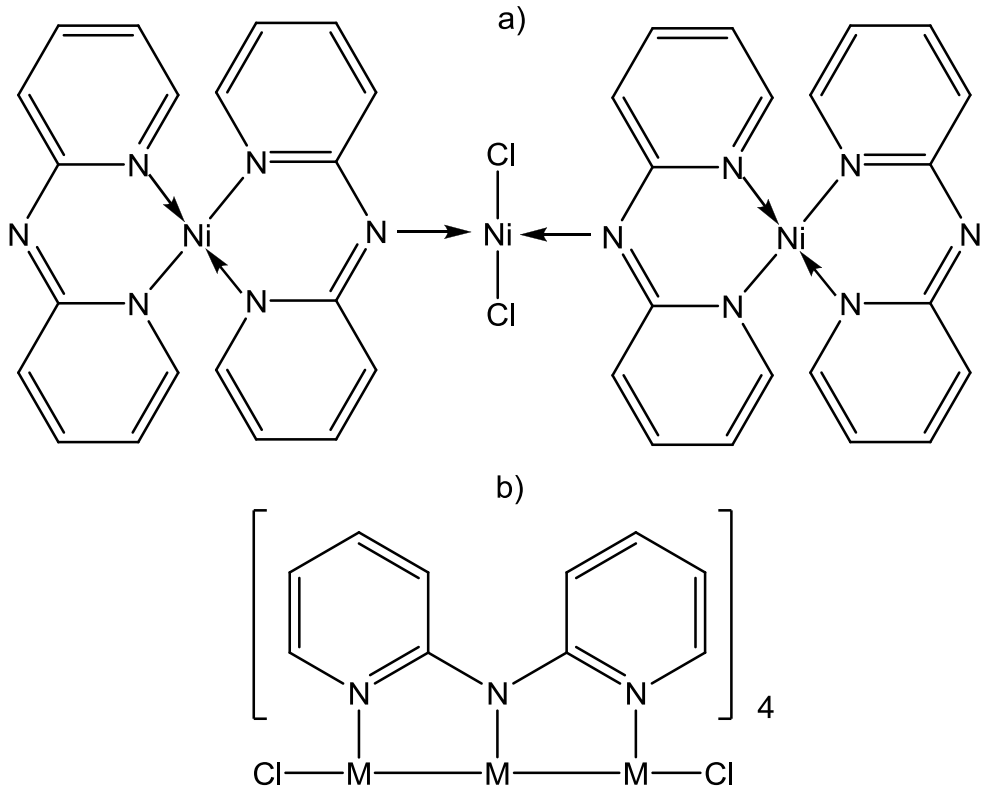

Figure 1-22: a) The structure for $Ni_3(dpa)_4Cl_2$ as proposed by Hurley and Robinson[154] and b) general form of $M_3(dpa)_2Cl_2$; dpa^-= dipyridylamido M = Co, Ni, Cr, Co, Rh, Rd or Cu; Cl^-.

Almost twenty five years later the same molecule, along with its copper analogue, was shown to contain a linear trimetallic chain supported by four dpa ligands in a helical array (Figure 1-22 b).[154-156] Soon after this Ru and Rh complexes were characterised[157] as sharing the linear chain structure now known to be characteristic of all metal complexes of this class. The electron transport properties of the Co_3, Cr_3, Ni_3 and $Co_{3/5/7}$ systems are the subject of Chapters 3, 4, 5, and 6, respectively, and the relevant chemistry of each system will be reviewed in detail at the start of each chapter. In the following paragraphs a brief overview of their chemistry is presented to establish the context of the following chapters.

The Extended Metal Atom Chains (EMACs) with a diverse range of metal centres are now known. Amongst the trimetallic complexes $[M_3(dpa)_4X_2]$ M can be Ni,[158,159] Co,[160-

[162] Cr,[163-165] Ru and Rh[166,167] and X can be NCO^-, CN^-, SCN^-, Cl^-, Br^-, PF_6, NO_3^-, $NCCH_3^-$, I^-, C≡C-R (R = antracyl, Ph, $FeCp_2$), while pentametallic complexes $[M_5(tpda)_4X_2]$ are known for M = Ni,[168,169] Co,[170,171] Cr[172,173] and Ru[174] ($tpda^{2-}$= tripyridyldiamido). Heptametallic complexes $[M_7(teptra)_4X_2]$ ($teptra^{3-}$ = tetrapyridyltriaminido) are known for M = Ni,[175] Cr[176] and Co,[177] while nonametallic complexes $[M_9(peptea)_4X_2]$ ($peptea^{4-}$ = pentapyridyltetraamido) have been synthesised for M = Ni and Cr[178]. The longest homo-metallic structure is built from ten[179] or eleven[180] nickel metal atoms. There are also some examples of heterometallic chains, such as $(CrWMo(dpa)_4Cl_2)$,[181] $Ru_2M(dpa)_4Cl_2$ (M = Cu, Ni),[182] $NiPdNi(dpa)_4Cl_2$,[183,184] $CoPdCo(dpa)_4Cl_2$,[185] $CuMCu(dpa)_4Cl_2$ (M = Pd, Pt),[186] $CrCrFe(dpa)_4Cl_2$,[187] $CrCrCo(dpa)_4Cl_2$ and $MoMoCo(dpa)_2Cl_4$.[188] The primary goal of this synthetic effort has been to design new metal strings for the future molecule wires. Their conductance and electron transport properties have therefore come under scrutiny, and scanning tunnelling microscopy with break junction (STM-BJ) technique has been used to measure the conductance of some of these systems.[189-191]

Peng and co-workers have made thousands of measurements of the conductance of trimetallic and pentametallic complexes.[191] The experiments suggest that the trimetallic (M_3) EMACs have lower resistance than their pentametallic (M_5) analogues and, moreover, than within a series, the resistance drops in the order Ni > Co > Cr. Thus, in the trimetallic chains the resistance drops from 3.4 MΩ to 1.9 MΩ and to 0.9 MΩ, moving from Ni_3, Co_3 and Cr_3. This trend has been reproduced using an extended Hückel model for the electronic structure, although the physical basis for this apparent success can be debated (see Chapter 3).[192] In the same paper the authors noted a remarkable stochastic switching phenomenon in the current-voltage data for

the $Cr_5(tpda)_4(NCS)_2$ chain. The Cr_5 chain conductance is distinctly biphasic, with some molecules showing higher conductance than others. The author proposed that the origin of this behaviour was switching between symmetric and unsymmetric chains, the latter having alternating quadruple and non-bonds.[191] An alternative model for this behaviour will be developed in Chapter 4.

Other EMACs have also been the subject of STM experiments. For example, Ru_5 chains appear to have resistance intermediate between the Co_5 and Cr_5 analogues,[174] while mixed-valence molecules, such as $[Ni_5(bna)_4(NCS)_2]^{2+}$, have much lower resistance (~18 MΩ) than the homovalent $Ni_5(tpda)_4(NCS)_2$ counterpart.[167] Yao and co-workers have shown that $Cu_3(dpa)_4Cl_2$ or $Ni_3(dpa)_4Cl_2$ EMAC can behave as single molecule transistors[193] where the molecules were supported between two gold electrodes with an aluminium gate electrode. The results were interpreted in terms of excitation of symmetric and unsymmetric metal-metal stretching modes of the trimetal complexes.

Recently the chemistry of naphthyridylamine ligands has been developed to create a new generation of metal string complexes. It is based on modulation of the existing oligo-α-pyridylamine structure with several naphthyridyl groups (Figure 1-23 b). So far only Ni EMACs with naphthyridylamine ligand have been reported. [194-197] The ligand is less anionic than its predecessors and, as a result, the metal complexes tend to form partially reduced mixed-valence $[Ni_2(napy)_4]^{3+}$ dinuclear unit within the linear metal chain.

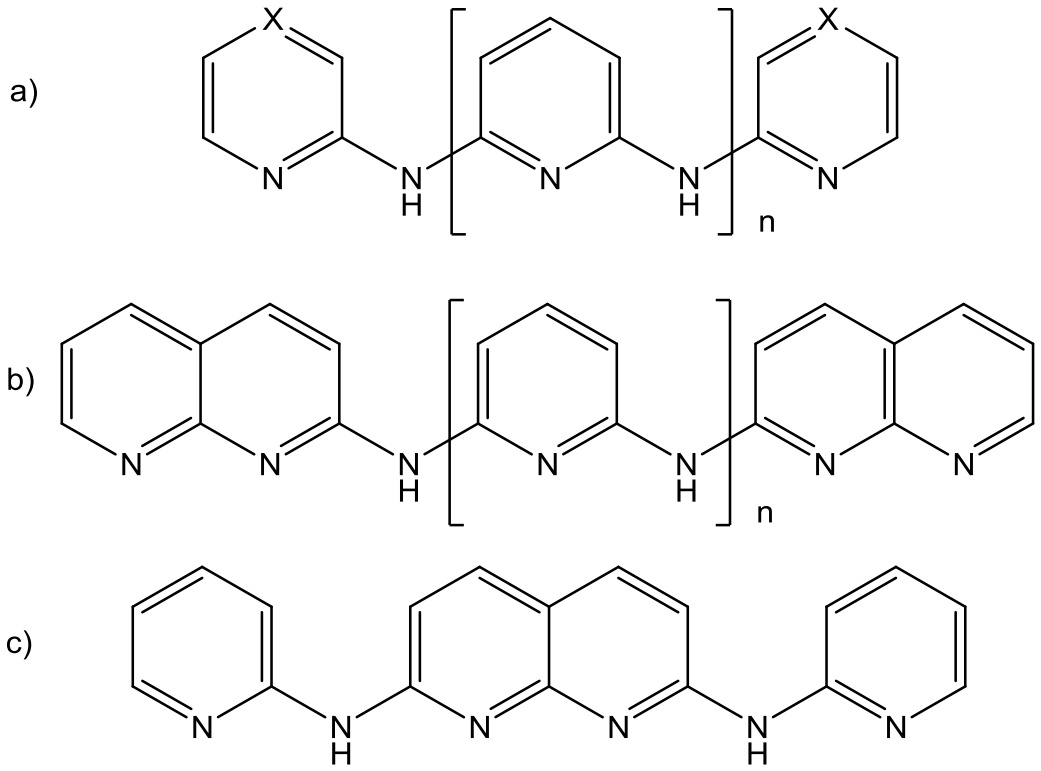

Figure 1-23: a) oligo-α-pyridylamino ligand (dpa), b) naphthyridylamine ligand described in the text; n = 0, 1, 2 and X=N,H; and c) 2,7-bis(a-pyridylamino)-1,8-naphthyridine (H_2bpyany).

All of the above examples of EMACs contain an odd number of metal centres, simply because the polypyridylamido architecture supports M = 3, 5, 7, 9 and 11. Even numbers of metal atoms in EMAC require new type of ligands. From an experimental point of view it is more difficult to synthesize even-numbered metal-chains than odd-numbered metal-chains. Despite these difficulties, Peng and co-workers have previously reported tetranickel,[198] hexanickel,[199,200] and octanickel chains.[201] The longest even-numbered metal chain, decanickel extended metal atom chain (EMAC) complex with a new pyridyl- and naphthyridyl-modulated ligand (H_4bdpdany) was synthesized.[179] A ligand architecture with six number of binding sites, such as 2,7-bis(α-pyridylamino)-1,8-naphthyridine (H_2 bpyany) (Figure 1-23 c), has been designed.

So far only two families of EMACs of this type have been reported: $[Co_6(\mu_6\text{-bpyany})_4(NCS)_2](PF_6)_n$ or $[Co_6(\mu_6\text{-bpyany})_4(OTf)_2](Otf)_n$ (n = 1 (1); n = 2 (2))[202] and $[Ni_6(\mu_6\text{-bpyany})_4(NCS)_2](PF_6)_n$ or $[Ni_6(\mu_6\text{-bpyany})_4(OTf)_2](Otf)_n$ (n = 1 (1); n = 2 (2)).[203] They are generally less stable than the odd analogues, and, as a result, they have not been subject of the same physico-chemical investigations as their odd counterparts.

1.4 Conclusions

In summary, linear chains of metal complexes are promising candidates for building blocks in molecular electronic. The analogy to macroscopic wires is to some extent superficial, but nevertheless initial studies of their electron transport properties show promise. The objective of this thesis is to establish a link between the fundamental electronic structure of these systems and their ability to transport current.

Chapter 2

Introduction to electron transport

2.1 Introduction and background

The study of electron transport is associated with the flow of current through conductors. The current is a measure of the amount of electrical charge transfer per unit time and it can be described from three distinct points of view (Figure 2-1).

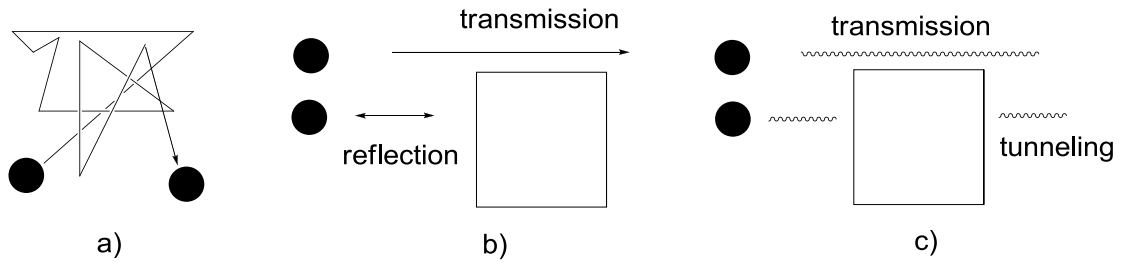

Figure 2-1: Classical (a), semi-classical (b) and quantum (c) pictures of electron transport.

In the first of these, the so-called 'classical' electron transport, the electrons are treated as atoms in gas which undergo random thermal motion with an average thermal velocity and also direct motion, characterized by the drift velocity (Figure 2-1 a). In the semi-classical transport model (Figure 2-1 b), the electrons are classical particles but the movement is in a spatially periodic potential where the electrons move between two collisions according to the classical equation of motions (Newton's laws). Electrons have well-defined mass and they behave like particles, unable to

tunnel through barriers. In the collision events the electrons can scatter inelastically – the kinetic energy of an incident particle is not conserved. Usually the semi-classical transport approach can be used to describe structures with length of around 10 µm – 1 µm. When the dimensions of the structure decrease below this limit, a quantum mechanical description of the electrons becomes essential (Figure 2-1 c). The third model of electron transport takes into account explicitly the wave-like behaviour of electrons. Upon reaching a barrier, tunnelling is possible in addition to reflection and classical transmittance. The Schrödinger equation is then the basis for the description of electron transport, and it is essential at the molecular or atomic scale.

Quantum transport can be further separated into several regimes determined by the length scales involved. The characteristic lengths are: (1) mean free path (L_{mfp}), which is the average distance in which the particles move freely; (2) the de Broglie wavelength (L_T) that is related to the kinetic energy of the electrons; (3) and the phase-relaxation length (L_ϕ), which is the average distance that the electrons travel without destroying their phase.

Regime	Condition
Ballistic	$L_x, L_y, L_z < L_{mfp}, L_T, L_\phi$
Diffusive	$L_{mfp}, L_T << L_x, L_y, L_z$
Dissipative	$L_\phi < L_x, L_y, L_z$

Table 2-1: Classified quantum electron transport.

Variations in the physical length of conductors allow three distinct transport regimes to be identified (Table 2-1), all of which have been identified in experiments. Dissipative conditions are characterised by inelastic and elastic scattering, where the particle loses previous information about momentum and energy. In diffusive conductors, in contrast, only elastic scattering is observed where the kinetic energy is conserved but the direction of the propagation is modified. In both diffusive and dissipative regimes transport is dominated by scattering processes. In the ballistic regime the dimensions of the conductor are much smaller than all length scales and, as a result, the electrons are not scattered and their momentum and energy are conserved. From this perspective, ballistic conductors should have infinite conductance and no resistivity at all. This has been confirmed by experiments where the contact resistance between the electron reservoir and ballistic conductor was eliminated.[204] Other experiments on quantum point contacts and atomic-size wires[205] show a step-like behaviour of the conductance as the point contact is narrowed or the wire elongated. To explain these phenomena a new perspective on resistance (and therefore conductance) is needed.

Landauer proposed that resistance on the molecular scale could be described in terms of the transmission probability of propagating electron modes in a one-dimensional conductor.[206-208] Later Büttiker modified Landauer's theory for multi-channel devices,[209,210] leading to the Landauer-Büttiker approach that is a widely used method for describing the quantum transport. An extensive overview of this approach can be found in Datta's books.[211,212] In the first part of this chapter we will present the main points of this formalism.

2.2 Landauer-Büttiker formalism: an introduction

In macroscopic conductors the conductance is described by Ohm's law

$$G = \sigma \frac{A}{L} \qquad \text{(Ohm)}$$

Equation 1

where A is an area of the cross section of the conductor, L is the length of the conductor, and σ is the conductivity. The latter is material- and temperature-dependant. According to Ohm's law, the conductance should vanish as the conductor gets narrower and A goes to 0 and it should become infinite for very short conductors, where L goes to 0. However, the experiment shows step-like behaviour of the conductance as the point contact is narrowed or the wire elongated.[205] Later it was proven that there is a maximum conductance for a conductor with one level (in energy range of interest), which is fundamental constant related to the charge on an electron and Planck's constant.[211,212]

$$G_0 = \frac{q^2}{h} = 38.7\mu S = 25.8k\Omega^{-1}$$

Equation 2

Actually, small conductors have maximum conductance of $2G_0$ due to the fact that they typically have two levels with the same energy: one for spin up and one for spin down. We can always measure conductance lower than this if the contacts are bad.

Therefore, the conductance has upper limit that exists even in the systems where the conductor is perfectly coupled to the electrodes.

As we already mentioned, in order to explain step-like behaviour of the conductance, Landauer and Büttiker developed a new theory. In the Landauer-Büttiker model the system is constructed as a central scattering region connected to macroscopic electron reservoirs by a set of idealised leads (Figure 2-2).

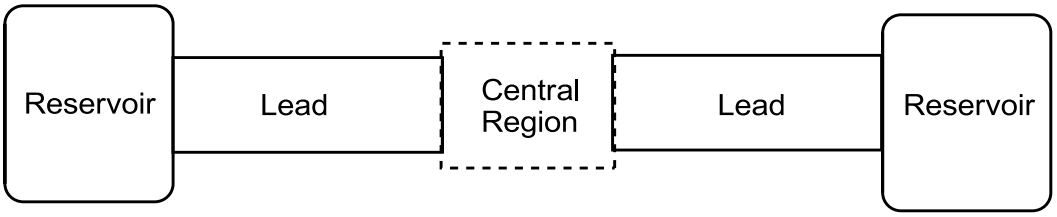

Figure 2-2: Schematic representation of the basic two-terminal scattering device in the Landauer-Büttiker approach.

The reservoirs are at thermal equilibrium with a well-defined temperature and chemical potential. The leads are semi-infinite with periodic boundary conditions connected with the reservoirs. The electrons do not lose their energy due to scattering and propagation in the leads. The interference between each lead and the reservoir is assumed to be reflectionless, i.e., an electron that travels from the lead to the reservoir has zero probability of being reflected back into the lead. All of these approximations have been introduced in order to simplify complex nature of the electron transport in nanosystems.

From the experiment it is well known that there is a maximum conductance for a conductor with one level (in energy range of interest), which is fundamental constant G_0. Hence, the conductance can be written in terms in G_0. The next step is to relate

the transport properties of the system to the way the central region modifies the propagating states between the leads. For this reason the conductance for atomic size systems can be written as:

$$G = \frac{e^2}{h}\sum_n T_n(E_F) = G_0 \sum_n T_n(E_F)$$

Equation 3

where G_0 (38.7 μS ≡ 25.8 $k\Omega^{-1}$) is the conductance quantum, the maximum conductance for a single level atomic conductor. T_n is the transmission probability of the wavefunction that propagates across the central region. The sum of all transmission probabilities over all the channels at the Fermi energy (E_F) gives the total transmission function. It is clear from the above that the conductance is a multiple of the conductance quantum. Most importantly it should be noted that the conductance is directly associated with the probability of the wave to pass through the central region. If the wave cannot penetrate, the transmission probability is zero and the conductance is zero. If the wave can easily pass through the central region, T_n is equal to 1 and the channel is perfectly transparent. Therefore, the conductance has an upper limit defined by the conductance quantum multiplied by the number of the channels. However, for reason which will be explained in the following paragraphs, only channels around the Fermi level are important for calculations of the conductance.

If we compare the two expressions for the conductance, Ohm's and Landauer-Büttiker's, it is clear that the conductivity, σ, in the Ohm's law can be identified with

the conductance quantum in Landauer-Büttiker's theory, while the ratio A/L is related to the transmission probability (Equation 4). This theoretical framework is the basis for much of our current understanding of electron transport at the molecular level.

$$G = \sigma \frac{A}{L} \text{ Ohm} \qquad G = \frac{2e^2}{h} \sum_n T_n(E_F) \text{ Landauer-Büttiker}$$

Equation 4

2.3 Electron transport through molecules

Figure 2-2 presents a schematic setup of a basic two-terminal device that is at the heart of the Landauer-Büttiker approach. The central region could in principle be made from any material, such as bulk metal semiconductor or atomic scale structures, such as, molecules or metal atomic chains. In metals and semiconductors, the electronic distribution is described by bands, whereas in molecules these bands collapse to discrete energy levels. Therefore, in the molecule each band corresponds to a single molecular orbital and the central region of Figure 2-2 (the channel) has discrete energy levels.

A third electrode (gate), in contact with the central region, can modulate the ability of the channel to conduct electrons, and this is the basis of the transistor (Figure 2-3). Modern transistors are typically built from a semiconductor material, such as Si or GaAs, and millions of transistors are present in modern computers and electronic devices.

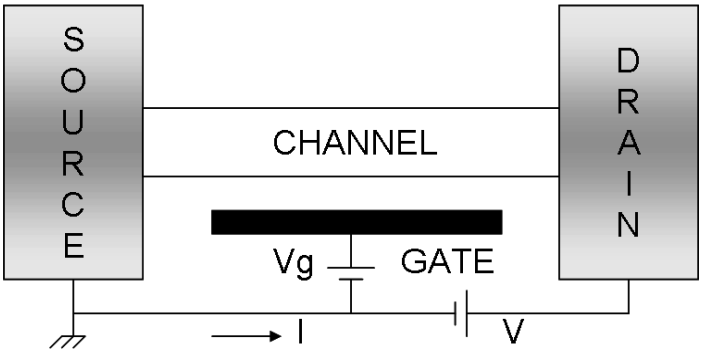

Figure 2-3: Schematic diagram of a transistor.

In principle, it is possible for the same central region to be replaced with a molecule or an atomic size conductor. To understand the electron transport through this type of conductor we consider the simplest possible model where the central region has only a single molecular orbital with energy ε or ε' (Figure 2-4). If the electrodes are chemically identical and there is no applied bias, the metallic contacts have identical Fermi levels. They have different Fermi levels if they are built from different material or if a bias is applied.

It is useful to clarify two terms at this point: Fermi level and Fermi function. The Fermi level *(E_F)* is the highest occupied electron energy level at absolute zero temperature. The Fermi function *f(E-μ)* gives the probability that a given available electron energy state will be occupied at a given temperature. In Equation 5, *E* is the energy of the level and μ is the electrochemical potential of the electrode.

$$f_0(E-\mu) = \frac{1}{1+\exp[(E-\mu)/k_B T]}$$

Equation 5

The basic nature of this function dictates that, at low temperatures, most of the levels up to the Fermi level E_F are filled and relatively few electrons have energies above the Fermi level. Energy levels far below μ are always full so that $f_0 = 1$, while energy levels far above μ are always empty with $f_0 = 0$. Energy levels within few k_bT of μ are occasionally empty and occasionally full so that the average number of electrons is between 0 and 1. This number cannot exceed one because the exclusion principle forbids more than one electron per level. In the discussion presented in this chapter the electrodes are presumed to be made from the same materials, providing the same Fermi level, and 0 K ensures a sharp distinction between the occupied and virtual levels.

When the molecule is placed between the two reservoirs, there are two possible scenarios: i) the molecule does not couple to the electrodes surface or ii) the interaction is strong and the channel forms good chemical bond with the bulk structures (Figure 2-4).

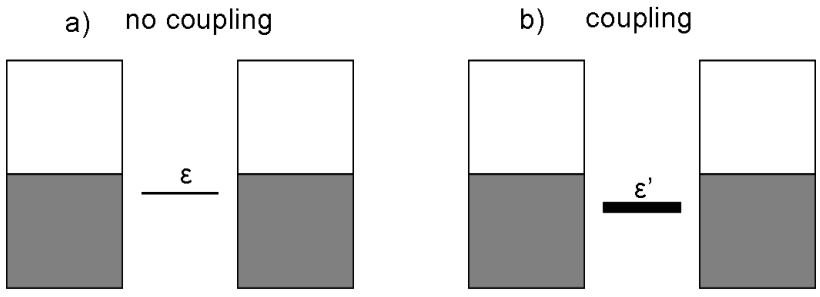

Figure 2-4: Molecule level with a) no coupling to the electrodes and b) the same level broadened and shifted in energy due to strong coupling with the electrodes.

In the first case the energy of the single level will be the same as in the isolated molecule because the molecule is not connected with the reservoirs. In the second

case the strong interaction between the molecular level and the extended wavefunction of the metallic contact results in shifting and broadening of the molecule level (Figure 2-4). Here the energy is denoted with ε' and we represent the broadening of the level with a thicker line. From a practical point of view the case when the molecule is strongly coupled to the electrodes is more important. In an extreme case of strong coupling the waves from the contact propagate through the entire system (electrode plus molecule) and the channel behaves as a metal. In this case the levels of the channel cannot be associated directly with those of the isolated molecule.

An applied bias, *V*, shifts the chemical potential of the electrodes relative to each other by *V/2*. The relative positions of the Fermi levels and the channel level, ε, play a crucial role in controlling the transport. Three possible situations can be considered at this point (Figure 2-5).

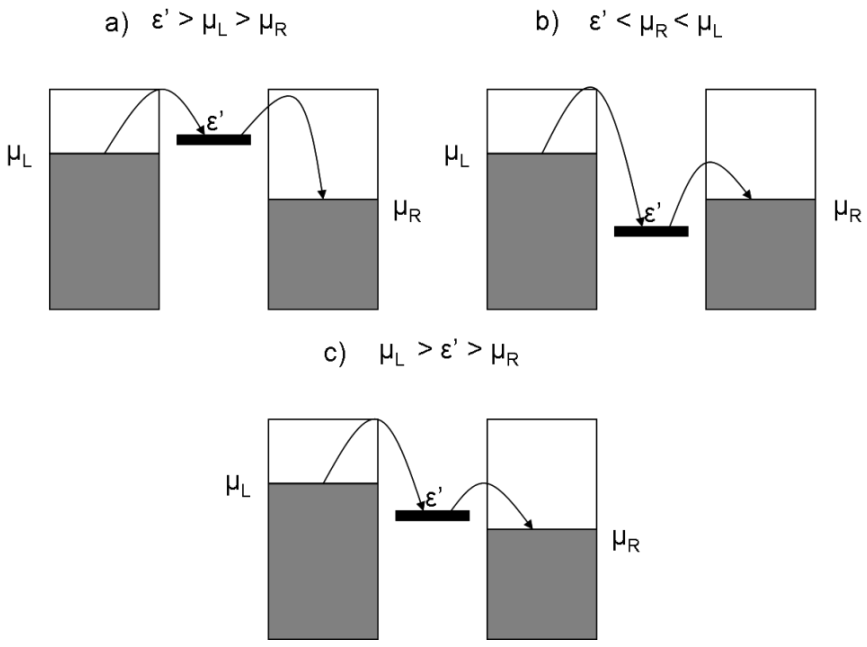

Figure 2-5: Electron transport through a single level: a) the level is above both chemical potentials; b) the level is below both of them; c) the level is between the left and right chemical potential.

In the first case, $\varepsilon' > \mu_L > \mu_R$, the molecule level is above both Fermi energies and the electron cannot be transferred from the left (source) electrode to the channel because the MO has higher energy (Figure 2-5 a). Therefore, no current flow is observed. In the second case, $\varepsilon' < \mu_R < \mu_L$, current again does not flow because now on the right hand (drain) side there are no available empty states to accept the electron (Figure 2-5 b). Therefore, the Pauli Exclusion Principle prevents the current flow. The most important case is the third one, $\mu_R < \varepsilon' < \mu_L$, where the molecular level lies between the chemical potentials of the source and drain electrodes (Figure 2-5 c). Electrons entering from the left hand side can flow into the molecular levels and then out into the drain lead where empty levels of appropriate energy are available. As a result, the current flows. Therefore, we can conclude that current flows only when the molecule level is positioned in the bias window, and, moreover, that the current will be proportional to the number of levels in the bias window. It is not important whether the channel is occupied or empty in the isolated molecule, only that the channel is in the bias window and is coupled to the both leads.

In the following sections we use the single-channel model to develop a quantitative model of electron transport.

2.4 Quantitative model of electron transport

In general, any computer simulation of the electron transport involves the solution of two main equations: the 'Poisson' and transport equations (Figure 2-6).[213,214]

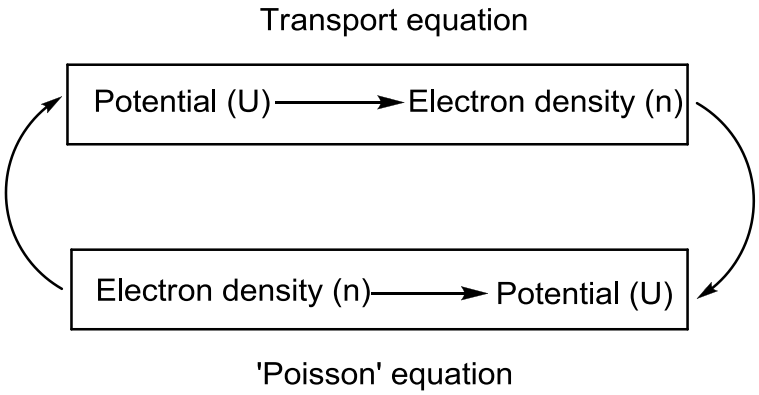

Figure 2-6: Iterative self-consistent solution of transport and 'Poisson' equations.

In the first equation, Transport equation, the effective potential *U* determines the number of electrons that flow into the device, changing the electron density. In the second equation, 'Poisson' equation, the electron density *n* then determines the potential that an electron feels due to the presence of the other electrons. An iterative approach is required to reach self-consistent values of *n* and *U*. We will discuss these equations one by one in the following paragraphs.

2.4.1 Transport equation

Our model system is a molecule device with a single MO with energy ε, and we assume that the molecule is well-coupled to the source and the drain. As a result, the level is shifted relative to the isolated molecule and it is also broadened (this is shown with thicker line in Figure 2-7). The strong coupling allows electrons from the source to leak into the channel and reach the drain. This poses the following question: what is the number of electrons (*N*) inside of the channel? If the system is in equilibrium

(i.e., zero bias), *N* is given by the common Fermi level of the source and the drain (i.e., if ε lies below E_f, the channel will be occupied).

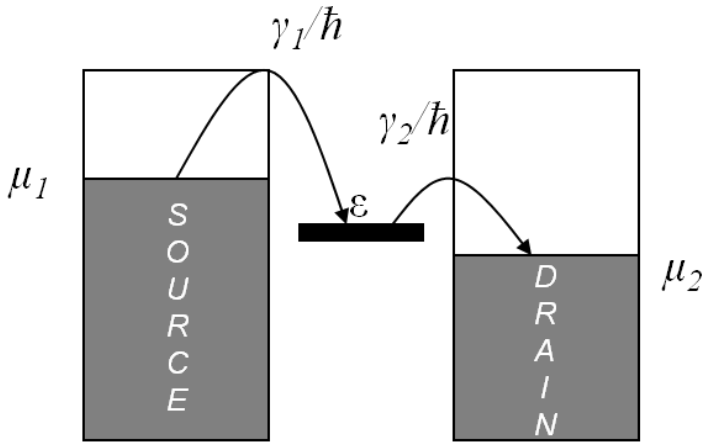

Figure 2-7: Quantitative picture of transport equation.

When bias is finite, however, the systems are not at equilibrium and the number of electrons inside of the scattering region differs from 1 or 0. In this bias the Fermi energies in the source (μ_1) and the drain (μ_2) contacts will separate as follows:

$$\mu_1 = E_f + (qV/2) \text{ Source} \qquad \mu_2 = E_f - (qV/2) \text{ Drain}$$

Equation 6

If the scattering (central) region is coupled only to the source, then the level is in equilibrium and the number of the electrons is determined by the Fermi function for this electrode only, f_1. On the other hand, if the same level is coupled only to the drain, the number of the electrons in the channel equals f_2. Hence, the number of

electrons inside of the scattering region is determined either by the source or the drain when the level has only one contact.

$$f_{1,2}(\varepsilon) = \frac{1}{\exp[(\varepsilon - \mu_{1,2})/k_B T]}$$

Equation 7

It is clear that when the level is coupled to both the source and the drain the actual number of the electrons in the channel is intermediate between f_1 and f_2. In order to obtain this number the following equations can be developed from the current $I_{1,2}$ coming from the source and the drain.

$$I_1 = \frac{q\gamma_1}{\hbar}[f_1 - N] \quad \text{and} \quad I_2 = \frac{q\gamma_2}{\hbar}[N - f_2]$$

Equation 8

where $\gamma_1/\hbar$ and $\gamma_2/\hbar$ represent the rates (per second) at which the electron inside the device escapes into the source and drain respectively. At steady-state $I_1=I_2 \equiv I$ leading to the following expressions for number of electrons, N, and current I:

$$N = \frac{\gamma_1}{\gamma_1+\gamma_2} f_1(\varepsilon) + \frac{\gamma_2}{\gamma_1+\gamma_2} f_2(\varepsilon) \qquad I = \frac{q}{\hbar}\frac{\gamma_1\gamma_2}{\gamma_1+\gamma_2}[f_1(\varepsilon) - f_2(\varepsilon)]$$

Equation 9

From the equations above we can draw some qualitative conclusions about the current flow and the number of the electrons in the one-level conductor. First, in

order to obtain electric current the chemical potentials of the source and the drain should be different ($f_1(\varepsilon) - f_2(\varepsilon) \neq 0$). Second, the number of the electrons inside of the scattering region is between $f_1(\varepsilon)$ and $f_2(\varepsilon)$. The drain keeps delivering electrons to the level, while the source keeps accepting them from the same level. As a result a constant flow of electrons from one reservoir to the other is observed, leading to a net current in the external circuit.

The number of the electrons inside of the scattering region does not depend only on the position of the molecule level if compared to the chemical potentials but also on how well the level is coupled to both reservoirs. The broadening is a consequence of coupling to the source or the drain, and it leads to a density of states described by the Lorentzian function

$$D(E) = \frac{\frac{\gamma}{2\pi}}{(E - \varepsilon - \Delta)^2 + (\frac{\gamma}{2})^2}$$

Equation 10

where $\gamma = \gamma_1 + \gamma_2$ is the width and $\Delta = \Delta_1 + \Delta_2$ is the shift in the level from ε to $\varepsilon + \Delta$. When we include the broadening and integrate all over the energies, the expressions for *N* and *I* take the following form:

$$N = \int_{-\infty}^{\infty} dED(E)\left[\frac{\gamma_1}{\gamma_1 + \gamma_2} f_1(E) + \frac{\gamma_2}{\gamma_1 + \gamma_2} f_2(E)\right] \quad I = \frac{q}{\hbar}\int_{-\infty}^{\infty} dED(E)\left[\frac{\gamma_1\gamma_2}{\gamma_1 + \gamma_2}[f_1(\varepsilon) - f_2(\varepsilon)]\right]$$

Equation 11

Further progress can be made by defining the Green's function, G, as $G = [E - \varepsilon - \sigma_1 - \sigma_2]^{-1}$ where $\sigma_{1,2} = \Delta_{1,2} - i\gamma_{1,2}/2$. Then the corresponding equations can be written as:

$$N = \int_{-\infty}^{\infty} \frac{dE}{2\pi} \left[A_1(E) f_1(E) + A_2 f_2(E) \right] \qquad I = \frac{q}{\hbar} \int_{-\infty}^{\infty} dE T(E) [f_1(E) - f_2(E)]$$

Equation 12

where $A_1 = G\,\gamma_1\,G^+$, $A_2 = G\,\gamma_2\,G^+$, $T(E) = \gamma_1\,G\,\gamma_2\,G^+$. The term *A* is known as the spectral function and it is responsible for the broadening and shifting of the energy level due to the coupling to the source or the drain. The Green's function describes the waves outgoing from the contact and waves incoming to the contact with *G* (retarded) and G^+ (advanced), respectively. *T(E)* is called a transmission spectra and it is describes how easily the electrons can transmit from the source to the drain. These equations describe the current flow and the number of the electrons in a system with a single channel with energy ε. Real devices, of course, have multiple energy levels in different ranges, the energies of which are described by the Hamiltonian matrix *[H]*. Thus, the single-level model can be extended to multiple channels simply by replacing the Green's functions and associated expressions with matrixes:

$$G = [EI - H - \Sigma_1 - \Sigma_2]^{-1} \qquad \Gamma_{1,2} = i[\Sigma_{1,2} - \Sigma_{1,2}^+]$$

$$A_{1,2}(E) = G\Gamma_{1,2}G^+ \qquad T(E) = \Gamma_1 G \Gamma_2 G^+$$

Equation 13

where *I* is an identity matrix of the same dimension as *G*. The number of the electrons is replaced by the density matrix given by an analogous equation.

$$[\rho] = \int_{-\infty}^{\infty} \frac{dE}{2\pi} [A_1(E) f_1(E) + A_2 f_2(E)]$$

Equation 14

The Hamiltonian matrix can, in principle, be obtained from semi-empirical, ab initio or DFT calculations. The diagonal elements of the density matrix *[ρ]* are interpreted as the number of electrons occupying the corresponding basis orbital. The total number of electrons is obtained by adding up all the diagonal elements (Trace*[ρ]*). Equation 14 needs to be multiplied by 2 for the spin degeneracy, unless the spin is explicitly accounted for in the *[H]* matrix itself.

The equations in this section do not represent a formal 'derivation' of the formalism but provide an intuitive feeling for the physics behind coherent ballistic transport.[214] They do not include the effects of incoherent scattering processes (such as electron-phonon interactions) inside the device which become increasingly important as the devices become larger. Scattering process can be included in the NEGF formalism by defining additional self-energy matrices, such as the ones that we defined for the source and the drain contact, but the details are much more complicated conceptually. For this reason we will focus on ballistic transport throughout this thesis.

In the previous sections we have developed a simple description for ballistic transport based on the Landauer-Büttiker formalism. In practice, this formalism involves either the Keldysh's[215-217] or Kadanoff-Baym's method,[215] both of which use non-equlibrium

Green's functions (NEGF) to deal with the elastic process during the electron propagation through the conductor. A quantitative treatment of electron transport is complicated due to electron-electron interactions which are typically dealt with using a mean-field approach at the Hartree-Fock or density functional theory (DFT) level.

2.4.2 'Poisson' equation

The 'Poisson' equation relates the electron density to the potential (Figure 2-6). For this reason most electron transport codes work with the simplest approximation, the Hartree potential U_H obtained from the 'Poisson' equation used in standard device simulation programs:

$$\nabla.\left[\varepsilon \nabla U_H(r)\right] = -q^2\left[n(r) - n_0(r)\right]$$

Equation 15

It is clear that the Hartree potential $U_H(r)$ depends on the electron density difference between the density of the unperturbed system, $n_0(r)$, and the density of the perturbed one, $n(r)$. $n_0(r)$ corresponds to the unperturbed Hamiltonian $[H_0]$. The perturbed Hamiltonian $[H]$ is equal to the $[H_0] + U_H(r)$. The Hartree approximation underestimates the electron-electron repulsion and, as a result, more electrons can enter the channel than we would otherwise expect, making the capacitance larger.

In order to find improved potentials, Hartree-Fock (HF) or density functional theory (DFT) can be used. However, all of these approaches are one-electron approximations to a complex many-body problem and the 'correct' potential remains an elusive goal.

We will introduce the main ideas behind HF and DFT theory in the following section. In the calculations presented in this thesis we use density functional theory to generate the effective potential.

2.5 Theoretical methods – fundamental concepts

Now we will introduce possible ways to calculate the electron distribution and the potential created by them and nuclei in molecules.

The major problem with calculating the electronic structure of real chemical structures is the many-particle nature of the problem in which hundreds of atoms and electrons have to be described. The equation to be solved in many-particle systems is the Schrödinger equation:[218,219]

$$\hat{H}\psi = E\psi$$

Equation 16

where $\hat{H}$ is the Hamiltonian operator. The Hamiltonian operator contains the operations associated with the kinetic and potential energies and it can be written as follows:

$$\hat{H} = \sum_{i}^{N_e} \frac{-\hbar^2}{2m_e}\nabla_{r_i}^2 + \sum_{I}^{N_N} \frac{-\hbar^2}{2M_I}\nabla_{R_I}^2 + \frac{1}{2}\sum_{I\neq J}^{N_N} \frac{e^2 Z_J Z_I}{\left|R_I - R_J\right|} - \frac{1}{2}\sum_{i,I}^{N_e,N_N} \frac{e^2 Z_I}{\left|r_i - R_I\right|} + \frac{1}{2}\sum_{i\neq j}^{N} \frac{e^2 Z}{\left|r_i - r_j\right|}$$

Equation 17

where r_i is the position operator for the *i*-th electron and R_I is the analogous position operator for *I*-th nucleus. In Equation 17 the first term represents the kinetic energy of the electrons of mass m_e, the second term represents the kinetic energy of the nuclei-with mass M_I and the last three terms describe the potential energy in the systems. The third term is the Coulomb interaction between different nuclei, the fourth term is the electrostatic attraction between nuclei and electrons and finally the fifth term is the electron-electron interaction.

Presented in this way, the Hamiltonian operator captures all interactions between the particles (nuclei and electrons). However, this Hamiltonian operator can be solved analytically only for very small systems, and extension to realistic molecular problems requires further assumptions. The first of these is the Born-Oppenheimer approximation (BO), which is based on the fact that the masses of the nuclei are much larger than those of the electrons.[220] In this case we can assume that electrons move much faster than the nuclei, which are therefore effectively stationary in space. Hence, one can separate the electronic wavefunction from that of the nuclei:

$$[\hat{H}_e + \hat{H}_N]\psi_e\psi_N = E\psi_e\psi_N$$

Equation 18

$$\hat{H}_e\psi_e = E\left(R_I\right)\psi_e$$

Equation 19

$$\hat{H}_e = \underbrace{\sum_i^{N_e} \frac{-\hbar^2}{2m_e}\nabla_{r_i}^2}_{T_e\{r_i\}} \underbrace{-\frac{1}{2}\sum_{i,I}^{N_e,N_N} \frac{e^2 Z_I}{|r_i - R_I|}}_{V_{eN}\{r_i\}\{\vec{R}_i\}} + \underbrace{\frac{1}{2}\sum_{i\neq j}^{N} \frac{e^2 Z}{|r_i - r_j|}}_{V_{ee}\{r_i\}} \qquad \psi_e = \psi_e\left(r_1, r_2, r_3, \ldots r_{N_e}\right)$$

Equation 20

The total electron energy $E(R_I)$ is parametrically dependent on the positions of the nuclei and it is valid for particular atomic configuration. In the framework of the BO approximation, the total electron energy $E(R_I)$ of the electronic Schrödinger equation provides a potential for the motion of the nuclei. For a diatomic molecule $E(R_I)$ will have the form of a potential curve, while for a polyatomic systems $E(R_I)$ will generate potential energy surface (PES). Thus, by leading the motion of the PES, the BO approximation has conceptual implications much more profound and far-reaching than those of a conventional mathematical trick. Most computational chemistry calculations involve characterisation of key features of potential energy surfaces.

Before discussing the methods to solve the electronic Schrödinger equation we have to propose a reasonable formulation for the electronic wavefunction. A wavefunction that describes a system of fermions must be antisymmetric with respect to the interchanges of coordinate of any two fermions.[221] The trial wavefunction is typically constructed as a Slater determinant which ensures that the total wavefunction is anti-symmetric.[222,223]

$$\psi_e = \frac{1}{\sqrt{N!}} \begin{vmatrix} \phi_1(\vec{r}_1) & \phi_2(\vec{r}_1) & \cdots & \phi_N(\vec{r}_1) \\ \phi_1(\vec{r}_2) & \phi_2(\vec{r}_2) & \cdots & \phi_N(\vec{r}_2) \\ \vdots & \vdots & \ddots & \vdots \\ \phi_1(\vec{r}_N) & \phi_2(\vec{r}_N) & \cdots & \phi_N(\vec{r}_N) \end{vmatrix} = \frac{1}{\sqrt{N!}} \det[\phi_i(\vec{r}_i)]$$

Equation 21

The columns in a Slater determinant are single electron wavefunctions (orbitals), which are products of a spatial and a spin function, while the electron indices are

along the rows. For a molecule each one-electron wavefunction will be a molecular orbital.

Use of a single Slater determinant to describe the wavefunction leads to the Hartree-Fock (HF) method.[224,225] The major drawback, however, is the absence of electron-electron correlation in this method. This can be overcome by including additional determinants in the expansion of the wavefunction (so-called post-HF methods) but the computational cost of this methodology increases dramatically with size. As a result, all current electron transport codes are based on an alternative strategy for dealing with correlation, which is density functional theory.[226,227]

2.6 The Hartree-Fock approximation

In the Hartree-Fock (HF)[224,225] method a single Slater determinant is used to represent the wavefunction. Electron-electron repulsions are treated in an average way, in which each electron is considered to be moving independently of the others in the mean field created by the other electrons. The single determinant described above gives rise to the lowest energy that can be obtained by using the varational principle.[228] The variational theorem is the fundamental concept in the computational chemistry calculations and, according to it, the approximate value of the energy that is calculated with a trial wavefunction (Ψ_{trial}) cannot be lower than the true energy of the systems E_0:

$$E_0 \leq \frac{\langle \psi_{trial} | \hat{H} | \psi_{trial} \rangle}{\left| \langle \psi_{trial} | \psi_{trial} \rangle \right|}$$

Equation 22

This approach provides a criterion for the optimisation of trial wavefunctions. Since the energy calculated from a trial wavefunction is always higher than the true (lowest) energy, a better wavefunction can be obtained by varying the parameters in terms of which Ψ_{trial} is expressed until the expectation value for the energy is minimised. This approach reduces the N-particle problem to a set of one-particle eigenvalue problems, the so called Hartree-Fock equations:

$$\hat{f}_i \psi_i = \varepsilon_i \psi_i$$

Equation 23

An orbital ψ_i is an eigenfunction of the effective one particle Hamiltonian $\hat{f}_i$, known as the Fock operator, with corresponding energy ε_i. The Fock operator for each electron *i* can be written as:

$$\hat{f}_i = -\frac{1}{2}\nabla_i^2 - \sum_{A=1}^{M} \frac{Z_A}{r_{iA}} + \hat{V}_i^{HF}$$

Equation 24

The last term of the equation represents the average potential experienced by electron *i* due to the presence of the other electrons and it has the form:

$$\hat{V}_i^{HF} = \sum_j (\hat{J}_i(j) - \hat{K}_i(j))$$

Equation 25

Where $\hat{J}_i$ and $\hat{K}_i$ are the Coulomb and the exchange operators, respectively, defined as

$$\hat{J}_i \left|\psi_j(2)\right\rangle = \left\langle \psi_i(1) \right| \frac{1}{r_{12}} \left|\psi_i(1)\right\rangle \left|\psi_j(2)\right\rangle$$

Equation 26

and

$$\hat{K}_i \left|\psi_j(2)\right\rangle = \left\langle \psi_i(1) \right| \frac{1}{r_{12}} \left|\psi_j(1)\right\rangle \left|\psi_i(2)\right\rangle$$

Equation 27

The Coulomb operator takes into account the Coulomb repulsion between electrons, whereas the exchange operator represents a modification of this energy that can be ascribed to the effects of spin correlation.

Each orbital ψ_i is obtained by solving the eigenvalue equation with the corresponding operator $\hat{f}_i$. However, $\hat{f}_i$ depends on the orbitals of all the other electrons, so an iterative procedure has to be followed for the solution of HF equations. This procedure is known as the self-consistent field (SCF) method and it works in the following manner: by making an initial guess for the orbitals the average potential can

be calculated; using this value for the field a new set of orbitals is obtained by solving the HF equations and the process is repeated until self-consistency is achieved.

In practice, the HF equations are solved by introducing a finite set of *M* known basis functions, ϕ_α, which form the basis set. Each molecular orbital is expanded in terms of these basis functions, which are conventionally called atomic orbitals. The procedure is known as linear combination of atomic orbitals to yield molecular orbitals (LCAO-MO).

$$\psi_i = \sum_{\alpha=1}^{M} c_{\alpha i}\phi_\alpha$$

Equation 28

Hence, the Hartree-Fock equations can be written as:

$$\hat{f}_i \sum_{\alpha=1}^{M} c_{\alpha i}\phi_\alpha = \varepsilon_i \sum_{\alpha=1}^{M} c_{\alpha i}\phi_\alpha$$

Equation 29

And all M equations can be collected in matrix equations for the expansion coefficients known as the Roothaan-Hall equation:

$$FC = SC\varepsilon$$

Equation 30

where ε is a diagonal matrix of the orbital energies ε_i, and *S* is the overlap matrix, $S_{\alpha\beta} = \langle \phi_\alpha | \phi_\beta \rangle$, the *F* matrix contains the Fock matrix elements, $F_{\alpha\beta} = \langle \phi_\alpha | \hat{f} | \phi_\beta \rangle$ and *C* in the *M x M* matrix of the expansion coefficient $c_{\alpha i}$. In this way the problem of determining the HF molecular orbitals Ψ_i and orbital energies ε_i is transformed into a matrix eigenvalue problem. The solution of the Roothaan-Hall equations with *M* basis function for a system with *N* electrons produces a total of *2M* spin orbitals, *N* of which will be occupied and *2M – N* unoccupied, or virtual. The Slater determinant is composed of the occupied orbitals in the HF wavefunction and it represents the best variational approximation to the ground state of the system within the limitation of the single determinant form and the basis set approximation. The larger and more complete the basis set is, the greater will be the flexibility in the expansion of the orbitals and the lower the expectation value for the energy. If an infinitely large basis set is used, the energy obtained will correspond to the so-called Hartree-Fock limit.

2.7 Post-HF methods

In the previous section we had shown that the Hartee-Fock method takes into account the average effective of electron repulsion but not the explicit electron-electron correlation. Physically, this means that the electrons in the HF model are allowed to be closer to each other than if the individual electron correlation were taken into account. Hence, an appropriate treatment of motion of electrons in the primary deficiency of HF theory which leads to calculated energies that are above the

exact values. The difference is energy between HF limit and the exact energy is defined as the correlation energy:[229,230]

$$E(correlation) = E(exact) - E(HF) < 0$$

Equation 31

We can distinguish between two types of correlation: dynamic and static correlation. The first correlation refers to the instantaneous electron-electron repulsion, where the static correlation refers to the inadequate representation of nearly degenerate configurations by a single determinant.[231]

Inclusion of correlation generally improves the accuracy of computed energies and molecular geometries, while in cases such as transition metal systems it improves the accuracy of an adequate treatment. The electron correlation is often essential in order to obtain results that are even qualitatively correct. A way to address the electron correlation is to include explicitly the interelectronic distance terms in the wavefunction. However, this approach is extremely expensive and it becomes impractical for more than three or four electrons. Instead, most of the current electron correlation methods (post-HF methods) normally use the HF wavefunction as a starting point and attempt to improve on the HF results.

The configuration interaction (CI) method is a theoretically elegant approach, which would, in the limit of full basis set, yield the physically correct energy.[232] The CI method begins from the HF wavefunction, and new determinants are included by promoting electrons from the occupied orbitals to the unoccupied orbitals. These new determinants are defined as singly (S), doubly (D), triply (T), and quadruply (Q) excited

determinants depending on how many electrons have been promoted to the unoccupied orbitals of the reference determinant. The expansion coefficients c_i are then determined variationally to yield the final CI wavefunction:

$$\Psi_{CI} = c_0\Psi_{HF} + \sum_S c_S\Psi_S + \sum_D c_D\Psi_D + \sum_T c_T\Psi_T$$

Equation 32

A full configuration interaction (FCI) calculation, including all possible excitations, would give the exact quantum mechanical result if an infinitely large basis set was used. Alternatively, FCI provides the lower possible energy in a finite basis set and the difference between the HF and the FCI energies corresponds to the correlation energy within the basis set. In practice, FCI calculations are impossible for all but the tiniest molecular systems. The computational cost is reduced by limiting the excitation order, usually up to doubly or triply excited determinants (CISD, CISDT) and by using the frozen core approximation, in which those occupied orbitals that correspond principally to inner-shell electrons are omitted from the CI treatment. Although both FCI and limited CI methods are variational, only FCI is size-consistent, i.e., it gives additive results when applied to isolated molecules. Substation computation cost of the CI methods has encouraged the development of several related methods.

One of them is the Multiconfigurational Self-Consistent Field (MCSCF) method where the wavefunction is written as a linear combination of configuration state functions and it varies not only in terms of the expansion coefficients c_i but also of the molecular orbitals.[233-236] The optimum MCSCF orbitals can be obtained by an iterative

process somewhat similar to that of the SCF approach. The most commonly used MCSF method is called the complete active space self-consistent field (CASSCF) approach, which includes all possible determinants that can be formed by distributing a set of active electrons among a set of active orbitals. The CASSCF method separates the orbitals into active and inactive space. Further, the active space is denoted as the CAS(*n*,*m*), where *n* is the number of electrons and *m* is the number of active orbitals. After that, a full expansion for the CI can be obtained by considering the defined active space. Due to the computational cost of the CASSCF approach, the size of the active space is minimized by including only a minimum number of orbitals for the CASSCF treatment. However, selecting an active space is a significant challenge as an appropriate choice can lead to inaccurate results.

Perturbation methods offer an alternative approach to electron correlation problem. The approach is based on the assumption that an already calculated solution to the problem at hand (the reference) is close to correct. Small corrections are then applied to the reference in the form of perturbations. In this approach, electron correlation is added as a perturbation to the HF wavefunction. A representative example of this kind of method is the Møller-Plesset (MP) perturbation theory.[237] Because of the way the MP theory defines the unperturbed systems, MP0 is the sum of HF one-electron energies and MP1 (first-order correction to energy) gives the correct HF energy (MP1 = HF). Second-order corrections (MP2) bring in contributions wherein doubly excited configurations interact with the reference configuration and this recovers most of the correlation energy. Fourth-order corrections (MP4) usually represent the practical limit for this type of calculations.

In general, MP2 usually recovers a large amount of the correlation energy (typically ~ 80 – 90 %) and it is quite efficient computationally. For these reasons, and also due to availability of analytic gradient and second derivates, MP2 has been, and still is, a very powerful correlated ab initio method. For transition metal systems, in particular, MP2 has been the only viable, routinely used approach for quite some time, although today it has been largely replaced by DFT methods, especially for first-row transition metals.

However, all of the methods described above are very expensive for large systems, such as proteins and large molecules. For this reason, nowadays the main method used by the computational chemist is the density functional theory (DFT). We will present the main features of the DFT theory in the following sections.

2.8 Density functional theory (DFT)

The basic philosophy of density functional theory is to use the electron density instead of a wavefunction in order to obtain information about chemical systems.[226,227,238-240] Using the electron density as the fundamental entity can provide significant advantages. First of all, the electron density depends only on three coordinates, regardless of how many electrons are present in the system, as compared to the wavefunction for *N*-electron system, which depends on *3N* coordinates and is expected to increase in complexity with the number of electrons. Additionally, since we start with the electron density, electron correlation is taken into account from the outset.

The main idea behind the DFT method is that the energy of an electronic system can be written in terms of the electron density *ρ(r).* More precisely, the electronic energy *E* is said to be a functional of the electron density, denoting with E[*ρ(r)*], in the sense that for a given function *ρ(r)* there is a single corresponding value for energy, i.e., there is a one-to-one mapping of density and energy.

The concept was first developed by Thomas and Fermi who proposed in 1927[241] that the kinetic energy of non-interacting electrons is proportional to $\rho(r)^{5/3}$, a result derived from the free electron model. The electrostatic potential acting on an electron in the system is determined by solving the 'Poisson' equation with the density *ρ(r)*. The total ground state energy is then calculated as an integral over a function that depends upon the local density of the ground state only.

$$E = \int dr^3 \rho(r) \varepsilon[\rho(r)]$$

Equation 33

This approach was extended during the 1950s by Slater and an improvement of this approximation appears in the Hartree-Fock-Slater (HFS) Xα method.[242-245] It was developed as an approximated solution to the HF equations. In this method, the HF exchange was approximated by:

$$E_{X\alpha}[\rho_\uparrow, \rho_\downarrow] = -\frac{9}{4}\alpha\left(\frac{3}{4\pi}\right)^{1/3} \int [\rho_\uparrow^{4/3}(r) + \rho_\downarrow^{4/3}(r)]dr$$

Equation 34

The exchange energy $E_{X\alpha}$ is a functional of density for spin up and spin down electrons and it contains an adjustable parameter α. This parameter was empirically optimised for each atom of the periodic table and its value was between 0.7-0.8 for most atoms.[246,247]

The real breakthrough came in the 1960s when Hohenberg and Kohn established the two theorems that are the foundations of modern DFT.[240] The first theorem states that the many-particle ground state is a unique functional of *ρ(r)*, as the external potential determining the Hamiltonian operator is a unique functional of *ρ(r)*. Or with other word, every observable of a stationary quantum mechanical system (including energy) can be calculated, in principle, exactly from the ground-state density alone, i.e., every observable property can be written as a function of the ground-state density. Therefore, all components, such as kinetic energy, electron-electron interaction and electron-nuclei interaction, can also be expressed as functional of the electron density:

$$E[\rho(r)] = T_e[\rho(r)] + V_{ee}[\rho(r)] + V_{eN}[\rho(r)]$$

Equation 35

Only the last term of the above equation is system-dependent. The first two terms corresponding to the kinetic energy and the electron-electron interaction, are universal, i.e., their form does not depend on the particular system under consideration. $T[\rho(r)]$ and $V_{ee}[\rho(r)]$ constitute the so-called universal functional, $F[\rho(r)]$. If $F[\rho(r)]$ was known exactly, we would be able, in principle, to obtain exact

solutions to the Schrödinger equation for any kind of systems. However, the explicit form of the universal function is unknown.

The second Hohenberg-Kohn theorem introduces the variational principle into this approach, stating that the functional, which delivers the 'true' ground state energy, must correspond with the 'true' ground state density *ρ(r*). Any other trial density of *ρ'(r)* leads to higher energy values.

$$E[\rho(r)] \leq E[\rho'(r)] = T_e[\rho'(r)] + V_{ee}[\rho'(r)] + V_{eN}[\rho'(r)]$$

Equation 36

This theorem gives an opportunity for variational optimization of the density functional. It should be noted that this formalism applies to the ground state that cannot be extended in a straightforward manner to excited states.

2.9 The Kohn-Sham approach

A practical solution to the solution of the Hohenberg-Kohn equations was introduced by Kohn and Sham.[248] In fact, especially in chemistry, DFT has become synonymous with the Kohn-Sham (KS) DFT approach.

Kohn and Sham introduced the idea of a reference system of non-interacting electrons and repartitioned the total energy functional into the following parts:

$$E[\rho] = T_S[\rho] + \int [\hat{V}_{ext}(r) + \hat{J}(r)]\rho(r)dr + E_{XC}[\rho]$$

Equation 37

where $T_S[\rho]$ corresponds to the kinetic energy of the electrons in a system which has the same density ρ as the real system, but in which there are no electron-electron interactions. $\hat{J}(r)$ is the classical Coulomb interaction between electrons:

$$\hat{J}(r) = \int \frac{\rho(r')}{|r' - r|} dr'$$

Equation 38

which includes electron self-interaction and $\hat{V}_{ext}(r)$ is the potential arising from the nuclei:

$$\hat{V}_{ext}(r) = \sum_A \frac{Z_A}{|R_A - r|}$$

Equation 39

The E_{xc} term is called the exchange-correlation functional and it incorporates all the contributions to the energy that are not accounted for by the previous terms. It includes not only the electron exchange and correlation energies, but also a correction for the self-interaction that was incorporated in the Coulomb term and the portion of the kinetic energy that corresponds to the difference between the non-interacting and the real system. E_{xc} has been described as a junkyard that contains

everything that is unknown or problematic, everything that we do not know how to handle appropriately.

The advantage of introducing a non-interactive system is that although $T_s[\rho]$ is not known exactly as a function of ρ, it can be expressed exactly in terms of one-electron function as

$$T_S[\rho] = -\frac{1}{2}\sum_{i=1}^{N}\langle \psi_i | \nabla_i^2 | \psi_i \rangle$$

Equation 40

Thus, one-electron functions are reintroduced in density function theory in the form of Kohn-Sham orbitals ψ_i. They can define the Kohn-Sham equation with a one-electron operator, similar to the HF equations, as:

$$\left[-\frac{\hbar^2}{2m}\nabla^2 + V_{eff}(r) \right] \psi_i(r) = \varepsilon_i \psi_i(r)$$

Equation 41

and the electron density can be obtained from the $\psi_i^* \psi_i$. The eigenstates, which are a solution to the above equations, are known as Kohn-Sham states. Now the trick is to choose the effective potential V_{eff} in such a way so that the density obtained for the non-interacting systems is the same as that of the real system of interest.

The effective potential V_{eff} corresponds to the effective single particle potential seen by an electron due to its interaction with the other *N-1* electrons, and it is defined as

$$V_{eff}(r) = V(r) + V_H(r) + V_{XC}(r)$$

Equation 42

The first term in the above equation is the external potential and it includes the potential originating from the nuclei as well as an external potential applied by the electrons. The middle term corresponds to the classical Coulomb potential for the electron density *ρ(r)*. Finally, the last term is the exchange-correlation potential defined as the functional derivatives of the exchange-correlation energy E_{xc} with respect to the electron density *ρ(r)*. This last term contains all the remaining contributions to the potential that are not known in detail. Finally, Equation 42 can be written as:

$$V_{eff}(r) = -\sum_A \frac{Z_A}{r_{iA}} + \int \frac{\rho_{r_2}}{r_{12}} dr_2 + \frac{\delta E_{XC}}{\delta \rho}$$

Equation 43

If E_{xc} and V_{xc} were known exactly, one could indeed obtain the exact ground state energy. However, this is not the case and a number of approximations to the true functional have emerged over the last 30 years. The main types of approximation can be classified as local density, generalized gradient, meta-general gradient and hybrid functional approximations (increasing in accuracy and suitability for molecular systems in the given order). These are briefly introduced in the following paragraphs.

2.9.1 Local density approximation (LDA)

The local density approximation is based on the concept of a homogeneous electron gas, where the electrons are distributed above a positively charged background. The basic formulation for E_{xc} in the LDA is as follows:

$$E_{XC}^{LDA}[\rho] = \int \rho(r)\varepsilon_{XC}(\rho(r))dr$$

Equation 44

where $\varepsilon_{xc}(\rho(r))$ is the exchange-correlation energy per particle of the uniform electron gas, which can be decomposed into an exchange and correlation part.

$$\varepsilon_{XC}(\rho(r)) = \varepsilon_X(\rho(r)) + \varepsilon_C(\rho(r))$$

Equation 45

According to an approximation by Slater, ε_x can be written as:

$$\varepsilon_X = -\frac{3}{4}\sqrt[3]{\frac{3\rho(r)}{\pi}}$$

Equation 46

Numerous expressions have been proposed for the correlation energy density ε_c because even for uniform electron gas no analytical derivation of this functional has proven possible. They are usually characterized by the initials of their authors and a

number representing the respective variant or publication year of the functional and its specific parameterization (e.g., VWN[249] or PW92[250]).

It is clear that whilst the LDA might be an acceptable approximation for simple metals, it is unlikely to provide a suitable model for a molecule with its very inhomogeneous distribution of electron density. The fact that the homogeneous electron gas is the only case where the exchange and correlation terms can be defined with high accuracy explains why LDA still plays such an important role in DFT.

2.9.2 Generalised gradient approximation (GGA)

The next logical step is to include the gradient of the electron density *ρ(r)*. Inhomogeneity of the electron density distribution can be described in this way:

$$E_{XC}^{GGA}[\rho] = \int F(\rho(r), \nabla\rho(r))dr$$

Equation 47

The functional *F* is of central importance in this approximation. Again, a large number of proposals exist, mostly obtained by fitting procedures, with the corresponding functionals being named again after their authors (e.g., PW91,[251] PBE,[252] LYP,[253] etc.)

One of the most popular GGA exchange functionals, known simply as B, was developed by Becke in 1988.[254] It incorporates a single empirical parameter optimised by fitting to the exchange energies to six noble gas atoms. Many other gradient-corrected exchange functionals have been developed by considering the physical

properties to which the parameters have been adjusted, and the physical constraints that have been applied to the nature of the solutions, such as long range cancellation of self-interaction. With respect to the correlation functionals, P86 is a popular GGA correlation functional[255] which holds one empirical parameter fitted for the Ne atom. This was modified later by Perdew and Wang (PW91).[251] Another widely used GGA correlation functional is LYP proposed by Lee, Yang and Parr.[253] It has empirical parameters fitted to the He atom and its overall performance may originate from an efficient handling of self-interaction error in many-electron system. Typical combinations (exchange and correlation functionals) in common use are BLYP,[256,257] BP86[258] and BPW91,[259] and these GGA functionals increase the accuracy of calculated energies compared to the LDA approach. From chemical perspective, the GGA is more appropriate because the electron density is not uniform everywhere in a molecule and it has been widely used to calculate bond lengths in organic structures and reaction paths.

The next obvious step is to include the second derivates of the density in order to improve the functional. Some scientists, such as Becke and Roussel, proposed an exchange functional (BR)[260] having such dependence, while Proynov, Salahub, and co-workers[261] examined the same option for the correlation functional. Such functionals are named meta-GGA (MGGA) functionals and they go beyond simply the gradient correction.

Nowadays a meta-GGA functional is referred more typically to one that includes a dependence on the kinetic energy density $\tau(r)$, i.e., on the laplacian of the orbitals

$$\tau(r) = \sum_{i}^{occupied} \frac{1}{2}\left|\nabla \psi_i(r)\right|^2$$

Equation 48

where the ψ_i are the self-consistent determined Kohn-Sham orbitals. An often used kinetic energy density functional (i.e., meta-GGA functional) is the TPSS functional developed by Tao, Perdew, Staroverov and Scuseria.[262] The TPSS functional is not fitted to experimental data, and therefore this functional is referred to as a 'nonempirical' functional. However, the extra complexity of this functional does not yield a very large improvement in accuracy over GGA functional.[239]

Unfortunately, meta-GGA functionals have not yet reached numerical performances comparable with the GGAs.[263,264] As a matter of fact, they can be considered as a significant improvement only for some properties (e.g., thermochemistry),[263,264] while poor performances are provided for other molecular parameters (e.g., geometries).[265] Furthermore, hybrid functionals, which mix a fraction of Hartree-Fock (HF) exchange with Kohn-Sham (KS) exchange, gained a prominent position, due to the quality of their numerical results.[266] Other option is hybrid meta GGA – a combination of meta GGA with Hartree-Fock exchange. Such functionals have been developed by Truhlar and co-workers – M06, M06HF, M062X, M05, and M052X.[98,267,268] The half-and-half functionals, namely BHandH and BHandHLYP, are also well-known, where these functionals hold 50% exact exchange.[269]

2.9.3 Hybrid functionals

The GGA, however, fails to describe systems with strong electron correlations, where the charge density changes sharply. For this reason the so-called hybrid functionals, where part or all of the exchange term from the HF method replaces the LDA term (keeping the correlation term intact), are proposed.

$$E_{XC} = E_X^{exact} + E_C^{KS}$$

Equation 49

A large number of such functionals can be found in literature, the most popular of which is B3LYP (Becke-3,[270] Lee, Yang, Parr[253]).

$$E_{XC}^{B3LYP} = (1-\alpha)E_X^{LDA} + aE_{XC}^{\lambda} + bE_X + cE_C^{LYP} + (1-c)E_C^{LDA}$$

Equation 50

where λ indicates the value obtained for non-interacting particles and a, b, c are parameters determined by fitting the functional to ionization energies, total energies and proton affinities of a set of molecules. So far the hybrid functionals give the best performance among all functionals. They have been applied successfully to transition metal systems, especially of the first row, and they are usually considered to perform better than many ab inition methods. This fact made them so popular among computational chemistry community. It is noted, however, that the correct amount of exact exchange included in a hybrid functional cannot be constant for all species.[271]

Accurate treatment of different systems usually requires the adjustment of the percentage of HF exchange.

2.10 Methods for calculating Kohn-Sham states

There are different methods for implementation of the DFT theory. In practical DFT implementations of the Kohn-Sham orbitals are typically described by a basis set.[272] An alternative approach is based on real-space grid, which does not require a basis set explicitly and which we will not discussed here.[273,274] In principle, an infinite basis set should provide an accurate solution but, in practice, the basis set is always terminated leading to an approximate solution.

Basis sets can be separated in two major groups: localized atomic orbitals and plane waves. It is also possible to construct a mixture of these two. Localized atomic orbitals are usually relatively small and suitable for describing nearly localized core electrons. On the contrary, the valence electrons can be nearly free and it is easier to describe them with plane waves. Therefore, the choice of the basis set needs to be determined by the systems that will be investigated. From the computational chemistry point of view a localized basis set has a number of advantages. One of these is that the range of interaction is finite, and consequently Hamiltonian matrix elements tend to zero for orbitals that are far apart. Therefore, the Hamiltonian and overlap matrices become relatively sparse saving memory and computational time.

Basis functions are classified with respect to their behaviour as a function of radial component. Slater-type orbitals (STOs) have a simple exponential form e^{-ar}, while Gaussian-type orbitals (GTOs) have the form e^{-ar2}. STOs represent better the

behaviour of the hydrogenic atomic orbitals, but GTOs are far easier to handle computationally because the product of two GTOs centred on different atoms is simply a third GTO located in between, something that is not true for STOs. In order to achieve accuracy and efficiency basis sets are constructed by using GTOs in the form of contacted basis functions: a basis function is not represented by an individual GTO but by a linear combination of primitive GTOs that aims to reproduce STO as accurately as possible. These types of contracted GTOs basis are widely used in computational chemistry. We can also distinguish different types of basis sets based on the number of the basis functions that represent each atomic orbital. If only one basis function is used to describe an atomic orbital, than the result is a minimal basis set. One example is STO-3G where each basis function meant to resemble STO is formed as a linear combination of three GTOs.[275] The term single-ζ is also used to describe this basis set. A basis set with two functions on each atom is called a double-ζ basis. It is possible to add more functions for each type of orbitals, leading to triple-ζ and multiple-ζ basis set. This basis set is used in our calculations presented in this thesis.

2.11 SIESTA code – main features

Our electron transport calculations are performed with a program based on Siesta code. In this method a localised basis set numerical orbitals with fine range is used.[276,277] Basis sets are used as solutions to the Schrodinger equation of the atom in hard-wall potential with the boundary condition that it should be zero at a specific

radius. The implementation includes the possibility of multiple zetas at a specific radius and the accuracy is similar to calculations with the Gaussian orbitals. The great advantage is that the interactions are strictly zero beyond some distance, which allows us to partition the system unambiguously and to define different regions in our system.

The atom cores are described by the Troullier-Martins pseudopotentials.[278] This technique allows separation of the core electrons from the valence electrons. The benefit is the reduction of the number of particles in our calculations and possibly an inclusion of relativistic effects. The drawbacks are that this is still a one-electron particle representation. Small-core approximation assumes there is no significant overlap between the core and valence electrons. However, the pseudopotential allows us to treat the valence electron only. This reduces the number of the basis function significantly and it also accelerates the calculations. Pseudo and all-electron valence eigenstates have the same energies and amplitude (density) outside a chosen core cut-off radius Rc. Shorter cut-off radii are said to be softer, hence, rapidly converging, less transferable and less accurate. Full detail of the electron transport calculations are presented in Chapter 3.

All vacuum calculations are performed with Amsterdam Density Functional program package (ADF) program versions 2008.1 and 2010.1.[279] It uses Slater-type orbitals (STO) as the basis functions and numerical integration throughout. The code offers excellent treatment of heavy and transition metals. Full details of methodology, including the basis set and the functional, are presented in Chapter 3. The chemical structures and figures have been carried out with ChemBioDraw level Ultra. Version 11.0.1[280] and GIMP programs.[281]

Chapter 3

Efficient spin filtering through tricobalt extended metal atom chains

3.1 Introduction

As discussed in the first chapter, one-dimensional metal string complexes are particularly attractive candidates as new building blocks for nanowires. One prominent example is extended metal atom chains (EMACs) which are unique in their chemical and electronic diversity. In this chapter we will discuss the prototype cobalt-based EMAC, $Co_3(dpa)_4(SCN)_2$ and establish the link between its basic electronic structure and its electron transport properties. The results reported in this chapter will also establish the framework for the remainder of the thesis, where we apply similar ideas to progressively more complicated members of the EMAC family. The contents of this chapter have been published in *Inorg. Chem.*, **2010**, 49(12), 5591-5597.

3.2 Structural and magnetic properties of tricobalt structure

Of all the known EMACs with oligo-α-pirydylamine ligands, the trinuclear cobalt complexes, $Co_3(dpa)_4X_2$ ($X = Br^-, Cl^-, CN^-, SCN^-$), have been the most extensively studied due to their remarkable structural and magnetic behaviour. The first cobalt

compound, $Co_3(dpa)_4Cl_2$, was reported by Peng and co-workers in 1994.[282] It was proposed to have an asymmetric structure, with one short and one long Co-Co bond (Co-Co distance 2.270(3) and 2.472(3) Å). The short Co-Co separation corresponded approximately to those found in covalently bonded Co-Co dimmers, while the other Co centre had the square pyramidal geometry typical of an isolated Co^{II} ion. The Co-N bonds were also significantly longer at the isolated Co centre than at the Co-Co dimer unit, while the terminal Co-Cl was somewhat shorter. The magnetic moment was observed to be highly temperature dependent, a phenomenon that was attributed to spin crossover (S = 1/2 -> 3/2) at the pentacoordinate Co^{II} center. However, In 1997 Cotton and co-workers reported a second structural study of $Co_3(dpa)_4Cl_2$, and argued instead for a symmetric form with equivalent Co-Co distances of 2.318(9) Å.[161] A subsequent study then revealed that both symmetric and unsymmetric (Co-Co = 2.459(1) and 2.285(1)[283]) isomers can crystallise separately from the same solution (Figure 3-1). The two polymorphs differed only in the number of solvent molecules (CH_2Cl_2) in the crystal. In 1999 the unsymmetric isomer was again reported in a different crystal polymorph,[162] with similar Co-Co distances (2.294(1)-2.466(1)). It seems unlikely, however, that both symmetric and unsymmetric forms persist in solution: in the NMR experiment all eight pyridine rings are equivalent on the NMR timescale, indicating either that only the symmetric structure is present or that the unsymmetric form is highly fluxional.[284] In either case, it seems clear that the two isomeric forms must be energetically close.

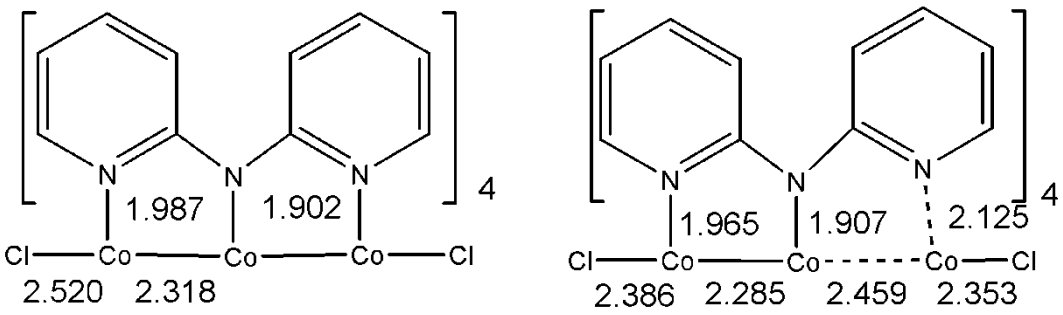

Figure 3-1: Bond lengths of symmetric (left) and unsymmetric (right) forms of $Co_3(dpa)_4Cl_2$.

Magnetic susceptibility measurements indicate that both symmetric and unsymmetric forms have doublet ground states,[285] although incomplete crossover behaviour to quartet (symmetric) or sextet (unsymmetric) states is apparent at high temperatrures. Basing on this body of experiment data, it has been suggested that the tricobalt systems represent genuine case of bond-stretch isomerism,[286] wherein the molecule exists in two structurally different forms that vary only in the lengths of one or more bonds.

It appears that this structural diversity is present only in halide-capped tricobalt chains, $Co_3(dpa)_4X_2$. Thus, although a very similar picture emerges in the $Co_3(dpa)_4Br_2$ analogues,[287] where both symmetric and unsymmetric structures have been detected, only symmetric forms have been characterised for $Co_3(dpa)_4X_2$, where X = NCS^-, CN^- and $N(CN)_2^-$.[288] In all cases the Co_3 chains are symmetrical with Co-Co distances in the range 2.31-2.32 Å and magnetic studies indicate that μ_{eff} = 1.9-2.0 at temperature between 1.8 and 200 K. Even at 400 K the high-spin states cannot be accessed.

3.3 Electronic structure: qualitative aspects

In order to understand the relation between the structural properties described above and the underlying electronic structure, it is useful to build a qualitative symmetry-based model.

The electronic structure of the EMACS in general can be discussed in terms of fifteen molecular orbitals with dominant metal character. Linear combinations of these fifteen orbitals can generate molecular orbitals with σ, π and δ symmetry with respect to the M-M-M axis (Figure 3-2). The σ MOs are formed from combinations of the atomic d_z^2 orbitals, while two sets of δ MOs are formed from d_{xy} and $d_{x^2-y^2}$ orbitals. Finally, two degenerate sets of π MOs are formed from d_{xz} and d_{yz} orbitals.

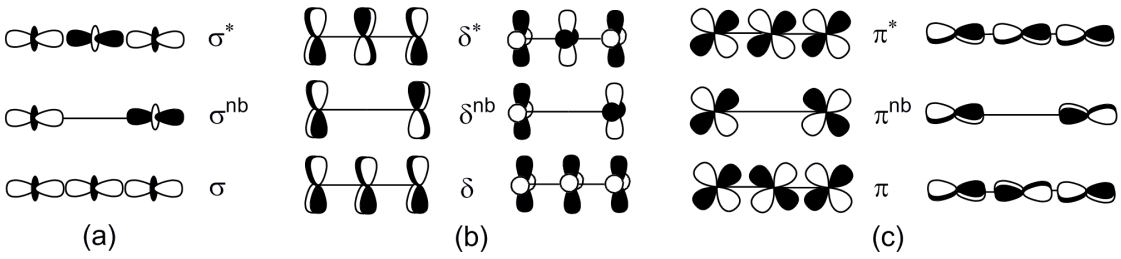

Figure 3-2: Bonding, nonbonding and antibonding combinations: (a) σ MOs from d_z^2, (b) δ from d_{xy} and $d_{x^2-y^2}$, (c) π MOs from d_{xz} and d_{yz}.

In the absence of ligands the atomic d_{xy} and $d_{x^2-y^2}$ orbitals are degenerate, but the presence of four nitrogen donors along the local x and y axes destabilises the latter. Within the remaining low-lying orbitals overlap between d_z^2 is greatest followed by d_{xz}/d_{yz} then d_{xy}, leading to the basic splitting diagram shown in Figure 3-3 Column B. We have thus far ignored the influence of the terminal ligands, which will destabilise the orbitals of σ symmetry by introducing antibonding overlap with appropriate

(occupied) linear combinations of lone pairs directed along the z axis (Columns C and D in Figure 3-3). In the case of $Co_3(dpa)_4Cl_2$ π-donor effects of the Cl^- ligand are minimal and they can be ignored here.

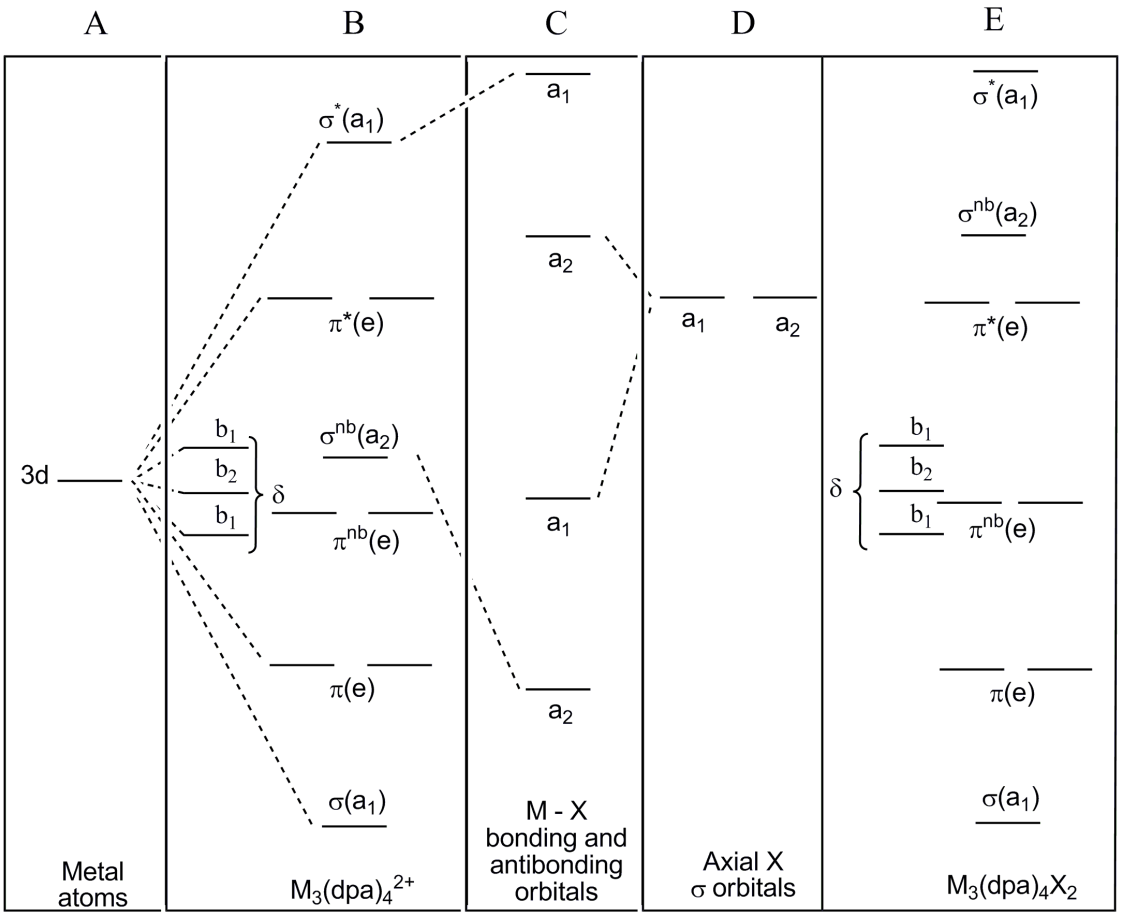

Figure 3-3: A generic diagram of the stepwise formation of molecular orbitals in symmetrical $M_3(dpa)_4X_2$ structures; X – σ donor ligand.

Approximate forms of the various molecular orbitals (which are common for all EMACs with D_4 symmetry), are presented in Figure 3-4. The upper three represent the high-lying, primarily M-Nσ*, orbitals with δ symmetry with respect to the M-M-M axis.

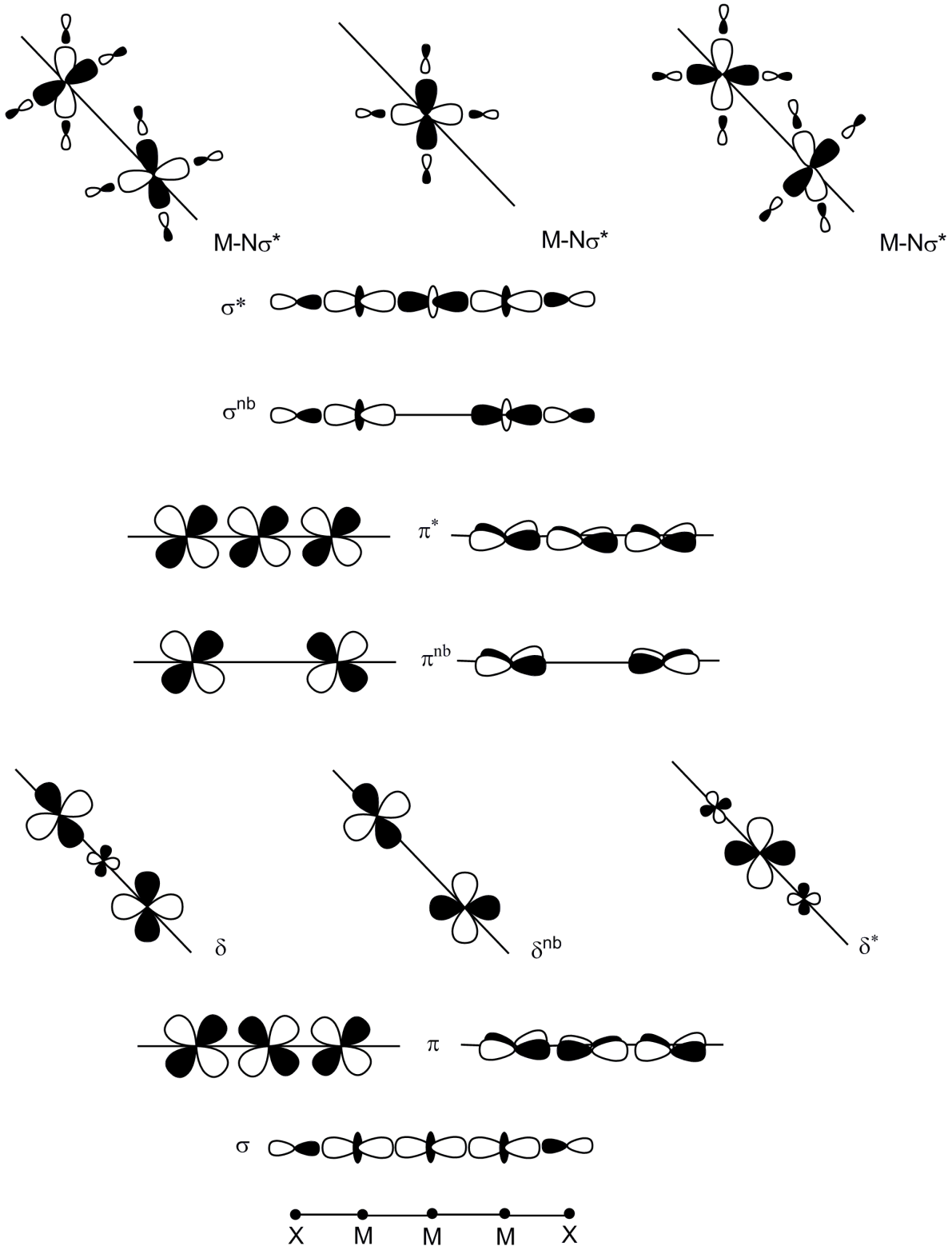

Figure 3-4: Qualitative molecular orbitals for $Co_3(dpa)X_2$; X – σ ligand.

Having established the anticipated ordering of the molecular orbitals in a generic EMAC, we can distribute the appropriate number of electrons to generate configurations for a particular example. For $Co_3(dpa)_4Cl_2$, three Co^{II} centres (d^7) give twenty one electrons and the configuration is shown in Figure 3-5 (spin-α and spin-β manifolds are separated to facilitate subsequent discussion of Cr and Ni-based analogues).

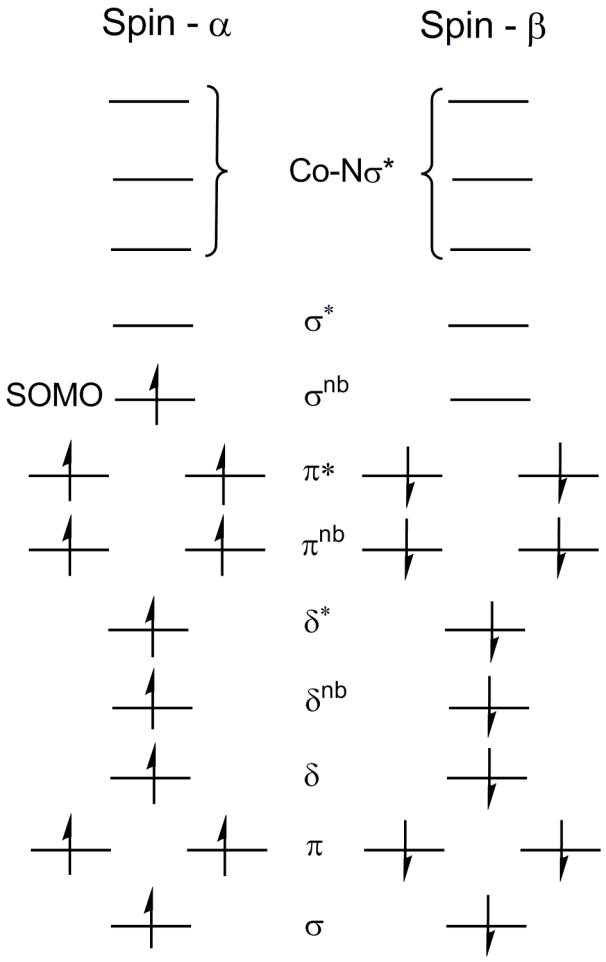

Figure 3-5: Spin-polarised molecular orbital diagram for $Co_3(dpa)_4Cl_2$.

The presence of one unpaired electron gives a doublet ground state and the SOMO (singly occupied molecule orbital) is the σ^{nb} orbital. The LUMO (lowest unoccupied

molecule orbital) has σ* character. Thus, the qualitative picture is consistent with the magnetic data which indicates that the symmetric $Co_3(dpa)_4Cl_2$ structure has a doublet ground state. The bonding can simply be considered as an example of a three-centre-three-electron bond ($(\sigma)^2(\sigma^{nb})^1(\sigma^*)^0$) of the type first described by Rundle and Pimentel for the triiodide anion (Figure 3-6)[289,290] and later applied to a variety of structures.[291-294]

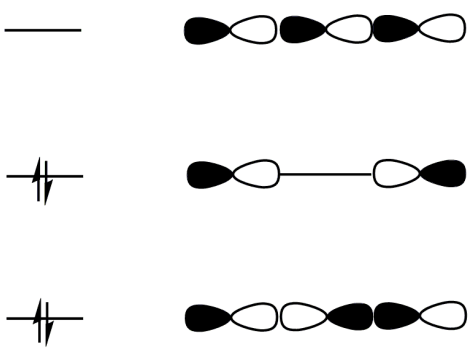

Figure 3-6: Rundle-Pimentel model of 3-centre-4-electron bonding.

The first quantitative discussion of the electronic structure of $Co_3(dpa)_4Cl_2$ using density functional theory was published by Rohmer and Bénard in 1998.[295] A symmetric minimum with doublet multiplicity was identified as the ground state, but no stable minimum corresponding to the unsymmetric structure was located. On this basis they concluded that the distorted isomer is a consequence of crystal packing effects. A few years later further computational work[296] led Bénard, Malrieu and co-workers to propose that the unsymmetric form corresponds to an excited quartet states, and the observed structural changes are then attributed to spin crossover. The problem was resolved in 2006 when Pantazis and McGrady[297] published work (again based on DFT calculations) that suggested that there are not two but three important

electronic states in the tricobalt complexes (Figure 3-7). The first state, ^{2}A (doublet), corresponds to the fully delocalised symmetric minimum found in the previous DFT studies. In the unsymmetric form a high-spin/low-spin transition on one of the Co atoms induces a 'break' in the wire and the molecule adopts an unsymmetrical structure. This is the second state named ^{4}B (quartet) that has high-spin Co (II) species attached to a low-spin Co-Co bonded unit. The third state, ^{2}B (doublet), provides a pathway between the symmetric (^{2}A) and highly unsymmetric (^{4}B) minima. In the ^{2}B state the high-spin Co (II) ion is coupled antiferromagnetically to a high-spin (S = 1) configuration of the Co-Co unit yielding S_{tot} = 1/2. The very flat energy surface for this state is the key to very flexible structural chemistry because it allows subtle changes in crystal packing to have a significant impact on the structures. On the basis of this work it can be concluded that structure and electronic properties of $Co_3(dpa)_4Cl_2$ molecule wires can be controlled by subtle changes to the environment. This naturally raises a question regarding their behaviour under a different type of perturbation, the electric field present between two electrodes in a putative electronic device. This is the primary motivation behind the work in this thesis.

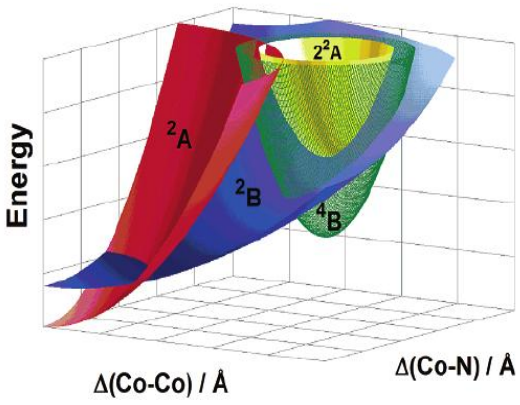

Figure 3-7: Potential energy diagram for $Co_3(dpa)_4Cl_2$ showing the states discussed in the work of Pantazis and McGrady.[297]

3.4 Conductance in EMACs

The standard experimental technique for measuring the electron transport properties or the effect of the electric field in molecules is scanning tunnelling microscope (STM). The STM was the first instrument used to generate real-space images of surface with atomic resolution. It is constructed from a conducting probe held close to the sample. Electrons tunnelling between the surface and the probe produce the current flow. The resulting tunnelling current is a function of the tip position, applied voltage and the local density of states. Based on this information it is possible to construct a three-dimensional image of the sample and individual atoms within material to be imaged and manipulated. Unlike electron microscopy, this new method does not require a partial vacuum but it can be observed in air at standard temperature and pressure or, while submerged, in a liquid reaction vessel. This allowed for the first time to observe and record current and conductance of organic molecules, such as DNA and proteins. In addition to several advantages, this method has some drawbacks too. For example, it is impossible to characterise in detail the junction between the electrodes and the molecules. Information about the geometry of the contact is crucial to reproduce the experiment and it is an important factor for the theoretical calculations. Additionally, during the measurements it is not clear if the recorded current corresponds to one or two molecules. Usually these problems are overcome by performing many distinct measurements in order to gather enough reliable statistical data. So far this has been the only experiment which can provide information about the conductance and the current-voltage characteristics in the molecules.

An experiment based on the STM spectroscopy was performed by Peng and co-workers where statistical analysis of thousands of measurements of trimetal (M_3) and pentametal (M_5) EMAC was recorded.[191] In the experiment the value of single molecule resistance and current-voltage dependence were recorded. Firstly, the experiment revealed that the M_3 EMAC has lower resistance if compared to M_5 analogues. Secondly, in the series of only three metal-atom chains the resistance drops from 3.4 MΩ to 1.9 MΩ and to 0.9 MΩ, moving from Ni_3, Co_3 and Cr_3. Similar measurements were performed on the Ni_5, Co_5 and Cr_5 EMAC, where again the Ni_5 structure has the highest resistance followed by the Co_5 and the lowest resistance is observed in the Cr_5. The trend of molecular conductance is successfully reproduced by theoretical calculations but for wrong reasons.[192]

In the same experiment a puzzling behaviour was observed in current-voltage data extracted from the $Cr_5(tpda)_4(NCS)_2$ chain. In the statistical data gathered from the experiment the Cr_5 chain has two curves: some of the molecules show high conductance and current flow, while others have significantly lower conductance and current at the same bias. The author proposed stochastic switching between the high conducting and low conducting structures, where the former structure is symmetric with equal double bonds between the metal atoms and the latter one has alternating quadruple and non-bonds.[191] The solution has not been revealed yet and additional work should be performed.

Other EMACs were objects of the STM experiment too. For example, the Ru_5 chain has resistance between the Co_5 and Cr_5 structures.[174] Mixed-valence molecules, such as $[Ni_5(bna)_4(NCS)_2]^{2+}$, determine resistance value of ~18 MΩ which is lower than the

homovalent $Ni_5(tpda)_4(NCS)_2$.[167] Hence, the electron mobility in the former structures is better than in the latter one.

Furthermore, a fascinating single molecule transistor was designed from the $Cu_3(dpa)_4Cl_2$ or $Ni_3(dpa)_4Cl_2$ EMAC.[193] The molecules were trapped between two gold electrodes and an aluminium gate electrode was placed on the top. Phenomena based on single electron properties were observed. The results can be explained by symmetric and unsymmetric metal-metal stretching mode of the trimetal complexes. Hence, it is possible to connect the electron transport mechanism of these trimetal EMACs with metal-metal vibrational excitations.

3.5 Computational methods

All calculations described below were performed using the Amsterdam Density Functional software (ADF2008 and ADF2010).[279] All atoms in the structures were modelled with a double-ζ Slater-type basis set, extended with a single polarization function, while the metal atoms were characterized with a triple-ζ single polarised basis set. Electrons in orbitals up to and including 1s (C,N), 2p (Cl), and 3p (Co) were considered a part of the core and treated in accordance with frozen core approximation. The local density was employed for the optimizations,[227] along with the local exchange (correlation potential of Vosko, Wilk, and Nusair; gradient corrections to electron exchange and correlations proposed by Becke and Perdew (BP86)).[249] Geometry optimizations of all symmetric structures were performed under the D_4 symmetry constraint. Different configurations were defined by the keyword

'occupations'. All structures were optimised using the gradient algorithm of Versluis and Ziegler.[298]

3.6 Results and discussion

3.6.1 Electronic structure of $Co_3(dpa)_4(SCN)_2$ based on DFT calculations

In this chapter the target of our investigation is $Co_3(dpa)_4(SCN)_2$, the system that has been extensively studied by Peng and co-workers.[191] This differs from the Cl-capped species discussed in previous sections only in the identity of the terminal ligand, but our first task is to establish that this change does not introduce any substantial change in electronic structure. A full molecular orbital diagram for $Co_3(dpa)_4(SCN)_2$, obtained by DFT calculations, is presented in Figure 3-8. The general features of the diagram are very much like those presented for $Co_3(dpa)_4Cl_2$ (Figure 3-5), with a doublet ground state and the SOMO corresponding to the σ^{nb} combination of d_z^2 orbitals on the metals. Within the occupied manifold, an additional set of orbitals with π symmetry appears. These orbitals are localised primarily on the sulphur atoms of the NCS ligand (denoted S_π in Figure 3-8). At higher energy, the σ^* orbital lies in the same energetic window as the three linear combinations of Co-Nσ^* orbitals, and in fact the LUMO is one of the latter and not Co-Co-Co σ^* as suggested by Figure 3-5. The energy difference between these orbitals is, however, very small.

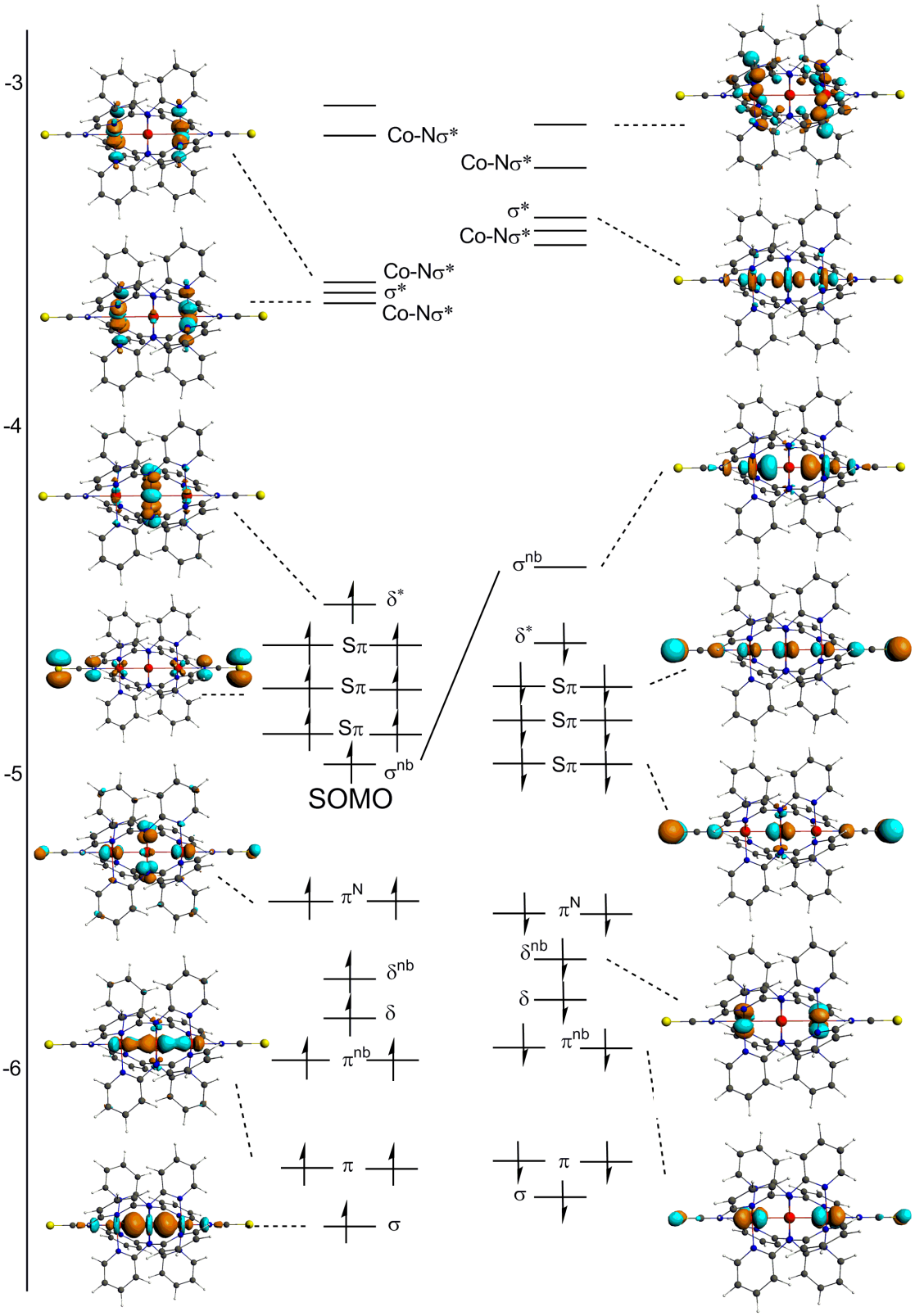

Figure 3-8: The valence molecular orbitals of $Co_3(dpa)_4(SCN)_2$ structure.

3.6.2 Moving from the real molecule to a model structure

In the previous few paragraphs the calculations relate to the isolated molecule: i.e., one which is surrounded by vacuum. Our primary concern in this thesis is with electron transport, where the molecule is attached to gold electrodes, and a realistic treatment of these is required for accurate results. The gold electrode calculations are computationally challenging, and some compromises in the treatment of the molecular system are unavoidable. The computational cost rises dramatically as the number of gold atoms in the simulation is increased, and therefore reducing the dimensions of the unit cell in direction perpendicular to the transport direction is highly desirable. If the unit cell is too small, however, then electrostatic interactions between neighbouring cells will compromise the results. For this reason, we adopt a model where the dipyridylamido ligand is replaced by the simpler model ligand L shown in Figure 3-9.

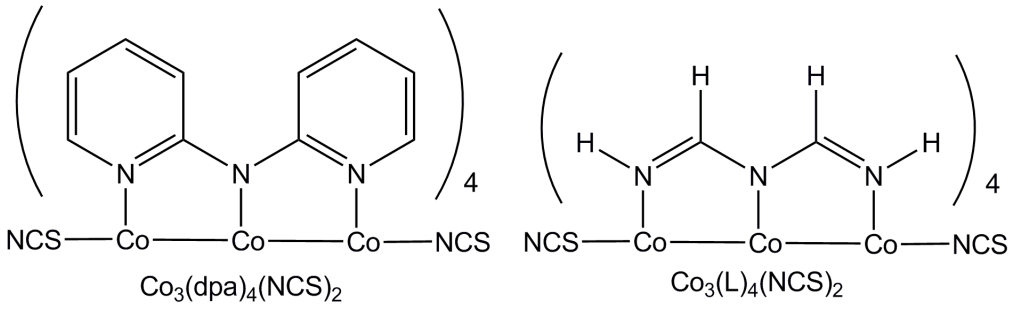

Figure 3-9: Structure of $Co_3(dpa)_4(SCN)_2$ (dpa=dipyridyamide) and the model ligand, L.

The geometry of the model complex is precisely as obtained from the optimisation of the complete (i.e., dpa) complex, but the unsaturated valences at C and N are capped with hydrogen atoms at 1.1 Å and 1.0 Å, respectively. To justify this simplification of

the structure we will now compare the molecular orbital distributions of the real and model structures.

The molecular orbital array for the model system is presented in Figure 3-10, and it is should be compared to that for the full system shown in Figure 3-8. The most important set of molecular orbitals are these close to the HOMO – LUMO gap, and indeed the SOMO is the same σ^{nb} in each case. Two sets of doubly degenerate orbitals with symmetry S_{π} also occur in the same region close to SOMO. These molecular orbitals have a significant character on the sulphur atoms. Orbitals with δ, δ^{nb} and δ* symmetry have lower energies and lie in the same region as the π molecule manifold, while the σ bonding combination has the lowest energy. Thus, although there are subtle differences in the distribution of orbitals in the real and model systems, the key conclusion, that the SOMO is the σ^{nb} orbital and therefore that a 3-centre-3-electron bond is present, remains unchanged. On this basis we believe that our simplified model captures the key features of the real structure, and hence is a valid basis for the study of electron transport properties.

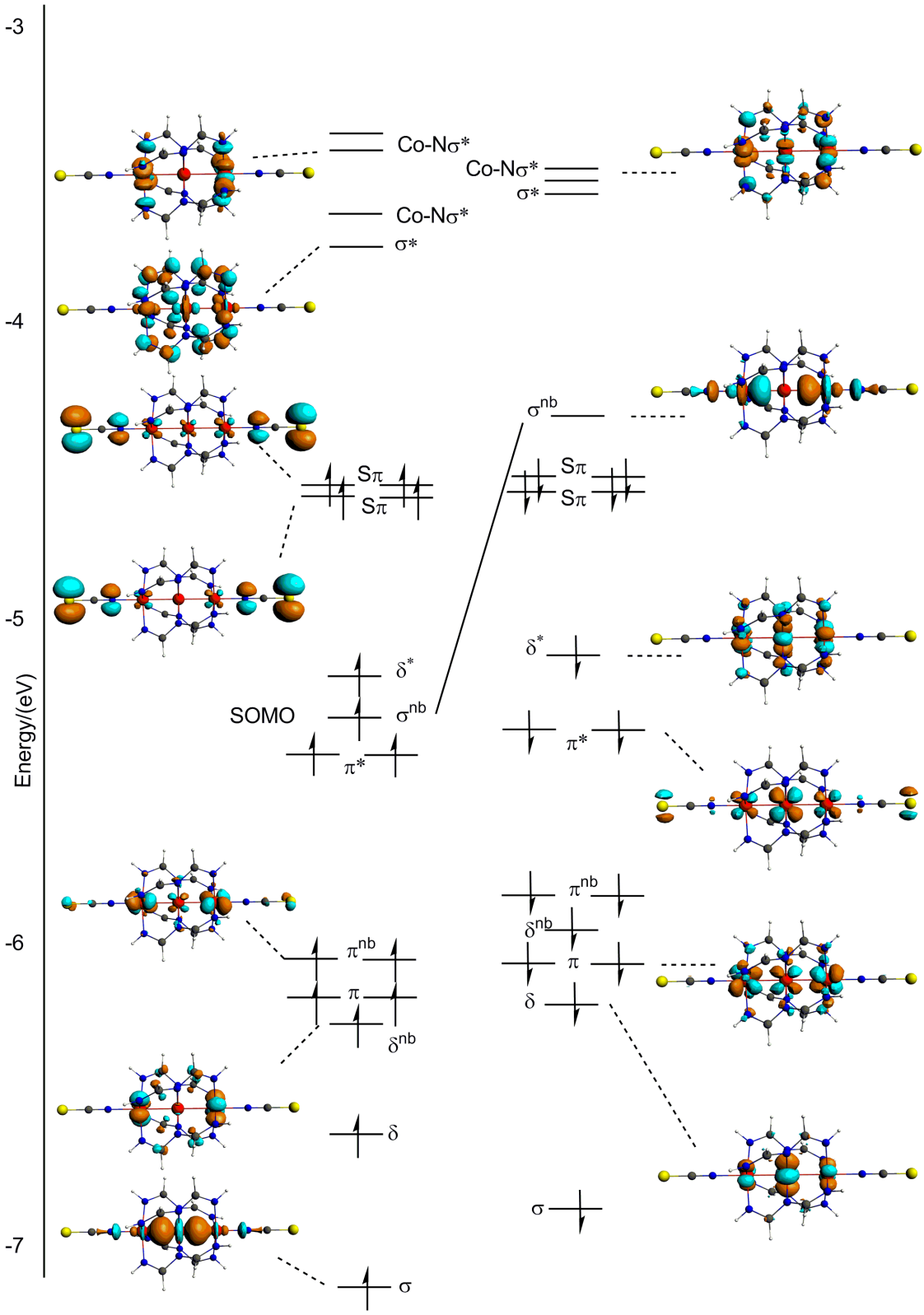

Figure 3-10: Molecular orbital distribution in $Co_3(L)_4(SCN)_2$ structure.

3.6.3 Electron transport properties: setup of the two-probe calculations

Next step is to relate the electronic structure of $Co_3(L)_4(NCS)_2$ molecule with electron transport properties. For this reason we placed our model structure between two gold electrodes and applied different bias voltages. All results obtained from these calculations are presented in the following sections.

We now turn to our primary goal of computing the electron transport properties of the EMAC from first principles. The key features of the 'two-probe' setup are shown in Figure 3-11, where the molecule is inserted between two gold electrodes.

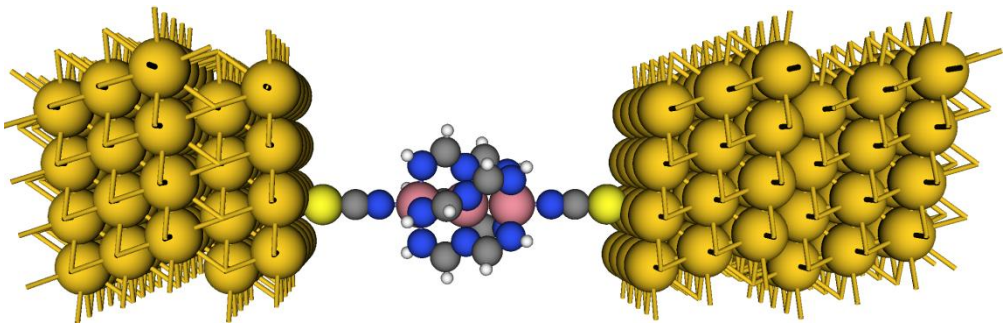

Figure 3-11: Two- probe set up in ATK software.

These electrodes represent the metal surface and the tip of the STM probe in the experimental work reported by Peng and co-workers.[191] The precise geometry of the contact between molecule and electrode is unknown and it remains one of the most pressing areas of concern in modelling electron transport properties. Along with most other authors, we choose to use a 4 x 4 section of the (111) surface of bulk gold, with the molecule anchored in a hollow site defined by three neighbouring gold atoms. The first few layers (two on the left, three on the right) of each electrode together with the molecule are the so-called 'scattering region' and they are treated as a continuous

molecular entity. The simplification of the ligand has been discussed previously: without this, a 5x5 section of the (111) face would be required, placing additional forty five gold atoms in the scattering region.

3.6.4 Computational methods for electron transport calculations

The spin-dependent electron transport properties of the cobalt-based EMAC were computed using the AtomisticToolkit software package, ATK2008.[299-302] The methodology used combines a density functional theory treatment of the electronic structure with the Keldysh non-equilibrium Green's function approach to simulating transport under non-equilibrium conditions which is described in the theoretical chapter.[211,212,303-305] The scattering region, $[Au_{32}]$-$Co_3(L)_4(NCS)_2$-$[Au_{48}]$, contains the EMAC sandwiched between two and three 4 x 4 layers of the Au (111) surface of the source and drain electrodes, respectively, with the sulphur atoms of the two NCS ligands located in hollow sites with Au-S distances of 2.52 Å. We used the Perdew Burke Ernzerhof (PBE) functional[306] in conjunction with numerical basis sets of double-zeta ς + polarization (DZP) quality on all atoms other than the nitrogens, where an additional polarization functional was added (DZDP). Core electrons were described by norm-conserving pseudopotentials.[307] The electronic structure of the two-probe systems at equilibrium was converged using a 350 Ry mesh cut-off, a finite temperature of 300 K at the electrodes and the density matrix constraint at the electrodes. Sampling of the Brillouin zone was performed using a Monkhorst-Pack grid[308] with 300 k-points along the transport direction. The molecular orbitals in the scattering region are the eigenfunctions of the Molecular Projected Self-consistent

Hamiltonian (MPSH). The current is computed using the Landauer-Büttiker[206,207,209,309] formula described. More information about the method can be found in the theoretical chapter (Chapter 2).

We note at this point that the methodology used in the transport calculations (pseudo-potential with numerical localized basis functions,[301] PBE functional) is necessarily somewhat different from that adopted for the previous gas-phase calculations performed using ADF (Slater basis sets, BP86 functional). In order to test the consequences of this we have compared the gas-phase molecular orbital arrays for $Co_3(L)_4(NCS)_2$ calculated using the ADF and ATK protocols.[299] The changes are minimal, and we are therefore confident that the analysis of electronic structure performed with the ADF[279] program can be translated to the electron transport calculations.

3.6.5 Device at equilibrium

The first issue to be addressed in a study of electron transport is whether the interactions with the electrode surface perturb the intrinsic molecular electronic structure to any significant extent. In the figure below (Figure 3-12) we present the molecular orbital distribution for the model structure placed between two electrodes. The basic features of the electronic structure are very similar to the molecule in vacuum (Figure 3-10), suggesting that the molecule/electrode interaction does not perturb the electron distribution in the two-probe system to any great extent. The general pattern of bonding, non-bonding and antibonding combination of σ, δ and π symmetry remains intact, the only major change being the removal from the frontier

region of the degenerate S_π levels which are strongly stabilised by interactions with the Au surface.

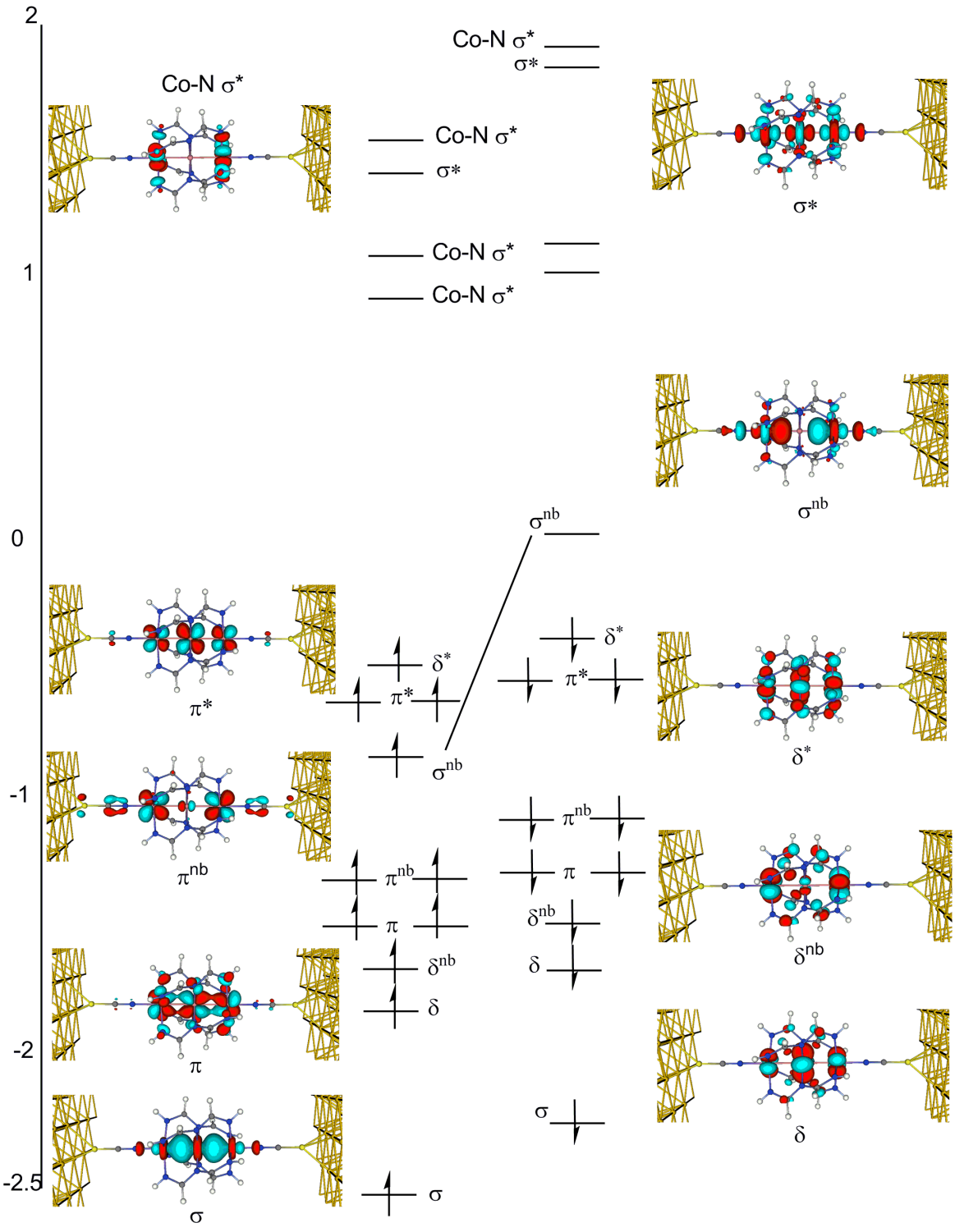

Figure 3-12: Molecular orbital diagram for the model structure sandwiched between gold electrodes.

An excess of approximately one spin-α electron in the molecular region remains localised on the outer cobalt atoms (Table 3-1), precisely as in the molecular system. A small amount of negative charge accumulates at the sulphur atoms of the thiocyanate ligand at the expense of the N and C, leading to a shift from the $^{-}$N=C=S resonance structure toward N≡C-S^{-}, but otherwise the electronic structure remains unchanged (Table 3-1).

		S	C	N	Co_o	Co_i
$Co_3(L)_4(NCS)_2$	$\rho_{\alpha+\beta}$	6.24	4.34	4.93	8.74	8.66
	$\rho_{\alpha-\beta}$	0.08	0.00	0.06	0.43	-0.05
$[Au_{32}]$-$Co_3(L)_4(NCS)_2$-$[Au_{48}]$	$\rho_{\alpha+\beta}$	6.36	4.26	4.84	8.69	8.65
	$\rho_{\alpha-\beta}$	0.00	0.00	0.04	0.50	-0.10

Table 3-1: Mulliken populations (α+β) and spin densities (α-β) for $Co_3(L)_4(NCS)_2$ and $[Au_{32}]$-$Co_3(L)_4(NCS)_2$-$[Au]_{48}$.

In the simple model of electron transport presented in Chapter 2, we emphasised that electron transport in molecular systems depends mainly on the alignment of the molecular orbitals relative to the Fermi level: the most influential orbitals are those which lie very close to the Fermi level. The connection between the molecular orbitals and the electron transport is established through the transmission spectrum, which defines the conductance through $G = (e^2/h)T(E_f)$. Separate spin-α (blue) and spin-β (red) transmission spectra for $Co_3(L_4)(NCS)_2$ at zero bias are shown in Figure 3-13: 0 eV corresponds to the Fermi energy.

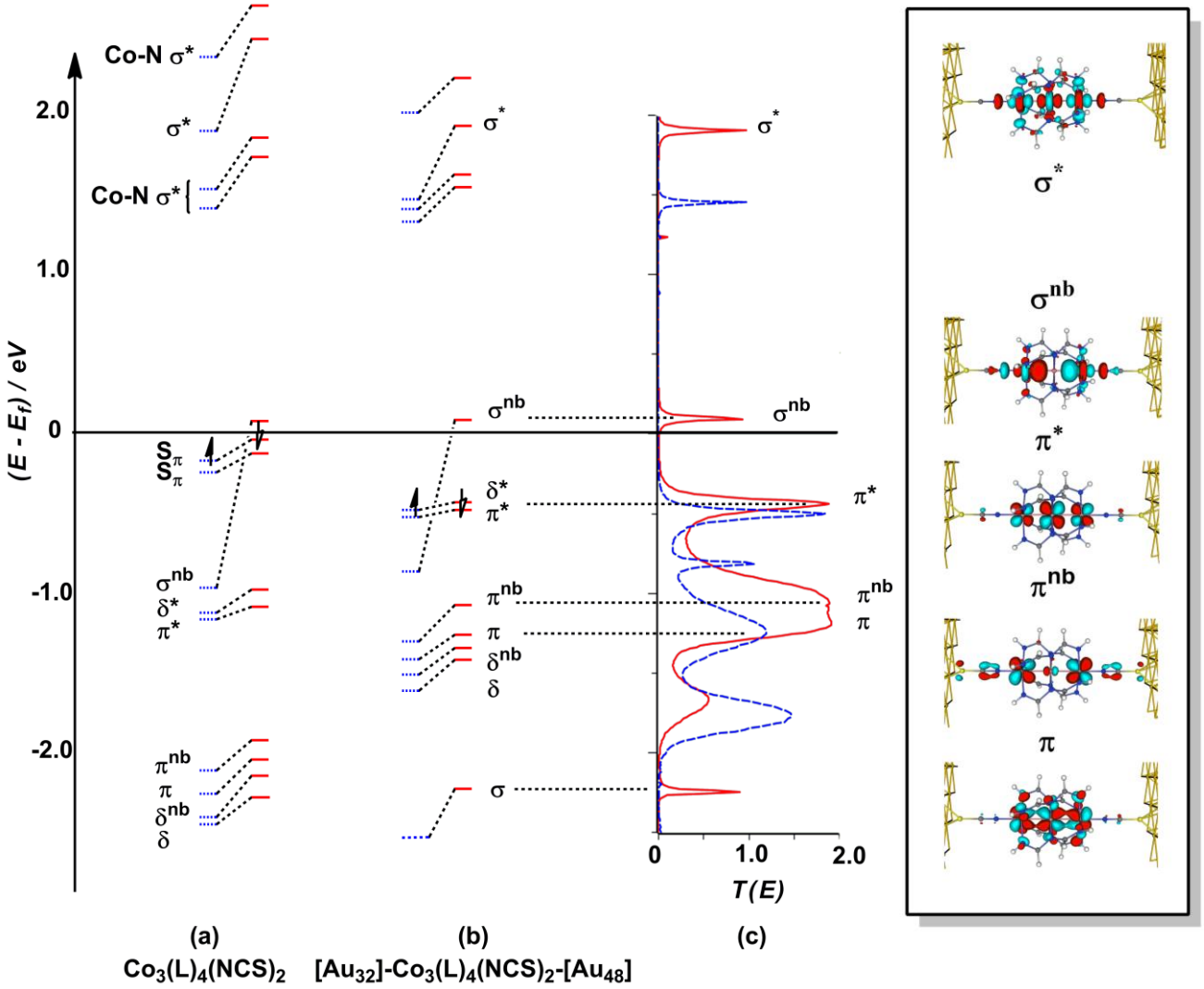

Figure 3-13: Molecular orbital diagram for (a) isolated $Co_3(L)_4(NCS)_2$, (b) sandwiched between gold electrodes and (c) the zero-bias transmission spectrum for $[Au_{32}]$-$Co_3(L)_4(NCS)_2$-$[Au_{48}]$. Spin-α and spin-β components are shown in blue (dashed) and red, respectively.

The peaks in the transmission spectrum (Figure 3-13 c) can be mapped directly onto the orbital energies of the scattering region (Figure 3-13 b), and from there to the orbitals of the molecule in isolation (Figure 3-13 a). The energy levels shown in Figure 3-13 a and Figure 3-13 b correspond exactly to those in Figure 3-10 and Figure 3-12, respectively. Each peak in the transmission spectrum corresponds directly to one or two levels in the molecular orbital array, although the peaks are broadened to different extents. The very broad peaks arise through strong coupling between the channel and the electrodes, while the narrow peaks correspond to weak contacts. The height of each peak is related to the effectiveness of the channel (i.e., delocalisation of the orbital) and also the degeneracy (i.e., the number of molecular orbitals in the specific energy window). Doubly degenerate π levels, therefore typically generate peaks with T(E) > 1.0.

In Figure 3-13 c a very broad peak (red line) can be found around -1.0 eV with T(E) ~ 2, corresponding to the double degenerate π and π^{nb} levels. The spin-α component of the transmission spectrum (dashed blue line) has similar features in the region between -1.0 and -1.5eV. The broadening is indicative of strong coupling with the electrodes which is a direct result of the S_π character present in the π manifold. The peaks corresponding to the degenerate π^* levels (spin-α and spin-β) also have T(E) > 1.0 and they are somewhat closer to the Fermi level (~ -0.5eV). Above them, and very close to the Fermi energy, is the spin-β component of the σ^{nb} molecular orbital with T(E) ~ 1.0. Similar features at +2.0 eV and -2.25 eV correspond to the σ^* and σ levels, respectively. The remaining metal-based orbitals have δ symmetry with respect to the Co-Co axis and hence they provide relatively poor conduction channels. Moreover,

they are weakly coupled to the electrode surface, and both factors mean that they do not generate intense peaks in the transmission spectrum.

From the perspective of electron transport, the most important molecular orbitals are the occupied spin-α and vacant spin-β components of the σ^{nb} orbital. The former lies 0.85 eV below E_f, while the latter lies only 0.20 eV above it. As a result, the zero-bias conduction is dominated almost entirely by the spin-β channels: G_α = 0.03 μ*S,* G_β = 0.57 μ*S*, G_{tot} = 0.60 μ*S*, corresponding to a spin-filtering efficiency (defined as (G_β - G_α)/(G_β + G_β) x 100%) of 90%, comparable to the values computed by Yang for ferroscene-based SMWs.[310] An analysis of the transmission channels reveals that, while almost all the spin-β current is carried through the σ^{nb} channel, the (much smaller) spin-α conductance is dominated by the broader π* channel. The computed total conductance of 0.60 μ*S* is also very similar to the value of 0.53 μ*S* measured by Peng and co-workers using STM (at 0.025 V).[191] The overestimation of conductance values using DFT is a general phenomenon[193] which has been ascribed variously to the limitations of the theory (in particular to the failure to account for the self-interaction energy) or to the idealised contact geometry (it should be noted that our chosen hollow site will maximise the interaction between molecule and the gold surface). In contrast, our computed values are two orders of magnitude larger than those calculated by Jin and co-workers using extended Hückel theory.[192] The origin of this discrepancy probably lies in the rather different alignment of molecular orbitals with respect to the electrode Fermi levels in the two methods: in the calculations of extended Hückel theory, the σ* channel was proposed to be the major carrier, whereas our calculations contribute to the current flow which is instead dominated by the σ^{nb} orbital. We return to the comparison between experiment and theory

following the discussion of the analogous trichromium (Chapter 4) and trinickel (Chapter 5) systems.

3.6.6 Device out of equilibrium

From the practical point of view the most interesting case is the behaviour of molecules under applied bias. The calculated current/voltage characteristic of $Co_3(L)_4(NCS)_2$ is presented in Figure 3-14. Three sets of current are shown in this figure: total (black), spin-β (blue) and spin-α (red). Below +/- 1.0 V the total current is dominated entirely by the spin-β component whereas at higher bias the spin-α manifold also makes a contribution. This strong polarisation of the current flow provides a basis for the high SFEs (spin filtering effect), at least at low bias. The SFE, defined at finite bias as $(I_\beta - I_\alpha) / (I_\beta + I_\alpha)$ x 100%, remains well in excess of 90% at 1.0V. Even at 2.0 V the SFE remains above 50%.

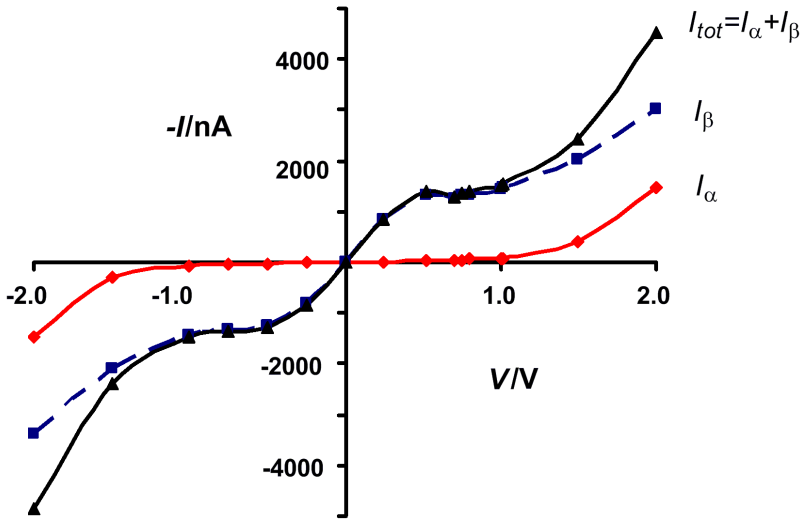

Figure 3-14: Computed current/voltage characteristics of $[Au_{32}]$-$Co_3(L)_4(NCS)_2$-$[Au_{48}]$.

To understand this behaviour we need to consider how the transmission spectrum evolves as a function of bias. Figure 3-15 presents *T(E)* for 0V, 0.5 V, 1.0 V and 1.5 V (the energies of the orbitals in the scattering region (calculated using the MPSH) are also shown for comparison). Changes in the electron density and electrostatic potential profile shown at 0.25 V and 1.0 V are also shown in Figure 3-16. In the region between 0V and 0.5 V only the vacant spin-β component of the σ^{nb} orbital falls within the bias window. For this reason a marginal build-up of spin-β electron density in the tricobalt region occurs (see Figure 3-16 a). The potential profile shows that the voltage drop is localised mainly at the nitrogen atom of the -NCS ligand connected to the drain. The transmission spectrum at 0.5 V is qualitatively very similar to that at 0 V but all peaks are shifted marginally upwards in energy due to the accumulation of electron density in the σ^{nb} orbital. Above 0.5 V, all peaks in the transmission spectra are shifted substantially downwards, following the potential of the drain. Thus, the molecular levels are effectively pinned to the drain potential. The reason for this is that the bias window begins to capture the upper tail of the peak due the occupied π^* levels, resulting in a depletion of charge (both spin-α and spin-β) from the molecular region. The fingerprint of the π^* level is apparent in Figure 3-16 b in the regions of charge depletion in both spin-α and spin-β density at the cobalt adjacent to the drain. The electrostatic potential therefore shows a more pronounced drop across the source-molecule junction in this case.[311]

At the same point that the peaks in the transmission spectrum begin to follow the drain, their shapes also become highly bias-dependent: those corresponding to the three π channels (π, π^{nb} and π^*) become substantially weaker, while the σ manifold remains essentially unperturbed. The π manifold is highly polarised because the three

components, π^*, π^{nb} and π, span less than 1 eV, as a result of which the applied electric field can induce significant rehybridisation. Thus, whilst all three orbitals have equal amplitude on the two terminal cobalt centres at 0 V, at 1.0 V the π^* orbital becomes somewhat localised on the source side, while its bonding counterpart has greater amplitude adjacent to the drain (Figure 3-15). This localisation reduces the ability of the π channels to transport charge and the corresponding peak high in the transmission spectrum is dramatically reduced. In marked contrast, the σ^{nb} orbital is energetically isolated from its bonding and antibonding counterparts which lie approximately 2 eV lower and higher, respectively. The σ framework is therefore substantially less polarisable than its π counterpart and the σ^{nb} channel remains unperturbed even up 2.0 V. The final result of these bias-induced changes in the distribution of the orbitals in the molecular region is that the resonances due to the spin-α and spin-β components of the π^* channel are largely quenched above 1.0 V, allowing the spin-β component of the σ^{nb} channel to continue to dominate charge transport and provide high spin filtering efficiencies.

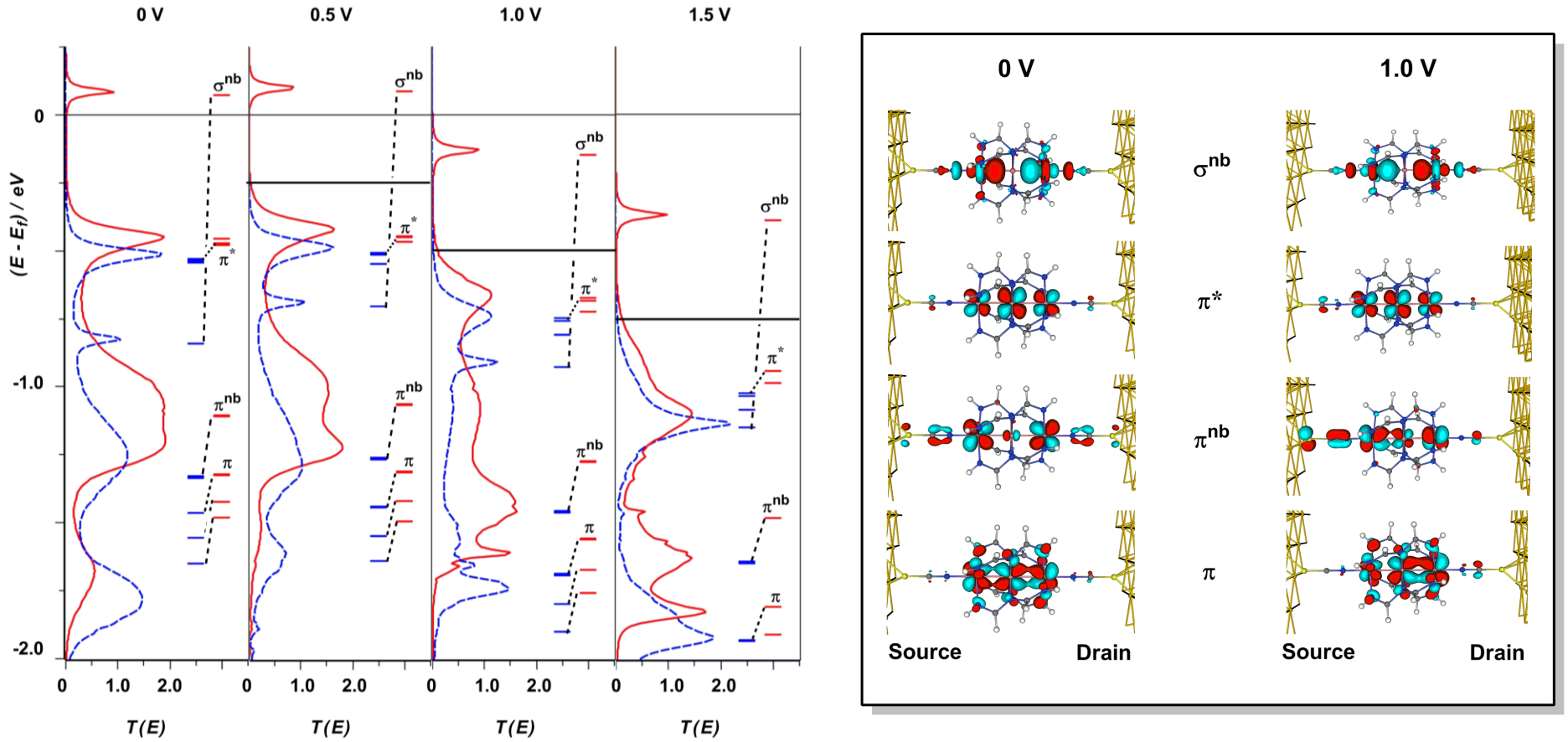

Figure 3-15: Changes in transmission spectrum (left) as a function of applied bias (0 V – 1.5 V) for $[Au_{32}]$-$Co_3(L)_4(NCS)_2$-$[Au_{48}]$. Red and blue (dashed) lines denote spin-β and spin-α, respectively. Horizontal black lines for 0.5, 1.0 and 1.5 V mark the lower limit of the bias window. MPSH orbitals (right) for the π, π^{nb}, π* and σ* channels at 0 and 1.0 V are also shown for comparison.

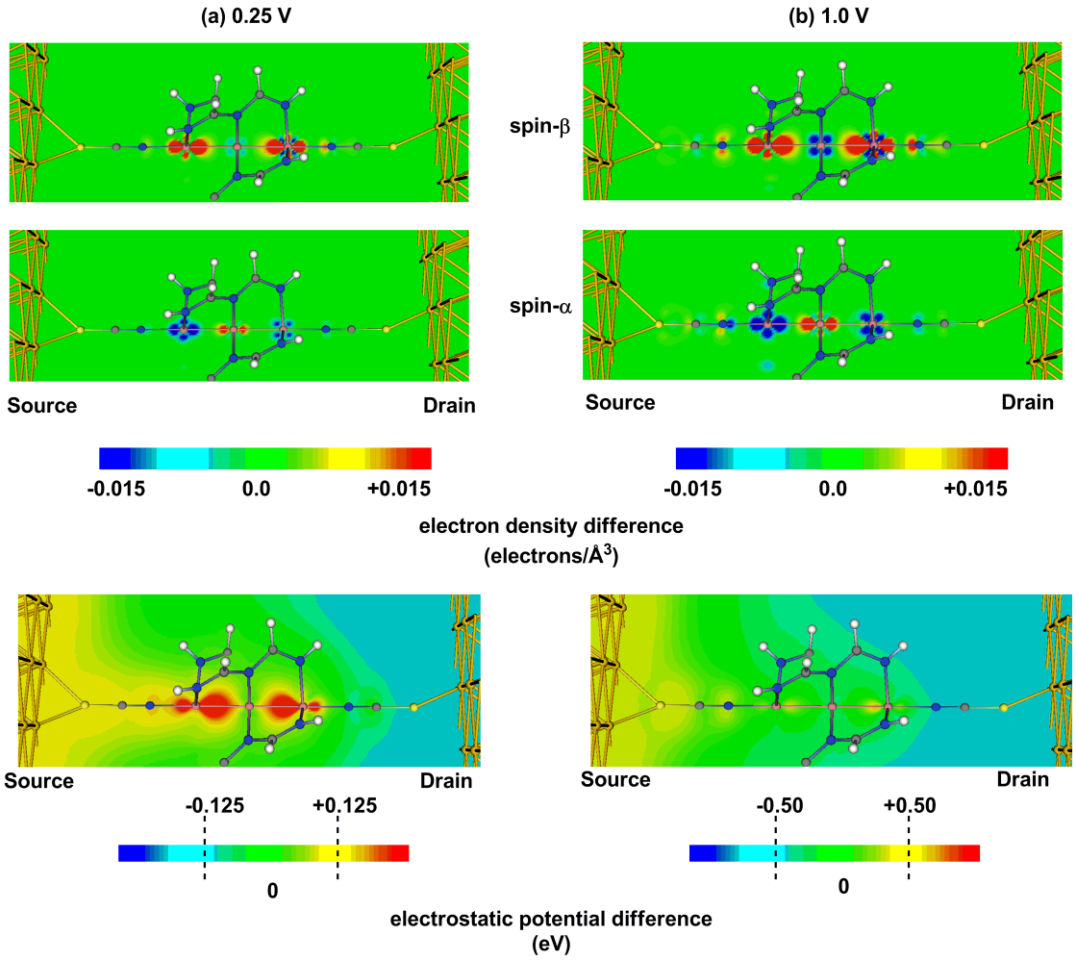

Figure 3-16: Charge redistribution (ρ(finite bias)- ρ(0V) and electrostatic potential profiles (V(finite bias) -V(0V) for $[Au_{32}]$-$Co_3(L)_4(NCS)_2$-$[Au_{48}]$ at (a) 0.25 V and (b) 1.0 V.

3.7 Conclusions

This chapter has set out to establish the framework of the thesis by tracing the fundamental electron structure of the molecule all the way through its bias-dependent electron transport properties. Specifically, we established that (i) the molecular orbital distribution remains the same in the isolated structure and in the two-probe system and (ii) that a one-to-one correspondence exists between the peaks in the transmission spectrum and the orbitals of the isolated molecule. The dominant electron transport channel in $Co_3(L)_4(NCS)_2$ is the σ non-bonding orbital which is singly occupied in the doublet ground state of the isolated molecule. With increasing bias the tail of a second channel with π^* character enters the bias window. These π orbitals are strongly connected to the source and the drain if compared to the σ analogues due to the S character on a sulphur atom, and they might therefore be expected to form an efficient conduction channel. They do not, however, because the applied bias strongly perturbs the pseudo-degenerate π manifold, causing the individual orbitals to localise at the source or drain, effectively it closes the channel. The σ^{nb} channel, in contrast, is far less polarisable due to a much greater splitting within the $\sigma/\sigma^{nb}/\sigma^*$ manifold at zero bias, and so it remains unperturbed and able to support current flow even at moderately high bias. The $Co_3(dpa)_4(NCS)_2$ EMAC therefore has two symmetry-distinct sets of molecular orbital which have quite different roles: the π channel secures the contact with the electrodes, while the σ^{nb} channel provides the dominant pathway for the electron transport. The implication of

this is that even when the highly polarisable π channels are strongly localised by the applied electric field, current flow is not affected.

Chapter 4

Electron transport through trichromium metal wires

4.1 Introduction

In this chapter we will discuss the electronic structure of the $Cr_3(dpa)_4Cl_2$ and $Cr_3(dpa)_4(SCN)_2$ molecules, and compare the electron transport properties of the latter to those of the cobalt analogue discussed in Chapter 3. Detailed structural studies suggest that these trichromium systems exist in both symmetric and unsymmetric forms and the geometry is strongly influenced by the identity of the axial ligand. Our calculations establish a link between the electronic structure and the electron transport properties of these trichromium wires. Specifically, we show that low-symmetry distortions of the metal frame reduce the effectiveness of the π channels but this is largely irrelevant to electron transport at low bias, simply because they lie far below the Fermi level. Instead the dominant pathway is through orbitals with σ symmetry which remains essentially unperturbed by even quite substantial distortions. In fact the conductance is actually increased by an order of magnitude by strong distortions because the key channel is displaced upward toward the Fermi level. The calculations presented in this chapter indicates a subtle and counterintuitive relationship between structure and function in these metal chains.

4.2 Electronic structure and characterisation of trichromium molecules

Early reports of the crystal structures of the trichromium EMACs suggested that the molecules were symmetric. However, later re-refinement of the crystallographic data showed that the chains were in fact generally unsymmetric (Figure 4-1). For example, although the dichloromethane solvate of the di-chloride capped species $Cr_3(dpa)_4Cl_2.CH_2Cl_2$ was initially reported to be perfectly symmetric (Cr-Cr = 2.366(1) Å),[312] subsequent analysis revealed a distinct asymmetry in the trichromium core, Cr-Cr = 2.254(4) and 2.477(4) Å.[313] The apparent symmetry is a result of crystallographic disorder, where the two possible molecular orientations (Cr≣Cr•••Cr and Cr•••Cr≣Cr) occur with equal probability. Similarly, the NCS-capped analogue is somewhat unsymmetric (Cr-Cr = 2.234(1) Å and 2.482(1) Å in benzene solvate).[313]

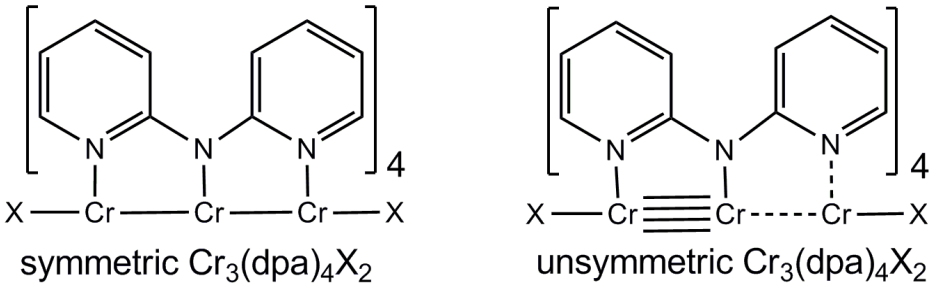

Figure 4-1: Molecular structures of symmetric and unsymmetric $Cr_3(dpa)_4X_2$.

In 2004 an extensive series of $Cr_3(dpa)_4X_2$ compounds was synthesized with various X anions,[313] and it was found that the nature of the Cr-Cr bond depends strongly on the axial ligands. For example, terminal ligands, such as tetrafluoroboarate (BF_4^-) or nitrate (NO_3^-), lead to unsymmetric structure with Cr≣Cr bond distance 1.934(5) Å

and 2.644(5) Å, the degree of asymmetry approaching that observed in $Cr_3(dap)_4(X)(Y)$ structures (Δd_{Cr-Cr}= 0.606 Å, X = Cl^-, Y = PF_6^-; Δd_{Cr-Cr} 0.648 Å X = Cl^-, Y = BF_4^-). Ligands, such as Cl^- and SCN^-, give less unsymmetric structures, where one of the Cr-Cr distances is ~2.24 Å and the other one is ~2.48 Å, while only strong σ donors, such as CN^- and $CCPh^-$, favour a symmetrical chain with two equivalent long distances (> 2.35 Å). The degree of asymmetry is inversely correlated to the σ donor strength of the terminal ligands. The dichloride-capped cation $[Cr_3(dpa)_4Cl_2]^+$ is also highly unsymmetric (Δd_{Cr-Cr}= 0.431 Å), as are all others containing the Cr_3^{7+} core.[164] The structure of the NCS-capped pentachromium analogue, $Cr_5(tpda)_4(NCS)_2$ (tpa = tripyridyldiamide), has been similarly controversial, but the disorder issues have been resolved to reveal a highly unsymmetric Cr_5^{10+} core with alternating long and short bonds.[314]

Evidence of a thermal equilibrium between distinct symmetric and unsymmetric isomers in $Cr_3(dpa)_4Cl_2$ and $Cr_3(dpa)_4(NCS)_2$ structures has been reported based on IR/Raman/Surface-enhanced Raman spectroscopy (SERS).[315] A line at 570 cm^{-1} in the SERS was assigned to the Cr≣Cr stretch in the unsymmetric form, while a second band at 346 cm^{-1} was assigned to an unsymmetric Cr-Cr-Cr stretch mode of the symmetric molecule. The intensity of the band at 570 cm^{-1} increased with increasing the temperature, suggesting that $Cr_3(dpa)_4Cl_2$ molecule undergoes temperature-dependent structural changes from a symmetric ground state to an unsymmetric excited state. The measured thermodynamic parameters are consistent with energy differences between the symmetric ground state and unsymmetric excited state of $Cr_3(dpa)_4Cl_2$ computed by Bénard and co-workers (vide infra).[313] As was the case for the tricobalt chains, explaining the unsymmetrical structure of $Cr_3(dpa)_4Cl_2$ has proved

to be a significant computational challenge. Bénard reported a rather flat potential energy surface with several local minima with S = 2 that are within ~ 40 kJ/mol of each other.[316] The most stable structure has equivalent Cr-Cr bond lengths of 2.35 Å. A slightly unsymmetric state with Δ(Cr-Cr) = 0.106 Å lies < 1 kcal/mol above the ground state, while a second unsymmetric form with Δ(Cr-Cr) = 0.679 Å was calculated to lie ~ 4 kcal/mol above the symmetric state. Thus, the energy required to distort the Cr_3 chain is quite small, and it has the same order of magnitude as *k*T. All these three states have similar electronic distribution: three unpaired electrons on each centre are coupled antiferromagnetically ($Cr^{\uparrow\uparrow\uparrow}$ — $Cr^{\downarrow\downarrow\downarrow}$ — $Cr^{\uparrow\uparrow\uparrow}$). The remaining three electrons form a three-centre three-electron σ bond, analogous to that in the $Co_3(dpa)_4Cl_2$ system.[317]

As we have already mentioned in the previous chapter, Peng and co-workers measured the value of single molecule resistance and current-voltage dependence of the conductance of trimetal (M_3) and pentametal (M_5) EMAC.[191] Here we will just summarise the main points. Firstly, experiment reveals that the M_3 EMAC has lower resistance if compared to M_5 analogues. Secondly, in the series of only three metal-atom chains the resistance drops from 3.4 MΩ to 1.9 MΩ and to 0.9 MΩ, moving from Ni_3, Co_3 and Cr_3. Similar measurements were performed on the Ni_5, Co_5 and Cr_5 EMAC, where again the Ni_5 structure has the highest resistance followed by the Co_5 and the lowest resistance is observed in the Cr_5. Inspired by this plethora of structural diversity, Peng and co-workers proposed that the highly conducting 'on' state observed in the CAFM experiments corresponds to a fully delocalised chain with four identical Cr –Cr bond distances, while the 'off' state features alternative long and short Cr–Cr bonds.[191] Indeed the idea that the symmetric (delocalised) structure is

synonymous with efficient charge transport, and therefore that a break in the delocalisation will increase the resistance, appears to be deeply embedded in the literature.[318] Our purpose here is to establish a direct connection between the electronic structure and electron transport from first principles.

4.3 Results and discussion

4.3.1 Electronic structure of $Cr_3(dpa)_4(SCN)_2$ based on DFT calculations

Our focus in this chapter is on the trichromium chain with the NCS^- axial ligands, where the NCS ligands are again used (experimentally and computationally) to ensure effective coupling to the gold electrodes. Both structures, $Cr_3(dpa)_4Cl_2$ and $Cr_3(dpa)_4(NCS)_2$, are slightly unsymmetric (2.24Å and 2.48Å Cr-Cr bonds),[313] and we anticipate that the basic features of the electronic structure described by Bénard for the Cl-capped species will be relatively unchanged in the NCS-capped analogue. Therefore, we review here only the key features that relate directly to the subsequent discussion of the electron transport properties. As was the case with the Cl-capped species, our calculations reveal equilibrium geometry with a symmetric Cr-Cr-Cr core, with Cr-Cr distance of 2.36 Å (Table 4-1). The ground state $Cr_3(dpa)_4(NCS)_2$ is also a quintet with net spin densities of +3.44 and -2.91 on the outer and inner chromium centres, respectively, along with the $\langle S^2 \rangle$ value of 8.46 (>> $S(S+1)$ = 6.0), all indicative of a highly localised broken-symmetry solution. The key features of the molecular orbital spectrum for $Cr_3(dpa)_4(NCS)_2$ are summarised in Figure 4-3, where spin-α and spin-β orbitals are shown on the left and right, respectively. The basic features are

broadly consistent with the symmetry-based analysis revealed in the previous chapter, although the spin polarisation has an effect of localising the occupied spin-α orbitals on the terminal chromium centres (π_t, δ_t) and their spin-β counterparts on the central metal (π_c, δ_c). Indeed, amongst the metal-based orbitals, only the orbitals of the σ symmetry show any delocalisation over the entire trichromium unit. In addition to the metal-based π orbitals, a pair of sulphur-based orbitals of π symmetry (π_S) is also present in the valence region. These mix extensively with their metal-based counterparts in the occupied spin-α manifold (where metal character is on the two terminal chromium atoms) but not in the spin-β set. The HOMO is the spin-α component of the σ^{nb} orbital, which is localised (by symmetry) on the terminal chromium centres, in agreement with the calculations performed by Bénard on the $Cr_3(dpa)_4Cl_2$ systems.[316] Hence, the Cr-Cr-Cr interaction is dominated by a three-centre three-electron σ bond,[316,317] just as in the case of the cobalt analogue,[297,319] and this favours a symmetric form.

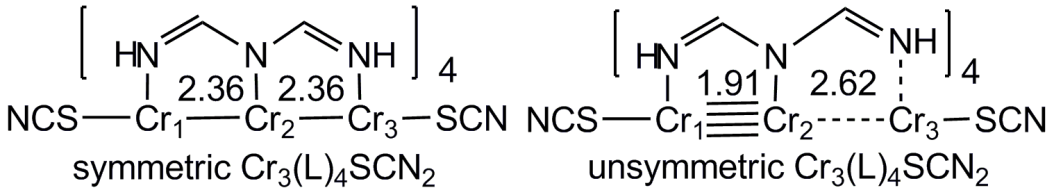

Figure 4-2: Symmetric and unsymmetric $Cr_3(L)_4(SCN)_2$.

		Bond lengths / Å		Spin densities			Conductance / μS)		
		Cr_1-Cr_2	Cr_2-Cr_3	Cr_1	Cr_2	Cr_3	total	α	β
Gas-phase (ADF)	**s-$Cr_3(L)_4(NCS)_2$**	**2.36**	**2.36**	**3.44**	**-2.91**	**3.44**			
	u-$Cr_3(L)_4(NCS)_2$	**1.91**	**2.62**	**2.04**	**-1.79**	**3.71**			
Two-probe (ATK)	**s-$Cr_3(L)_4(NCS)_2$**	**2.36**	**2.36**	**3.83**	**-3.57**	**3.83**	**0.08**	**0.08**	**0.00**
	u-$Cr_3(L)_4(NCS)_2$	**1.91**	**2.62**	**3.29**	**-3.20**	**3.71**	**2.91**	**2.91**	**0.00**
	$Co_3(L)_4(NCS)_2$	**2.32**	**2.32**	**0.50**	**-0.10**	**0.50**	**0.60**	**0.03**	**0.57**

Table 4-1: Spin densities and the conductance for $[Au_{32}]$-$M_3(L)_4(NCS)_2$-$[Au_{48}]$.

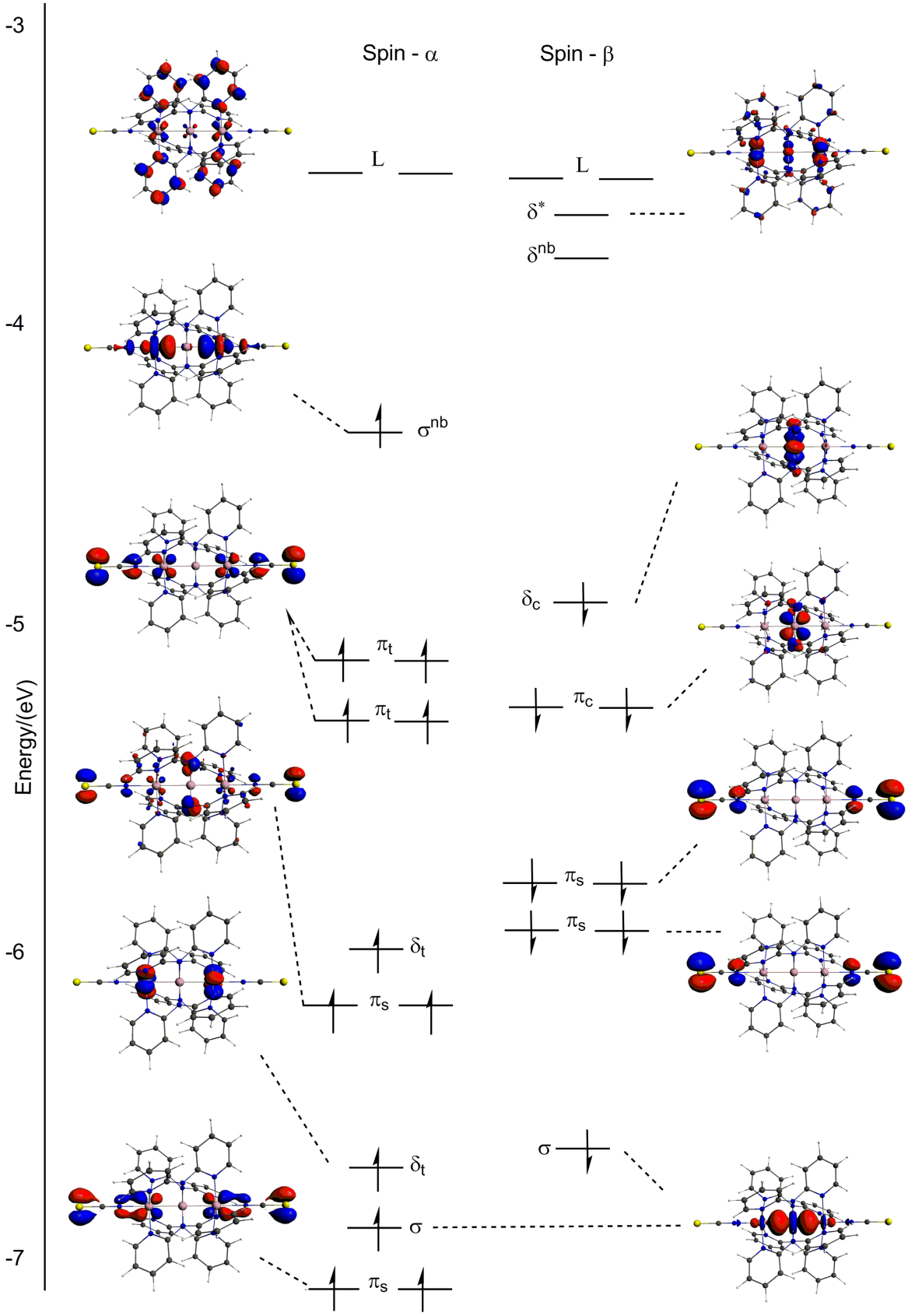

Figure 4-3: The valence molecular orbitals of the $Cr_3(dpa)_4(SCN)_2$ molecule.

4.3.2 Two-probe calculations

The model structure used for our transport calculations was as described in the previous chapter – specifically, the dpa ligand has been simplified by truncation of the pyridyl groups. A comparison of the gas-phase Kohn-Sham orbitals suggests that this does not have any significant impact on the energies or distribution of the frontier orbitals. The model system was then placed between the (111) faces of two gold electrodes as described previously. The zero-bias transmission spectra for the trichromium EMAC is presented in Figure 4-4. The region around the Fermi level is remarkably clean. A spin-α molecular orbital with σ^{nb} character, localised on the outer metal centres, lies close to the Fermi level. This level corresponds to a peak with transmission T(E)~ 1.0 at $E-E_f$ = - 0.2 eV. A similarly shaped peak is observed at $E-E_f$ = - 1.2 eV corresponds to the σ bonding orbital. A broad peak from the spin-α set with T(E) ~ 2.0 lies between 1.5 and 2.0 eV and it corresponds to the in- and out-of-phase combination of the π orbitals on the terminal chromium atoms. In the gas phase calculations (Figure 4-3), a significant mixing is observed between the metal and sulphur-based orbitals with π-symmetry. In the two-probe calculation, however, the latter are removed from the valence region due to strong bonding with the gold electrodes, but the residual sulphur character broadens the peak. As a result these peaks are broad and intense, but they are far away from the Fermi level and their contribution to electron transport at moderate bias will therefore be negligible. The π orbitals from the spin-β manifold are in the same region but as they are located on the central metal atom they do not generate a significant feature in the transmission

spectra. π^* orbitals localised on the organic ligand lie above the Fermi level and form a sharp, narrow peak due to weak coupling with the gold electrodes.

The transmission spectrum for $Cr_3(dpa)_4(NCS)_2$ suggests, perhaps surprisingly, that the dominant electron transport pathway is similar to that in the tricobalt chain presented in the previous chapter. In both cases, a σ^{nb} orbital localised on the terminal metals lies close to the Fermi level, and it will dominate current flow at low bias. There are subtle differences: in the trichromium chain, it is the occupied spin-α component that lies closest to E_f, whilst in the tricobalt case, it is the vacant spin-β orbital.

The position of this peak in the spectra relative to the Fermi level also has a significant influence on the conductance. In the trichromium case, the spin-α peak lies further below the Fermi level than the spin-β peak lies above it in the cobalt structure (see Chapter 3): $E - E_f$ = +0.1 eV for $Cr_3(dpa)_4(NCS)_2$ but -0.2 eV for $Co_3(dpa)_4(NCS)_2$. From the discussion in Chapter 2, we reiterate that the occupation of the level at zero bias does not have any effect on the conductance, only on its position being relative to E_f. Therefore, the computed total conductance is considerably larger in the cobalt case (0.57 μS) than in chromium (0.08 μS) not because of any fundamental difference in metal-metal bonding but simply because the dominant σ^{nb} channel lies closer to the Fermi level.

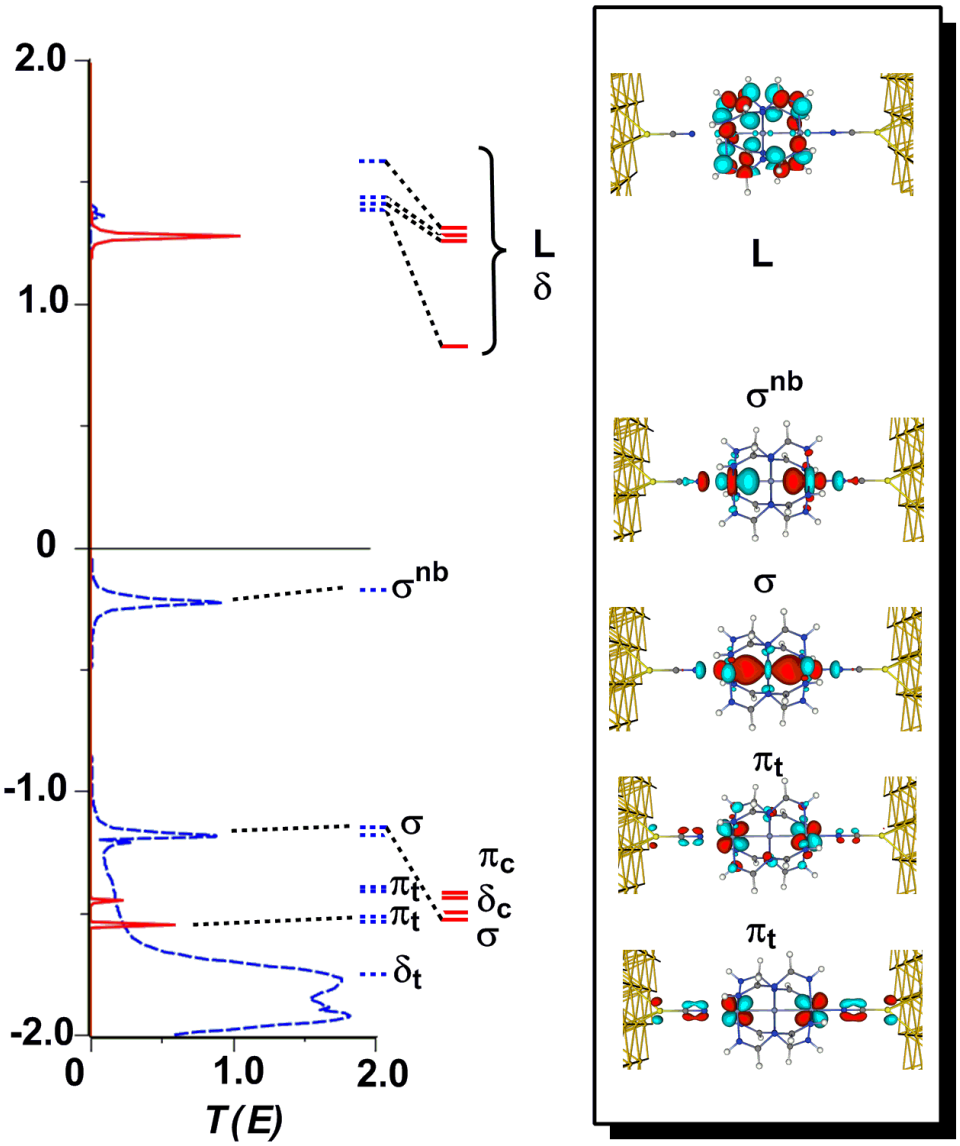

Figure 4-4: Transmission spectrum and molecular orbital diagram for $Cr_3(L)_4(NCS)_2$.

4.3.3 Comparison of symmetric and unsymmetric forms

The computed conductance is, however, clearly inconsistent with the experiment, which shows that the chromium chain is a better conductor than the cobalt one.[191] It has been mentioned already that the chains can exist both in symmetric and unsymmetric form and distortion of $Cr_3(dpa)_4Cl_2$ systems carries only small energetic penalties.[316] Our own calculations show that the same is true for the $Cr_3(dpa)_4(SCN)_2$ chain, where a strong distortion (ΔCr-Cr ~ 0.7 Å) (Figure 4-2) destabilises the system by less than 5 kcal/mol.

The distorted structure has been interpreted as a chain with one localised quadruple bond between Cr_1 and Cr_2 and longer, non-bonded distance between the Cr_2 and Cr_3 atoms. The reduction of the spin densities at Cr_1 and Cr_2 in the unsymmetric form (Table 4-1) indicates a greater degree of delocalization but the spin densities remain substantial even for very short Cr-Cr separation of ~ 1.9 Å. Hence, the internal distortion of the trichromium chain appears to be a result of the intrinsic flexibility of the three-centre three-electron σ bond rather than of any substantial redistribution of the π framework.

This leads naturally to the question of how the conductance varies with the structural distortion. To address this problem we have computed the transmission spectra and conductance of a highly distorted geometry of $Cr_3(L)_4(SCN)_2$, where Cr–Cr separation is fixed at the value found for $Cr_3(dpa)_4(Cl)(PF_6)$ (unsymmetric form in Figure 4-2). The computed conductance in the unsymmetric structure is significantly better than in the symmetric structure (Table 4-2). To understand the reason for this we need to compare the transmission spectra for the symmetric and unsymmetric cases (Figure

4-5). The two are qualitatively very similar, although the broad peaks from the spin-α set in the region of $E-E_f$ = -1.7 eV have disappeared completely. The MPSH eigenfunctions indicate the origin of this effect: the structural asymmetry induces substantial mixing of the in- and out-of-phase combinations of the π orbitals on the outer chromium centres, leading to orbitals that are localised on one side or the other of the molecule and effectively closing off the π channels. We have previously noted similar features for the cobalt complex under applied bias, where the electric field, rather than any intrinsic geometric asymmetry, was responsible for the closure of the π channels. Thus, the simple expectation that structural asymmetry should reduce transport through the π channels is valid, but this has negligible impact on the computed conductance, simply because the levels are so far below the Fermi level.

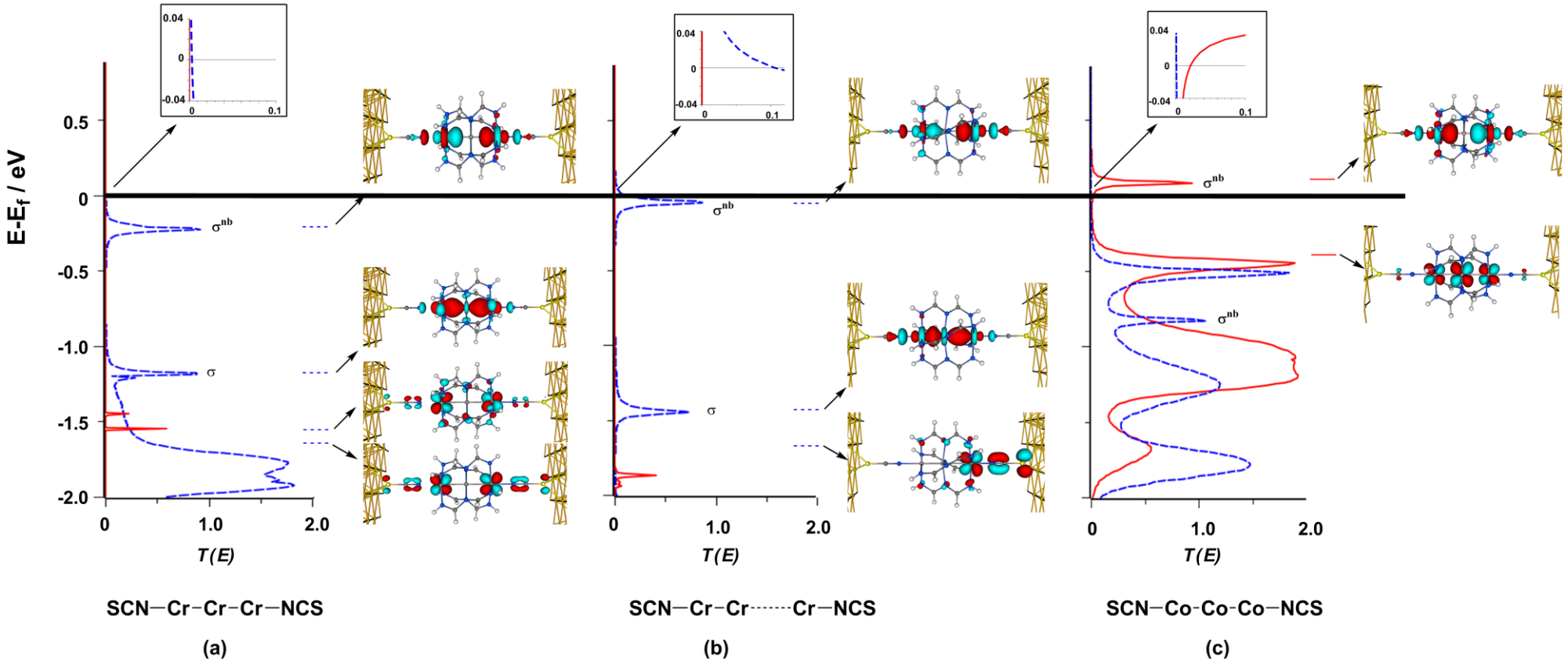

Figure 4-5: Transmission spectra of (a) symmetric-$Cr_3(dpa)_4(NCS)_2$, (b) unsymmetric-$Cr_3(dpa)_4(NCS)_2$, (c) $Co_3(dpa)_4(NCS)_2$.

The most important consequence of lowering the symmetry, from the electron transport point of view, is instead the destabilization of the σ^{nb} MO, the dominant transport channel. In the symmetric case the level is ~ 0.2 eV below E_f but in the unsymmetric structure it has been raised so that it is almost coincident with E_f. The result is a much greater transmission coefficient at E_f and, as a consequence, much higher conductance:

$$G = \frac{2e^2}{h}\sum_n T_n(E_F) = G_0 \sum_n T_n(E_F)$$

Equation 3

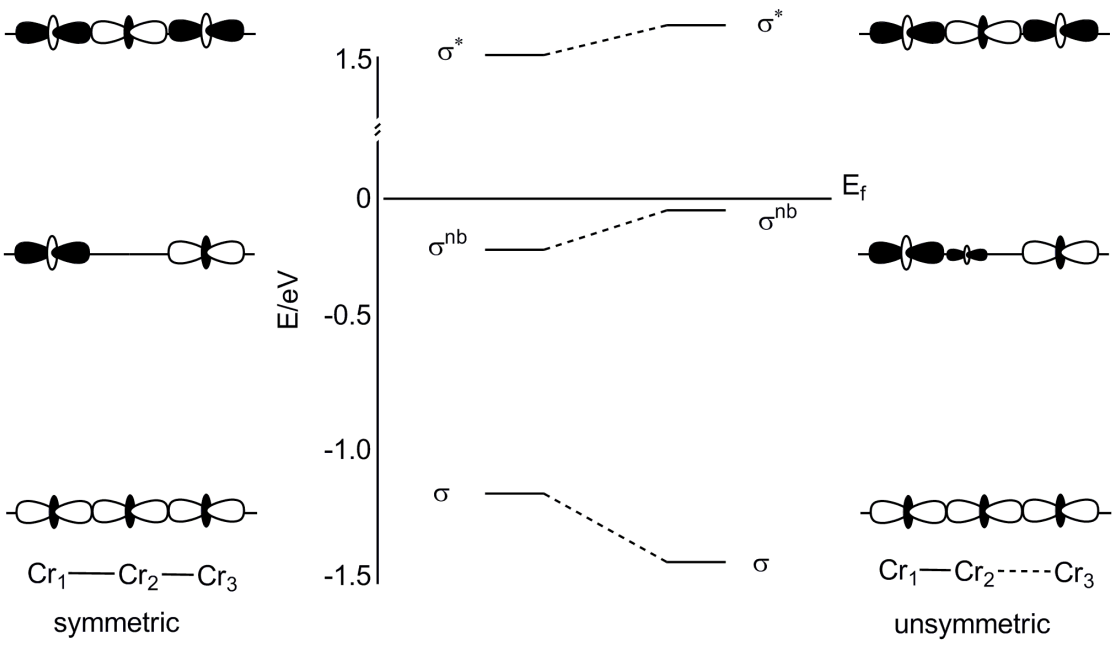

Figure 4-6: σ orbitals symmetric and unsymmetric trichromium structures.

This behavior can be explained by rehybridisation of the $\sigma/\sigma^{nb}/\sigma^*$ framework. Moving from the symmetric to unsymmetric form, the nonbonding combination of the σ molecule orbital is destabilised due to the emergence of some d_z^2 character in the

middle atom (Figure 4-6). This leads to an antibonding interaction between the central atom Cr_2 and the isolated Cr_3 metal atom. The reduction in spin polarisation across the short Cr-Cr distance also lowers the exchange splitting between the spin-α and spin-β components in the σ^{nb} orbital, pushing the former up and the latter down. Hence, if the Fermi level lies above the spin-α σ^{nb} orbital in the symmetric structure, the structural distortion will necessarily force the channel closer to E_f. The changes in the other σ levels are less significant as they are far away from the Fermi level and they do not contribute to the electron transport mechanism (Figure 4-6).

The changes in transmission spectra as a function of asymmetry are summarised in Figure 4-7, where two intermediate points are included along with the symmetric (Cr-Cr = 2.36 Å) and highly unsymmetric (Cr-Cr = 2.62, 1.93 Å), the latter corresponding to the experimental geometry observed in $Cr_3(dpa)_4(Cl)(PF_6)$. The two intermediate structures were constructed by increasing one Cr-Cr bond in steps of 0.1 Å, while allowing all other structural parameters to optimise freely. The transmission spectra for all four structures are presented in Figure 4-7. Our discussion will concentrate only on the spin-α σ manifolds because their dependence on distortion is most pronounced, and they dominate the electron transport. The corresponding changes in the σ-σ^{nb} separation in the isolated molecules are also shown (inset) and the computed conductance values are collected in the table below:

Cr_2 – Cr_3 distance/Å	**2.36**	**2.46**	**2.56**	**2.62**
Conductance/μS	**0.08**	**0.20**	**0.20**	**2.91**

Table 4-2: Conductance compared with the Cr_2 – Cr_3 distance.

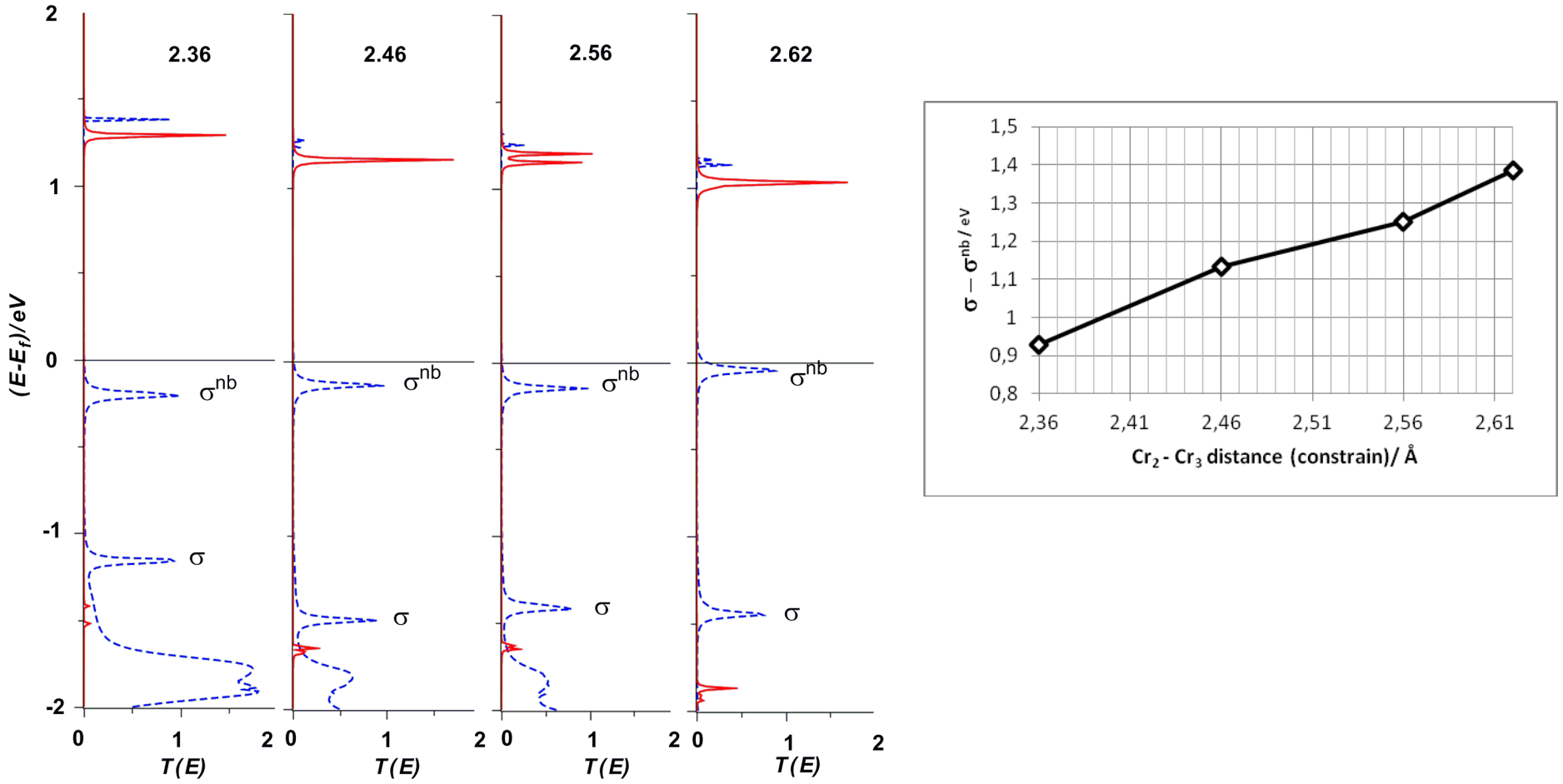

Figure 4-7:. On the left: transmission spectra with different Cr_2-Cr_3 bond length – 2.36, 2.46, 2.56, 2.62 Å. On the right: plot of the σ-σ^{nb} gap (spin-α set) vs the same Cr_2-Cr_3 distances.

The increasing asymmetry causes an approximately linear increase in the σ-σ^{nb} separation in the isolated molecule, corresponding to a destabilisation of the latter relative to E_f. The same upward shift is apparent in the transmission spectra but this only has a dramatic impact on the conductance when the tail of the transmission peak approaches the Fermi level very closely. Thus, $T(E_f)$ (and hence G) remains very small until the geometry becomes extremely unsymmetric (Cr-Cr = 2.62 Å, 1.91 Å), indicating that conductance is not a linear function of asymmetry. Thus, only in the most unsymmetric cases we see a dramatic rise in conductance.

Nevertheless, it is clear that an unsymmetric distortion of the Cr-Cr-Cr unit leads not to a loss in conductance but precisely the opposite – it increases dramatically for highly unsymmetric geometries. The origins of this effect lie in the rehybridisation within the $\sigma/\sigma^{nb}/\sigma^*$ framework which destabilises the σ^{nb} levels. As a consequence, the level is placed close to the Fermi level and the conductance increases with increasing of the level of asymmetry in the molecule. The wire is therefore far from 'broken' even in the least symmetric structure.

4.3.4 Devices out of equilibrium

All of the discussion presented so far in this chapter has been based on calculations at zero bias, and it is important to know how the electronic distribution responds to an applied voltage. Figure 4-8 presents the current-voltage characteristic of the symmetric and unsymmetric trichromium metal chains.

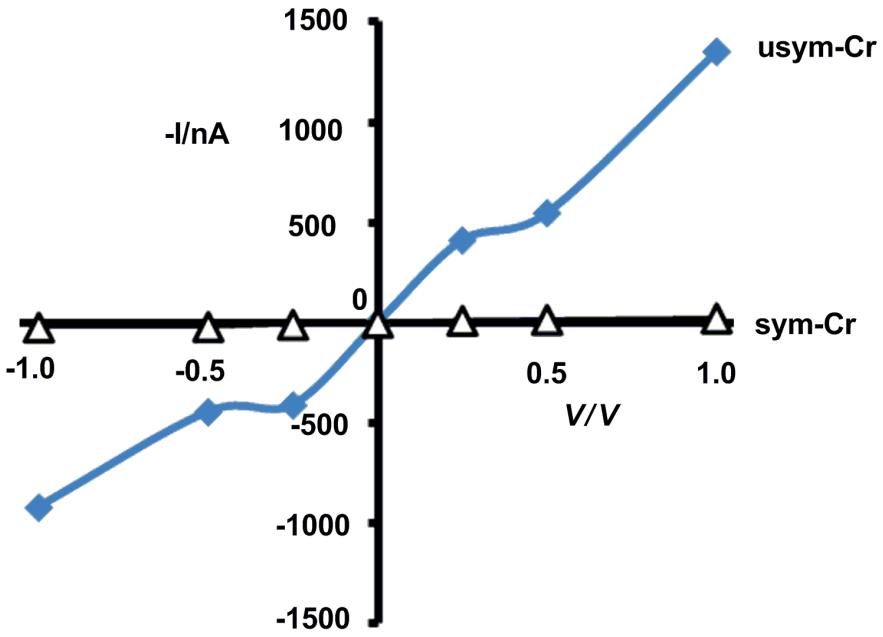

Figure 4-8: Computed current/voltage characteristics of the unsymmetric and symmetric trichromium chains.

Consistent with the computed zero-bias conductance, the current flow through the symmetric structure is significantly lower than through its unsymmetric analogue. The variations in the transmission spectrum with bias for the symmetric structure are collected in left hand side in Figure 4-9 . The most striking feature is that the dominant channel, the spin-α σ^{nb} component, is pinned to the drain chemical potential. Thus, at all voltages the relative distance between the HOMO (σ^{nb} spin-α component) and the chemical potential of the drain remains constant and the σ^{nb} level never enters the bias window. The charge redistribution and the electrostatic profile of the symmetric metal chain at 1.0 V are shown on the right hand side in Figure 4-9. The only perceptible feature is a very marginal depletion of spin-α density from the σ^{nb} orbital, the fingerprint of which is apparent in the changes in electron density. As a result, the electrostatic potential drop is localised between the source and the molecule, and so the occupied molecular levels follow the drain.

The transmission spectra of the unsymmetric trichromium EMAC show similar voltage dependence, but with the significant difference that the σ^{nb} level lies much closer to the Fermi level at 0V. The σ^{nb} level again follows the drain chemical potential, but in this case a significant part of the peak enters inside the bias window (Figure 4-10 left). The fingerprint of the σ^{nb} level is now very pronounced in the depletion of electron density in the spin-α manifold, and the potential again drops at the source/molecule junction (Figure 4-10 right). The fingerprints in the electron density maps are qualitatively similar to the tricobalt chain discussed in Chapter 3 except that they are most prominent in the occupied spin α set (blue coloured), while in the tricobalt case they are found in the vacant spin β component.

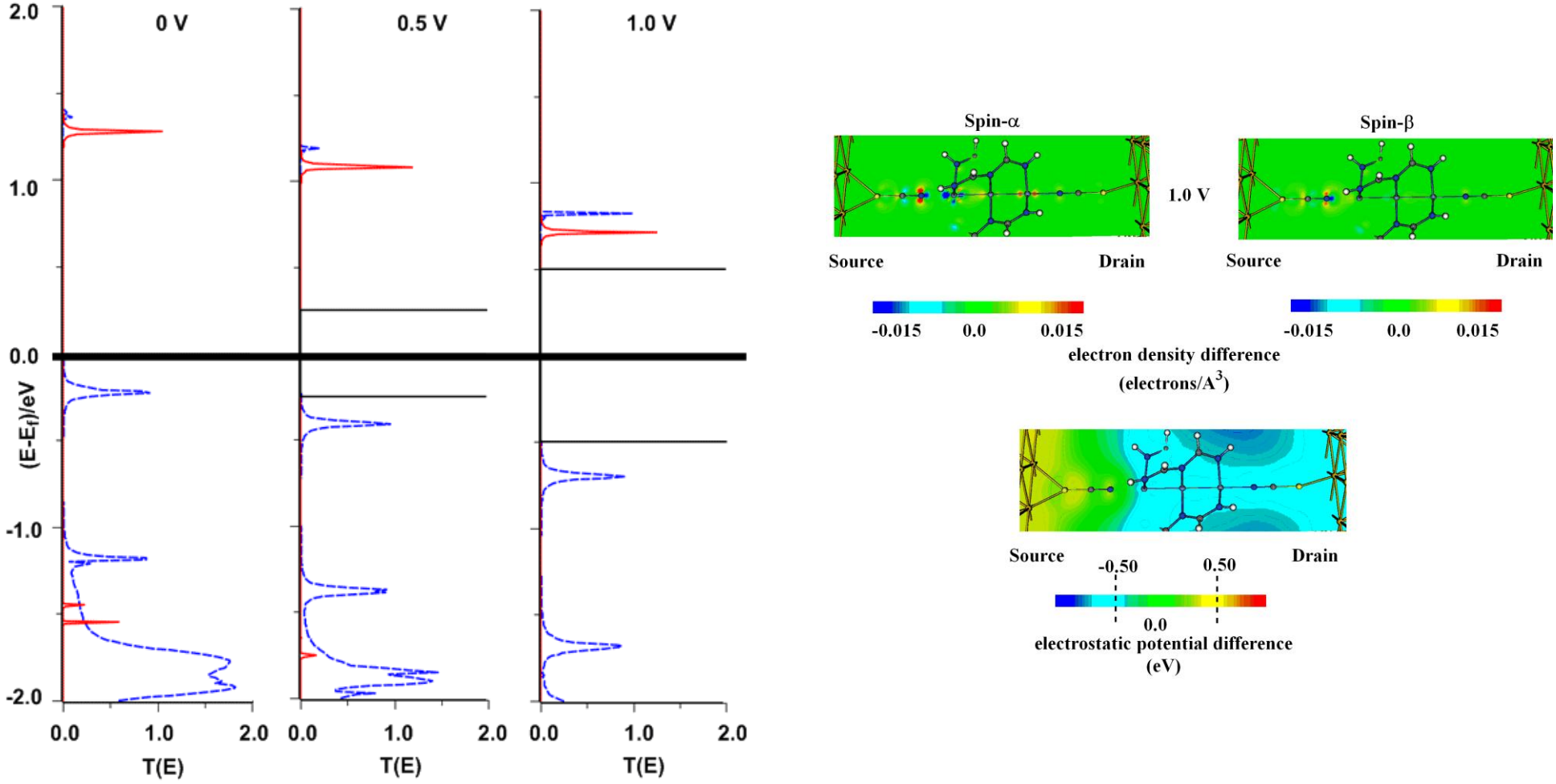

Figure 4-9: On the left: changes in transmission spectra as a function of the bias (0V – 1 V) for the symmetric trichromium EMAC. Red and blue (dashed) lines denote spin-β and spin-α components. Horizontal black lines for 0.5 V and 1.0 V mark the chemical potential of the source and the drain. On the right: charge redistribution and electrostatic potential profiles for the symmetric trichromium EMAC at 1.0 V.

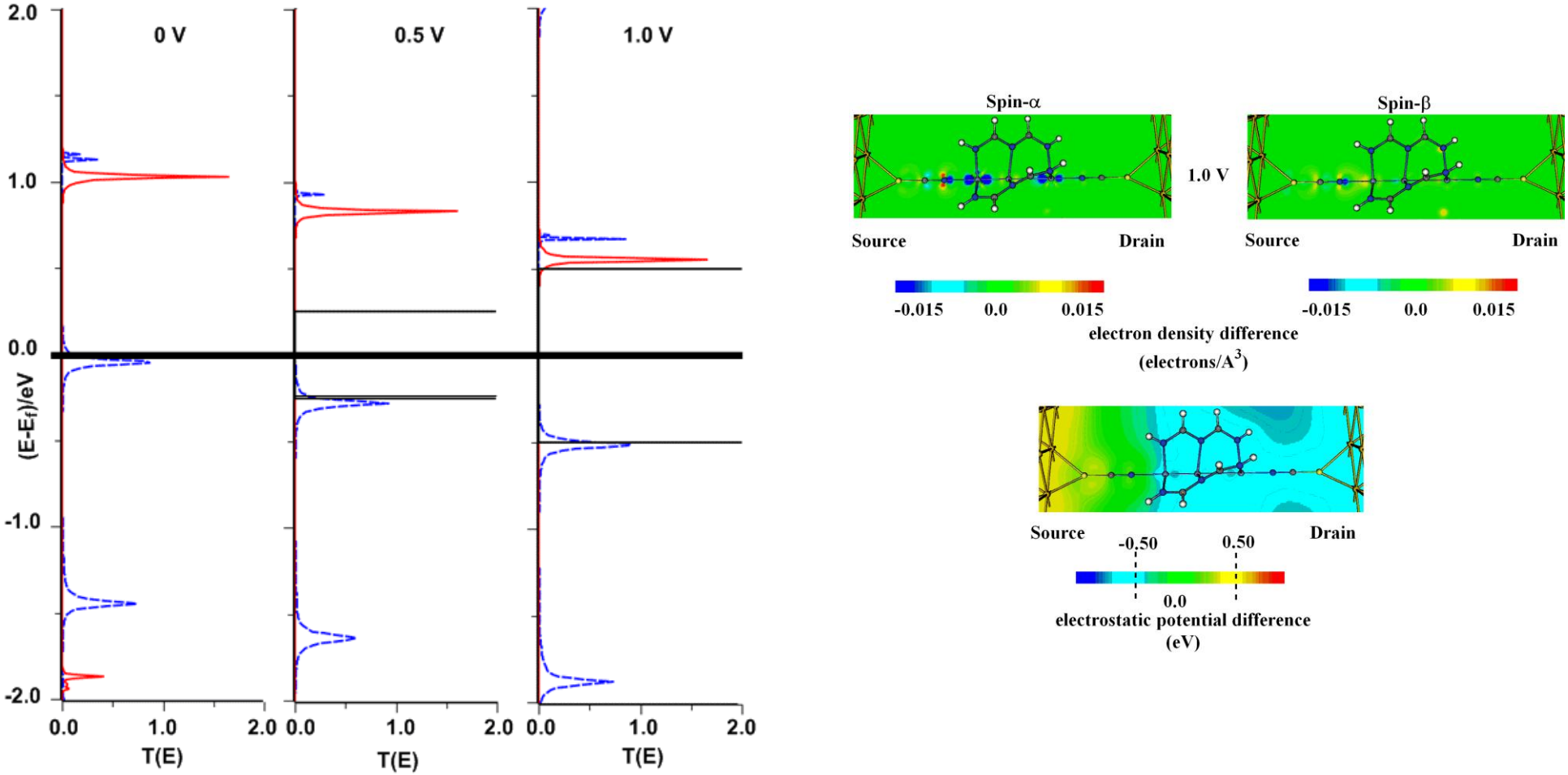

Figure 4-10: Changes in transmission spectra as a function of the bias (0V – 1 V) for the unsymmetric-trichromium EMAC. Red and blue (dashed) lines denote spin-β and spin-α components. Horizontal black lines for 0.5 V and 1.0 V mark the chemical potential of the source and the drain. On the right: charge redistribution and electrostatic potential profiles for the unsymmetric trichromim EMAC at 1.0 V.

4.4 Conclusions

In summary, our computational analysis suggests the rather counterintuitive conclusion that a low-symmetry distortion of the $Cr_3(dpa)_4(NCS)_2$ chain serves to enhance, rather than diminish, its ability to transport electrons. The impact of the distortion is not a consequence of any dramatic shift in the bonding regime (for example, a transition from Cr=Cr=Cr to Cr...Cr≣Cr), but of rather a more subtle shift in the σ manifold, which remains largely intact irrespective of the magnitude of the distortion. The unsymmetric trichromium EMACs could in principle be used as spin filters in the same way as the tricobalt analogues presented in the previous chapter. In both cases the σ^{nb} MO is close to the Fermi energy and the spin filtering properties remain significant even at biases as high as 1.0 V. It should be noted, however, that the tricobalt and trichromium chains 'filter' different spin components: the cobalt chain is transparent to spin-β electrons, while in the chromium structures the current flow is dominated by the spin-α set.

The orthogonal σ and π channels are common to both systems, and they differ from typical organic molecules, where only the π set is close to the Fermi level. The π orbitals provide a strong contact to the electrodes, while the σ set dominates current flow. The orthogonality of the two sets means that while the π channels are easily polarised by the bias applied to the electrodes, the σ-set remains independent and provides an effective pathway for electron transport and the current is not affected.

Finally, these trichromium systems emphasise a very important point – apparently intuitive extrapolations from macroscopic systems of organic-based conductors cannot readily be extended to transition metal systems. In this case, the π levels are

largely irrelevant to electron transport, and the apparently ‘broken’ unsymmetric wires are in fact the better conductors.

Chapter 5

Electron transport through trinickel chain: a basis for electronic switching?

5.1 Introduction

In this chapter we will discuss the electronic structure of the nickel member of the M_3 EMAC family, $Ni_3(dpa)_4(SCN)_2$, and its relationship to charge transport. The primary motivation is to establish a link to STM and CAFM experiments, both of which suggest that the nickel compound has a higher resistance than either the cobalt or chromium analogue.[191] Simple addition of three electrons to the qualitative scheme shown in Figure 3-5 would suggest a singlet ground state with no net Ni-Ni bonding, in which case the poor conductance would correlate inversely with metal-metal bond order, as proposed by Peng and co-workers. The magnetic data, which will be reviewed in details below, suggest a more complex situation where the Ni-Nσ* orbitals are occupied and the terminal metal centres are only weakly antiferromagnetically coupled in the ground state.[320]

The presence of weak antiferromagnetic coupling between the terminal centres represents a significant difference from the tricobalt and trichromium cases, where the corresponding spin density was aligned parallel, and it raises the possibility that

the trinickel chains could be used as a basis for a molecular switch. Baranger and Yang have discussed this possibility in the context of a dicobaltocene species (Figure 5-1), where the ferromagnetically coupled state (S = 1) is substantially more transparent than its antiferromagnetic counterpart.[120]

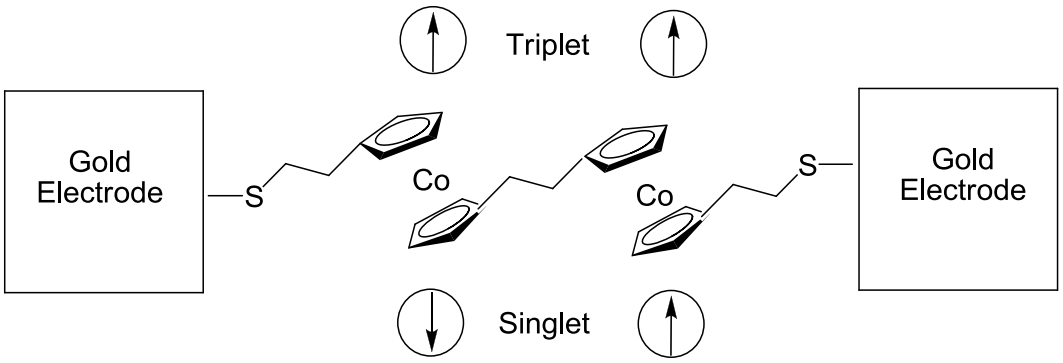

Figure 5-1: Two cobaltocene units in singlet and triplet states.

The authors and, subsequently, Sanvito and co-workers,[321] have raised the possibility that a magnetic-field induced transition between ferro- and antiferromagnetic states in systems such as these might provide a basis for a molecular switch. The organic linkers between the two cobaltocene units in Figure 5-1 do not, however, offer a great deal of flexibility in terms of tuning the strength of the interaction (measured by the Heisenberg exchange coupling constant, *J*) between the metal centres. Moreover, the systems are likely to be conformationally rather flexible, adding a further element of uncertainty to the value of *J*. The EMACs, in contrast, offer an absolutely rigid architecture, where the positions of the terminal metals are fixed within a very narrow range. Moreover, the identity of the central metal ion, which in this context acts as a diamagnetic bridging ligand, can, in principle, be varied to tune the strength of coupling. Although they have not yet been synthesised, calculations by Bénard and

Rohmer suggest that NiPdNi and PdPdPd chains show substantially stronger coupling than the all-nickel compounds.[322]

As in the previous chapters, we begin with a brief review of the key structural, magnetic and STM/CAFM data for trinickel chains and then provide an overview of previous computational work which has focussed on the Cl-capped species $Ni_3(dpa)_4Cl_2$. We then establish the basic electronic structure of the SCN-capped analogue as a precursor to exploring its behaviour in a two-probe setup. In this case we consider both ferro- and antiferromagnetically coupled states and contrast their ability to transport current. Finally we consider the perturbations introduced by replacing one Ni centre with the 4d analogue Pd, and whether the anticipated increase in exchange coupling influences the electron transport properties to any significant extent.

5.2 Experimental characterisation of trinickel EMACs

The first EMAC with three nickel atoms, $Ni_3(dpa)_4Cl_2$, was synthesized by Hurley and Robinson as long ago as 1968, but the molecule was incorrectly formulated as containing a central tetrahedral NiN_2Cl_2 unit and two terminal rhombic square coplanar NiN_4 chromophores (Chapter 1 Figure 1-22).[154] Only when the molecule was characterised by X-ray diffraction, by Aduldecha and Hathaway in 1991, was the correct helical structure revealed.[158] The $Ni_3(dpa)_4Cl_2$ complex has a symmetric structure with two equivalent Ni-Ni bonds of 2.437 Å, somewhat longer than those in the cobalt and chromium analogues. The same symmetric structural motif appears to

be common to all $[Ni_3]^{6+}$ chains that have subsequently been characterised, including the NCS-capped $Ni_3(dpa)_4(SCN)_2$ that we are directly concerned with here. The Ni-Ni bond lengths of 2.431 Å in the latter are very similar to the Cl-capped archetype.[169] The relatively weak Ni-Ni bonding in these species has been confirmed by Raman and Infrared spectroscopy, where the antisymmetric Ni-Ni-Ni stretching mode appears at 311 cm^{-1}. The closed-shell singlet formulation would imply rigid diamagnetism, and indeed at very low temperatures the effective magnetic moment of $Ni_3(dpa)_4Cl_2$ does approach zero. Above 50 K, however, it is strongly temperature dependent, rising to ~ 3 μB at 300 K. Such behaviour is highly characteristic of an antiferromagnetically coupled ground state, and the value J ($H = -2JS_1S_2$) has been reported variously as -99[178] cm^{-1} and -108[323] cm^{-1}.

5.3 Previous computational studies of trinickel EMACs

The first attempts to explore the electronic structure of the trinickel systems using density functional theory were reported by Rohmer and co-workers.[324] They have located a broken-symmetry ground state ($M_S = 0$), where the two terminal Ni(II) centres are in high-spin (S = 1) configurations. A Heisenberg exchange coupling constant J of -91 cm^{-1} was calculated, which is in excellent agreement with experiment. The central Ni atom, in contrast, is in a low-spin configuration, consistent with its approximate square planar coordination geometry, and it acts as a diamagnetic bridge between the two paramagnetic centres. The corresponding ferromagnetically coupled state with S = 2 has also been located, and it is lies +0.52

kJ/mol higher in energy. The closed shell singlet state has also been located, + 30.8 kJ/mol higher in energy. The detailed electronic structure of the singlet and quintet states will be discussed in the results section.

Rohmer and co-workers have also extended their studies to the hypothetical heterometallic chains, $NiPdNi(dpa)_4Cl_2$ and $Pd_3(dpa)_4Cl_2$.[183] In both structures the antiferromagnetic coupling between metal based electrons on the terminal atoms persists and J is larger by a factor of three for $NiPdNi(dpa)_4Cl_2$. In the case of $Pd_3(dpa)_4Cl_2$ the more diffuse 4d orbitals lead to low-spin configurations at the terminal metals, and, hence, diamagnetism regardless of which equatorial or axial ligands are used.[184] There are two possible exchange pathways: direct exchange via the central metal and super exchange via the bridging dpa ligands.[183] In these cases it appears that direct coupling via the σ orbitals dominates over super exchange via the ligands.[325,326] The more diffuse orbitals of the Pd atom clearly provide more efficient overlap with the two terminal nickel centres and, hence, magnify direct exchange pathway. Very recently de Graaf and co-workers[325,326] have applied the CASSCF/CASPT2 methodology to the computation of exchange coupling constants in these systems. The computed J value of -97.5 cm^{-1} is encouragingly close to both the experimental and DFT-computed values.

5.4 Results and discussion

5.4.1 Gas-phase electronic structure of $Ni_3(dpa)_4(SCN)_2$ in its quintet ($S = 2$) and broken-symmetry singlet ($M_S = 0$) states

A detailed understanding of the equilibrium electronic structure again forms the basis for our understanding of the transmission spectrum, and, hence, the electron transport. We therefore now present a detailed description of the Kohn-Sham orbital arrays for both the quintet (ferromagnetic) and open-shell singlet (antiferromagnetic) states of $Ni_3(dpa)_4(SCN)_2$. The optimised structural parameters for the quintet and broken-symmetry singlet states are collected in Table 5-1.

	Ferromagnetic	Antiferromagnetic	Experiment[327]
Ni – Ni	2.439	2.441	2.431
Ni – N (NCS)	1.954	1.958	2.004
Ni – N_t (dpa)	2.096	2.089	2.090
Ni – N_c (dpa)	1.913	1.913	1.885

Table 5-1: Optimised structural parameters for quintet (ferromagnetic) and broken-symmetry singlet (antiferromagnetic) states.

The Ni-Ni and Ni-N separations are almost identical in the two states, and the value of 2.439 Å for the former is in excellent agreement with the experimental values of 2.431 Å. The separation between the two states is 16.11 kJ/mol, corresponding to the

Heisenberg J value of -168.2 cm^{-1} (computed using Noodleman's approximation). Thus, the basic features of the electronic structure are very similar to those reported by Rohmer and co-workers for $Ni_3(dpa)_4Cl_2$.

The molecular orbital array for the quintet state is presented in Figure 5-2. The configuration can be generated by adding three spin-α electrons to the appropriate diagram for $Co_3(dpa)_4(NCS)_2$ (Chapter 3, Figure 3-8), one in the Ni-Ni-Ni σ^* orbital and two in the in- and out-of-phase combinations of Ni-Nσ^* (Ni-Ni-Ni δ) orbitals. The presence of only a single electron in the σ^* orbital does not completely offset the bonding effect of the fully filled σ bonding level. There remains, therefore, some residual Ni-Ni bonding, albeit not as strong as that in either the tricobalt or trichromium EMACs discussed in the previous chapters. The band of sulfur-based orbitals, $S_{\pi,}$, is again apparent in the occupied manifold, and it will ensure effective coupling to the gold electrodes in the two-probe calculation. The basic shape of the molecular orbitals, and in particular their delocalisation, is almost identical to the corresponding orbitals in the tricobalt case, emphasising the fact that gross changes in electronic structure cannot be invoked to rationalise the trends in electron transport phenomena.

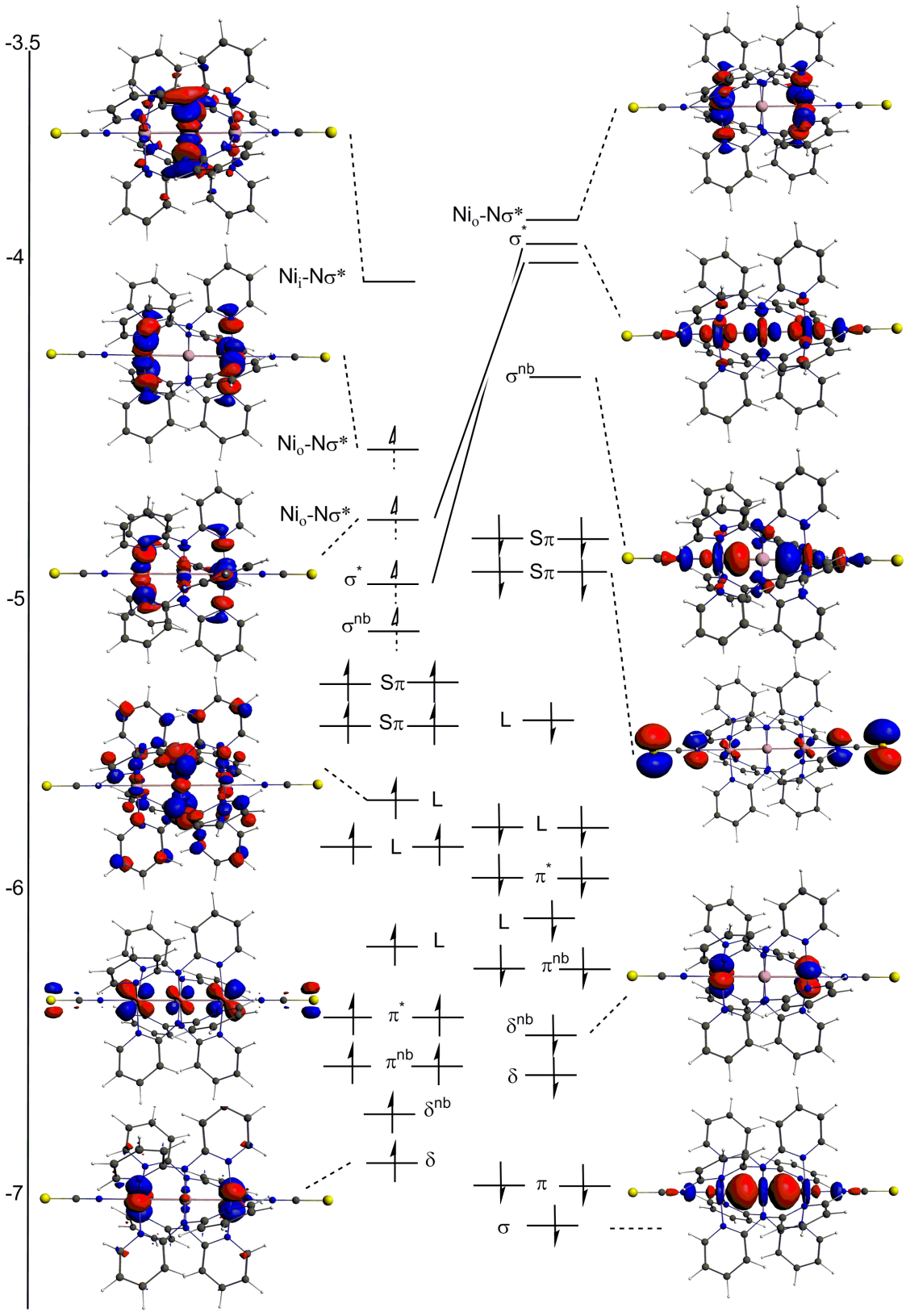

Figure 5-2: Frontier manifold of Kohn-Sham orbitals in the quintet state of $Ni_3(dpa)_4(SCN)_2$.

In the open-shell singlet state (Figure 5-3) the metal-based orbitals are strongly localised on one or other of the terminal nickel centres, as a result of which the bonding/non-bonding designations used for the quintet are less valid (a so-called broken-symmetry solution). Nevertheless the local spin density at the metal centres is very similar to that in the quintet, indicating that the two states are simply related by a spin flip at one of the centres. The localisation is most complete in the Ni-Nσ* orbitals, where the δ orientation of the metal-based components makes overlap on adjacent centres negligible. Overlap is more pronounced in the σ manifold, and, as a result, both σ^{nb} and σ* orbitals are somewhat delocalised over both sides of the molecule (this delocalisation being the origin of the relatively large value of *J*). The partial delocalisation within the σ manifold also has the effect of reducing the magnitude of the net spin densities at the individual metal centres from 1.39 in the quintet to ±1.30 in the/ open-shell singlet (Table 5-2).

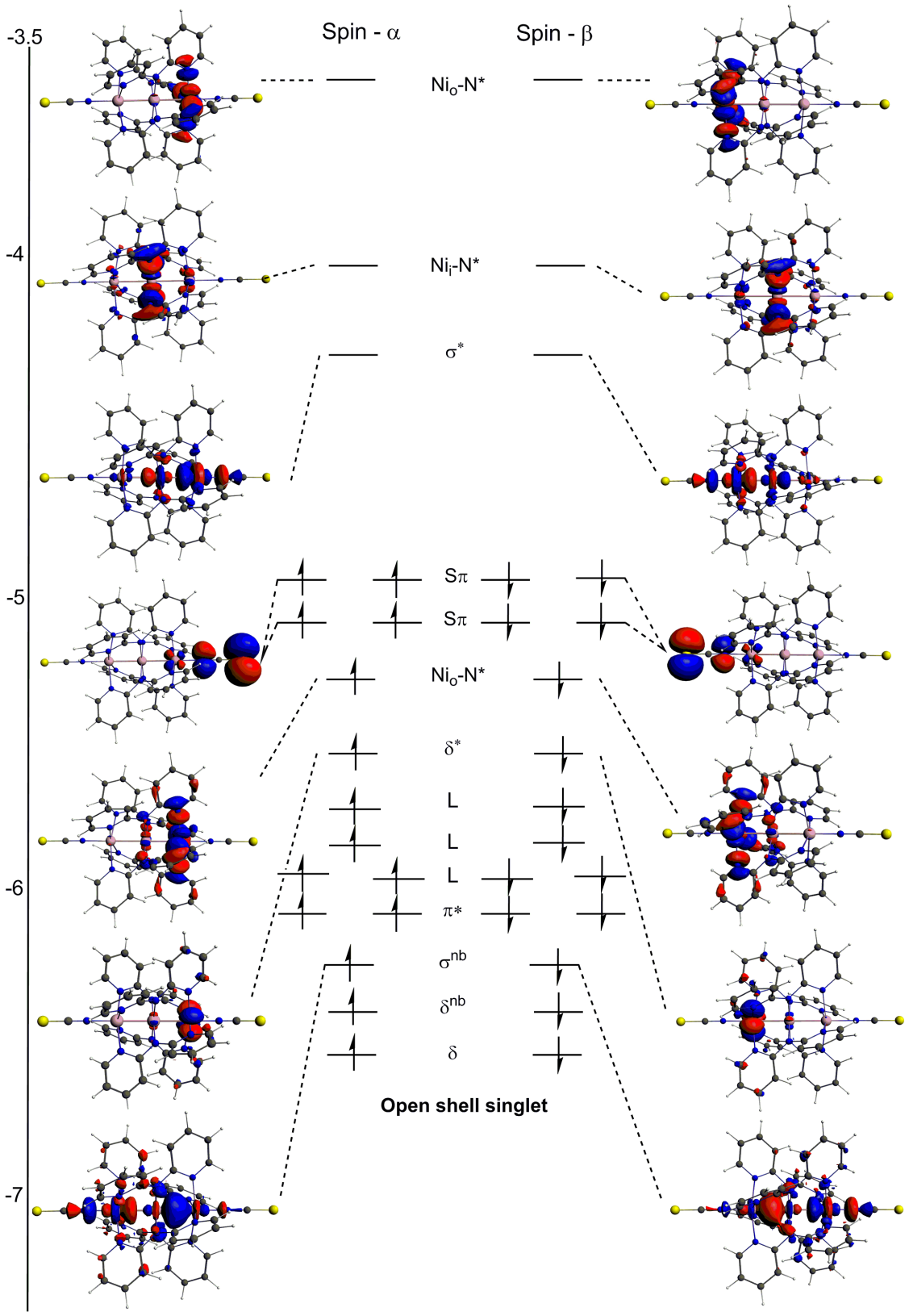

Figure 5-3: Frontier manifold of Kohn-Sham orbitals in the open-shell singlet state of $Ni_3(dpa)_4(SCN)_2$.

5.4.2 Two-probe calculations

All calculations were made following the calculations protocol presented in the previous chapters. The spin densities along with conductance are presented in Table 5-2.

		Spin densities						Conductance/μS		
		S	N	C	M_1	M_2	M_3	Total	α	β
Gas-phase (ADF)										
Ferromagnetic	**$Ni_3(dpa)_4(NCS)_2$**	**0.00**	**0.00**	**0.01**	**1.39**	**0.25**	**1.39**			
Antiferromagnetic	**$Ni_3(dpa)_4(NCS)_2$**	**0.00**	**0.00**	**0.02**	**1.30**	**0.00**	**-1.30**			
Two-probe (ATK)										
Ferromagnetic	**$Ni_3(L)_4(NCS)_2$**	**0.01**	**0.02**	**0.04**	**1.46**	**0.36**	**1.46**	**0.79**	**0.00**	**0.79**
Antiferromagnetic	**$Ni_3(L)_4(NCS)_2$**	**0.00**	**0.01**	**0.05**	**1.39**	**0.00**	**-1.39**	**0.02**	**0.01**	**0.01**
	$Co_3(L)_4(NCS)_2$	**0.00**	**0.00**	**0.00**	**0.50**	**-0.10**	**0.50**	**0.60**	**0.03**	**0.57**
Symmetric	**$Cr_3(L)_4(NCS)_2$**	**0.00**	**0.00**	**0.00**	**3.83**	**-3.57**	**3.83**	**0.08**	**0.08**	**0.00**
Unsymmetric	**$Cr_3(L)_4(NCS)_2$**	**0.00**	**0.00**	**0.00**	**3.29**	**-0.10**	**3.71**	**2.91**	**2.91**	**0.00**

Table 5-2: Spin densities and conductance for $[Au_{32}]$-$M_3(L)_4(NCS)_2$-$[Au_{48}]$.

Data for tricobalt and the symmetric and unsymmetric forms of trichromium are included for comparison. As was the case for the tricobalt and trichromium systems, placing the trinickel EMAC between the electrodes has only relatively minor effects on the electron density distribution, and the substantial spin densities are retained in both the ferromagnetic and antiferromagnetic states. The zero-bias conductance is negligible (0.02 μS) in the antiferromagnetically coupled state but substantially larger

in the ferromagnetic counterpart. Given that the gas-phase calculations indicate that the former is the ground state, the order of computed values of the conductance, trinickel < tricobal < unsymmetric trichromium, is fully consistent with the data obtained from STM and CAFM experiments.[191] The decomposition into separate spin channels indicates that the minority-spin (β) channel is entirely dominant in the ferromagnetic state. This situation is therefore qualitatively rather similar to that found in the $Co_3(dpa)_4(NCS)_2$ analogue.

5.4.3 Transmission spectra

The transmission spectra for the ferromagnetic and antiferromagnetic states of $Ni_3(L)_4(NCS)_2$ are summarised in Figure 5-4, along with the relevant MPSH orbitals. For the former, the spin-α and spin-β components are strongly split, but each component shows very similar features to those described previously for $Co_3(L)_4(NCS)_2$. Thus, within the spin-β set, the σ^{nb} level lies just above E_f level (Figure 5-4 a), while a broad and intense feature approximately 1.0 eV lower marks the position of the degenerate π levels which couple strongly to the electrode. The σ^* orbital forms a sharp and weak channel ~1 eV above E_f. In the spin-α manifold the same features are shifted downwards by ~1.5 eV, so that the occupied σ^* orbital falls 0.5 eV below the Fermi level. No intense peaks corresponding to the Ni-Nσ^* orbitals are apparent in either spectrum because these orbitals have negligible overlap along the z direction and they are only very weakly coupled to the electrodes.

The zero-bias conductance in the ferromagnetic configuration (quintet) of $Ni_3(L)_4(NCS)_2$, therefore dominated entirely by the spin-β component of the σ^{nb} orbital, emphasises once again the qualitative similarities to the tricobalt analogue. Indeed, the computed results for conductance are strikingly similar for the two chains. From the qualitative point of view the transmission spectra of triplet ferromagnetic trinickel chain is remarkably similar to the tricobalt structure described in Chapter 3. In both cases the σ^{nb} spin-β component is the main pathway for the electrons to transmit from the source to the drain. Similarly as before, the high spin trinickel structure can be described as a spin filter.

The transmission spectrum of the antiferromagnetic configuration is strikingly different from its ferromagnetic counterpart, and indeed from any of the examples explored previously (Figure 5-4 b). Most obviously, the spin-α and spin-β components are now identical (as they must be for a singlet state) but there is a complete absence of broad intense peaks. The featureless spectrum can be traced to the strong localisation of the metal-based orbitals on either side of the molecule, which effectively closes off the channels from one electrode to the other. The occupied spin-α orbitals are strongly localised on the left, while their spin-β counterparts are localised on the right. The only peaks with significant intensity are those corresponding to the σ levels (labelled σ_1, σ_2, σ_3 rather than σ, σ^{nb} and σ^* to reflect the fact that they do not have the full D_4 spatial symmetry of the molecule) which retain some partial delocalisation. Of these, the spin-α and spin-β components of σ_3 lie just above the Fermi level, and therefore provide the dominant contribution to the (very low) conductance at zero bias. The contour plots confirm that whilst this orbital is substantially localised on the right hand side, there is considerable character from

the central Ni atom and a minor component on the left – the orbital can be considered to arise from mixing of the σ^* and σ^{nb} orbitals of the fully delocalised system.

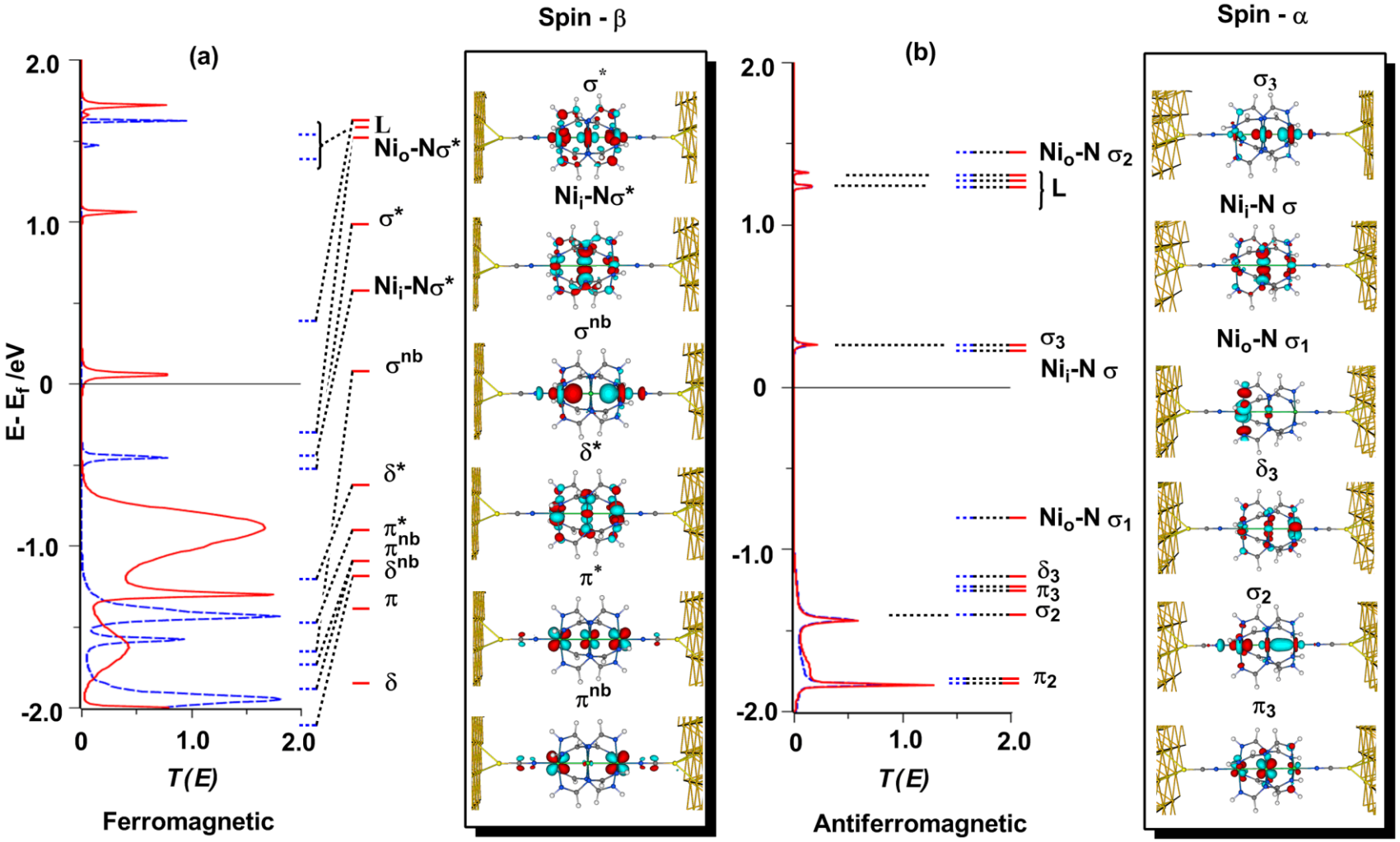

Figure 5-4: Spin-α (blue dashed) and spin-β (red full lines) transmission spectra for (a) ferromagnetic and (b) antiferromagnetic $Ni_3(L)_4(SCN)_2$.

5.4.4 Devices out of equilibrium

We have emphasised above the qualitative and quantitative similarities between the ferromagnetic state of $Ni_3(L)_4(NCS)_2$ and the cobalt analogue, $Co_3(L)_4(NCS)_2$, and it is perhaps unsurprising that they also behave similarly under applied bias. The current-voltage plot shown in Figure 5-5 shows that the current increases rapidly to a value of ~1000 nA at 0.25 V, and then plateaus off at higher bias.

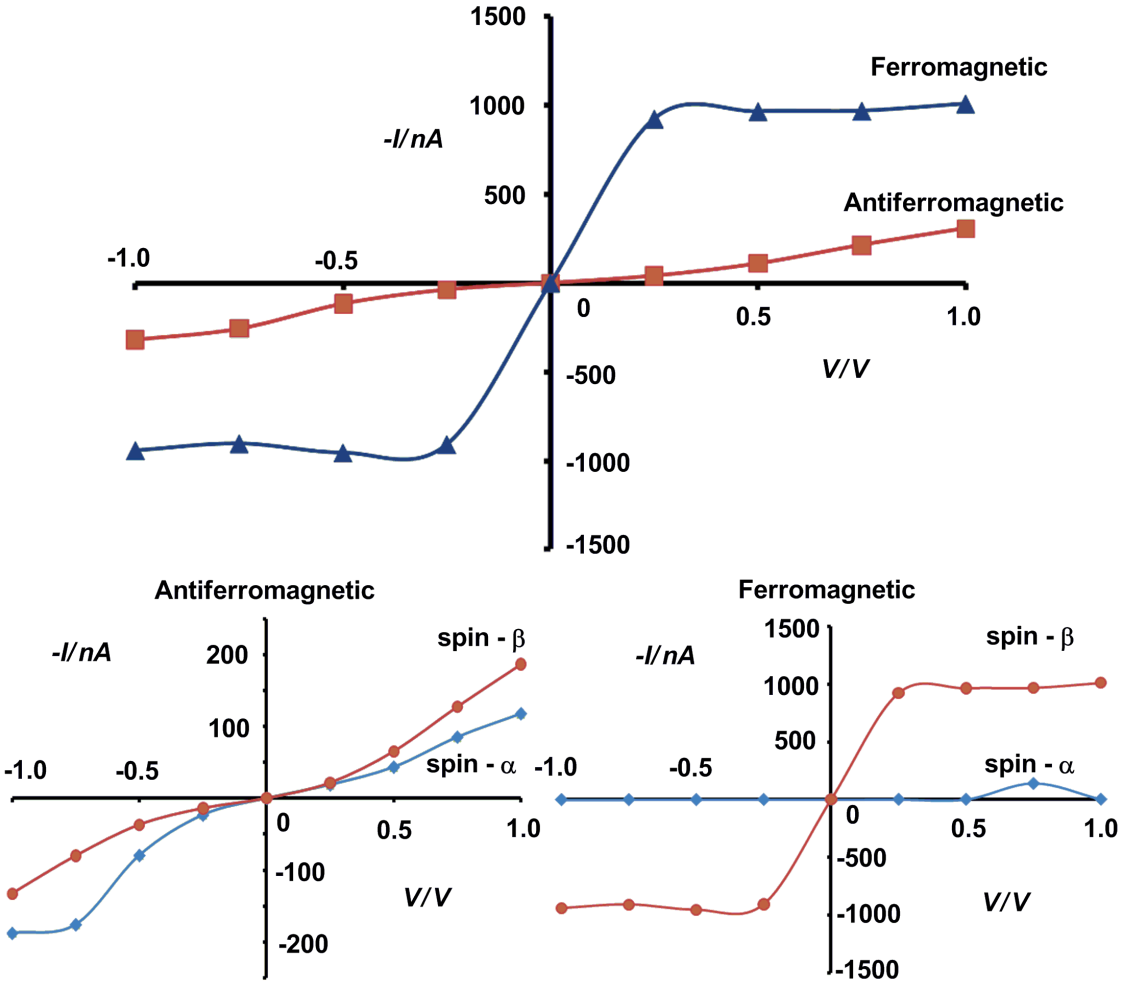

Figure 5-5: Computer current/voltage characteristics for ferromagnetic and antiferromagnetic states of the trinickel chain.

The evolution of the transmission spectra as a function of bias shows that at 0.5 V the bias window captures the entire spin-β σ^{nb} channel, causing the rapid rise in current flow (Figure 5-6). At higher biases (> 1.0 V) the lower edge of the bias window begins to cut into the occupied spin-α channels (note that the occupied spin-α Ni-Nσ* levels lie above the peak corresponding to the spin-α σ* orbital, but are not visible in the transmission spectrum due to their poor delocalisation). However, the fingerprint of these levels is apparent in the changes in electron density in the spin-α manifold. At 1.0 V and beyond the potential drops most dramatically at molecule/drain junction and all peaks therefore follow the potential of the latter. The characteristic rehybridisation within the π* levels also causes a reduction in intensity of the corresponding peaks.

The characteristics of charge transport in the antiferromagnetic case are, in contrast, very different to anything that has been discussed previously. At low biases (<0.5 V) current flow is very small, as the corresponding bias window is completely empty (Figure 5-7). At 0.5 V, however, a distinct increase in current flow occurs as the bias window begins to capture the lower tail of the σ_3 orbital discussed above. Somewhat surprisingly, the increase in current flow is also accompanied by a splitting of the spin-α and spin-β manifolds which is indicative of non-zero net spin density in the scattering region. Related to this, it is significant that at positive bias the current flow occurs primarily through the spin-β manifold, while at negative bias the opposite is true.

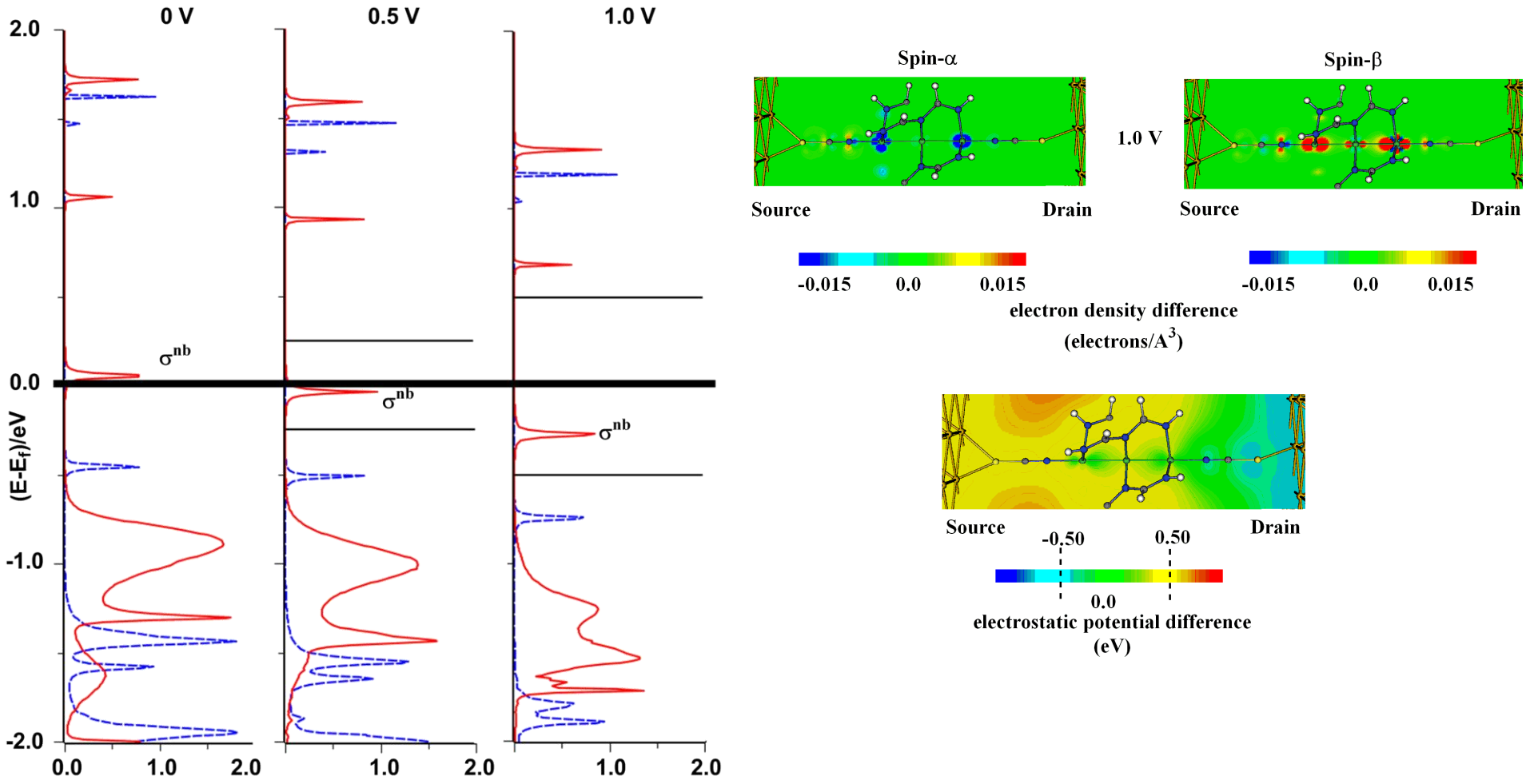

Figure 5-6: On the left: changes in the transmission spectra as a function of the bias (0V – 1 V) for the ferromagnetic trinickel EMAC. Red and blue (dashed) lines denote spin-β and spin-α components. Horizontal black lines for 0.5 V and 1.0 V mark the chemical potential of the source and the drain. On the right: charge redistribution and electrostatic potential profiles for the ferromagnetic trinickel EMAC at 1.0 V.

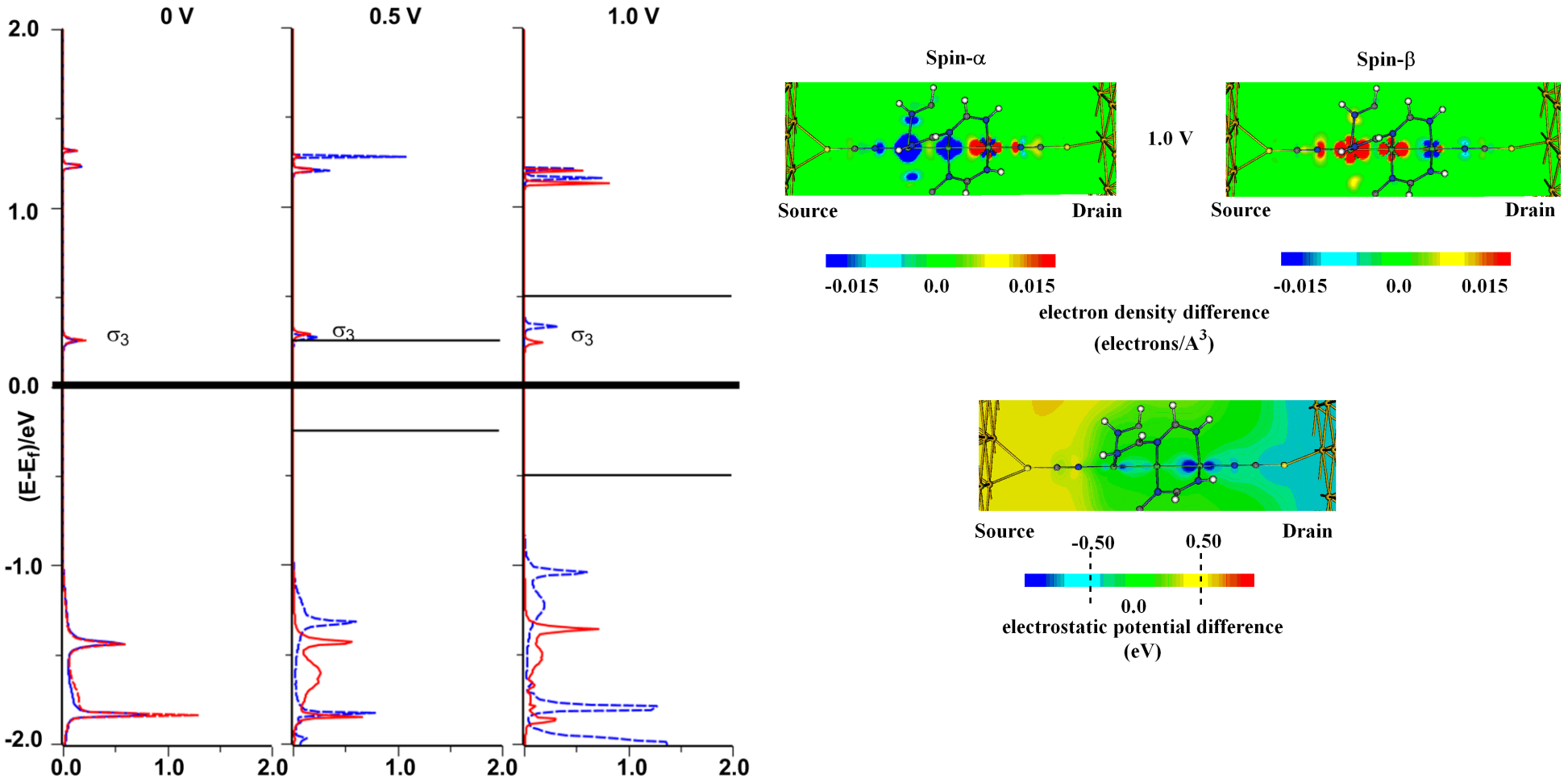

Figure 5-7: On the left: changes in the transmission spectra as a function of the bias (0V – 1 V) for the antiferromagnetic trinickel EMAC. Red and blue (dashed) lines denote spin-β and spin-α components. Horizontal black lines for 0.5 V and 1.0 V mark the chemical potential of the source and the drain. On the right: charge redistribution and electrostatic potential profiles for the antiferromagnetic trinickel EMAC at 1.0 V.

The origins of this bias-induced splitting can be understood in terms of the schematic picture shown in Figure 5-8.

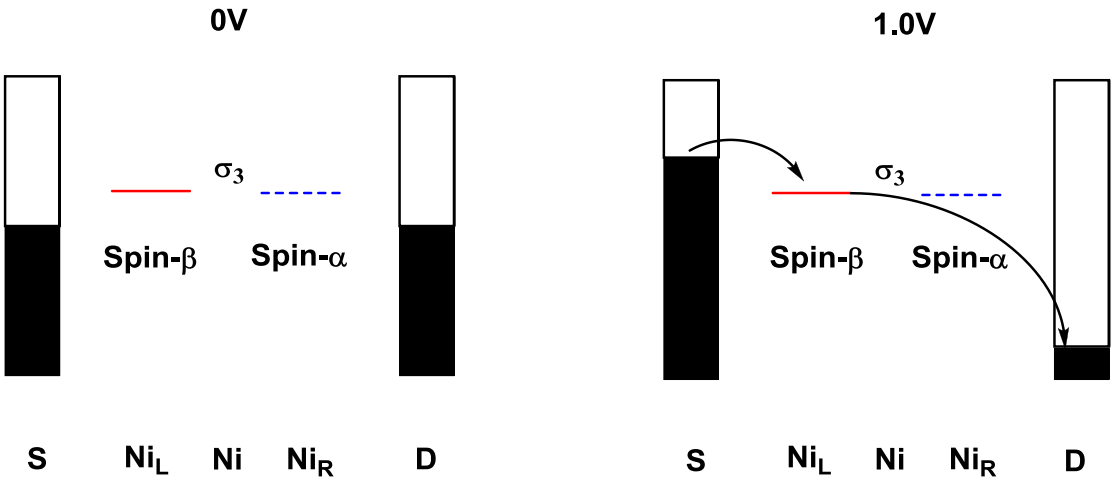

Figure 5-8: Schematic diagram of current flow in antiferromagnetic $Ni_3(L)_4(SCN)_2$ chain at 0 V and 1.0 V bias. Spin-β (red solid) and spin-α(blue dashed line) are localised on the left and right Ni atom, respectively; S – source and D – drain.

At zero bias, the vacant spin-α component of the σ_3 orbital is localised on Ni_R, while the vacant spin-β component is localised on Ni_L. Thus, under an applied positive voltage (i.e., the right hand side is the drain) only the spin-β component of the channel will be effectively coupled to the source. As a result, spin-β electron density flows into the left hand side of the scattering region, stabilising the spin-β manifold. The fingerprint of this charge accumulation on the left hand side of the molecule is apparent in the spin-β electron density difference map shown in Figure 5-7. Conversely, if the polarity of the bias is reversed, then charge flows into the scattering region via the spin-α manifold as only this component of the σ_3 channel is effectively coupled to the source (the right hand electrode).

5.4.5 Two-probe calculations of ferromagnetic and antiferromagnetic $NiPdNi(L)_4(NCS)_2$ chains

It was noted in the introduction that Bénard and co-workers have computed a substantially higher exchange coupling constant, *J*, for the hypothetical heterometallic chain $NiPdN(dpa)_4Cl_2$ ($2J$ = 320 cm^{-1}) if compared to $Ni_3(dpa)_4Cl_2$ ($2J$ = -98 cm^{-1}).[322] Our purpose here is to establish whether a similar trend is apparent in the NCS-capped species, and whether this difference translates to a substantial shift in the electron transport properties. Following the established protocol we first optimise the ferromagnetic and antiferromagnetic forms of the $NiPdNi(dpa)_4(SCN)_2$ chain in vacuum, and then use the optimised structure as a basis for the two-probe calculations. The results obtained from the gas-phase calculations, summarised in Table 5-3, are qualitatively very similar to those for $Ni_3(dpa)_4Cl_2$ molecule. The ferromagnetic alignment of spins (S = 2) lies 22.09 kJ/mol above the singlet ground state (S = 0), corresponding to a Heisenberg $2J$ value of -230.9 cm^{-1} (computed using Noodleman's approximation), approximately twice that in the $Ni_3(dpa)_4Cl_2$ analogue. Thus, direct exchange via the central Pd atom is somewhat more efficient in the heterometallic chain.

The computed conductance values (along with their decomposition into spin-α and spin-β channels) for both ferro- and antiferromagnetically coupled NiPdNi chains are summarised in Table 5-3. The transmission spectra for both states, along with the relevant orbitals, are shown in Figure 5-9, while the transmission spectra for trinickel and NiPdNi are compared in Figure 5-10.

		Spin densities						Conductance/μS		
		S	N	C	M_1	M_2	M_3	Total	α	β
Gas-phase (ADF)										
Ferromagnetic	**$Ni_3(dpa)_4(NCS)_2$**	**0.00**	**0.00**	**0.01**	**1.39**	**0.25**	**1.39**			
Antiferromagnetic	**$Ni_3(dpa)_4(NCS)_2$**	**0.00**	**0.00**	**0.02**	**1.30**	**0.00**	**-1.30**			
Ferromagnetic	**$NiPdNI(dpa)_4(NCS)_2$**	**0.00**	**0.00**	**0.01**	**1.45**	**0.15**	**1.45**			
Antiferromagnetic	**$NiPdNI(dpa)_4(NCS)_2$**	**0.01**	**0.01**	**0.01**	**1.32**	**0.00**	**-1.32**			
Two-probe (ATK)										
Ferromagnetic	**$Ni_3(L)_4(NCS)_2$**	**0.01**	**0.02**	**0.04**	**1.46**	**0.36**	**1.46**	**1.12**	**0.00**	**1.12**
Antiferromagnetic	**$Ni_3(L)_4(NCS)_2$**	**0.00**	**0.01**	**0.05**	**1.39**	**0.00**	**-1.39**	**0.02**	**0.01**	**0.01**
Ferromagnetic	**$NiPdNI(L)_4(NCS)_2$**	**0.01**	**0.00**	**0.00**	**1.54**	**0.19**	**1.54**	**0.02**	**0.02**	**0.00**
Antiferromagnetic	**$NiPdNI(L)_4(NCS)_2$**	**0.00**	**0.00**	**0.00**	**1.41**	**0.00**	**-1.41**	**0.00**	**0.00**	**0.00**

Table 5-3: Spin densities and conductance for $[Au_{32}]$-$M_3(L)_4(NCS)_2$-$[Au_{48}]$.

Considering first the ferromagnetic cases, we note that the computed conductance is substantially lower for the NiPdNi case. A comparison of the two transmission spectra (Figure 5-10 a and b) confirms that the basic structure is the same in both cases, but that the spin-β σ^{nb} peak that dominates conductance in the Ni_3 system is shifted upwards to~0.4 eV above E_f, substantially reducing $T(E_f)$, and therefore *G*. This orbital is entirely localised on the terminal Ni centres (by symmetry) and the shifts relative to E_f are therefore only indirectly related to the interactions with the central metal (Ni or Pd). The increased spin density at the Ni centres in NiPdNi causes a greater splitting of the spin-α and spin-β manifolds, and this has the effect of pushing the major transmission channel upwards, away from E_f. Of course, the substantial exchange splitting means that the major state will be the antiferromagnetically coupled singlet,

where differences between the trinickel and NiPdNi transmission spectra (and therefore conductance) are negligible.

In summary, it appears that there is no direct correlation between the exchange coupling, *J*, and the conductance, G, in the trinickel and NiPdNi chains. In the antiferromagnetic ground states the channels of σ symmetry, where major changes might be anticipated, are ~2 eV below E_f, and therefore have little influence on the low-bias conductance. In the ferromagnetic state changes are indirect, in the sense that a node is present at the central metal in the dominant channel. In this case subtle second-order effects associated with changes in spin density shift the position of the channel relative to E_f.

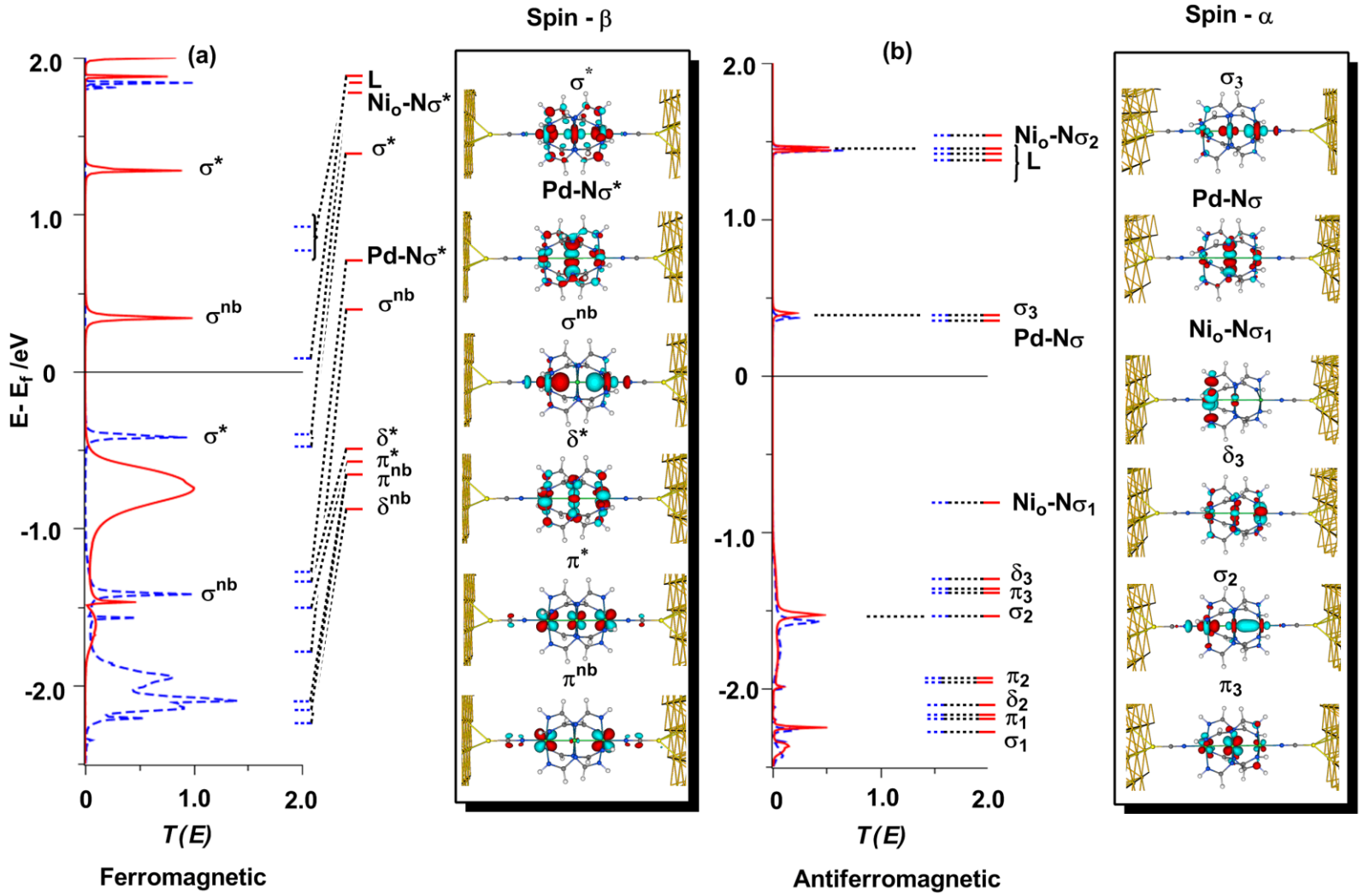

Figure 5-9: Spin-α (blue dashed) and spin-β (red full lines) transmission spectra for (a) ferromagnetic and (b) antiferromagnetic $NiPdNi(L)_4(SCN)_2$.

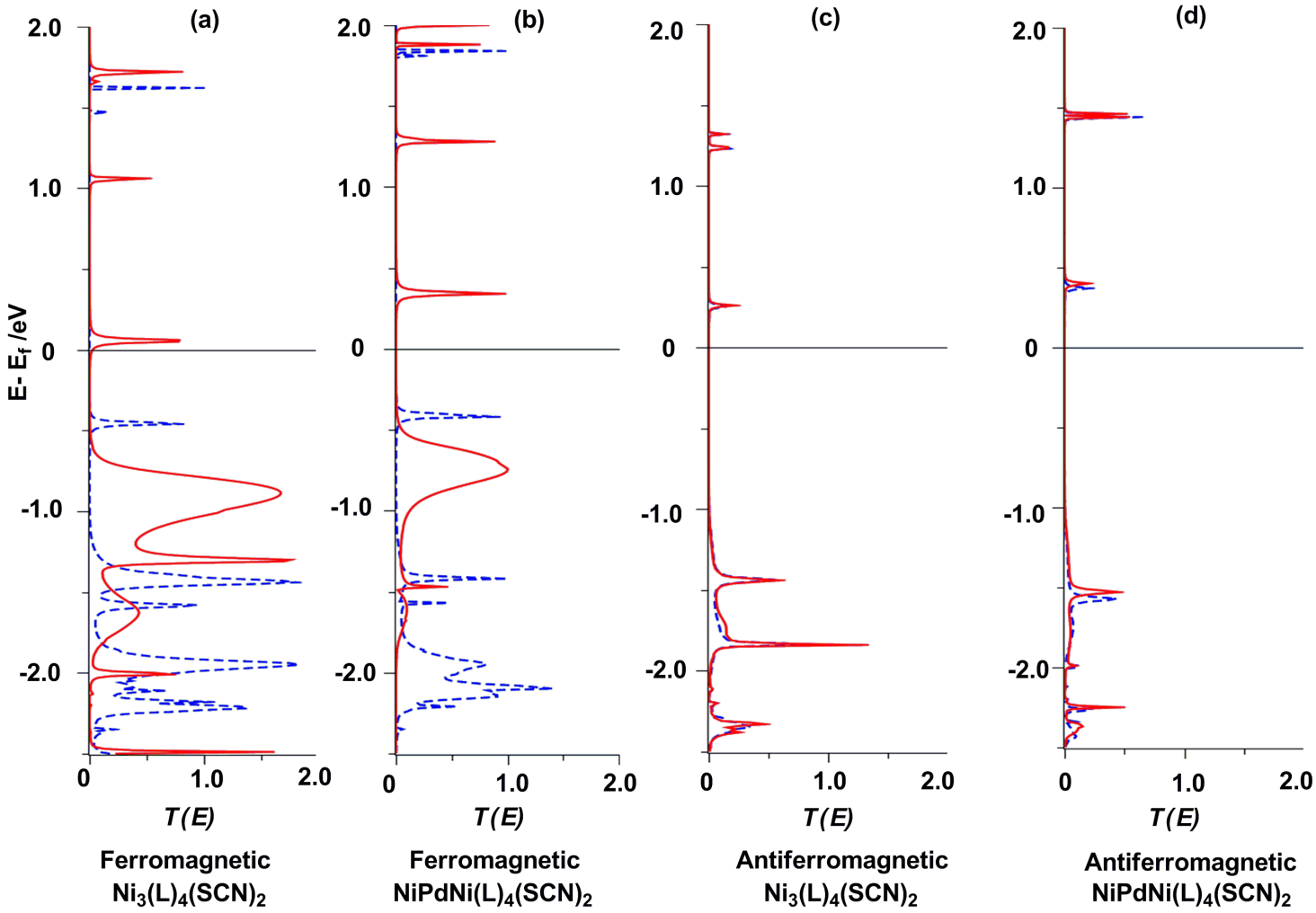

Figure 5-10: Spin-α (blue dashed) and spin-β (red full lines) transmission spectra for (a) ferromagnetic $Ni_3(L)_4(SCN)_2$, (b) ferromagnetic $NiPdNi(L)_4(SCN)_2$, (c) antiferromagnetic $Ni_3(L)_4(SCN)_2$ and (d) antiferromagnetic $NiPdNi(L)_4(SCN)_2$.

5.5 Conclusions

In summary, our calculations suggest that the ferromagnetic and antiferromagnetic states of the trinickel extended metal chain have dramatically different electron transport properties, the former being far more transparent than the latter. Thus, the system could, in principle, be the basis of a molecular switch although the large singlet-quintet splitting would probably prevent controlled switching between the two states via any reasonable mechanism.[321]

In the ferromagnetic state the transport properties are very similar to those of $Co_3(L)_4(NCS)_2$, where the vacant spin-β component of the σ^{nb} orbital lies just above the Fermi level and forms the dominant channel. In the antiferromagnetic counterpart, the strong localisation of the spin-components of the orbitals on opposite sides of the molecule means that the conduction channels are much less effective. A channel of σ symmetry remains the dominant one, with π channels making negligible contribution to the current flow. Somewhat surprisingly, even though the scattering region is diamagnetic at zero bias in the antiferromagnetic state, it is still able to support spin-polarised current flow. The reason for this is that the spin-α and spin-β components of the channel are localised on opposite sides of the molecule, and therefore couple differently to source and drain.

The picture described for NiPdNi chains is very similar to trinickel analogue. The replacement of the middle Ni atom with Pd atom shows no direct correlation between the exchange coupling, *J*, and the conductance, G, in the trinickel and NiPdNi chains.

Chapter 6

Linear tricobalt, pentacobalt and heptacobalt chains

6.1 Introduction

The previous three chapters have focussed exclusively on the trimetallic EMACs of cobalt, chromium and nickel, and in particular on the role of the electronic configuration on structure and electron transport. In this chapter we extend the discussion to consider the impact of lengthening the metal chain from three to five and seven cobalt atoms (Figure 6-1).

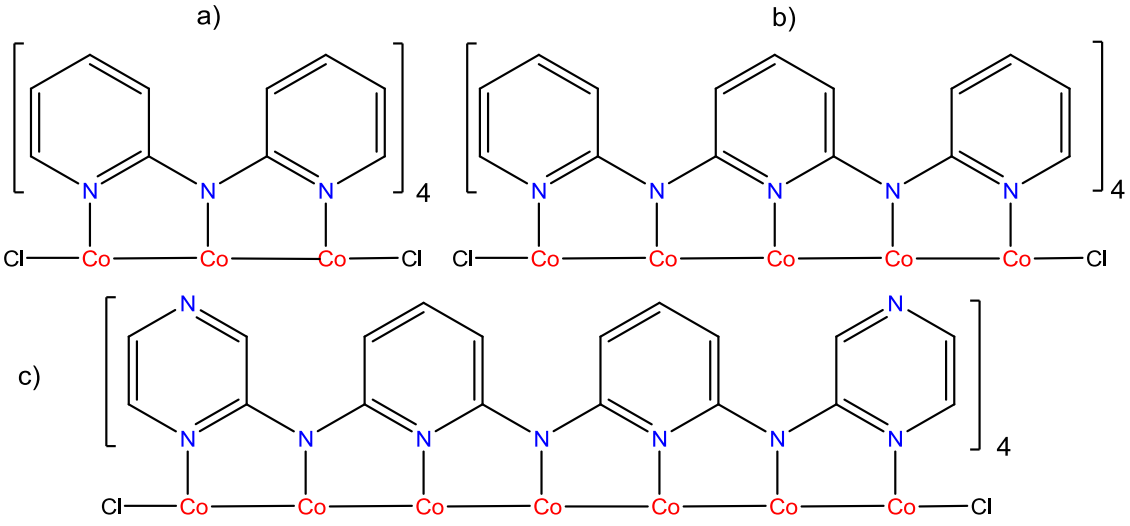

Figure 6-1: Structures of the tri-, penta- and heptacobalt chains.

The dependence of conductance on length of a molecular conductor has been extensively discussed in the context of organic compounds. It is generally found to decrease exponentially with the length of the chain – $G = G_0 \exp(-\beta L)$ where G_0 is the contact conductance, β is the attenuation factor, L controls the length dependence, and is strongly influenced by the nature of the bonds in the conductor (Figure 6-2 a and b). Thus, saturated alkanes have large attenuation factors approaching unity, implying a rapid increase in resistance with chain length (~1 $Å^{-1}$),[328-331] while unsaturated alkene and aromatic units reduce the value to as low as (0.5 - 0.1 $Å^{-1}$),[332-334] implying a much weaker length dependence. Some highly conjugated and low-band-gap systems, such as alkyne-bridged complexes[335] and oligo-zinc porphyrin,[336,337] have very low β value (<0.1 $Å^{-1}$). From this plethora of β values it can be concluded that the conductance of organic molecules depends strongly on molecule structure. A simple relation between the attenuation factor and the energy gap was reported: $\beta = -0.19 + 0.32*(E_g)^{1/2}$, where E_g is the HOMO – LUMO band gap of the molecule.[338] This relationship infers that when the energy gap E_g is smaller than a threshold (0.35 eV), the attenuation factor tends to go to zero. Hence, the electrons may travel a long distance without attenuation. Molecules with small attenuation factor are of great possible interest in the context of molecular wires.

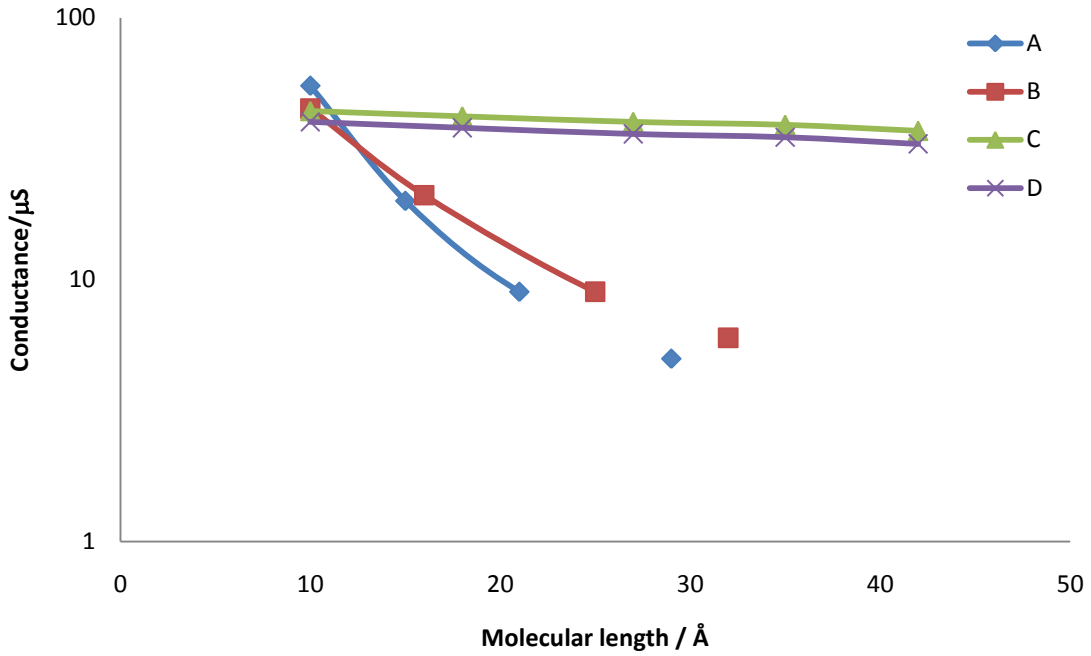

Figure 6-2: Plot of the conductance in logarithmic scale of a) oligothiophene,[339] b) oligopyrrole,[340] c) oligoporphine[341] and d) oligo magnesium (II) porphyrin[336,337] as a function of the molecule length.

An exponential relationship between the conductance and length of the structures is not always observed. Some molecules, such as magnesium porphyrin oligomers, show a linear dependence of the conductance with the molecule length (Figure 6-2 c and d).[336,337] One possible explanation of this is based on quantum effect where electrons with certain energies may tunnel easier if compared to others. Another possibility is that the repeat units are connected with more than one chemical bond. At the moment it is not clear what the real reason for this phenomenon is and more computational and experimental work is required.

From an analysis of the relationship between β and computed transmission spectra in organic compounds, Zhao and co-workers[342] have argued that the former is determined by two distinct factors: (i) changes in the intensity of peaks (which do not shift in energy) and (ii) shifts in the frontier orbitals, and therefore in transmission

peaks. In the context of the metal-atom chains described in the preceding chapters we have encountered examples of both phenomena: shifts in intensity are critical in closing of the π manifold of both tricobalt and trichromium chains, while shifts in the position of the σ^{nb} peak control the changes in conductance. Thus, by analysing the impact of elongating the cobalt chains on the transmission spectra, we hope to establish where the metal chains fit in the context of exponential or linear trend found in organic conductors.

Unlike the work in the previous chapters, there has been no previous theoretical study of these chains beyond the extended Hückel level. Before exploring charge transport properties, we therefore present a detailed survey of the electronic structure. The primary goal here is to establish whether the structural and electronic complexity of the shorter tricobalt chains is also prevalent in their longer analogues. As with the other chapters, however, we start with a review of the key experimental data.

6.2 Structural and magnetic properties of the pentacobalt and heptacobalt extended metal atom chains

We already discussed the tricobalt structure in Chapter 3. Now we will present experimental data only for penta- and heptacobalt EMAC. The first reported five-cobalt EMAC, $Co_5(tpda)_4Cl_2$, was reported in 1997 by Peng and co-workers (tpda = trypyradyldiamine).[170] In 2002 the same group extended the series to $Co_5(tpda)_4X_2$ complexes, where X = SCN^-, Cl^-, N_3^-, CN^-, CF_3^-, ClO_4^- or $SO_3CF_3^-$.[171] In marked contrast to

the tricobalt chains, where symmetric and unsymmetric forms have been observed, all of the above complexes have a symmetric metal core wrapped helically by the tpda ligands. The crystallographic data reveal two distinct sets of Co-Co, where the inner bond is in a region of 2.22 – 2.24 Å and the outer one is between 2.27 – 2.29 Å (Figure 6-4 b). One-electron oxidation has a very limited impact on the Co-Co and Co-N distances, but the Co-X (X = axial ligand) bond length decreases marginally. Susceptibility measurements indicate that the neutral molecule has a doublet ground state (S = 1/2) with a temperature-independent magnetic moment. The one-electron oxidised compound, in contrast, has a triplet ground state (S = 1). In addition to the tpda ligands (which are the direct analogues of dpa used for the trimetallic chains), two closely-related derivatives, dpzpda and bna (Figure 6-3 left), are also able to form pentametal (M_5) chains. In dpzpda pyrazine rings are present in place of pyridine, while in bna a naphthyridine group is present instead of a pyridylamido group.

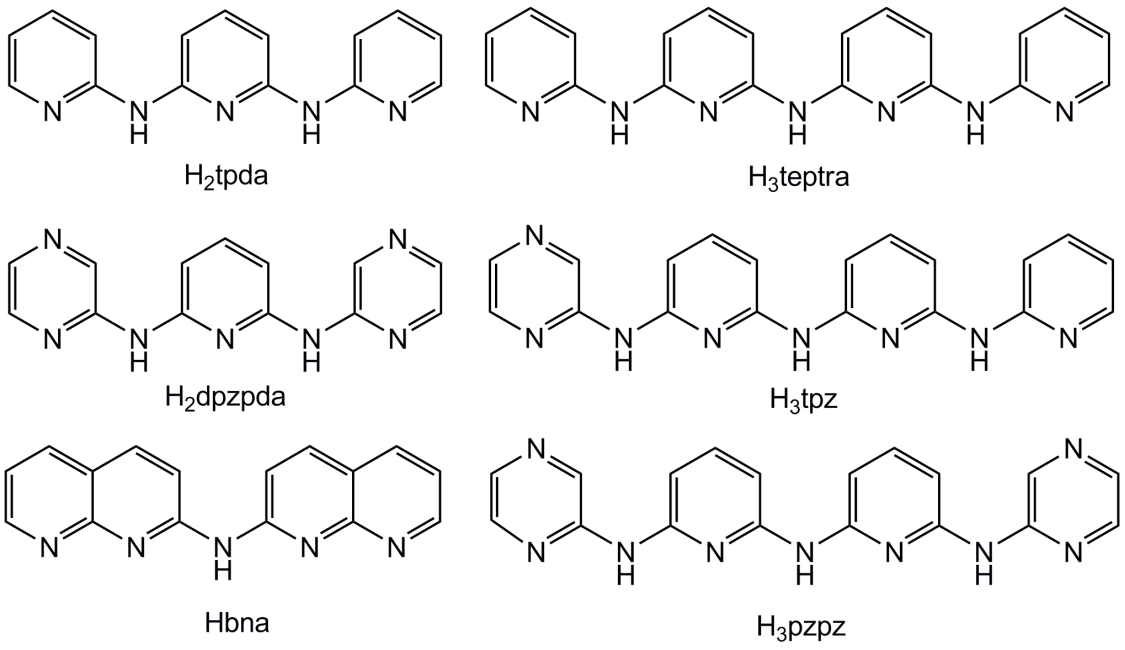

Figure 6-3: Possible pentadentate (left) and heptadentate (right) ligands.

In 2008 the complexes $Co_5(dpzpda)_4Cl_2$ and $Co_5(dpzpda)_4(NSC)_2$ were reported, with rather similar structural properties to the tpda analogues.[343] The Co – Co and Co – N outer distances, where axial ligand is Cl^-, are longer if compared to the structures where X = SCN^- because Cl^- provides a stronger ligand field than SCN^- (Figure 6-4 b). However, electrochemistry shows that these two complexes undergo reversible one-electron reductions (Co_5^{10+} to Co_5^{9+}) rather than the oxidations observed for tricobalt analogue. In the reduced species the Co-X (X=axial ligand Cl^- or SCN^-) distance is elongated by 0.05 Å, while the 'inner' Co-Co bond is elongated by ~0.02 Å. In contrast, the outer Co-Co distances are not perturbed by the reduction. The magnetic data also show rather different behaviour if compared to the tpda analogues. The neutral species have a magnetic moment intermediate between the characteristic values for a doublet and quartet state over the entire temperature range from 2 to 300 K. This has been rationalised by the presence of a spin equilibrium or spin-admixture between distinct states. The magnetism of the reduced form is similarly complex, lying intermediate between diamagnetic (singlet) and triplet states in the temperature range 5-300 K.

Three distinct ligand types have also been used to generate heptacobalt chains: teptra (an oligo-α-(pyridyl)amido ligand), pzpz (N^2-(pyrazin-2-yl)-N^6-(6-(pyrazin-2-yalamino)pyridine-2-yl)pyridine-2,6-diamine) and tpz (N^2-(pyrazin-2-yl)-N^6-(6-(pyridin-2-yalamino)pyridine-2-yl)pyridine-2,6-diamine). Only the heptanickel[175] and heptachromium derivatives of teptra have been reported,[344] but both pzpz and tpz have been used to form complexes of the formula $Co_7(L)_4X_2$, (X =Cl^- or NCS^- and L = pzpz or tpz). In all structures Co-Co bond distances can be separated into three groups: terminal Co-Co bonds (2.28 – 2.31 Å), intermediate Co-Co atoms (2.52 – 2.61

Å), and inner Co-Co bonds (2.19 – 2.20 Å) (Figure 6-4 c and d). The terminal Co-Co distances in chloride complexes are longer than those in thiocyanate, as it was noted for the pentacobalt chains. The Co-N bonds can be combined in two groups: $Co\text{-}N_{pyridyl}$ and $Co\text{-}N_{amido}$. $Co\text{-}N_{amido}$ bonds are stronger than $Co\text{-}N_{pyridyl}$ bonds due to more negative density on amido N atom, and consequently the $Co\text{-}N_{amido}$ bond distance is shorter (Figure 6-4).

The magnetic behaviour of the heptacobalt chains is ambiguous. $Co_7(pzpz)_4Cl_2$ and $Co_7(pzpz)_4(SCN)_2$ have magnetic moments of 2.70 μ_B and 2.95 μ_B, respectively, significantly higher than the theoretical value for a doublet state (1.73 μ_B) but much lower than quartet ground state (3.87 μ_B).[177] However, the complexes with the pzpz ligands systematically show a lower magnetic moment than those with tpz (ligands are showed in Figure 6-3). The former has a value significantly higher than the limiting value for the doublet state but much lower than the quartet state, while the latter is closer to the quartet state with three unpaired electrons.

Peng and co-workers have proposed that two-pyrazine-contain ligands (pzpz) provide a stronger ligand field than one-pyrazine-contain (tpz), leading to shorter Co-N bond lengths and lower magnetic moment. In both cases two oxidations and reversible reduction processes were observed, but no structural data for the oxidised or reduced species has been reported.[177]

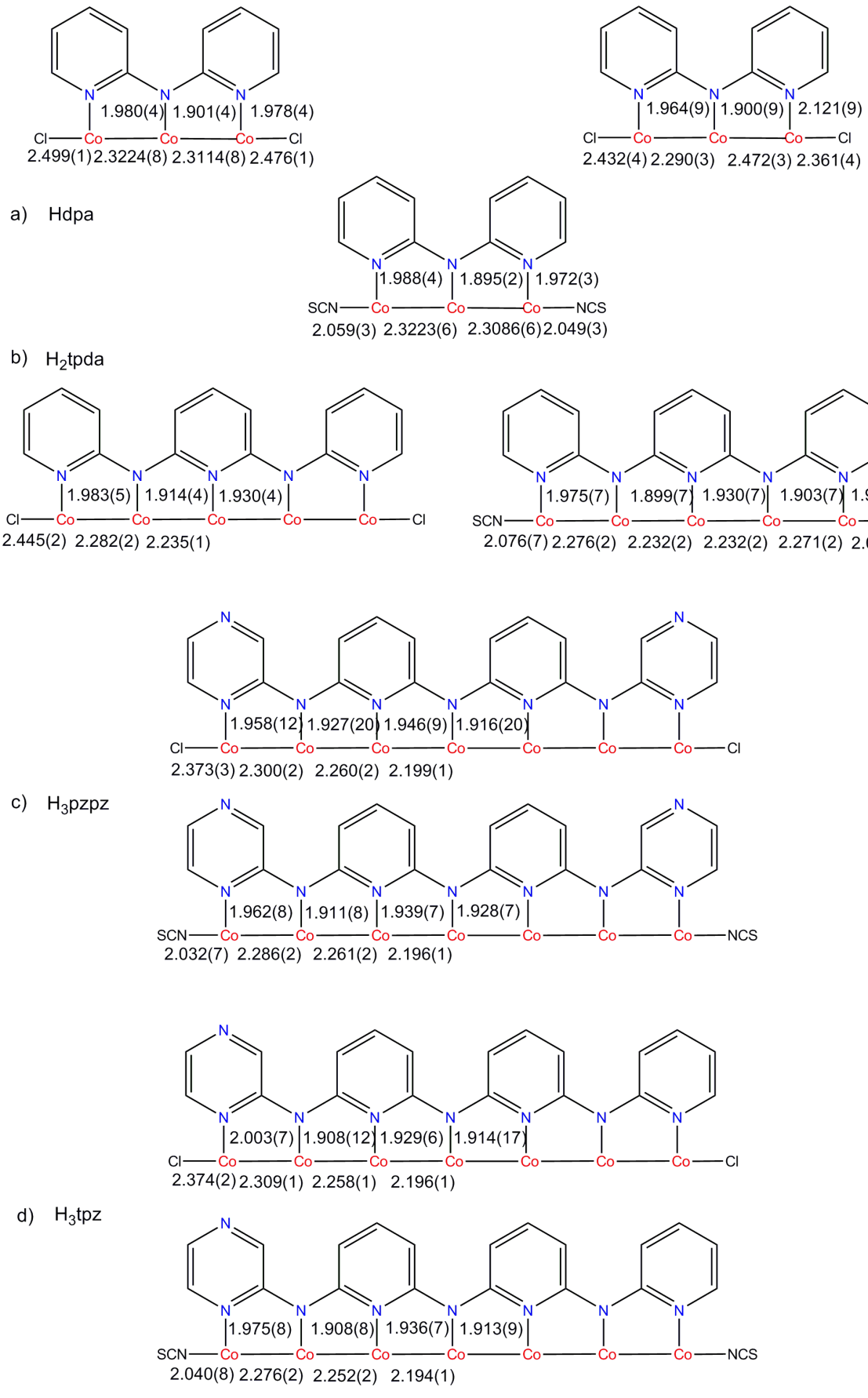

Figure 6-4: Comparison of bond distances in: a) tricobal, b) pentacobalt and c),d) heptacobalt EMACs.

The structural data offers a marked contrast to the tricobalt chains described in Chapter 3. There is no evidence for the striking symmetric – unsymmetric transitions that are characteristic of the shorter chains, and all Co-Co and Co-N bond lengths lie within a rather narrow range. Despite the structural similarities, there is clear evidence for spin-state equilibria, with magnetic moments well above those expected for a doublet ground state. In the tricobalt chains localised high-spin/low-spin transitions were found to be the origin of the structural complexity. It is not clear, a priori, why the same changes in multiplicity in the longer chains are apparently not associated with structural changes of the same sort.

6.3 Electronic structure – qualitative overview

The initial reports of structural and magnetic properties of the penta- and hepta-cobalt chains were accompanied by extended Hückel calculations aimed at interpreting the data.[168] Schematic molecular orbital diagrams based on these reported calculations and qualitative models presented in this thesis are collected in Figure 6-5, where the corresponding data for thricobalt are also included for comparison. In all cases the basic structure of the MO array is similar: for an n-cobalt array (n is equal to the number of metal atoms) the lower region contains n linear combinations of π symmetry and n linear combinations of δ symmetry. At much higher energy lies a band of n linear combinations of Co-N$\sigma*$ antibonding orbitals. Dispersed throughout the array are n combinations of the d_z^2 orbitals on the individual centres, ranging from a strongly bonding combination at low energy to a

strongly antibonding combination in a similar region to the Co-N$\sigma*$ antibonding orbitals. In between these limits, orbitals of σ symmetry increase in energy as the number of nodes increases, and those with little net Co-Co bonding character are found near the top of the occupied π/δ band. In the tricobalt chain the Co-Co non-bonding orbital with a node at the central cobalt is the SOMO and it also proved to be the dominant electron transport channel. In the pentacobalt case, the qualitative analyse and extended Hückel calculations proposed that the SOMO is the third of the combinations of σ symmetry, again with a node at the central cobalt, precisely analogous to the tricobalt chain. In the heptacobalt analogue, in contrast, the SOMO is an orbital of δ symmetry, the corresponding σ_4 orbital (the fourth of the seven in the σ manifold) is now doubly occupied. Calculations based on one-electron approximation and the qualitative pictures of the orbital array discussed until now do not explicitly incorporate the electron-electron repulsions that are critical to spin-state equilibrium. To include to some extend the electron-electron interaction we used a density functional theory. In both the pentacobalt and heptacobalt cases we have allowed the electronic configuration (and geometry) to optimise freely without constraint, and then used the initial converged configuration as a basis for generating alternative single-determinant states, either of doublet or quartet symmetry. More information about the computational details and the results of the DFT calculations can be found in the next couple of sections.

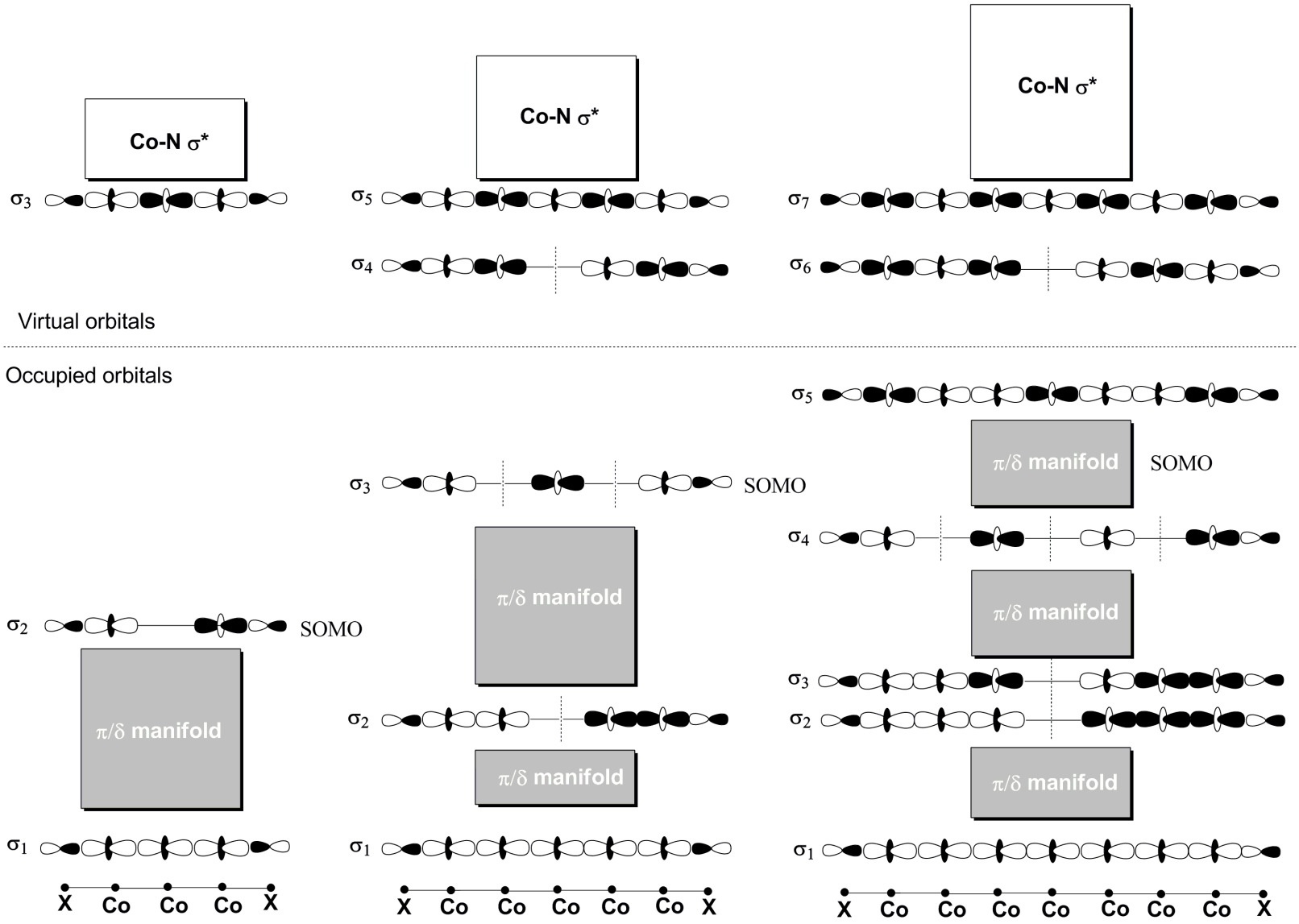

Figure 6-5: Schematic molecular orbital diagrams for tricobalt, pentacobalt and heptacobalt EMACs where X is an axial ligand.

6.4 Results and discussion

6.4.1 Electronic structure of $Co_5(tpda)_4(SCN)_2$

According to the crystallographic data, the pentacobalt chain is symmetric and the ground state is a doublet.[9] We have optimised geometries of more than ten different doublet spin states with the D_4 symmetry, all of which can be generated by permuting orbitals around HOMO – LUMO region. The configurations, optimised structural parameters, Mulliken populations, spin densities and relative energies of the four most stable electronic configurations are summarised in Table 6-1 and Figure 6-6. Of all possible doublets configurations, the ^2E proves to be the most stable. A full molecular orbital diagram for this state is presented in Figure 6-7.

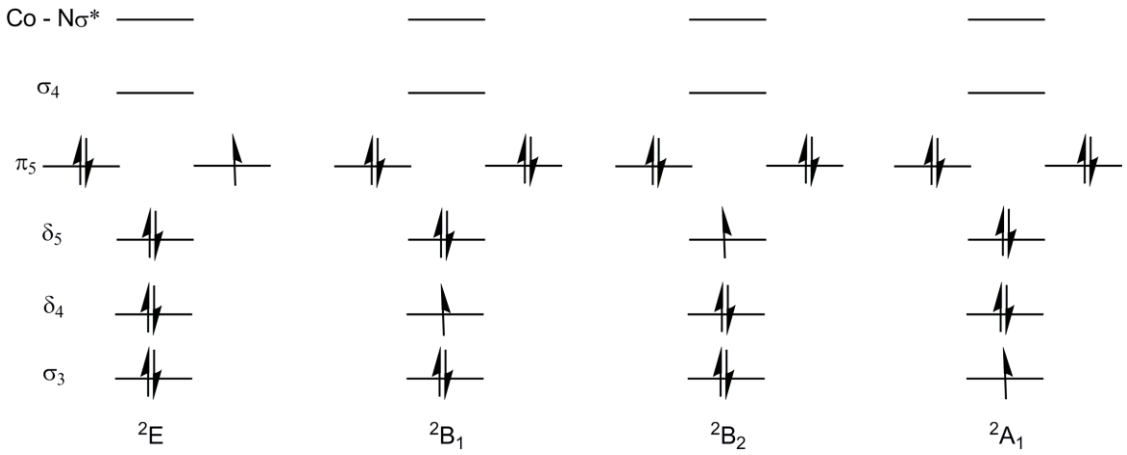

Figure 6-6: Configurations of doublet states discussed in the text.

Electronic State	Experiment	Theory			
		^2E	$^2B_1$	$^2B_2$	$^2A_1$
Assigned occupations		a_1: 31//31 a_2: 29//29 b_1: 27//27 b_2: 27//27 e: 116//115	a_1: 31//31 a_2: 29//29 b_1: 27//26 b_2: 27//27 e: 116//116	a_1: 31//31 a_2: 29//29 b_1: 27//27 b_2: 27//26 e: 116//116	a_1: 31//31 a_2: 29//28 b_1: 27//27 b_2: 27//27 e: 116//116
Bond lengths/ Å					
SCN – Co_1	2.076(7)	2.0214	2.0386	2.0322	1.9983
SCN – Co_2	2.071(8)	2.0214	2.0386	2.0322	1.9983
Co_1 – Co_2	2.276(2)	2.2664	2.2828	2.2747	2.2843
Co_2 – Co_3	2.232(2)	2.2453	2.2582	2.2595	2.2481
Co_3 – Co_4	2.232(2)	2.2453	2.2582	2.2595	2.2481
Co_4 – Co_5	2.271(2)	2.2664	2.2828	2.2746	2.2843
Co_1 – N	1.975(7)	1.9996	1.9943	1.9944	1.9988
Co_2 – N	1.899(7)	1.9374	1.9276	1.9276	1.9347
Co_3 – N	1.930(7)	1.9511	1.9387	1.9361	1.9484
Co_4 – N	1.903(7)	1.9374	1.9276	1.9276	1.9347
Co_5 – N	1.970(8)	1.9994	1.9943	1.9943	1.9988
Spin Density					
Co_1 and Co_5		0.06	0.00	-0.01	0.27
Co_2 and Co_4		0.26	0.25	0.24	-0.09
Co_3		0.33	0.00	0.20	0.26
Mulliken Populations					
Co_1 and Co_5		0.22	0.21	0.20	0.21
Co_2 and Co_4		0.71	0.71	0.69	0.71
Co_3		0.30	0.30	0.29	0.30
Δ Energy /eV		***0.00***	***0.15***	***0.13***	***0.48***

Table 6-1: Optimized structural parameters and spin densities for the $Co_5(tpda)_4SCN_2$ chain. Different electronic states are labelled according to the D_4 point group.

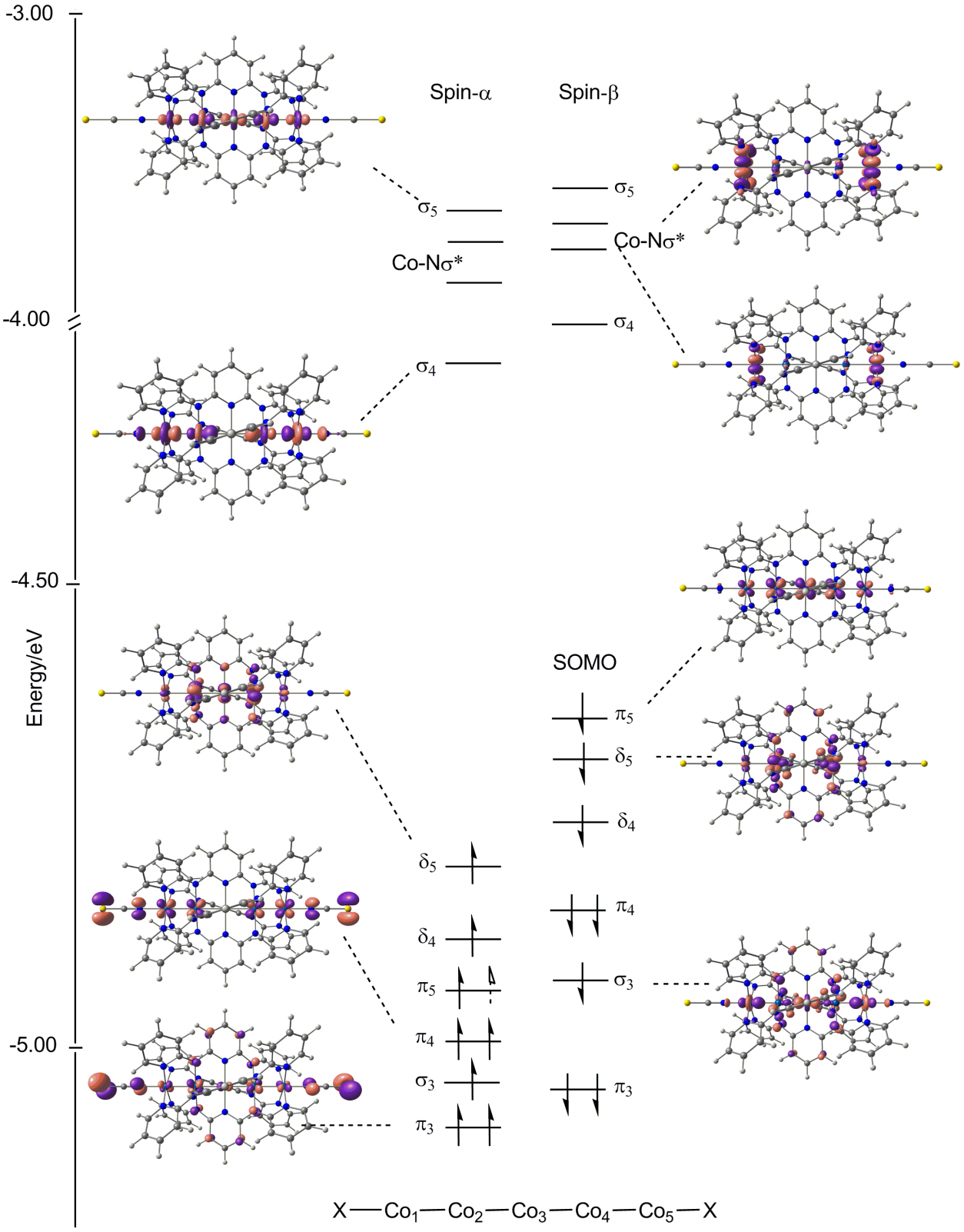

Figure 6-7: Molecular orbital diagram for the ^{2}E state of the $Co_5(tpda)_4(SCN)_2$molecule – the dashed arrow represents the unpaired electron.

The unpaired electron in ^{2}E doublet, marked with dashed arrow in Figure 6-7, occupies an orbital with local π symmetry made up of linear combinations of the d_{yz} metal atomic orbitals (π_5). The net spin densities in Table 6-1 reflect the localisation of this orbital, with ~0.3 spin-α electrons on each of Co_2, Co_3 and Co_4. Marginally lower in energy are two linear combinations of orbitals of δ symmetry, δ_5 and δ_4, localised on Co_2 and Co_4, the π-donor amide ligands displacing them upwards relative to those on Co_1, Co_3 and Co_5. Approximately 0.5 eV lower down in the orbital manifold are the spin-α and spin-β components of the approximately Co-Co-Co non-bonding σ_3, the orbital proposed to be the SOMO based on the extended Hückel calculations and our qualitative model. In the vacant manifold, the LUMO, σ_4, lies approximately 0.5 eV higher in energy, followed by two linear combinations of terminal Co-Nσ* antibonding orbitals and then the entirely Co-Co σ* and σ_5.

The very densely packed energetic window around the SOMO means that a number of alternative configurations are likely to be relatively stable (Figure 6-6). Amongst these, $^2B_1$ and $^2B_2$ states arising from the promotion of electrons from the orbitals of local δ symmetry (δ_5 and δ_4) lie only 0.15 eV higher in energy (Table 6-1). The $Co_{2/4}$-N amide nonbonding character of these orbitals results in a marginal decrease in these bond lengths, but the metal chain is otherwise remarkably invariant. The net spin densities in these states again reflect the localisation of the orbital, with major density being transferred to Co_2 and Co_4. The $^2A_1$ state corresponding to the configuration proposed on the basis of extended Hückel theory lies almost 0.5 eV above the ^{2}E ground state. The depopulation of the σ_3 orbital, with its significant Co-NCS σ* character, results in a contraction of ~0.03 Å in the Co-NCS bonds but the structure is otherwise only affected to a small extent. The net spin densities in the $^2A_1$ are now

localised almost entirely on the terminal and central cobalt centres, Co_1, Co_3 and Co_5, reflecting the non-bonding nature of this orbital.

In the tricobalt chain, we found that a transition from doublet to quartet multiplicity induced a distinct asymmetry in the chain, with two equivalent Co-Co distances and strongly elongated Co-N bonds at one centre. In simple terms, this can be understood in terms of population of a terminal Co-Nσ*, rather than a Co-Co-Co σ*, orbital. The negligible overlap between the Co-Nσ* orbitals (δ with respect to the metal-metal axis) on the opposite centres then favours symmetry breaking. We have generated a number of quartet states arising from transfer of a single electron from one of π_5, δ_5 or σ_3 spin β into the low-lying spin-α LUMO shown in Figure 6-6. However, even starting from strongly distorted starting geometries, we have been unable to locate any unsymmetric minima: the structure always reverts to a symmetric structure with no elongation of the Co-N bonds. A significant lengthening of the Co_1-Co_2 and Co_4-Co_5 bonds is observed due to the population of the σ_4 LUMO which is antibonding with respect to these contacts. The lowest-lying quartet state lies 0.37 eV above the ^2E ground state, suggesting that thermal population is unlikely.

In terms of agreement with the experimental data, the very similar structural parameters in each of the electronic states mean that it is difficult to reach a definitive conclusion regarding the ground state. All four states have a five cobalt core in reasonable agreement with experiment, with terminal Co-Co bonds longer than the inner ones. The rather short optimised Co-NCS bond lengths in the $^2A_1$ state (0.08 Å shorter than found experimentally) suggest that the non-bonding σ_3 is doubly occupied in the ground state.

6.4.2 Electronic structure of $Co_7(pzpz)_4(SCN)_2$

Based on the experimental observation of a symmetric structure, we have again based our initial studies of the ground state on D_4 symmetry. Structural parameters for lowest energy structures with doublet and quartet multiplicity are collected in Figure 6-8 and Table 6-2, and an MO diagram for the most stable, $^4A_1$, is presented in Figure 6-9.

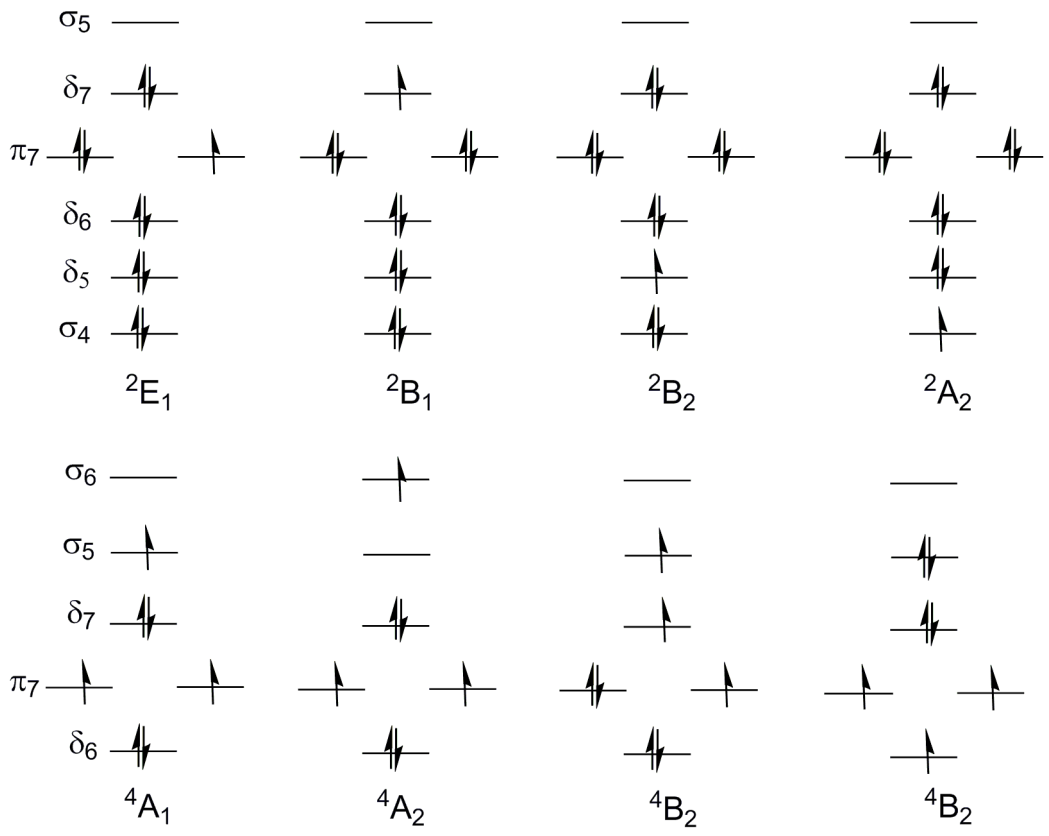

Figure 6-8: The most stable doublet and quartet configurations for the $Co_7(pzpz)_4(SCN)_2$ discussed in the text.

Electronic State	Experiment	Theory					
		^2E	$^2B_1$	$^2B_2$	$^2A_2$	$^4A_1$	$^4B_1$
Assigned occupations		a_1:46//46 a_2:46//46 b_1:37//37 b_2:36//36 e: 168//167	a_1:46//46 a_2:46//46 b_1:37//36 b_2:36//36 e: 168//168	a_1:46//46 a_2:46//46 b_1:37//37 b_2:36//35 e: 168//168	a_1:46//46 a_2:46//45 b_1:37//37 b_2:36//36 e: 168//168	a_1:47//46 a_2:46//46 b_1:37//37 b_2:36//36 e: 168//166	a_1:47//47 a_2:46//46 b_1:37//36 b_2:36//36 e: 168//166
Bond lengths/ Å							
SCN – Co_1	2.032(7)	1.949	1.961	1.960	1.952	1.981	2.028
Co_1 – Co_2	2.286(2)	2.269	2.271	2.275	2.275	2.283	2.294
Co_2 – Co_3	2.261(2)	2.257	2.269	2.268	2.262	2.241	2.236
Co_3 – Co_4	2.196(1)	2.201	2.222	2.214	2.218	2.204	2.217
Co_1 – N	1.962(8)	1.969	1.966	1.964	1.968	1.970	1.965
Co_2 – N	1.911(8)	1.910	1.907	1.902	1.909	1.914	1.915
Co_3 – N	1.939(7)	1.929	1.919	1.920	1.923	1.935	1.933
Co_4 – N	1.928(7)	1.924	1.912	1.920	1.918	1.927	1.923
Spin Density							
Co_1 and Co_7		0.01	0.01	0.02	0.09	0.40	0.04
Co_2 and Co_6		0.15	0.10	0.14	0.03	0.22	0.36
Co_3 and Co_5		0.21	0.00	0.23	0.09	0.47	0.46
Co_4		0.27	0.27	0.26	0.05	0.78	0.76
Mulliken Populations							
Co_1 and Co_7		0.47	0.47	0.47	0.47	0.46	0.44
Co_2 and Co_6		0.90	0.90	0.89	0.88	0.90	0.89
Co_3 and Co_5		0.49	0.48	0.50	0.49	0.49	0.49
Co_4		0.85	0.84	0.86	0.83	0.86	0.87
Energy/eV		***0.00***	***0.06***	***0.17***	***0.54***	***-0.11***	***0.29***

Table 6-2: Optimized structural parameters and Mulliken spin populations for the $Co_7(\mu_7\text{-pzpz})_4(SCN)_2$ chain. Different electronic states are labelled according to the D_4 point group.

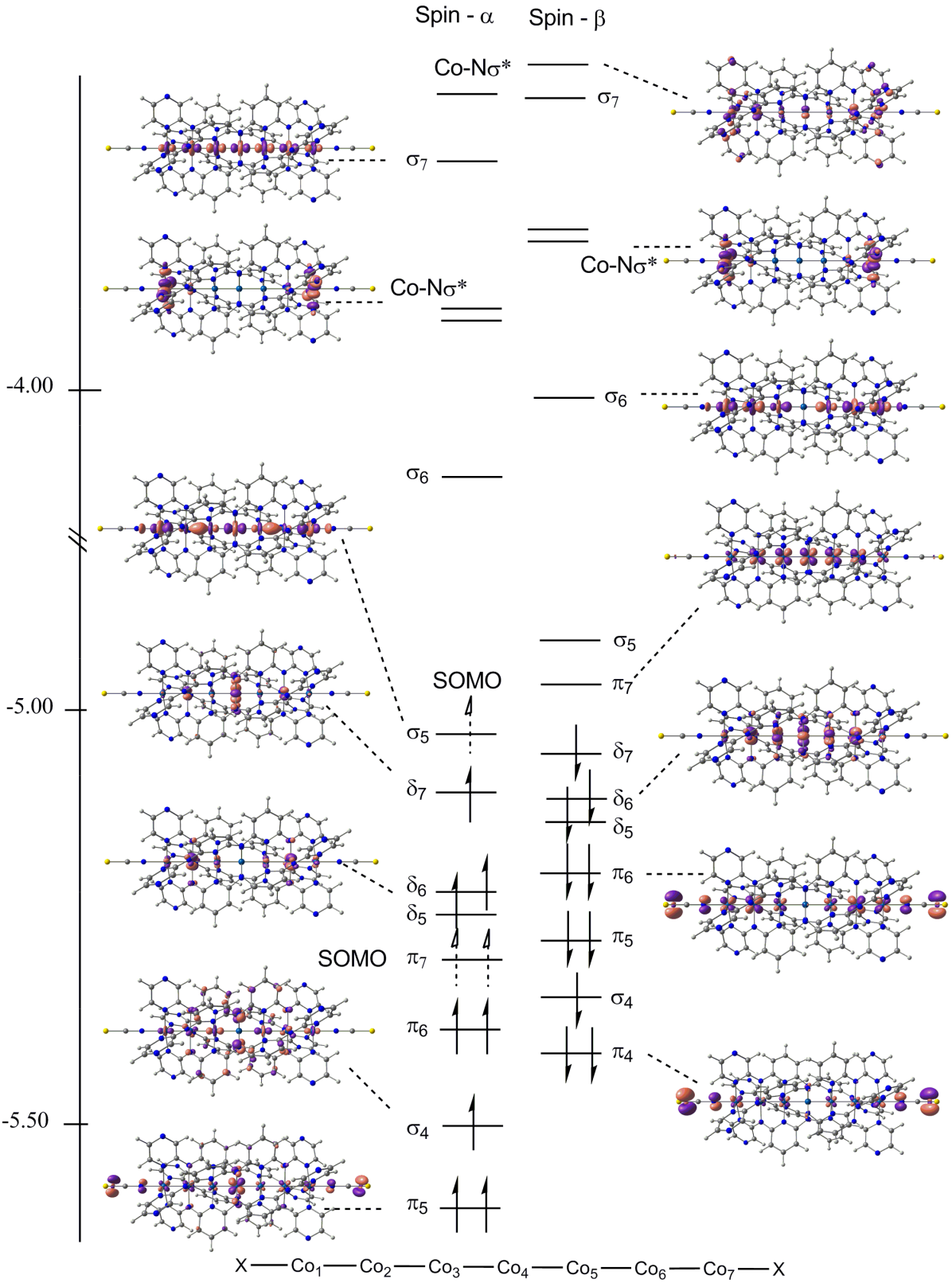

Figure 6-9: Molecular orbital diagram for the $^4A_1$ state of $Co_7(pzpz)_4(SCN)_2$ where the three dashed arrows correspond to the unpaired electrons.

According to data in Table 6-2, the structure with the lowest energy is a quartet with $^4A_1$ symmetry. This quartet arises from the promotion of an electron from π_7 β set to σ_5 α set which is in fact 0.11 eV more stable than the most stable doublet ^2E state. Another quartet, $^4A_2$, arising from δ_7 β –> σ_5 α levels, has energy around 0.40 eV above the $^4A_1$. The transition from ^2E to $^4A_1$ states causes only small change to the Co-Co bond distances but it is does elongate the Co-NCS by ~0.05 Å. A comparison with crystallographic data shows that all the doublet states have Co-NCS distances approximately 0.04 Å shorter than those observed experimentally, the values in the quartet states are in excellent agreement with experiment. Thus, the comparison between experiment and theory suggests that it is a quartet where the σ_5 orbital is singly occupied.

Two doublets, $^2B_1$ and $^2B_2$, have energies slightly higher if compared to ^2E state. In both cases the configuration is obtained by promotion of electron from Co-Co δ to level π_7 β set orbital (Figure 6-8). The structural changes associated with these promotions are marginal, a contraction of ~0.01 Å in the Co_3-N bond being the only significant feature. Mulliken charges are almost with constant value in all doublet and quartet configurations (Table 6-2).

The most significant difference between the molecular orbital diagrams for the heptacobalt (Figure 6-7) and hexacobalt (Figure 6-9) cases is found in the region just above the SOMO. In the five cobalt chain, the next available vacant orbital, σ_4, lies ~0.7 eV above the SOMO whereas in the doublet state of the seven cobalt molecule the σ_5 orbital lies only 0.1 eV higher than δ_7. Due to this small HOMO – LUMO gap the doublet-quartet equilibrium is highly likely. We have again attempted to localise

unsymmetric quartet states, but all such starting geometries reverted to the symmetric forms shown in Table 6-2.

6.4.3 Summary of the electronic structure

The results of our computations on the pentacobalt and heptacobalt chains are fully consistent with experiment; in so much as they predict a switch in ground state multiplicity from doublet (pentacobalt) to quartet (heptacobalt), as indicated by the available magnetic data. The optimised structural parameters are also in good agreement with the crystallographic data, although the key Co-Co bond lengths prove to be rather insensitive to the precise configuration, making a definitive assignment of ground state difficult. The most compelling structural information is found in the terminal Co-NCS bond lengths, which are very sensitive to the population of the manifold.

As the length of the chain is increased, we note two related trends in structure and stability of the electronic states. First, the doublet-quartet separation decreases in the order tricobalt < pentacobalt < heptacobalt, to the extent that the quartet is the ground state for the longest chain. Second, the quartet in the tricobalt case is distinctly unsymmetric, while in both pentacobalt and heptacobalt cases it remains symmetric. The origin of this trend, summarised in Figure 6-10, can be traced to the nodal characteristics of the σ manifold and the emergence of a one-dimensional band structure as the chain length increases. In each case the central orbital in the σ manifold (i.e., the second, third and fourth in the three, five and seven cobalt chain)

lies at or just below the top of the occupied π/δ band. In the tricobalt case, the next available vacant $\sigma*$ orbital is completely antibonding, and it lies in the band of Co-N $\sigma*$ (pyridyl) antibonding orbitals. In the five cobalt chain the corresponding orbital, σ_4, the fourth of five, has only one node and two bonding interactions, and it is therefore rather less strongly antibonding. Finally, in the heptacobalt chain, in doublet case, the first vacant orbital of σ symmetry is the fifth of seven σ_5, and the sixth of seven σ_6 in quartet structure. The net effect is that in the longer chains one or more orbitals of σ symmetry are present in the window between the occupied (π, δ, σ) manifold and the array of Co-Nσ* antibonding orbitals at higher energy. The quartet state is therefore stabilised and its population involves occupation of an orbital of σ, rather than δ (and more importantly Co-N(pyr)σ*) symmetry. The significance of this latter point is that it is the weak overlap between these Co-N(pyr)σ* orbitals that triggers the low-symmetry distortions observed in the tricobalt chain. In the cobalt chain with more than three metal atoms, the unsymmetric structure is not possible to achieve.

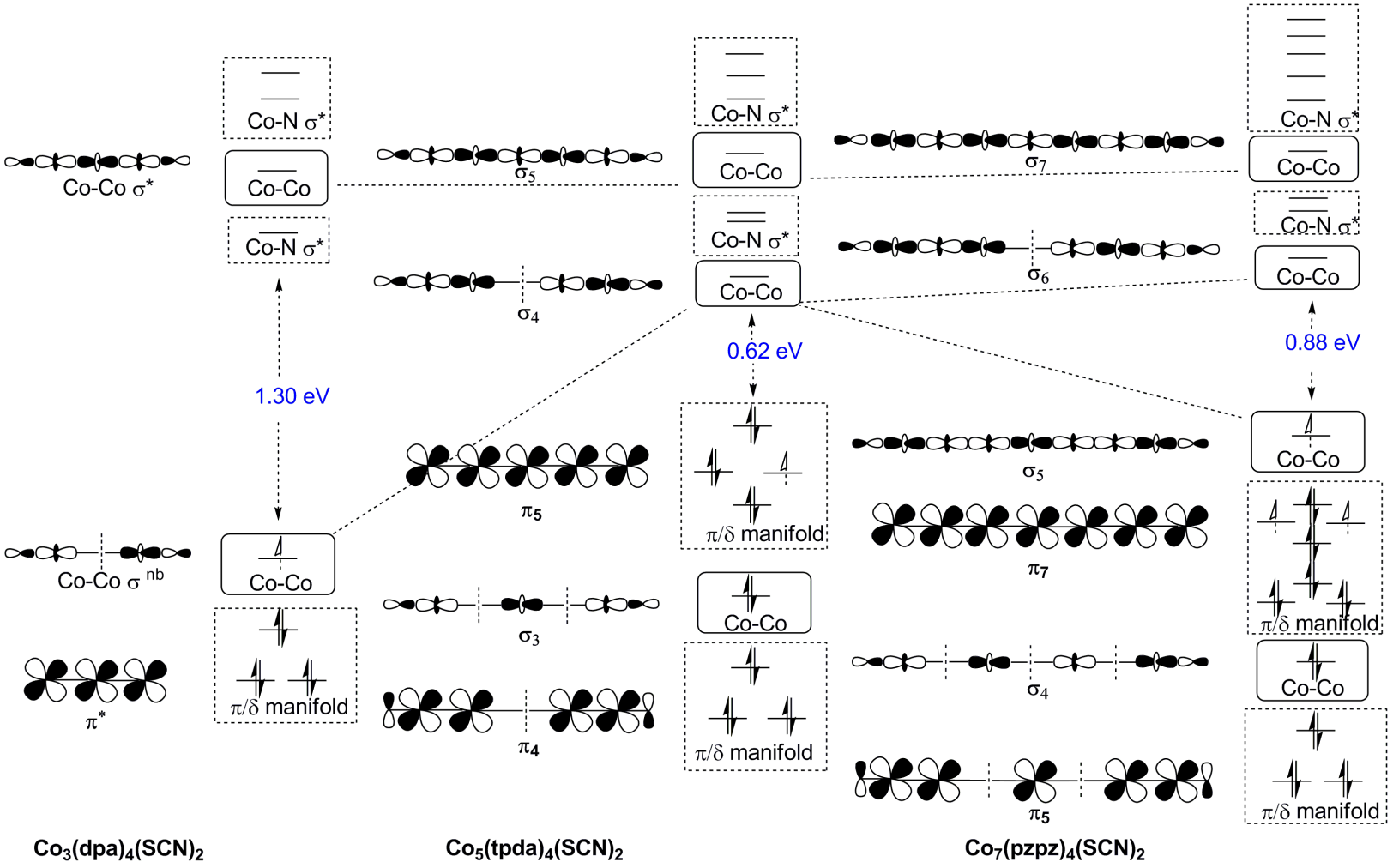

Figure 6-10: Schematic molecular orbital diagrams of $Co_3(tpa)_4(SCN)_2$,$Co_5(tpda)_4(SCN)_2$ and $Co_7(pzpz)_4(SCN)_2$: the unpaired electrons are represented with dashed arrows.

6.4.4 Electron transport properties

In the following sections we explore how the basic features of the electronic structure of the pentacobalt and heptacobalt outlined above are expressed in the computed electron transport properties. The tricobalt chain discussed in Chapter 3 provides a convenient point of reference. Based on these calculations we hope to reveal the connection between the electron transport properties and the electronic structure in cobalt based EMAC.

In order to explore the electron transport properties of these structures we placed them between two gold electrodes (Figure 6-11).

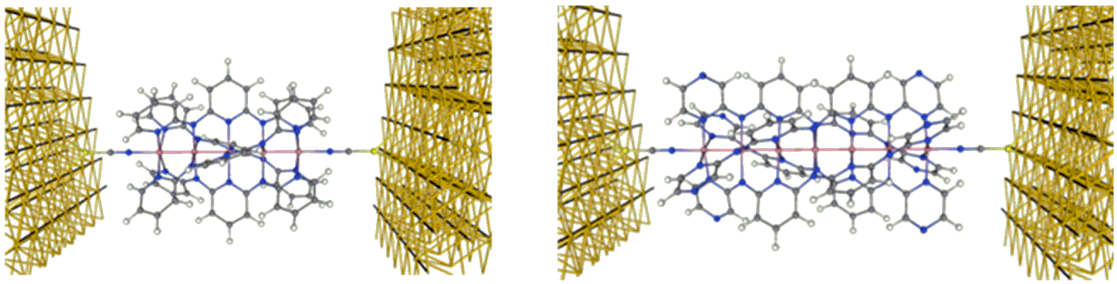

Figure 6-11: Structure of a $Co_5(tpda)_4(NCS)_2$ on the left and a $Co_7(pzpz)_4(NCS)_2$ on the right in a two-probe configuration between (111) faces of two semi-infinite gold electrodes.

6.4.5 Computational methodology

All calculations were performed with ATK2008.10 software where all atoms were treated with double-ζ basis set, extended with single polarization function and GGA.PBE functional was used. The electronic structure of the two-probe systems at

equilibrium was converged using a 100 Ry mesh cut-off, finite temperature of 300K at the electrodes, and the real space density constrain at the electrodes. The scattering region contained the EMAC sandwiched between 6 x 6 layer of the Au (111) surface of the source and the drain, respectively, with the sulphur atoms of the two NCS^- ligands located in the hollow site with Au-S distance 2.52 Å. Initial spin polarisation was performed and all molecules were symmetric if compared with the previous sections, the electrodes were bigger and the mesh cut-off was smaller. The reasons for these changes are explained in the following paragraphs.

The structure of the tpda and pzpz ligands in the longer cobalt chains has forced us to revise the computational approach applied in the previous chapters. Specifically, we have used the entire oligo-polypyridyl ligand in the model, rather than the simplified version discussed in Chapter 3. The reason for this change is summarised in Figure 6-12, where the effect of cutting the oligo-polypyridyl ligands is shown.

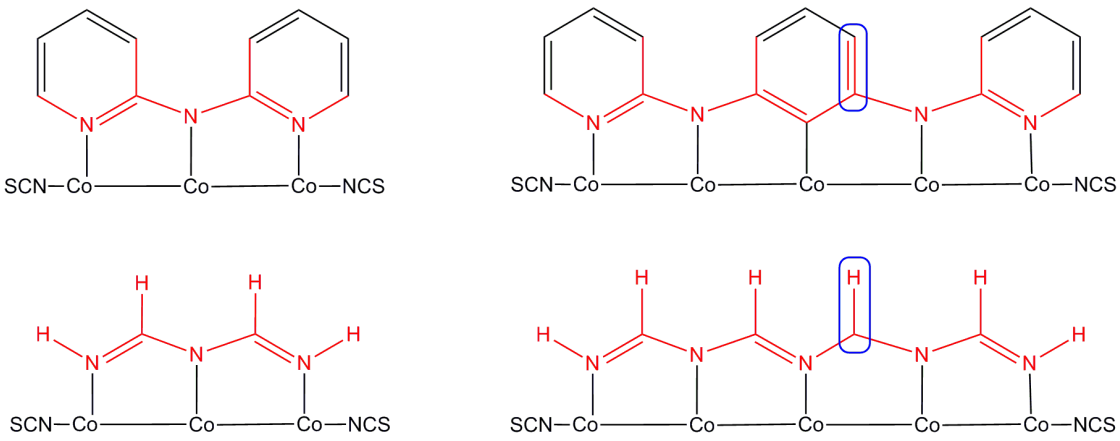

Figure 6-12: Comparison of model and real structure of tricobalt and pentacobalt chains.

In the tridentate ligand dpa the simplification of the ligand involves cutting the system only across C-C single bonds, and the dangling valence can therefore be effectively

capped with a single hydrogen. In the longer chains, however, cutting across a double bond of the central polypyridyl ring is inevitable, and capping with a divalent atom (such as O) would be necessary to saturate the ligand. This in turn would reduce the symmetry of the molecule, and test calculations suggest that such protocols result in a very strong perturbation to the electronic structure. Thus, we chose to perform all calculations in this chapter using the full ligand. The greater extent of the molecular scattering region in the x and y directions (i.e., orthogonal to the transport axis) means that a 6 x 6 array of gold atoms (rather than 4 x 4 as used above) was necessary to avoid Coulomb interaction with molecules in neighbouring unit cells. The dramatic expansion of the central region and the electrodes required some compromises in other aspects of the calculation, most notably a decrease of the mesh cut-off from 350 to 100 Ry. The mesh cut-off is a parameter which defines the density of the real space grid in order to solve the Poisson equation. From the practical point of view, the mesh cut-off is strongly correlated with the memory (denser mesh requires more memory). With increasing the size of the electrodes from 4 x 4 to 6 x 6, the mesh cut-off was decreased in order to perform the calculations. A further change involved changing the constraints applied to the electrodes. Within the ATK algorithm, it is possible to match the scattering region and electrodes by matching either the density matrix, the Hamiltonian or the real-space density. In the limit of an infinite number of electrode layers in the scattering region, these approaches should be convergent but in practice, where we have only five such layers (three on one side, two on the other), the choice makes a substantial difference to the performance of the calculations.

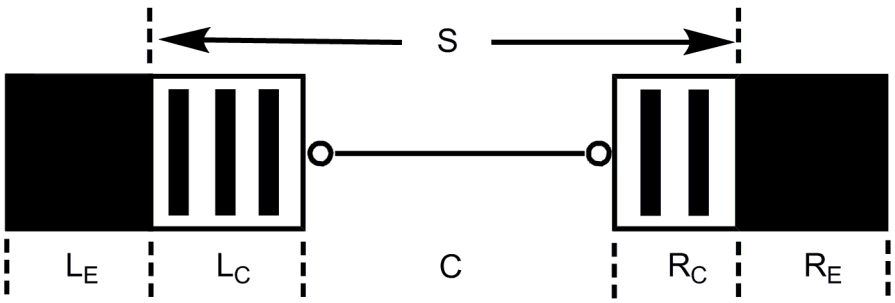

Figure 6-13: Schematic diagram of the two-probe calculations used in this work; L_E – left bulk electrode, R_E – right bulk electrode, L_C – left electrode layers in the central region, R_C – right electrode layers in the central region, C – central region, S – scattering region.

In previous chapters we have applied the 'DensityMatrix' constraint which constrains the density matrix in electrode layers inside of the central region (L_C and R_C in Figure 6-13) to bulk electrode values (L_E and R_E in Figure 6-13). It is correct in the limit of infinitely many screening layers, the electron density is continuous and it generally provides an accurate picture of the voltage drop. However sometimes it can lead to significant convergence problems. The 'real-space density' constraint, in contrast, matches the real-space density in L_C and R_C in Figure 6-13 to the bulk density (L_E and R_E in Figure 6-13). Again, it is correct in the limit of infinitely many screening layers, but if they are not sufficient, the density becomes discontinuous. This discontinuity gives bad description of the voltage when the bias is applied. However, convergence proves to be faster using this constraint, although the resultant voltage drop is less reliable. In the present case, convergence using the density matrix constraint proved impossible to achieve, and we therefore adopted the alternative real space density. All other computational parameters, along with the structure of the gold-molecule contact, were as employed in the previous chapters. The changes in protocol (change in mesh cut-off, change in electrode constraint) will necessarily have an impact on the calculation, and in particular on the position of the Fermi level of the electrodes

relative to the molecular levels. Thus, the results on the pentacobalt and heptacobalt metal chains are not exactly comparable to those presented in Chapter 3 for the tricobalt molecule. Hence, in the initial section of this chapter we present a comparison of the transmission spectra of the tricobalt chains using the different protocols to establish the sensitivity of the results.

6.4.6 Impact of computational protocol on the transport properties of the tricobalt extended metal atom chain

In Chapter 3 we explored in detail the link between the transmission spectrum of the tricobalt EMAC (calculated using the simplified ligand, density matrix constraint and 350 Ry cut-off) and its underlying gas-phase electronic structure. In Figure 6-14 we compare this spectrum with corresponding spectra for (i) the simplified molecule with the same density matrix constraint and a 100 Ry cut-off (Figure 6-14 b), (ii) the simplified molecule with real-space density constraint and a 100 Ry cut-off (Figure 6-14 c) and (iii) the full molecule with the real-space density constraint and a 100 Ry cut-off (Figure 6-14 d). A comparison of Figure 6-14 a) and b) shows that the reduction in mesh cut-off from 350Ry to 100Ry has almost no impact on the transmission spectrum. All peaks and corresponding molecular orbitals are with the same energy and transmission coefficient as before. The only minor difference is destabilisation of σ_{α}^{nb} with around 0.2 eV. Comparing Figure 6-14 b and Figure 6-14 c, in contrast, shows that changing the electrode constraint from density matrix (DM) to a real-space density constraint (RSD) has a significant impact. Specifically, the Fermi level is shifted upwards marginally, with the result that the spin-β component of the σ_{β}^{nb} orbital

becomes partially occupied. This in turn reduces the spin polarisation, reducing the gap between spin-α and spin-β components, and further stabilising the spin-β component of the σ_{β}^{nb} orbital. Due to this process the π^* levels have lower energies and the corresponding peak is placed below the spin-α and spin-β components of the σ_{β}^{nb} orbital. All other peaks remain with almost the same intensity and shape, shifting marginally downward to lower energy. The last step is to compare the model structure with the real molecule when the mesh cut-off is 100Ry and RSD constrained is applied (Figure 6-14 d). Some major changes are observed. First, the spin-β component of the σ_{β}^{nb} is almost on the top of the Fermi level. Second, two peaks corresponding to π^* molecule orbital which is similar to trend observed in Figure 6-14 a) and b) are placed between the spin-β and spin-α component of the σ^{nb}. However, in the model structure the π^* peak has energy around -0.50 eV and transmission coefficient almost equal to two, while in the Figure 6-14 d) case the same peak is divided into two peaks. Both peaks have transmission coefficient ~ 1, half of the corresponding peak in the model structures. This result indicates that the π^* levels are not degenerate. Additionally, the π^* levels are destabilised and they have higher energies if compared to before. The other two π levels , π^{nb} and π, have transmission coefficient around two and they are placed almost at the same energy as in the model structure. The only difference is that they are slightly less broad if compared to the model structures.

As a result, at equilibrium, the two spin components of the transmission spectrum are far more similar than those reported in Chapter 3, suggesting a reduced capacity for spin filtering. However, despite these subtle differences the basic features of the electron transport remain the same in both protocols. The dominant transport

channel is the spin-β (minority-spin) component of the σ_{β}^{nb} orbital, which lies very close to the Fermi level.

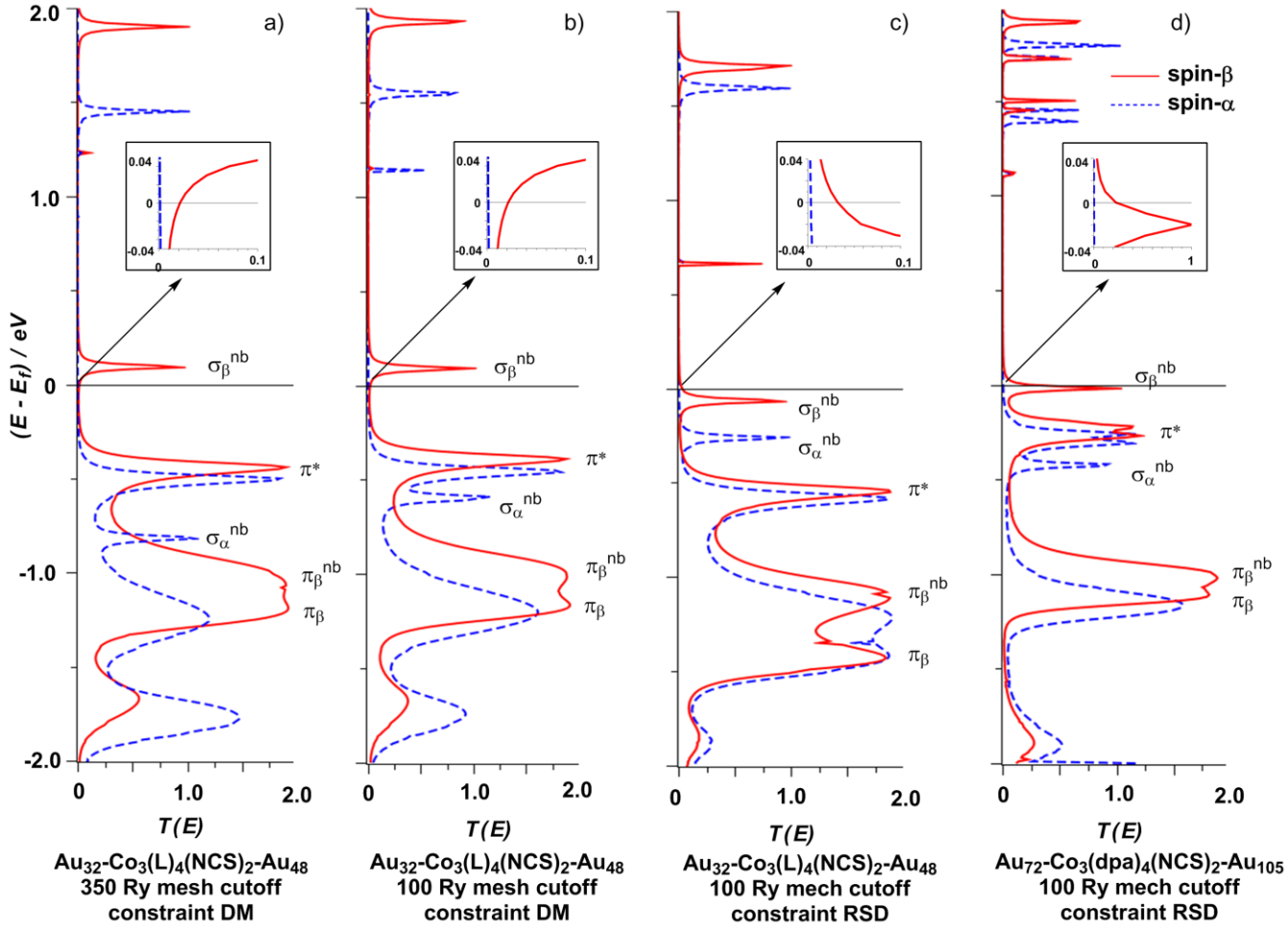

Figure 6-14: Transmission spectra of tricobalt structures placed between two electrodes: a) model structure with 350 Ry mesh cut-off with density matrix constraint, b) model structure with 100 Ry mesh cut-off with density matrix constraint, c) model structure with 100 Ry mesh cut-off with real space density constraint, d) full molecule with 100 Ry mesh cut-off and real space density constraint on the electrodes. DM – density matrix constraint; RSD – real space density constraint.

6.4.7 Pentacobalt and heptacobalt chains

Following the format established in Chapters 3-5, we first establish a link between the electronic structures of the molecule in the gas phase and between two gold electrodes, allowing us to gauge the extent to which the electrodes perturb the molecule. The Mulliken spin densities of tri-, penta- and heptacobalt molecules summarised in Table 6-3 suggest that this perturbation is not dramatic in any case. The small spin densities at the sulphur atoms in the gas phase are eliminated by bonding to the gold electrodes but otherwise the basic electronic structure described in the previous section remains the same. The transmission spectra for the tri-, penta- and heptacobalt chains are compared in Figure 6-17. The gas-phase electronic structure maps very well onto the transmission spectra in all three cases.

	$Co_3(dpa)_4(NCS)_2$		$Co_5(tpda)_4(NCS)_2$		$Co_7(teptra)_4(NCS)_2$	
	Isolated molecule $\rho_{\alpha-\beta}$	Two – probe system $\rho_{\alpha-\beta}$	Isolated molecule $\rho_{\alpha-\beta}$	Two – probe system $\rho_{\alpha-\beta}$	Isolated molecule $\rho_{\alpha-\beta}$	Two – probe system $\rho_{\alpha-\beta}$
Co_1	0.34	0.22	0.06	0.004	0.39	0.32
Co_2	0.07	0.05	0.29	0.005	0.27	0.15
Co_3	-	-	0.35	0.016	0.43	0.36
Co_4	-	-	-	-	0.79	0.68
N	0.00	0.00	0.00	0.00	0.04	0.00
C	0.00	0.01	0.00	0.01	0.01	0.01
S	0.08	0.00	0.06	0.00	0.14	0.05
G_α	-	0.18	-	0.04	-	0.01
G_β	-	7.19	-	0.05	-	6.31
G_{tot}	-	7.37	-	0.09	-	6.32

Table 6-3: Spin density (α-β) and conductance in μS for α (G_α), β (G_β) and total (G_{tot}) for $Co_3(dpa)_4(NCS)_2$ and $[Au_{72}]$-$Co_3(dpa)_4(NCS)_2$-$[Au_{108}]$,$Co_5(tpda)_4(NCS)_2$ and $[Au_{72}]$-$Co_5(tpda)_4(NCS)_2$-$[Au_{108}]$, $Co_7(teptra)_4(NCS)_2$ and $[Au_{72}]$-$Co_7(teptra)_4(NCS)_2$-$[Au_{108}]$.

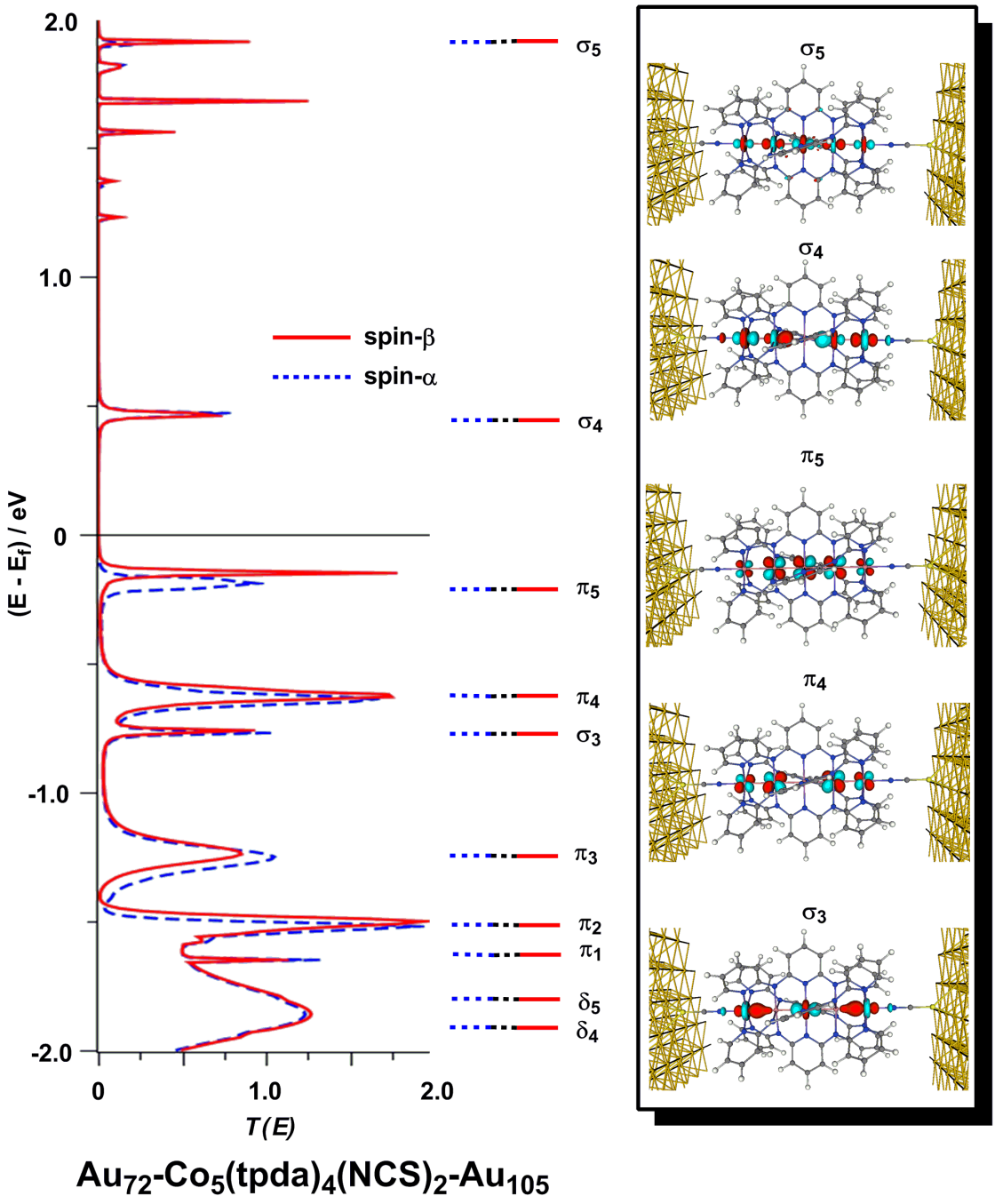

Figure 6-15: Pentacobalt transmission spectra.

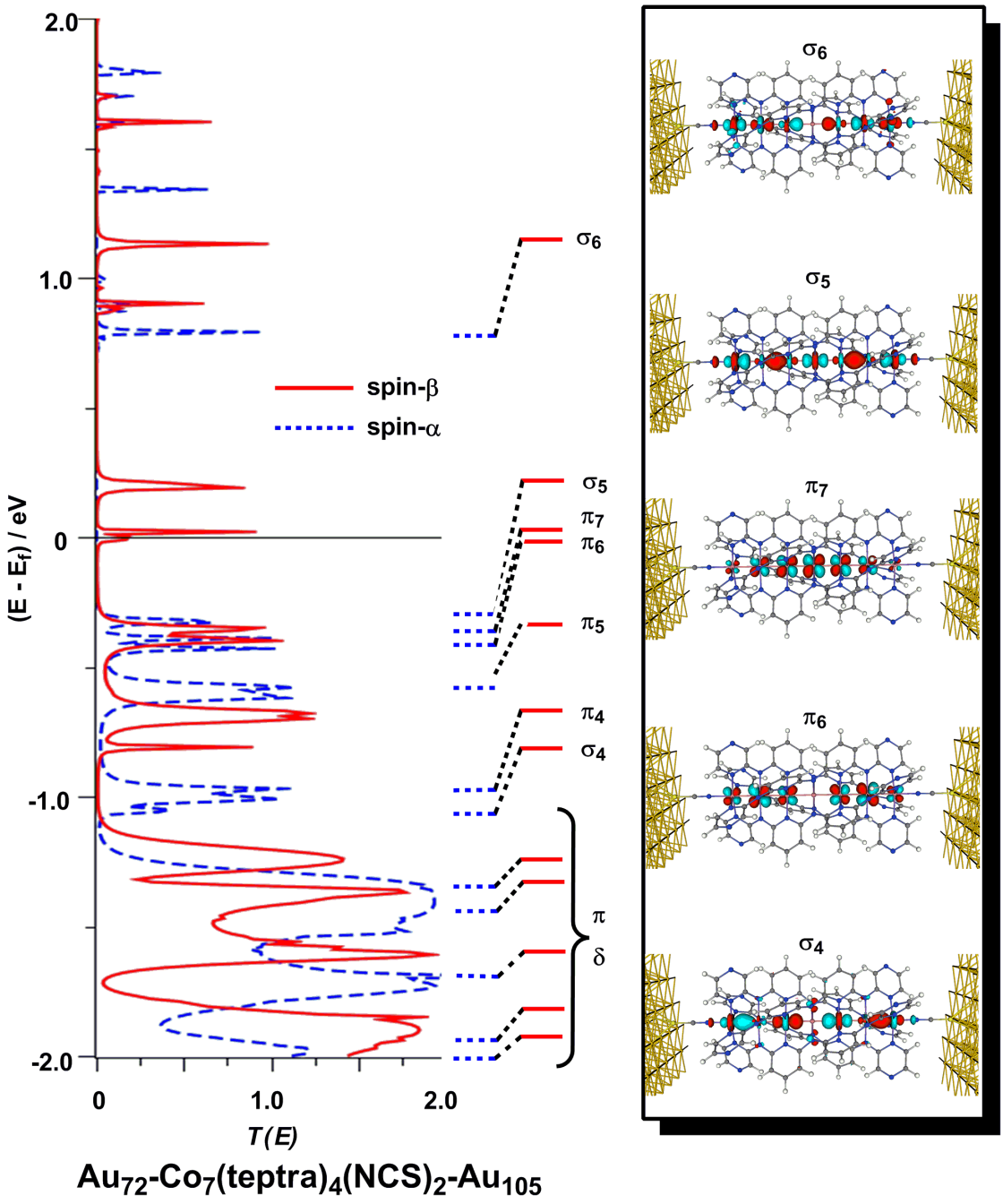

Figure 6-16: Heptacobalt transmission spectra.

Thus, in the pentacobalt chain the components of the σ manifold, σ_4 (two nodes) and σ_3 (three nodes), lie ~0.8 eV below and ~0.5 eV above the Fermi level, respectively (Figure 6-15). The π_5 orbital, which has a single vacancy in the gas phase (see Figure 6-7), lies ~0.3 eV below the Fermi level, indicating that binding to the gold electrode has resulted in effective one-electron reduction of the metal core. Consistent with this, the total Mulliken populations at the inner cobalt centers decrease by 0.1 ~ 0.2 electrons in the two-probe calculation (Table 6-3). We note in this context that the isolated pentacobalt chains are particularly susceptible to one-electron reduction, unlike either the three- or heptacobalt analogues.

Turning to the heptacobalt system, the large spin densities in the two-probe system indicate that the quartet multiplicity of the gas-phase ground state is not perturbed by the presence of the electrodes, leading to a substantial splitting of the spin-α and spin-β manifolds (Figure 6-16). The Fermi level is densely populated, with a number of spin-β orbitals that are vacant in the gas phase lying within <0.3 eV above E_f. The lowest of these, lying almost exactly on the Fermi level, are the π_7 and π_6 orbitals of Figure 6-17. Both have limited sulfur character, and so the corresponding peaks in the transmission spectrum are rather weak and narrow. 0.3 eV higher is a broader peak corresponding to σ_5 orbital. Therefore, we conclude that in the heptacobalt chain the spin-β component of the π^* orbital, rather than a member of the σ manifold, provides the dominant conduction pathway.

The value of the transmission coefficient at the Fermi level is directly proportional to the conductance, reported in Table 6-3. Extending the chain from three to five metal atoms results in a dramatic drop in the computed conductance, from 7.37 μS to 0.09 μS, simply because the dominant channel in the latter, the π_5 orbital, lies substantially

below the Fermi level. Moreover, the equalization of spin densities caused by bulk transfer of an electron from the gold electrode to the molecule results in negligible spin-filtering efficiency (0.04/0.05). Our computed values replicate the trend measured by Peng and co-workers, where the conductance of $Co_3(dpa)_4(NCS)_2$ (0.53 μS) is substantially greater than that of $Co_5(tpda)_4(NCS)_2$ (0.10 μS), although the computed attenuation factor is rather larger.[191] No data are available for the conductance of the heptacobalt chains, but our prediction is that it should rise again to a value comparable to the tricobalt chain, with a substantial spin-filtering efficiency.

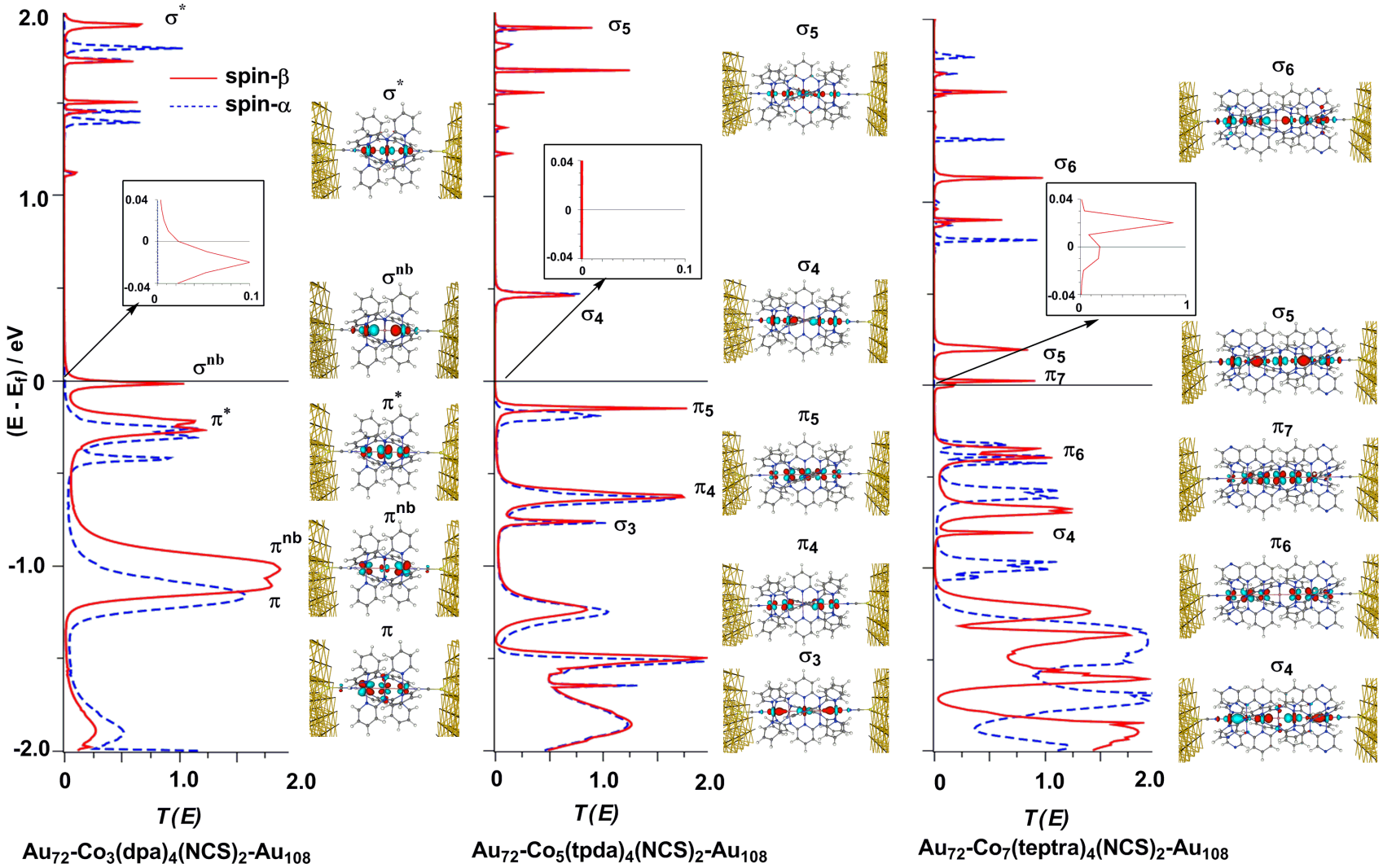

Figure 6-17: Comparison of transmission spectra in tri-, penta-, heptacobalt metal chains.

6.5 Conclusions

In summary, our calculations suggest that the evolution of the electron transport properties of the n-cobalt (n is number of metal atoms) chains is a complex one, with significant oscillations in conductance due to the developing one-dimensional band structure about the Fermi level. Thus, strong conductance is found when orbitals of either σ (threecobalt) or π (pentacobalt) symmetry are located near the Fermi level, while higher resistance is encountered when the Fermi level lies in a band gap. The strong non-linearity of the length dependence precludes the definition of a simple attenuation factor of the type used in organic molecular wires. It is important to once again acknowledge the limitations of the DFT-based approach to transport, and in particular likely errors in the relative placement of the electrode Fermi level and the molecular levels. Moderate shifts in the latter may reverse the trends in conductance, but it is clear that the narrowing of the band gap in the longer chains makes it increasingly likely that the Fermi level will be in resonance with one or more of the orbitals in the scattering region.

References

(1) Moore, G. E. *Electronics* **1965**, *38*, 114.

(2) Schiltz, M. *Nature* **1999**, *399*, 729.

(3) Mathur, N. *Nature* **2002**, *419*, 573.

(4) Reed, M. A.; Tour, J. *Sci. Am.* **2000**, *282*, 86.

(5) Moore, G. E. *P. SPIE* **1995**, *2437*, 2.

(6) Powell, J. R. *P. IEEE* **2008**, *96*, 1247.

(7) Muller, D. A.; Sorsch, T.; Moccio, S.; Baumann, F. H.; Evans-Lutterodt, K.; Timp, G. *Nature* **1999**, *399*, 758.

(8) Wolf, E. L. *Quantum Nanoelectronics*; Second ed.; WILEY-VCH Verlag GmbH & Co. KGaA: Weinheim, 2009.

(9) Heath, J. R.; Ratner, M. A. *Phys. Today* **2003**, 43.

(10) Joachim, C.; Gimzevski, J. M.; Schitler, R. R.; Chavy, C. *Phys. Rev. Lett.* **1995**, *74*, 2002.

(11) Joachim, C.; Gimzevski, J. M.; Schitler, R. R.; Chavy, C. *Science* **1999**, *283*, 1683.

(12) Datta, S.; Tain, W.; Hong, S.; Reifenberg, R.; Henderson, J. I.; Kubiak, P. C. *Phys. Rev. Lett.* **1997**, *79*, 2530.

(13) Xue, Y.; Datta, S.; Reifenberg, R.; Henderson, J. I.; Kubiak, P. C. *Phys. Rev. B.* **1999**, *59*, 7852.

(14) Reed, M. A.; Zhou, C.; Muller, C. J.; Burgin, T. P.; Tour, J. M. *Science* **1997**, *278*, 252.

(15) Wold, D. J.; Frosbie, C. D. *J. Am. Chem. Soc.* **2001**, *123*, 5549.

(16) Rawlet, A. A.; Hopson, T. J.; Nagahara, L. A.; Tsui, R. K.; Ramachadran, G. K.; Lindsay, S. M. *Appl. Phys. Lett.* **2002**, *81*, 3043.

(17) Cui, X. D.; Primak, A.; Zarate, X.; Tomfohr, J.; Sankey, O. F.; Moore, A. L.; Moore, T. A.; Gust, D.; Nagahara, L. A.; Lindsay, S. M. *J. Phys. Chem.* **2002**, *106*, 8602.

(18) Cui, X. D.; Primak, A.; Zarate, X.; Tomfohr, J.; Sankey, O. F.; Moore, A. L.; Moore, T. A.; Gust, D.; Nagahara, L. A.; Lindsay, S. M. *Nanotech.* **2002**, *13*, 5.

(19) Wang, W.; Lee, T.; Reed, M. A. *Phys. Rev. B* **2003**, *68*, 035416.

(20) Chen, J.; Reed, A. M.; Rawlet, A. M.; Tour, J. M. *Science* **1999**, *286*, 1550.

(21) Chen, J.; Reed, A. M.; Rawlet, A. A.; Tour, J. M. *Appl. Phys. Lett.* **2000**, *77*, 1224.

(22) Xiao, X.; Xu, B.; Tao, N. J. *Nano Lett.* **2004**, *4*, 267.

(23) Xu, B.; Zhaung, P.; Li, X.; Tao, N. J. *Nano Lett.* **2004**, *4*, 1105.

(24) Venkataraman, L.; Klare, J. E.; Tam, I. W.; Nuckolls, C.; Hybertsen, M. S.; Steigerwald, M. L. *Nano Lett.* **2006**, *6*, 458.

(25) Xiao, X.; Xu, B.; Tao, N. J. *J. Am. Chem. Soc.* **2004**, *126*, 5370.

(26) Xiao, X.; Xu, B.; Tao, N. J. *Angew. Chem. Int. Ed.* **2004**, *433*, 6148.

(27) Xu, B.; Xiao, X.; Yang, X. M.; Zang, L.; Tao, N. J. *J. Am. Chem. Soc.* **2005**, *127*, 2386.

(28) Venkataraman, L.; Klare, J. E.; Nuckolls, C.; Hybertsen, M. S.; Steigerwald, M. L. *Nature* **2006**, *442*, 904.

(29) Venkataraman, L.; Park, Y. S.; Whalley, A. C.; Nuckolls, C.; Hybertsen, M. S.; Steigerwald, M. L. *Nano Lett.* **2007**, *7*, 502.

(30) Yamada, R.; Kumuzawa, H.; Noutoshi, T.; Tanaka, S.; Tada, H. *Nano Lett.* **2008**, *8*, 1237.

(31) Quinn, J. R.; Foss, F. W.; Venkataraman, L.; Hybertsen, M. S.; Breslow, R. *J. Am. Chem. Soc.* **2007**, *129*, 6714.

(32) Hybertsen, M. S.; Venkataraman, L.; Klare, J. E.; Whalley, A. C.; Steigerwald, M. L.; Nuckolls, C. *J. Phys. Condens. Mat.* **2008**, 374115.

(33) Lindsay, S. M.; Ratner, M. A. *Adv. Mater.* **2007**, *19*, 23.

(34) Emberly, E. G.; Kirczenow, G. *Phys. Rev. Lett.* **2000**, *61*, 5740.

(35) May, V. *Phys. Rev. B.* **2002**, *66*, 245411.

(36) Chen, Y. C.; Zwolak, M.; Di Ventura, M. *Nano Lett.* **2003**, *3*, 1691.

(37) Chen, Y. C.; Zwolak, M.; Di Ventura, M. *Nano Lett.* **2005**, *5*, 621.

(38) Galperin, M.; Ratner, M. A.; Nitzan, A. *J.Chem. Phys.* **2004**, *121*, 11965.

(39) Galperin, M.; Ratner, M. A.; Nitzan, A. *Phys. Rev. B.* **2007**, *75*, 035301.

(40) Galperin, M.; Ratner, M. A.; Nitzan, A. *J. Phys. Condens. Matter* **2007**, *19*, 103201.

(41) Jean, N.; Sanvito, S. *Phys. Rev. B.* **2006**, *73*, 094433.

(42) Walczak, K. *Chem. Phys.* **2007**, *333*, 63.

(43) Yan, L. J. *J. Phys. Chem. A* **2006**, *110*, 13249.

(44) Kula, M.; Luo, Y. J. *J. Chem. Phys.* **2008**, *128*, 064705.

(45) Ferrer, J.; Garcia-Suarez, V. M. *J. Mater. Chem.* **2009**, *19*, 1696.

(46) Franson, J.; Galperin, M. *Phys. Rev. B* **2010**, *81*, 075311.

(47) McCoy, H. N.; Moore, W. C. *J. Am. Chem. Soc.* **1911**, *33*, 273.

(48) Aviram, A.; Ratner, M. *Chem. Phys. Lett.* **1974**, *29*, 277.

(49) Aviram, A.; Joachim, C.; Pomerantz, M. *Chem. Phys. Lett.* **1988**, *146*, 490.

(50) Carroll, R. L.; Gorman, C. B. *Angew. Chem. Int. Ed.* **2002**, *41*, 4378.

(51) Metzger, R. M.; Chen, B.; Hopfner, U.; Lakshmikantham, D. V.; Kawai, T.; Wu, X. L.; Tachibana, H.; Hughes, T. V.; Sakurai, H.; Baldwin, J. W.; Hosch, C.; Cava, M. P.; Brehmer, L.; Ashwell, G. J. *J. Am. Chem. Soc.* **1997**, *119*, 10455.

(52) Reichert, J.; Ochs, R.; Beckman, D.; Weber, H. B.; Mayor, M.; Lohneysen, H. *Phys. Rev. Lett.* **2002**, *88*, 176804.

(53) M. Zhuang; Ernzerhof, M. *J. Chem. Phys.* **2009**, *130*, 114704.

(54) Sirringhaus, H.; Brown, P. J.; Friend, R. H.; Nielsen, M. M.; Bechgaard, K.; Langeveld-Voss, B. M. W.; Spiering, A. J. H.; Janssen, R. A. J.; Meijer, E. W.; Herwig, P.; Leeuw, D. M. *Nature* **1999**, *401*, 685.

(55) Burroughes, J. H.; Bradley, D. D. C.; Brown, A. R.; Marks, R. N.; Mackay, K.; Friend, R. H.; Burns, P. L.; Holmes, A. B. *Nature* **1990**, *347*, 539.

(56) Friend, R. H.; Gymer, R. W.; Holmes, A. B.; Burroughes, J. H.; Marks, R. N.; Taliani, C.; Bradley, D. D. C.; Santos, D. A. D.; Bredas, J. L.; Logdlund, M.; Salaneck, W. R. *Nature* **1999**, *397*, 121.

(57) Bernius, M. T.; Inbasekaran, M.; O'Brien, J.; Wu, W. S. *Adv. Mater.* **2000**, *12*, 1737.

(58) Mcculloch, I.; Heeney, M.; Bailey, C.; Genevicius, K.; Macdonald, I.; Shkunov, M.; Sparrowe, D.; Tierney, S.; Wagner, R.; Zhang, W. M.; Chabinyc, M. L.; Kline, R. J.; Mcgehee, M. D.; Toney, M. F. *Nature Mat.* **2006**, *5*, 328.

(59) Coropceanu, V.; Cornil, J.; Filho, D. A. S.; Olivier, Y.; Silbey, R.; Brédas, J.-L. **2007**, *107*, 926.

(60) Joachim, C.; Gimzevski, J. K.; Schitler, R. R.; Chavy, C. *Phys. Rev. Lett.* **1995**, *74*, 2102.

(61) Taylor, J.; Guo, H.; Wang, J. *Phys. Rev. B.* **1999**, *63*, 121104.

(62) Iijima, S. *Nature* **1991**, *354*, 56.

(63) Saito, R.; Dresselhaus, G.; Dresselhaus, M. *Physical Properties of Carbon Nanotudes*; Imperial College Press: London, 1998.

(64) McEuen, P. L. *Nature* **1998**, *393*, 15.

(65) Dekker, C. *Phys. Today* **1999**, *52*, 22.

(66) Odom, T. W.; Huang, J.; Kim, P.; Lieber, C. M. *J. Phys. Chem. B* **2000**, *104*, 2794.

(67) Wildoer, J. W. G.; Venema, L. C.; Rinzler, A. G.; Smalley, R. E.; Dekker, C. *Nature* **1998**, *391*, 59.

(68) Odom, T. W.; Huang, J.; Kim, P.; Lieber, C. M. *Nature* **1998**, *391*, 62.

(69) Javey, A.; Guo, J.; Wang, Q.; Lundstrom, M.; Dai, H. *Nature* **2003**, *424*, 654.

(70) Kwon, Y. K.; Tomanek, D.; Iijima, S. *Phys. Rev. Lett.* **1999**, *82*, 1470.

(71) Rodriguez-Manzo, J. A.; Banhart, F.; Terrones, M.; Terrones, H.; Grobert, N.; Ajayan, P. M.; Sumpter, B. G.; Meunier, V.; Wang, M.; Bando, Y.; Golberg, D. *Proc. Natl. Acad. Science* **2009**, *106*, 4591.

(72) Tans, S. J.; Verschueren, R. M.; Dekker, C. *Nature* **1998**, *391*, 775.

(73) Novoselov, K. S.; Geim, A. K.; Morozov, S. V.; Jiang, D.; Zhang, Y.; Dubonos, S. V.; Grigorieva, I. V.; Firsov, A. A. *Science* **2004**, *306*, 666.

(74) Bolotin, K. I.; Sikes, K. J.; Jiang, Z.; Klima, M.; Fudenberg, G.; Hone, J.; Kim, P.; Stormer, H. L. *Solid State Commun.* **2008**, *146*, 351.

(75) Novoselov, K. S.; Geim, A. K.; Morozov, S. V.; Jiang, D.; Katsnelson, M. I.; Grigorieva, I. V.; Dubonos, S. V.; Firsov, A. A. *Nature* **2005**, *438*, 197.

(76) Geim, A. K.; Novoselov, K. S. *Nature Mat.* **2007**, *6*, 183.

(77) Novoselov, K. S.; McCann, E.; Morozov, S. V.; Falko, V. I.; Katsnelson, M. I.; Zeitler, U.; Jiang, D.; Schedin, F.; Geim, A. K. *Nature Phys.* **2006**, *2*, 177.

(78) Jiang, Z.; Zhang, Y.; Tan, Y. W.; Stormer, H. L.; Kim, P. *Solid State Commun.* **2007**, *143*, 14.

(79) Jiang, Z.; Zhang, Y.; Stormer, H. L.; Kim, P. *Phys. Rev. Lett.* **2007**, *99*, 106802.

(80) Zhang, Y.; Tan, Y.-W.; Stormer, H. L.; Kim, P. *Nature* **2005**, *438*, 201.

(81) Novoselov, K. S.; Jiang, Z.; Zhang, Y.; Morozov, S. V.; Stormer, H. L.; Zeitler, U.; Maan, J. C.; Boebinger, G. S.; Kim, P.; Geim, A. K. *Science* **2007**, *315*, 1379.

(82) Schedin, F.; Geim, A. K.; Morozov, S. V.; Hill, E. W.; Blake, P.; Katsnelson, M. I.; Novoselov, K. S. *Nature Mat.* **2007**, *6*, 652.

(83) Allen, M. J.; Tung, V. C.; Kaner, R. B. *Chem. Rev.* **2009**, *110*, 132.

(84) Liu, L.-H.; Lerner, M. M.; Yan, M. *Nano Lett.* **2010**, *10*, 3754.

(85) Geim, A. K. *Science* **2009**, *324*, 1530.

(86) Rao, C. N. R.; Biswas, K.; Subrahmanyam, K. S.; Govindaraj, A. *J. Mater. Chem.* **2009**, *19*, 2457.

(87) Braun, E.; Eichen, Y.; Sivan, U.; Ben-Yoseph, G. *Nature* **1998**, *391*, 775.

(88) Fink, H. W.; Schonenberger, C. *Nature* **1999**, *398*, 407.

(89) Xu, B.; Zhang, P.; Li, X.; Tao, N.-J. *Nano Lett.* **2004**, *4*, 1105.

(90) Yoo, K. H.; Ha, D. H.; Lee, J. O.; Park, J. W.; Kim, J.; Kim, J. J.; Lee, H. Y.; Kawai, T.; Choi, H. Y. *Phys. Rev. Lett.* **2001**, *87*, 198102.

(91) Maruccio, G.; Visconti, P.; Arima, V.; D'Amico, S.; Biasco, A.; D'Amone, E.; Cingolani, R.; Rinaldi, R. *Nano Lett.* **2003**, *3*, 479.

(92) Storm, A. J.; van Noort, S.; de Vries, S.; Dekker, C. *Appl. Phys. Lett.* **2001**, *79*.

(93) Porath, D.; Bezryadin, A.; de Vries, S.; Dekker, C. *Nature* **2000**, *403*, 635.

(94) Cohen, H.; Nogues, C.; Naaman, R.; Porath, D. *Proc. Natl. Acad. Science* **2005**, *102*, 11589.

(95) Kosumov, A. Y.; Kociak, M.; Gueron, S.; Ruelet, B.; Volkov, V. T.; Klinov, D. V.; Bouchiat, H. *Science* **2001**, *291*, 280.

(96) Shinwari, M. W.; Deen, M. J.; Starikov, E. B.; Cunibert, G. *Adv. Funct. Mater.* **2010**, *20*, 1865.

(97) Taguchi, M.; Yamada, K.; Suzuki, K.; Sato, O.; Einaga, Y. *Chem. Matt.* **2005**, *17*, 4554.

(98) Liu, H.; long Du, X.; Gao, P.; Zhao, J. h.; Fang, J.; Shen, W. *J. Magn. Magn. Mater* **2010**, *322*, 572.

(99) Maruccio, G.; Biasco, A.; Visconti, P.; Bramanti, A.; Pompa, P. P.; Calabi, F.; Cingolani, R.; Rinaldi, R.; Corni, S.; Felice, R. D.; Molinari, E.; Verbeet, M. P.; Canters, G. W. *Adv. Mater.* **2005**, *17*, 816.

(100) Mas-Balleste, R.; Castillo, O.; Miguel, P. J. S.; Olea, D.; Gomez-Herrero, J.; Zamora, F. *Eur. J. Inorg. Chem.* **2009**, 2885.

(101) Agraït, N.; Yeyati, A. L.; Ruitenbeek, J. M. *Phys. Rev.* **2003**, *377*, 81.

(102) Obermair, C.; Xie, F.-Q.; Schimmel, T. *Europhysics News* **2010**, *41*, 25.

(103) Krans, J. M.; van Ruitenbeek, J. M.; Fisun, V. V.; Yanson, I. K.; de Jongh, L. J. *Nature* **1995**, *375*, 767.

(104) Agratiuml, N.; Rodrigo, J. G.; Vieira, S. *Phys. Rev. B* **1993**, *47*, 12345.

(105) Li, C. Z.; Tao, N. J. *Appl. Phys. Lett.* **1998**, 894.

(106) Li, C. Z.; Bogozi, A.; Huang, W.; Tao, N. J. *Nanotech.* **1998**, *10*, 221.

(107) Ohnishi, H.; Kondo, Y.; Takayanagi, K. *Nature* **1998**, *395*, 780.

(108) Park, J.; Pasupathy, A. N.; Jonas I. Goldsmith; Chang, C.; Yaish, Y.; Petta, J. R.; Rinkoski, M.; Sethna, J. P.; Abruna, H. D.; McEuen, P. L.; Ralph, D. C. *Nature* **2002**, *417*, 722.

(109) Otsuki, J.; Akasaka, T.; Araki, K. *Coordin. Chem. Rev.* **2008**, *252*, 32.

(110) Li, Z.; Liu, Y.; Mertens, S. F. L.; Pobelov, I. V.; Wandlowski, T. *J. Am. Chem. Soc.* **2010**, *132*, 8187.

(111) Petrangolini, P.; Alessandrini, A.; Berti, L.; Facci, P. *J. Am. Chem. Soc.* **2010**, *132*, 7445.

(112) Ricci, A. M.; Calvo, E. J.; Martin, S.; Nichols, R. J. *J. Am. Chem. Soc.* **2009**, *132*, 2494.

(113) Seo, K.; Konchenko, A. V.; Lee, J.; Bang, G. S.; Lee, H. *J. Mater. Chem.* **2009**, *19*, 7617

(114) Albrecht, T.; Guckian, A.; Ulstrup, J.; Vos, J. G. *Nano Lett.* **2005**, *5*, 1451.

(115) Esen, G.; Fuhrer, M. S. *Appl. Phys. Lett.*, *87*, 263101.

(116) Bredow, T.; Tegenkamp, C.; Pfnür, H.; Meyer, J.; Maslyuk, V. V.; Mertig, I. *J. Chem. Phys.* **2008**, *128*, 064704

(117) Engtrakul, C.; Sita, L. R. *Nano Lett.* **2001**, *1*, 541.

(118) Dinglasan, J. A. M.; Bailey, M.; Park, J. B.; Dhirani, A.-A. *J. Am. Chem. Soc.* **2004**, *126*, 6491.

(119) Getty, S. A.; Engtrakul, C.; Wang, L.; Liu, R.; Ke, S.-H.; Baranger, H. U.; Yang, W.; Fuhrer, M. S.; Sita, L. R. *Phys. Rev. B* **2005**, *71*, 241401.

(120) Liu, R.; Ke, S.-H.; Baranger, H. U.; Yang, W. *Nano Lett.* **2005**, *5*, 1959.

(121) Liu, R.; Ke, S.-H.; Baranger, H. U.; Yang, W. *J. Am. Chem. Soc.* **2006**, *128*, 6274.

(122) Garcia-Suarez, V. M.; Ferrer, J.; Lambert, C. J. *Phys. Rev. Lett.* **2006**, *96*, 106804.

(123) L.Wang; Z.Cai; J.Wang; J.Lu; Luo, G.; L.Lai; Zhou, J.; Qui, R.; Gao, Z.; Yu, D.; Li, G.; Mei, W. N.; Sanvito, S. *Nano Lett.* **2008**, *8*, 3640.

(124) Zhu, L.; Wang, J. *J. Phys. Chem. C* **2009**, *113*, 8767.

(125) Zhang, X.; Wang, J. *J. Phys. Chem. A.* **2010**, *114*, 2319.

(126) Han, M.; Ozyilmaz, B.; Zhang, Y.; Jarillo-Herero, P.; Kim, P. *Phys. Status Solidi B* **2007**, *244*, 4134.

(127) Zhu, L.; Wang, J. *J. Phys. Chem. C* **2009**, *113*, 8767.

(128) Miyajima, K.; Nakajima, A.; Yabushita, S.; Knickelbein, M. B.; Kaya, K. *J. Am. Chem. Soc.* **2004**, *126*, 13202.

(129) Wang, J.; Acioli, P. H.; Jellinek, J. *J. Am. Chem. Soc.* **2005**, *127*, 2812.

(130) Maslyuk, V. V.; Bagrets, A.; Meded, V.; Arnold, A.; Evers, F.; Brandbyge, M.; Bredow, T.; Mertig, I. *Phys. Rev. B.* **2006**, *97*, 097201.

(131) Koleini, M.; Paulsson, M.; Brandbyge, M. *Phys. Rev. Lett.* **2007**, *98*, 197202.

(132) Nagao, S.; Kato, A.; Nakajima, A.; Kaya, K. *J. Am. Chem. Soc.* **2000**, *122*, 4221.

(133) Zhou, L.; Yang, S. W.; Ng, M. F.; Sullivan, M. B.; Tan, V. B. C.; Shen, L. *J. Am. Chem. Soc.* **2007**.

(134) Heersche, H. B.; de Groot, Z.; Folk, J. A.; van der Zant, H. S. J.; Romeike, C.; Wegewijs, M. R.; Zobbi, L.; Barreca, D.; Tondello, E.; Cornia, A. *Phys. Rev. Lett.* **2006**, *96*, 206801.

(135) Jo, M.-H.; Grose, J. E.; Baheti, K.; Deshmukh, M. M.; Sokol, J. J.; Rumberger, E. M.; Hendrickson, D. N.; Long, J. R.; Park, H.; Ralph, D. C. *Nano Lett.* **2006**, *6*, 2014.

(136) Pemmaraju, C. D.; Rungger, I.; Sanvito, S. *Phys. Rev. B* **2009**, *80*, 104422.

(137) Corkery, R. W. *Curr. Opin. Colloid In.* **2008**, *13*, 288.

(138) Rybak, J. C.; Schellenberg, I.; Pöttgen, R.; Müller-Buschbaum, K. *Z. Anorg. Allg. Chem.* **2010**, *636*, 1720.

(139) Guijarro, A.; Castillo, O.; Welte, L.; Calzolari, A.; Miguel, P. J. S.; Gómez-García, C. J.; Olea, D.; di Felice, R.; Gómez-Herrero, J.; Zamora, F. *Adv. Funct. Mater.* **2010**, *20*, 1451.

(140) Amo-Ochoa, P.; Welte, L.; Gonzalez-Prieto, R.; Sanz Miguel, P. J.; Gomez-Garcia, C. J.; Mateo-Marti, E.; Delgado, S.; Gomez-Herrero, J.; Zamora, F. *Chem. Commun.* **2010**, *46*, 3262.

(141) Olea, D.; Alexandre, S.; Amo-Ochoa, P.; Guijarro, A.; de Jesús, F.; Soler, J.; de Pablo, P.; Zamora, F.; Gómez-Herrero, J. *Advan. Mat.* **2005**, *17*, 1761.

(142) Bellitto, C.; Flamini, A.; Gastaldi, L.; Scaramuzza, L. *Inorg. Chem.* **1983**, *22*, 444.

(143) Kitagawa, H.; Onodera, N.; Ahn, J.-S.; Mitani, T.; Toriumi, K.; Yamashita, M. *Synthetic Met.* **1997**, *86*, 1931.

(144) Kitagawa, H.; Onodera, N.; Sonoyama, T.; Yamamoto, M.; Fukawa, T.; Mitani, T.; Seto, M.; Maeda, Y. *J. Am. Chem. Soc.* **1999**, *121*, 10068.

(145) Mitsumi, M.; Murase, T.; Kishida, H.; Yoshinari, T.; Ozawa, Y.; Toriumi, K.; Sonoyama, T.; Kitagawa, H.; Mitani, T. *J. Am. Chem. Soc.* **2001**, *123*, 11179.

(146) Mitsumi, M.; Kitamura, K.; Morinaga, A.; Ozawa, Y.; Kobayashi, M.; Toriumi, K.; Iso, Y.; Kitagawa, H.; Mitani, T. *Angew. Chem. Int. Ed.* **2002**, *41*, 2767.

(147) Krogmann, K. *Angew. Chem. Int. Ed.* **1969**, *8*, 35.

(148) Miller, J. S.; Epstein, A. J. *Prog. Inorg. Chem.* **1976**, *20*, 1.

(149) Ferraro, J. R.; Mertes, K. B. *Coordin. Chem. Radiochem.* **1983**, *26*, 235.

(150) J. R. Ferraro; Mertes, K. B. *Coordin. Chem. Rev.* **1981**, *36*, 357.

(151) Finniss, G. M.; E. Canadell; C. Campana; Dunbar, K. R. *Angew. Chem. Int. Ed.* **1996**, *35*, 2772.

(152) Murashashi, T.; Mochizuki, E.; Kai, Y.; Kurosowa, H. *J. Am. Chem. Soc.* **1999**, *121*, 10660.

(153) Leung, M.-K.; Mandal, A. B.; Wang, C.-C.; Lee, G.-H.; Peng, S.-M.; Cheng, H.-L.; Her, G.-R.; Chao, I.; Lu, H.-F.; Sun, Y.-C.; Shiao, M.-Y.; Chou, P.-T. *J. Am. Chem. Soc.* **2002**, *142*, 4287.

(154) Hurley, T. J.; Robinson, M. A. *Inorg. Chem.* **1968**, *7*, 33.

(155) Wu, L.-P.; Field, P.; Morrissey, T.; Murphy, C.; Nagle, P.; Hathaway, B.; Simmons, C.; Thornton, P. *Dalton Trans.* **1990**, 3835.

(156) Pyrka, G. J.; El-Mekki, M.; Pinkerton, A. A. *Chem. Commun.* **1991**, 84.

(157) Sheu, J.-T.; Lin, C.-C.; Chao, I.; Wang, C.-C.; Peng, S.-M. *J. Chem. Soc., Chem.Commun.* **1996**, 315.

(158) Aduldecha, S.; Hathaway, B. *Dalton Trans.* **1991**, 993.

(159) A.Cotton, F.; Chao, H.; Li, Z.; Murillo, C. A.; Wang, Q. *Organometallics Chem.* **2008**, *639*, 1412.

(160) Yang, E.-C.; Cheng, M.-C.; Tsai, M.-S.; Peng, S.-M. *J. Chem. Soc., Chem. Commun.* **1994**, *321*, 224.

(161) Cotton, F. A.; Daniels, L. M.; Jordan, G. T. *Chem. Commun.* **1997**, 421.

(162) Cotton, F. A.; Murillo, C. A.; Wang, X. *J. Chem. Soc., Dalton Trans.* **1999**, 3327.

(163) Cotton, F. A.; Daniels, L. M.; Murillo, C. A.; Pascual, I. *J. Am. Chem. Soc.* **1997**, *119*, 10223.

(164) Clérac, R.; Cotton, F. A.; Daniels, L. M.; Dunbar, K. R.; Murillo, C. A.; Pascual, I. *Inorg. Chem.* **2000**, *39*, 748.

(165) Cotton, F. A.; Daniels, L. M.; Murillo, C. A.; Wang, X. *Chem. Commun.* **1998**, 39.

(166) Sheu, J.-T.; Lin, C.-C.; Chao, S.; Wanga, C.-C.; Peng, S.-M. *Chem. Commun.* **1996**, 315.

(167) Kuo, C.-K.; Liu, I. P.-C.; Yeh, C.-Y.; Chou, C.-H.; Tsao, T.-B.; Lee, G.-H.; Peng, S.-M. *Chem. Eur. J.* **2007**, *13*, 1442.

(168) Wang, C.-C.; Lo, W.-C.; Chou, C.-C.; Lee, G.-H.; Chen, J.-M.; Peng, S.-M. *Inorg. Chem.* **1998**, *37*, 4059.

(169) Lai, S.-H.; Hsiao, C.-J.; Ling, J.-W.; Wang, W.-Z.; Peng, S.-M.; Chen, I. C. *Chem. Phys. Lett.* **2008**, *456*, 181.

(170) Shieh, S.-J.; Chou, C.-C.; Lee, G.-H.; Wang, C.-C.; Peng, S.-M. *Angew. Chem. Int. Ed.* **1997**, *36*, 56.

(171) Yeh, C.-Y.; Chou, C. H.; Pan, K. C.; Wang, C.-C.; Lee, G. H.; Su, Y. O.; Peng, S. H. *J.Chem.Soc., Dalton Trans.* **2002**, 2670.

(172) Chang, H.-C.; Li, J.-T.; Wang, C.-C.; Lin, T.-W.; Lee, H.-C.; Lee, G.-H.; Peng, S.-M. *Inorg. Chem.* **1999**, *243*, 1254.

(173) Cotton, F. A.; Daniels, L. M.; Lu, T.; Murillo, C. A.; Wang, X. *J. Chem. Soc., Dalton Trans.* **1999**, 517.

(174) Yin, C.; Huang, G.-C.; Kuo, C.-K.; Fu, M.-D.; Lu, H.-C.; Ke, J.-H.; Shih, K.-N.; Huan, Y.-L.; Lee, G.-H.; Ye, C.-Y.; Chen, C.-H.; Peng, S.-M. *J. Am. Chem. Soc.* **2008**, *130*, 10030.

(175) Lai, S.-Y.; Lin, T.-W.; Chen, Y.-H.; Wang, C.-C.; Lee, G.-H.; Yang, M.-H.; Leung, M.-K.; Peng, S.-M. *J. Am. Chem. Soc.* **1999**, *121*, 250.

(176) Chen, Y.-H.; Lee, C.-C.; Wang, C.-C.; Lee, G.-H.; Lai, S.-Y.; Li, F.-Y.; Mou, C.-Y.; Peng, S.-M. *Inorg. Chem.* **1999**, *1243*, 1251.

(177) Wang, W.-Z.; Ismayilov, R. H.; Lee, G.-H.; Liu, I. P.-C.; Yeh, C. Y.; Peng, S.-M. *Dalton Trans.* **2007**, 830.

(178) Peng, S.-M.; Wang, C. C.; Jang, Y. L.; Chen, Y. H.; Li, F. Y.; Mou, C. Y.; Leung, M. K. *J. Magn. Magn. Mater* **2000**, *209*, 80.

(179) Kuo, J.-H.; Tsao, T.-B.; Lee, G.-H.; Lee, H.-W.; Yeh, C.-Y.; Peng, S.-M. *Eur. J. Inorg. Chem.* **2011**, *38*, 2025.

(180) Ismayilov, R. H.; Wang, W.-Z.; Lee, G.-H.; Yeh, C.-Y.; Hua, S.-A.; Song, Y.; Rohmer, M.-M.; Bénard, M.; Peng, S.-M. *Angew. Chem. Int. Ed.* **2011**, *50*, 1.

(181) Nippe, M.; Timmer, G. H.; Berry, J. F. *Chem. Commun.* **2009**, 4357.

(182) Huang, G.-C.; Bénard, M.; Rohmer, M.-M.; Li, L.-A.; Chiu, M.-J.; Yeh, C.-Y.; Lee, G.-H.; Peng, S.-M. *Eur. J. Inorg. Chem.* **2008**, 1767.

(183) Lopez, X.; Benard, M.; Rohmer, M.-M. *J. Mol. Struct. Theochem.* **2006**, *777*, 53.

(184) López, X.; Rohmer, M.-M.; Bénard, M. *J. Mol. Struct.* **2008**, *890*, 18.

(185) Rohmer, M.-M.; Lui, I.; Lin, J. C.; Chiu, M.-J.; Lee, G. H.; Bénard, M.; López, X.; Peng, S. M. *Angew. Chem. Int. Ed.* **2007**, *46*, 3533.

(186) Liu, I. P.-C.; Lee, G. H.; Peng, S. H.; Bénard, M.; Rohmer, M.-M. *Inorg. Chem.* **2007**, *46*, 9602.

(187) Nippe, M.; Berry, J. F. *J. Am. Chem. Soc.* **2007**, *129*, 12684.

(188) Nippe, M.; Victor, E.; Berry, J. F. *Eur. J. Inorg. Chem.* **2008**, 5569.

(189) Bumm, L. A.; Arnold, J. J.; Cygan, M. T.; Dunbar, T. D.; Burgin, T. P.; Jones, L.; Allara, D. L.; Tour, J. M.; Weiss, P. S. *Science* **1996**, *271*, 1705.

(190) Lin, S.-Y.; Chen, I.-W. P.; Chen, C.-H.; Hsieh, M.-H.; Yeh, C.-Y.; Lin, T.-W.; Chen, Y.-H.; Peng, S.-M. *J. Phys. Chem. B* **2004**, *108*, 959.

(191) Chen, I.-W.; Fu, M.-D.; Tseng, W.-H.; Yu, J.-Y.; Wu, S.-H.; Ku, C.-J.; Chen, C.-H.; Peng, S.-M. *Angew. Chem. Int. Ed.* **2006**, *45*, 5814.

(192) Hsu, L. Y.; Huang, Q. R.; Jin, B. Y. *J. Phys. Chem. C.* **2008**, *112*, 10538.

(193) Chae, D.-H.; Berry, J. F.; Jung, S.; Cotton, F. A.; Murillo, C. A.; Yao, Z. *Nano Lett.* **2006**, *6*, 165.

(194) Hua, S.-A.; Liu, I. P.-C.; Hasanov, H.; Huang, G.-C.; Ismayilov, R. H.; Chiu, C.-L.; Yeh, C.-Y.; Lee, G.-H.; Peng, S.-M. *Dalton Trans.* **2010**, *39*, 3890.

(195) Hua, S.-A.; Huang, G.-C.; Liu, I. P.-C.; Kuo, J.-H.; Jiang, C.-H.; Chiu, C.-L.; Yeh, C.-Y.; Lee, G.-H.; Peng, S.-M. *Chem. Commun.* **2010**, *46*, 5018.

(196) Po-Chun Liu, I.; Wang, W.-Z.; Peng, S.-M. *Chem. Commun.* **2009**, 4323.

(197) Ismayilov, R. H.; Wang, W. Z.; Wang, R. R.; Huang, Y. L.; Yeh, C. Y.; Lee, G. H.; Peng, S. M. *Eur. J. Inorg. Chem.* **2008**, *16*, 4290.

(198) López, X.; Huang, M.-Y.; Huang, G.-C.; Peng, S.-M.; F.-Y. Li; Bénard, M.; Rohmer, M.-M. *Inorg. Chem.* **2006**, *45*, 9057.

(199) Chien, C.-H.; Chang, J.-C.; Yeh, C.-Y.; Lee, G.-H.; Fang, J.-M.; Song, Y.; Peng, S.-M. *Dalton Trans.* **2006**, *26*, 3249.

(200) Tsao, T.-B.; Lo, S. S.; Yeh, C.-Y.; Lee, G.-H.; Peng, S.-M. *Polyhedron* **2004**, *26*, 3833.

(201) Hasan, H.; Tan, U.-K.; Lee, G.-H.; Peng, S.-M. *Inorg. Chem.* **2007**, *10*, 983.

(202) Chien, C.-H.; Chang, J.-C.; Yeh, C.-Y.; Lee, G.-H.; Fanga, J.-M.; Peng, S.-M. *Dalton Trans.* **2006**, 2106.

(203) Chien, C.-H.; Chang, J.-C.; Yeh, C.-Y.; Lee, G.-H.; Fanga, J.-M.; Peng, S.-M. *Dalton Trans.* **2006**, 3249.

(204) de Picciotto, R.; Stormer, H. L.; Pfeiffer, L. N.; Baldwin, K. W.; West, K. W. *Nature* **2001**, *411*, 51.

(205) Agraït, N.; Yeyati, A. L.; Ruitenbeek, J. M. *Phys. Reps.* **2003**, *377*, 81.

(206) Landauer, R. *Philos. Mag.* **1970**, *21*, 863.

(207) Landauer, R. *IBM J. Res. Dev.* **1957**, *1*, 233.

(208) Landauer, R. *J. Phys. Condens. Mat.* **1996**, *227*, 156.

(209) Büttiker, M. *Phys. Rev. Lett.* **1986**, *57*, 1761.

(210) Büttiker, M.; Imry, Y.; Landauer, R.; Pinhas, S. *Phys. Rev. B.* **1985**, *31*, 6207.

(211) Datta, S. *Quantum Transport: Atom to Transistor*; Cambridge University Press: Cambridge, 2005.

(212) Datta, S. *Electron Transport in Mesoscopic Systems*; Cambridge University Press: Cambridge, 1997.

(213) Datta, S. *Superlattices and Microstructures* **2000**, *28*, 253.

(214) Datta, S. *Non-Equilibrium Green's Function (NEGF) Formalism: An Elementary Introduction*; IEEE Press 2002.

(215) Kadanoff, L. P.; Baym, G. *Quantum Statistical Mechanics*, 1962.

(216) Keldysh, L. V. *Sov. Phys. JETP* **1965**, *20*, 1018.

(217) Rammer, J.; Smith, H. *Rev. Mod. Phys.* **1986**, *58*, 323.

(218) Merzbacher, E. *Quantum Mechanics*; Second ed.; Wiley New York, 1970.

(219) Szabo, A.; Ostlund, N. S. *Modern Theoretical Chemistry*; MacMillan Pub. Inc.: New York, 1982.

(220) Born, M.; Oppenheimer, R. *Annu. Phys.* **1927**, *389*, 457.

(221) Massimi, M. *Pauli's Exclusion Principle*; Cambridge University Press, 2005.

(222) Slater, J. C. *Phys. Rev.* **1929**, *34*, 1293.

(223) Slater, J. C. *Phys. Rev.* **1930**, *35*, 509.

(224) Fock, V. *Z. Phys.* **1930**, *61*, 126.

(225) Pauli, W. *Z. Phys.* **1925**, *31*, 765.

(226) Koch, W.; Holthausen, M. C. *A Chemist's Guide to Density Functional Theory*; Wiley-VCH: Weinheim, 2002.

(227) Parr, R. G.; Yang, W. *Density Functional Theory of Atoms and Molecules*; Oxford University Press: New York, 1989.

(228) Hugenholtz, N. M. *Phys. Rev.* **1954**, *96*, 1158.

(229) Löwdin, P. *Phys. Rev.* **1955**, *97*, 1509.

(230) Quintanilla, J.; Hooley, C. *Phys. World* **2009**, *22*, 37.

(231) Kaltsoyannis, N. In *Computational Inorganic and Bioinorganic Chemistry*; Solomon, E. I., Scott, R. A., King, R. B., Eds.; John Wiley & Sons, Ltd.: 2009, p 517.

(232) Cramer, C. J. *Essentials of Computational Chemistry*; John Wiley & Sons, Ltd., 2002.

(233) McWeeny, R. *Coulson's Valence*; Oxford University Press, 1979.

(234) Jensen, F. *Introduction to Computational Chemistry*; John Wiley & Sons: Chichester, England, 2007.

(235) McWeeny, R. *Methods of Molecular Quantum Mechanics*; Academic Press, London, 1992.

(236) Bartlett, R. J. *Annu. Rev. Phys. Chem.* **1981**, *32*, 359.

(237) Springborg, M. *Methods of Electronic-Structure Claculations: From Molecules to Solids*; John Wiley & Sons Ltd.: Chichester, England 2000.

(238) Harvey, J. N. *Annu. Rep. Prog. Chem.* **2006**, *102*, 203.

(239) Neese, F. *Coordin. Chem. Rev.* **2009**, *253*, 526.

(240) Hohenberg, P.; Kohn, W. *Phys. Rev* **1964**, *136*, B864.

(241) Fermi, E. *Z. Phys.* **1928**, *48*, 73.

(242) Slater, J. C. *Phys. Rev.* **1951**, *81*, 385.

(243) Slater, J. C. *Quantum Theory of Molecules and Solids*; McGraw-Hill: New York, 1974; Vol. 4.

(244) Johnson, K. H. *Adv. Quantum Chem.* **1973**, *7*, 143.

(245) Johnson, K. H. *Annu. Rev. Phys. Chem.* **1975**, *26*, 39.

(246) Schwartz, K. *Phys. Rev. B* **1972**, *5*, 2466.

(247) Schwartz, K. *Theor. Chim. Acta.* **1974**, *34*, 225.

(248) Kohn, W.; Sham, L. J. *Phys. Rev.* **1965**, *140*, A1133.

(249) Vosko, S. H.; Wilk, L.; Nusair, M. *Can. J. Phys.* **1980**, *58*, 1200.

(250) Perdew, J. P.; Wang, Y. *Phys. Rev. B.* **1992**, *45*, 13244.

(251) Perdew, J. P.; Chevary, J. A.; Vosko, S. H.; Jackson, K. A.; Pederson, M. R.; Singh, D. J.; Fiolhais, C. *Phys. Rev. B.* **1992**, *46*.

(252) Perdew, J.; Burke, K.; Ernzerhof, M. *Phys. Rev. Lett.* **1996**, *77*, 3865.

(253) Lee, C.; Yang, W.; Parr, R. G. *Phys. Rev. B* **1998**, *37*, 785.

(254) Becke, A. D. *Phys. Rev. A* **1988**, *38*, 3098.

(255) Perdew, J. P. *Phys. Rev. B* **1986**, *33*, 8822.

(256) Becke, A. D. *Phys. Rev. A* **1988**, *38*, 3098.

(257) Lee, C.; Yang, W.; Parr, R. G. *Phys. Rev. B* **1988**, *37*, 785.

(258) Perdew, J. P. *Phys. Rev. B* **1986**, *33*, 8822.

(259) Perdew, J. P.; Wang, Y. *Phys. Rev. B* **1992**, *45*, 13244.

(260) Becke, A. D.; Roussel, M. *Phys. Rev. A* **1989**, *39*, 3761.

(261) Proynov, E. I.; Vela, A.; Salahub, D. R. *Chem. Phys. Lett.* **1994**, *230*, 419.

(262) Tao, J.; Perdew, J. P.; Staroverov, V. N.; Scuseria, G. E. *Phys. Rev. Lett.* **2003**, *91*, 146401.

(263) Kurth, S.; Perdew, J. P.; Blaha, P. *Int. J. Quantum. Chem.* **1999**, *75*, 889.

(264) Tao, J. *J. Chem. Phys.* **2002**, *116*, 2335.

(265) Adamo, C.; Ernzerhof, M.; Scuseria, G. E. *J. Chem. Phys.* **2000**, *112*, 2643.

(266) Becke, A. D. *J. Chem. Phys.* **1993**, *98*, 5648.

(267) Zhao, Y.; Truhlar, D. G. *Theor. Chem. Acc.* **2008**, *120*, 215.

(268) Zhao, Y.; Schuitz, N. E.; Truhlar, D. G. *J. Chem. Theor. Comput.* **2006**, *2*, 364.

(269) Becke, A. D. *J. Chem. Phys.* **1993**, *98*, 1372.

(270) Becke, A. D. *J.Chem. Phys.* **1993**, *98*, 5648.

(271) G.Frenking; Wagener, T. *Encyclopedia of Computational Chemistry*; Wiley: Chichester, 1998.

(272) Ihm, J.; Zunger, A.; Cohen, M. L. *Sol. State Phys.* **1979**, *12*, 4409.

(273) Marques, M.; Castro, A.; Bertsch, G. F.; Rubio, A. *Comput. Phys. Commun.* **2003**, *151*, 60.

(274) Chelikowsky, J. R.; Kronik, L.; Vasiliev, I.; Jain, M.; Saad, Y. *Using Real Space Pseudopotentials for the Electronic Structure Problem*; Elsevier Science: Amsterdam, 2006.

(275) Hehre, W. J.; Stewart, R. F.; Pople, J. A. *J.Chem. Phys.* **1969**, *51*, 2657.

(276) Sankey, O. F.; Niklewski, D. J. *Phys. Rev. B.* **1989**, *40*, 3979.

(277) Artacho, E.; Sánchez-Portal, D.; Ordejón, P.; García, A.; Soler, J. M. *Phys. Status Solidi B* **1999**, *215*, 809.

(278) Toullier, N.; Martins, J. L. *Phys. Rev. B.* **1991**, *43*, 1993.

(279) Baerends, E. J.; Autschbach, J.; Bérces, A.; Bickelhaupt, F. M.; Bo, C.; Boerrigter, P. M.; Cavallo, L.; Chong, D. P.; Deng, L.; Dickson, R. M.; Ellis, D. E.; van Faassen, M.; Fan, L.; Fischer, T. H.; Fonseca Guerra, C.; van Gisbergen, S. J. A.; Götz, A. W.; Groeneveld, J. A.; Gritsenko, O. V.; Grüning, M.; Harris, F. E.; van den Hoek, P.; Jacob, C. R.; Jacobsen, H.; Jensen, L.; van Kessel, G.; Kootstra, F.; Krykunov, M. V.; van Lenthe, E.; McCormack, D. A.; Michalak, A.; Neugebauer, J.; Nicu, V. P.; Osinga, V. P.; Patchkovskii, S.; Philipsen, P. H. T.; Post, D.; Pye, C. C.; Ravenek, W.; Rodriguez, J. I.; Ros, P.; Schipper, P. R. T.; Schreckenbach, G.; Snijders, J. G.; Solà, M.; Swart, M.; Swerhone, D.; te Velde, G.; Vernooijs, P.; Versluis, L.; Visscher, L.; Visser, O.; Wang, F.; Wesolowski, T. A.; van Wezenbeek, E. M.; Wiesenekker, G.; Wolff, S. K.; Woo, T. K.; Yakovlev, A. L.; Ziegler, T.; ADF2008.01, *SCM, Theoretical Chemistry, Vrije Universiteit: Amsterdam, The Netherlands* http://www.scm.com.

(280) http://www.cambridgesoft.com/.

(281) http://www.gimp.org/.

(282) Yang, E.-C.; Cheng, M.-C.; Tsai, M.-S.; Peng, S.-M. *J. Chem. Soc., Chem. Commun.* **1994**, 2377.

(283) Cotton, F. A.; Daniels, L. M.; Jordan, G. T.; Murillo, C. A. *J. Am. Chem. Soc.* **1997**, *119*, 10377.

(284) Cotton, F. A.; Murillo, C. A.; Wang, X. *Inorg. Chem.* **1999**, *38*, 6294.

(285) Clérac, R.; Cotton, F. A.; Daniels, L. M.; Dunbar, K. R.; Kirschbaum, K.; Murillo, C. A.; Pinkerton, A. A.; Schultz, A. J.; Wang, X. *J. Am. Chem. Soc.* **2000**, *122*, 6226.

(286) Stohrer, W.-D.; Hoffman, R. *J. Am. Chem. Soc.* **1972**, *94*, 779.

(287) Clérac, R.; Cotton, F. A.; Daniels, L. M.; Dunbar, K. R.; Murillo, C. A. *Dalton Trans.* **2001**, 386.

(288) Clérac, R.; Cotton, F. A.; Jeffery, S. P.; Murillo, C. A.; Wang, X. *Inorg. Chem.* **2001**, *40*, 1265.

(289) Hach, R. J.; Rundle, R. E. *J. Am. Chem. Soc.* **1951**, *73*, 4321.

(290) Pimental, G. C. *J. Chem. Phys.* **1951**, *19*, 446.

(291) Cahill, P. A.; Dykstra, C. E.; Martin, J. C. *J. Am. Chem. Soc.* **1985**, *107*, 6359.

(292) Munzarová, M. L.; Hoffmann, R. *J. Am. Chem. Soc.* **2002**, *124*, 4787.

(293) Landrum, G. A.; Goldberg, N.; Hoffmann, R. *J. Chem. Soc., Dalton Trans.* **1997**, 3605.

(294) Pantazis, D. A., Ph.D University of York, 2005.

(295) Rohmer, A.; Bénard, M. *J. Am. Chem. Soc.* **1998**, *120*, 9372.

(296) Rohmer, M.-M.; Strich, A.; Bénard, M.; Malrieu, J. *J. Am. Chem. Soc.* **2001**, *123*, 9126.

(297) Pantazis, D. A.; McGrady, J. E. *J. Am. Chem. Soc.* **2006**, *128*, 4128.

(298) L.Versuis; T.Ziegler *J. Chem. Phys.* **1988**, *88*, 322.

(299) http://www.quantumwise.com/.

(300) Brandbyge, M.; Mozos, J.-L.; Ordejon, P.; Taylor, P.; Stokbro, K. *Phys. Rev. B* **2002**, *65*, 165401.

(301) Soler, J. M.; Artacho, E.; Gale, J. D.; Garcia, A.; Unquera, J.; Ordejon, J. P.; Sanchez-Portal, D. *J. Phys. Condens. Mat.* **2002**, *14*, 2745

(302) Taylor, J.; Guo, H.; Wang, J. *Phys. Rev. B.* **2001**, *63*, 245407.

(303) Narlikar, A. V.; Fu, Y. Y. *Oxford Handbook of Nanoscience and Technology*; Oxford University Press: Oxford, 2010; Vol. 1: Basic Aspects

(304) Jortner, J.; Nitzan, A.; Ratner, M. A. *Lecture Notes in Physics: Introducing Molecular Electronics*; Spinger: New York, 2005; Vol. 14.

(305) Lindsar, S. *Farad. Disc.* **2006**, *131*, 403.

(306) Perdew, J. P.; Burke, K.; Ernzerhof, M. *Phys. Rev. Lett.* **1996**, *77*, 3865.

(307) Troullier, N.; Martins, J. L. *Phys. Rev. B.* **1993**, *43*.

(308) Monkhorst, H. J.; Pack, J. D. *Phys. Rev. B.* **1976**, *13*, 5188.

(309) Meir, J.; Wingreen, N. S. *Phys. Rev. Lett.* **1992**, *68*, 2512.

(310) Wang, P.; Cai, Z.; Wang, J.; Luo, G.; Lai, L.; Zhou, J.; Qin, R.; Gao, Z.; Yu, D.; Li, G.; Mei, W. N.; Sanvito, S. *Nano Lett.* **2008**, *8*, 3640.

(311) Garcia-Suarez, V.; Lambert, C. J. *Nanotech.* **2008**, *19*, 455203.

(312) Berry, J. F.; Cotton, F. A.; Daniels, L. M.; Dunbar, K. R.; Pascual, I. *Inorg. Chem.* **2000**, *39*, 748.

(313) Berry, J. F.; Cotton, F. A.; Lu, T.; Murillo, C. A.; Roberts, B. K.; Wang, X. *J. Am. Chem. Soc.* **2004**, *126*, 7082.

(314) Chang, H.-C.; Li, J.-T.; Wang, C.-C.; Lin, T.-W.; Lee, H.-C.; Lee, G.-H.; Peng, S.-M. *Eur. J. Inorg. Chem.* **1999**, *1*, 1243.

(315) Hsiao, C. J.; Lai, S. H.; Chen, I. C.; Wang, W.-Z.; Peng, S.-M. *J. Phys. Chem. A.* **2008**, *112*, 13528.

(316) Benbellat, N.; Rohmer, M.-M.; Bénard, M. *Chem. Commun.* **2001**, *2368*.

(317) Rohmer, M.-M.; Bénard, M. *J. Clust. Sci.* **2002**, *13*, 333.

(318) Berry, J. F. *Struct. Bond.* **2010**, *136*, 1.

(319) Georgiev, V.; McGragy, J. *Inorg. Chem.* **2010**, *49*, 5591.

(320) Berry, J. F.; Cotton, F. A.; Murillo, C. A. *Dalton Trans.* **2003**, *3015*.

(321) Baadji, N.; Piacenza, M.; Tugsuz, T.; Sala, F. D.; Maruccio, G.; Sanvito, S. *Nature Mat.* **2009**, *8*, 813.

(322) López, X.; Bénard, M.; Rohmer, M.-M. *J. Mol. Struct. Theochem.* **2006**, *777*, 53.

(323) Clérac, R.; Cotton, F. A.; Dunbar, K. R.; Murillo, C. A.; Pascual, I.; Wang, X. *Inorg. Chem.* **1999**, *38*, 2655.

(324) Kiehl, P.; Rohmer, M.-M.; Bénard, M. *Inorg. Chem.* **2004**, *43*, 3151.

(325) Tabookht, Z.; López, X.; Bénard, M.; de-Graaf, C. *J. Phys. Chem. A* **2010**, *114*, 12291.

(326) Tabookht, Z.; López, X.; de-Graaf, C. *J. Phys. Chem. A* **2010**, *114*, 2028.

(327) Cheng, C.-H.; Hung, R. D.; Wang, W. Z.; Peng, S. M.; Chen, I.-C. *ChemPhysChem.* **2010**, *11*, 517.

(328) Li, C.; Pobelov, I.; Wandlowski, T.; Bagrets, A.; Arnold, A.; Evers, F. *J. Am. Chem. Soc.* **2007**, *130*, 318.

(329) Li, X.; He, J.; Hihath, J.; Xu, B.; Lindsay, S. M.; Tao, N. *J. Am. Chem. Soc.* **2006**, *128*, 2135.

(330) Chen, F.; Li, X.; Hihath, J.; Huang, Z.; Tao, N. *J. Am. Chem. Soc.* **2006**, *128*, 15874.

(331) Meggers, E.; Michel-Beyerle, M. E.; Giese, B. *J. Am. Chem. Soc.* **1998**, *120*, 12950.

(332) Kim; Beebe, J. M.; Jun, Y.; Zhu, X. Y.; Frisbie, C. D. *J. Am. Chem. Soc.* **2006**, *128*, 4970.

(333) Ishida, T.; Mizutani, W.; Aya, Y.; Ogiso, H.; Sasaki, S.; Tokumoto, H. *J. Phys. Chem.* **2002**, *106*, 5886.

(334) He, J.; Chen, F.; Li, J.; Sankey, O. F.; Terazono, Y.; Herrero, C.; Gust, D.; Moore, T. A.; Moore, A. L.; Lindsay, S. M. *J. Am. Chem. Soc.* **2005**, *127*, 1384.

(335) Grosshenny, V.; Harriman, A.; Ziessel, R. *Angew. Chem. Int. Ed.* **1995**, *107*, 2921.

(336) Sedghi, G.; Sawada, K.; Esdaile, L. J.; Hoffmann, M.; Anderson, H. L.; Bethell, D.; Haiss, W.; Higgins, S. J.; Nichols, R. J. *J. Am. Chem. Soc.* **2008**, *130*, 8582.

(337) Meier, H. *Angew. Chem. Int. Ed.* **2009**, *121*, 3969.

(338) Liu, H.; Wang, N.; Zhao, J.; Guo, Y.; Yin, X.; Boey, F.; Zhang, H. *ChemPhysChem.* **2008**, *9*, 1416.

(339) Magoga, M.; Joachim, C. *Phys. Rev. B.* **1997**, *56*, 4722.

(340) Peng, G.; Strange, M.; Thygesen, K. S.; Mavrikakis, M. *J. Phys. Chem. C* **2009**, *113*, 20967.

(341) Sedghi, G.; K. Sawada; Esdaile, L. J.; Hoffmann, M.; Anderson, H. L.; Bethell, D.; Haiss, W.; Higgins, S. J.; Nichols, R. J. *J. Am. Chem. Soc.* **2008**, *130*, 8582.

(342) Liu, H.; Yu, C.; Gao, N.; Zhao, J. *ChemPhysChem.* **2010**, *11*, 1895.

(343) Wang, W.-Z.; Ismayilov, R. H.; Wang, R.-R.; Huang, Y.-L.; Yeh, C.-Y.; Lee, G.-H.; Peng, S.-M. *Dalton Trans.* **2008**, 6808.

(344) Chen, Y. H.; Lee, C.-C.; Wang, C.-C.; Lee, G. H.; Lai, S.-Y.; Li, F.; Mou, C. Y.; Peng, S. H. *Chem. Commun.* **1999**, 1667.